Photoinduced nonequilibrium states in Mott insulators

Yuta Murakami*

Institute for Materials Research, Tohoku University, Sendai, 980-8577, Japan and Center for Emergent Matter Science, RIKEN, Wako, Saitama 351-0198, Japan

Denis Golež*

Jožef Stefan Institute, Jamova 39, SI-1000 Ljubljana, Slovenia and Faculty of Mathematics and Physics, University of Ljubljana, Jadranska 19, 1000 Ljubljana, Slovenia

Martin Eckstein*

Institute of Theoretical Physics, University of Hamburg, 20355 Hamburg, Germany

Philipp Werner*

Department of Physics, University of Fribourg, 1700 Fribourg, Switzerland

(published 31 July 2025)

The study of nonequilibrium phenomena in interacting lattice systems can provide new perspectives on correlation effects and information on metastable states of matter. Mott insulators are a promising class of systems for nonequilibrium studies since they exhibit exotic phenomena and complex phase diagrams upon doping and because a large Mott gap provides protection against fast thermalization and heating after photoexcitations. One can thus expect the emergence of interesting nonlinear responses, transient states, and photoinduced phases in Mott systems. This review provides a comprehensive overview of the current understanding of photoexcited Mott insulators by discussing excitation protocols, nonlinear optical responses, the underlying mechanisms governing photocarrier dynamics, and the pathways leading to photoinduced metastable states. The review focuses on recent theoretical progress, identifies the relevant underlying concepts, and links them to experimental observations. The review starts with a general discussion of field-induced nonequilibrium setups and an overview of key experiments that revealed characteristic properties of photoexcited Mott states, proceeds with an overview of the theoretical tools that have been developed to investigate these strongly correlated nonequilibrium states, and then analyzes Mott insulators driven out of equilibrium by static electric fields, periodic fields, and short laser pulses. The appearance of nonthermal electronic orders in photoexcited Mott systems, including nonthermal spin and orbital orders, η-pairing states, and novel types of excitonic orders, is also discussed.

DOI: 10.1103/tkjh-lr83

CONTENTS

*All authors contributed equally to this work.

I. INTRODUCTION

The manipulation of material properties by intense laser pulses or other nonequilibrium protocols has led to surprising discoveries with potential for future technological applications, as discussed in various reviews (Giannetti *et al.*, 2016; Basov, Averitt, and Hsieh, 2017; Oka and Kitamura, 2019; de la Torre *et al.*, 2021; Koshihara *et al.*, 2022; Boschini, Zonno, and Damascelli, 2024). Mott insulators, or strongly correlated systems near a Mott phase, are particularly interesting platforms in this regard. They combine a high sensitivity to small perturbations—present already in equilibrium (see Sec. I.A)—with a robust energy gap that prevents trivial heating by the laser. While interesting nonequilibrium phenomena have been reported in these systems, both in experiments and in model studies, a full understanding of the underlying physics is often lacking. The aim of this review is to identify generic concepts governing the nonequilibrium physics of Mott systems, to explain their current theoretical interpretation, and to link them to prototypical experimental results.

A. Doped Mott insulators in equilibrium

Mott insulators are materials that should be metals according to band theory but are insulating because strong electron-electron interactions suppress charge fluctuations. If mobile electronlike or holelike charge carriers are introduced into these systems, many interesting phenomena can be induced, ranging from non-Fermi-liquid behavior to unconventional superconductivity (Imada, Fujimori, and Tokura, 1998). Mott-insulating phases exist in different classes of compounds, including transition metal oxides (NiO, La_2CuO_4, etc.) and molecular crystals (Cs_3C_{60}, κ-$[(BEDT\text{-}TTF)]_2Cu[N(CN)_2]Cl$, etc.). These materials exhibit partially filled narrow bands near the Fermi level, while Coulomb interactions comparable to or larger than the bandwidth act on the corresponding d, f, or molecular orbitals. Mott insulators often exhibit magnetic and/or orbital orders at low temperature (Tokura and Nagaosa, 2000; Dagotto, 2005), but, in contrast to weakly correlated systems with long-range order such as Slater antiferromagnets, a charge gap persists even above the ordering temperature.

In multiorbital systems, Mott-insulating behavior can be found for each open shell integer filling. The stability of these phases depends sensitively on the degeneracy of the levels, the crystal field splittings, and the Hund coupling (Georges, de' Medici, and Mravlje, 2013). In an orbitally degenerate system, a rough estimate of the interaction strength for which Mott-insulating behavior is expected can be obtained by comparing the charge excitation gap in the atomic limit, $E_{N+1} + E_{N-1} - 2E_N$, to the bandwidth. Here E_N denotes the energy for a filling of N electrons. Such an analysis reveals that in the usual case of a positive Hund coupling, the half-filled Mott phase with dominant high-spin configurations is the most stable one. The fullerides A_3C_{60}, however, exhibit an effectively negative Hund coupling owing to the dynamical Jahn-Teller effect (Fabrizio and Tosatti, 1997), which leads to qualitatively different properties, such as dominant low-spin states and a destabilization of the half-filled Mott phase (Capone *et al.*, 2009).

In some materials, such as transition metal oxides, ligand states can be energetically close to the partially filled narrow bands such that after the splitting of the narrow bands into lower and upper Hubbard bands, these states may overlap with or even appear above the lower Hubbard band. In such a situation, the lowest-energy charge excitation is not from the lower Hubbard band to the upper Hubbard band, but instead from the ligand band to the upper Hubbard band, and the material is classified as a charge-transfer insulator (Zaanen, Sawatzky, and Allen, 1985).

In equilibrium the Mott insulator-to-metal transition can be studied experimentally by changing the carrier concentration through chemical doping or by varying the bandwidth via the application of pressure. A sketch of the phase diagram of hole-doped cuprates is shown in Fig. 1(a), while the pressure-dependent phase diagram of fulleride compounds is illustrated in Fig. 1(b). These examples demonstrate a close connection among Mott-insulating behavior, magnetism, and superconductivity, as well as the appearance of other complex phases of matter, such as spin glass states or Jahn-Teller metals (Zadik *et al.*, 2015) near the Mott phase. Close to a Mott phase, one

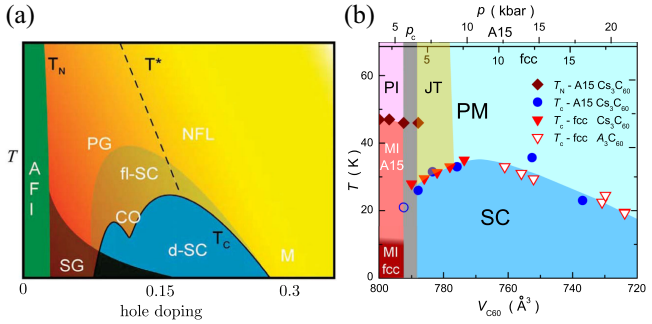

FIG. 1. (a) Schematic phase diagram of hole-doped cuprates featuring an antiferromagnetic (Mott) insulating (AFI) phase, a spin glass (SG) phase, a *d*-wave superconducting (d-SC) phase, a charge ordered (CO) phase, and a pseudogapped (PG) metal that crosses over into a non-Fermi-liquid (NFL) metal and conventional Fermi-liquid-like metal (M). The Néel temperature T_N, superconducting critical temperature T_c, and pseudogap crossover temperature T^* are also indicated. Adapted from Shen and Davis, 2008. (b) Phase diagram of fulleride compounds, with the bandwidth-controlled Mott transition marked by the vertical gray line. Magnetic-insulating (MI), paramagnetic-insulating (PI), paramagnetic metallic (PM), and superconducting (SC) phases are shown. We also sketch the Jahn-Teller (JT) metal phase reported by Zadik *et al.* (2015). Adapted from Ihara *et al.*, 2011.

typically observes an incoherent metallic state resulting from barely itinerant electrons (Imada, Fujimori, and Tokura, 1998) and the freezing of magnetic or orbital moments. Strong interactions between the charge carriers and spin, orbital, or lattice degrees of freedom can lead to the formation of polarons with heavy masses and non-Fermi-liquid behavior (Lee, Nagaosa, and Wen, 2006). Farther away from the Mott phase in the filling-versus-interaction plane, this incoherent metal crosses over into a more conventional Fermi-liquid metal (de' Medici, Mravlje, and Georges, 2011). Especially in the case of multiorbital systems, this crossover region is characterized by distinct non-Fermi-liquid properties (Werner *et al.*, 2008), and the enhanced fluctuations of local moments can lead to unconventional forms of superconductivity or excitonic order (Kuneš, 2015; Hoshino and Werner, 2016), which may compete with magnetic, orbital, and charge orders.

Several important properties of Mott insulators can be deduced from the single-particle spectral function, which shows the states accessible by adding or removing an electron. A good starting point for the theoretical analysis is the atomic limit. For example, in the most basic model for correlated electron systems, the single-band Hubbard model (Gutzwiller, 1963; Hubbard, 1963), the local Hamiltonian has the form $H_{\mathrm{loc}} = Un_\uparrow n_\downarrow - \mu(n_\uparrow + n_\downarrow)$, with n_σ measuring the number of electrons with spin σ, U the local interaction, and μ the chemical potential. In the particle-hole symmetric case ($\mu = U/2$), this becomes $H_{\mathrm{loc}} = U(n_\uparrow - 1/2)(n_\downarrow - 1/2)$ up to an irrelevant constant. The eigenenergies are $E_0 = E_2 = U/4$ for the empty and doubly occupied states and $E_\uparrow = E_\downarrow = -U/4$ for the singly occupied states. Hence, in the half-filled ground state, the electron addition spectrum exhibits a peak at $\omega = E_2 - E_\sigma = U/2$, while the energy removal spectrum has a peak at $\omega = E_\sigma - E_0 = -U/2$ corresponding to a gap of size U. If a small hopping between the lattice sites is turned on, these δ-function peaks broaden into Hubbard bands. The resulting local spectral function is sketched for a paramagnetic (PM) system in the top row of Fig. 2(a), where the gray shaded area indicates the electron removal spectrum (filled states). The filled lower Hubbard band and the empty upper Hubbard band represent the addition and removal of an electron to or from the Mott ground state, respectively. As the ground state consists of predominantly singly occupied sites, up to virtual charge fluctuations, adding (removing) electrons leads to excitations that are mainly of doubly occupied (empty) character. These mobile excitations, which also play a key role in photoexcited systems, are therefore called doublons and holes (or holons) in the following.

If the chemical potential is shifted into the upper Hubbard band, a certain population of doublons is produced by chemical doping. In the PM state, these doublons can move in the background of half-filled sites, which turns the Mott insulator into a correlated metal. As shown in the bottom row of Fig. 2(a), the doublons form a narrow quasiparticle band at the edge of the Hubbard band, while the gap to the lower Hubbard band persists. This doped Mott insulator state can exhibit Fermi-liquid properties, albeit with a strongly enhanced effective mass of the charge carriers (Lee, Nagaosa, and Wen, 2006; Werner and Millis, 2007a).

Below the Néel temperature, the Hubbard bands split into spin-polaron bands (Dagotto, 1994; Sangiovanni *et al.*, 2006), as illustrated in the second column of Fig. 2(a), which shows the minority-spin spectral function of the half-filled system. These features (which are absent in $D = 1$ owing to spin-charge separation) are the result of the strong spin-charge coupling in dimensions $D \geq 2$. If a doublon or holon moves in an antiferromagnetic (AFM) spin background, each hop breaks several AFM bonds, at an energy cost proportional to the spin exchange J_{ex}. This leads to a large effective mass and near localization of the charge carriers. The properties of the spin-polaron peaks were worked out in detail for a single hole in the *t*-*J* model (Trugman, 1988; Kane, Lee, and Read, 1989; Strack and Vollhardt, 1992; Dagotto, 1994; Jaklič and Prelovšek, 2000). The fine structures with characteristic energy J_{ex} can be understood as signatures of a particle moving in a linear potential (produced by so-called string states), and they indicate a large polaron mass. Further doping leads to intricate low-energy phenomena that require a proper description of short-range correlations and that were analyzed in previous reviews (Dagotto, 1994; Maier *et al.*, 2005; Lee, Nagaosa, and Wen, 2006). At high enough doping, the AFM spin background is reduced or completely suppressed, resulting in a spectral function similar or identical to that of the doped PM system.

Substructures in the Hubbard bands can also result from a strong coupling to optical phonons or other bosonic excitations, such as collective charge excitations (plasmons), as shown in the third column of Fig. 2(a). In the former case, the separation between the polaronic subbands is given by the phonon frequency ω_0. For large couplings, the entire electronic band can split up into sidebands with exponentially decaying weights at high energies. In the case of the upper (lower) Hubbard band, the high-energy subbands correspond to an electron insertion (removal) with multiple phonon

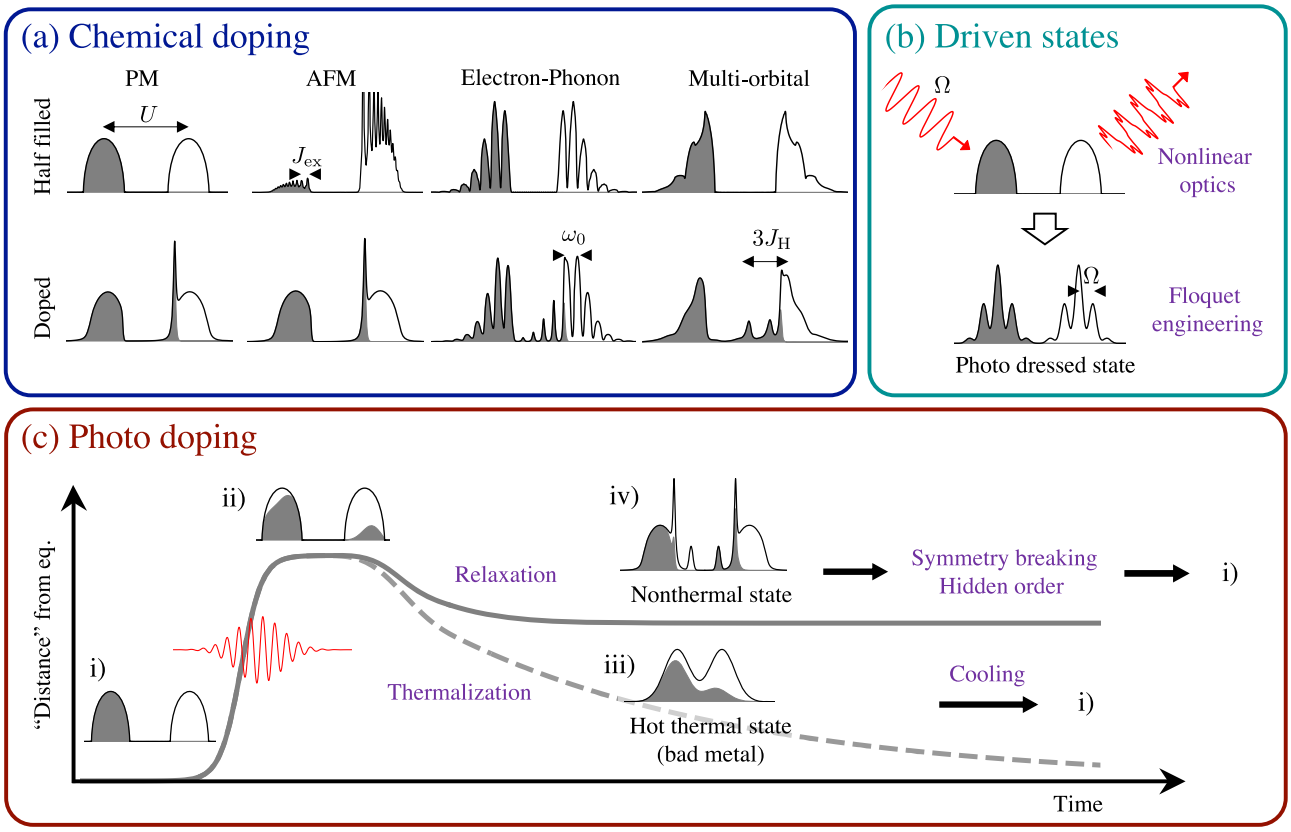

FIG. 2. Single-particle spectral functions of Mott systems. (a) Spectral functions of undoped and doped Mott insulators. The panels in the top row show the spectral functions (black line) and occupations (gray shading) of the paramagnetic (PM) Hubbard model, the minority-spin component of the antiferromagnetic (AFM) Hubbard model, the Holstein-Hubbard model, and the two-orbital Hubbard model at half filling. The panels in the bottom row show the spectra and occupations for doped systems. The arrows indicate how the different energy scales (Hubbard U, antiferromagnetic exchange J_{ex}, phonon frequency ω_0, and Hund coupling J_H) are imprinted in the spectrum. (b) Modification of the spectrum of a Mott insulator by periodic driving with frequency Ω. (c) Illustration of stages (i)–(iv) in the excitation and relaxation process of photodoped Mott system. In large-gap Mott insulators [stage (iv)], the intraband relaxation leads to distinct nonthermal quasiparticle distributions. In small-gap Mott insulators [stage (iii)], fast thermalization to a bad metallic state with elevated temperature is expected.

emissions. (If the temperature is of order ω_0, phonons become thermally occupied and sidebands associated with phonon absorption upon electron addition would show up in the gap region.) In addition, chemically doped doublons form dressed polarons. Hence, the removal of a doublon can partially release the phonon cloud and leave the system with additional phonon excitations, as manifested by a series of new in-gap sidebands in the electron removal spectrum, which extends from the upper Hubbard band into the gap region. At least in simple model calculations, the phonon sidebands are much more robust against doping (and heating) than the spin-polaron sidebands.

Finally, multiorbital Hubbard models exhibit rich multiplet structures (Kanamori, 1963; Georges, de' Medici, and Mravlje, 2013). For example, in the case of a two-orbital model with density-density interactions, the Hund coupling J_H distinguishes the energies of the half-filled configurations with two electrons in the same orbital ($E_{\text{int}} = U$) in both orbitals with opposite spin ($E_{\text{int}} = U - 2J_H$) and in both orbitals with parallel spin ($E_{\text{int}} = U - 3J_H$). At low temperatures almost all the sites of the half-filled Mott insulator are in the high-spin configuration, which results in Hubbard bands with a separation of approximately $U + J_H$. The higher-energy substructures seen in the spectral function in the fourth row of Fig. 2(a) can be associated with electron insertion or removal processes with additional high-spin or low-spin excitations on neighboring sites. Once the chemical potential is shifted into the upper Hubbard band, long-lived "triplons" are inserted into the half-filled background of high-spin doublon states. Removing an electron from these triplons can produce any of the three possible half-filled configurations, which results in three occupied (side) peaks near the upper Hubbard band. The partial occupation of the main Hubbard band is associated with the creation of a high-spin doublon with $E_{\text{int}} = U - 3J_H$, the first sideband with a low-spin doublon with $E_{\text{int}} = U - 2J_H$ and the second sideband with a low-spin doublon with $E_{\text{int}} = U$. Similar in-gap features would also show up at half filling, once the temperature becomes of the order of J_H. The existence of long-lived triplons in the doped case also leads to the appearance of high-energy features in the unoccupied part of the spectrum, which can be linked to the creation of quadruplons.

The aforementioned summary of how chemical doping affects the spectral function of equilibrium Mott insulators

provides a useful guide to the discussion of photoexcited Mott insulators. These photoexcited systems can sometimes be interpreted as being simultaneously electron and hole doped.

B. Photoexcited Mott insulators: An overview

For the understanding of photoexcited Mott states, it is useful to distinguish two types of nonequilibrium settings. The first type involves states whose nonthermal properties are induced and supported by a persistent external drive, such as quasistatic or time-periodic fields; see Fig. 2(b). In the second setting, a pulsed field or other perturbation produces electronic excitations across the Mott gap and triggers a sequence of characteristic relaxation steps; see Figs. 2(c)(i)–2(c)(iv). This can lead to thermalization at an elevated temperature [path (iii)] or, under suitable conditions, to the realization of photoinduced phases with interesting properties [path (iv)]. In Secs. I.B.1 and I.B.2, we summarize important concepts and phenomena related to these settings. This overview is meant to serve as a guide for the review.

1. Driven states

A widely studied class of nonequilibrium states encompasses (quasi)steady or time-periodic states emerging in the presence of an external drive; see Fig. 2(b). The application of external fields can result in modified effective Hamiltonian parameters, which is the basis of Floquet engineering (Bukov, D'Alessio, and Polkovnikov, 2015; Eckardt, 2017; Oka and Kitamura, 2019; de la Torre *et al.*, 2021). A well-known example is the realization of the Haldane model in a honeycomb lattice system subject to circularly polarized fields (Oka and Aoki, 2009; Kitagawa *et al.*, 2011). This theoretical proposal has been realized in cold-atom simulators (Jotzu *et al.*, 2014) and in solids (McIver *et al.*, 2020), where the latter are generally more challenging owing to the strong energy absorption from the drive. Band structure engineering can also be achieved in Mott systems; see Sec. V.A. Here unwanted heating can be suppressed if the driving frequency lies within the transparency window set by the Mott gap. In addition to the band structure renormalization, the spectrum of the driven state can exhibit Floquet sidebands (photon-dressed states) (Wang *et al.*, 2013), which can effectively reduce the gap in Mott systems; see Fig. 2(b). Moreover, Mott insulators provide interesting opportunities for controlling the low-energy physics of spins and orbitals using external driving; see Sec. V.D.

As in the case of Floquet engineering, the application of strong dc fields dresses the many-body ground state. This effect is relevant, for example, in experiments with strong terahertz fields, which can be regarded as quasistatic fields on the femtosecond electronic timescale. Floquet and strong-field physics are closely related in many ways. Quasistatic fields can give rise to sidebands (Wannier-Stark bands) (see Sec. IV.A), and they may be used to modify low-energy Hamiltonians in a manner than is analogous to Floquet engineering (see Sec. IV.B).

Not only the laser field itself but also coherent excitations in the material can produce a periodic driving. The most prominent mechanism along these lines is nonlinear phononics (Först *et al.*, 2011), where the coherent oscillation of one phonon mode can—in the presence of anharmonicity—lead to a nonzero time-averaged displacive force on other phonon modes. Similarly, the nonlinear coupling to the coherently excited phonon can affect the electrons, for example, through induced magnetic or pairing interactions, or the modification of the Hubbard U; see Sec. V.H. An interesting question is whether related protocols enable efficient switching pathways between different phases.

Finally, excitations with strong fields are accompanied by nonlinear optical effects such as high-harmonic generation; see Sec. V.G. Nonlinear responses can be used to explore the energy landscape around equilibrium states or to track the quasiparticle dynamics in driven states. It is thus important to understand the mechanisms that control these nonlinear optical responses.

2. Photodoped states

In this subsection we discuss the different stages in the evolution of a Mott system after a pulsed excitation; see Fig. 2(c). Strong electric fields acting on a Mott insulator can create mobile charge carriers, such as doublons and holons in the single-orbital case. This amounts to a transfer of occupied spectral weight from the lower to the upper Hubbard band; see Figs. 2(c)(i) and 2(c)(ii). Although the total number of electrons remains unchanged, this process is referred to in this review as photodoping. The formation of photodoped states and their properties, lifetime, and decay have been subject to numerous experimental (see Sec. I.C) and theoretical (see Sec. VI) investigations, and the analysis of these processes and phenomena constitutes a main part of this review.

Excitation across the Mott gap. To begin, the possible excitation pathways deserve a closer look, as their detailed understanding may help to design tailored excitation protocols. Both the creation of doublons and holons within the same band and the charge transfer between different bands correspond to optically active transitions and can be achieved in linear absorption using frequencies resonant to the gap; see Sec. VI.A. Moreover, carriers can be generated via nonlinear (strong-field) processes, such as tunneling across the Mott gap (see Sec. IV.C) or multiphoton absorption (see Sec. V.F). The crossover between the two nonlinear mechanisms is the many-body analog of the Keldysh crossover.

Electron thermalization. The common assumption for an interacting electron system is that electron-electron scattering leads to fast thermalization, even before the energy is passed on to phonons or other degrees of freedom. A thermal state is entirely characterized by the total electron number and the electronic temperature T_e, so the total absorbed energy would be all that matters for the electronic excitation process. Whether, and on what timescale, an interacting isolated quantum system shows such ergodic behavior is a fundamental question in many-body physics (Polkovnikov *et al.*, 2011; D'Alessio *et al.*, 2016).

In laser-excited metals, on timescales larger than a few hundred femtoseconds, the formation of a quasithermal "hot-electron state" is commonly assumed, even in good metals where the electron-electron interaction is weak. This provides

the basis for the conventional few-temperature descriptions of photoexcited phases (Allen, 1987). However, increasing the interaction strength to the strong correlation regime does not necessarily lead to faster thermalization. In particular, theoretical and experimental evidence shows that the Mott gap provides a bottleneck against rapid thermalization (see Sec. VI.G), which is a key ingredient for the realization of interesting nonequilibrium states (see Sec. VII). Fast thermalization, in contrast, is still expected in the metal-insulator crossover regime and for small-gap Mott insulators; see Fig. 2(c)(iii). In this case, however, even a thermal hot-electron state can be highly nontrivial. For example, strong interactions can lead to unconventional bad metallic behavior at temperatures as high as the electronic bandwidth. In equilibrium, this regime lies beyond the melting temperature of most solids and needs to be studied in model calculations or cold-atom simulators. Ultrafast laser experiments can access this regime in transient states and help to clarify the properties of correlated electrons at high temperatures (Choi *et al.*, 2024), as noted early on in the context of time-resolved angle-resolved photoemission spectroscopy (ARPES) studies (Perfetti *et al.*, 2006); see Sec. I.C.

Electron relaxation. If the Mott gap is sufficiently large to prevent rapid thermalization, the system relaxes to a transient nonthermal state; see the evolution from (ii) to (iv) in Fig. 2(c). In this nonthermal state, the relative populations of the local states are no longer fixed by the electronic temperature, as they would be in a thermal state. This also implies that the thermalization process, which takes place on longer timescales, generically involves charge carrier production or recombination.

In the initial relaxation to the nonthermal state, photodoped carriers lose kinetic energy owing to their interactions with bosonic degrees of freedom, such as antiferromagnetically correlated spins, phonons, or plasmons; see Sec. VI.D. This intra-Hubbard-band relaxation eventually leads to doublon and holon populations with a thermal-like distribution, but separate chemical potentials for the doublons and holons. Theoretically, such (quasi)steady states can often be described using methods specifically adapted to nonequilibrium stationary states or to quasiequilibrium states; see Sec. III.D. Since effectively cold photodoped states may exhibit nontrivial electronic orders, it is relevant to think about nonequilibrium protocols that actively cool the charge carrier distributions in the Hubbard bands; see Sec. VI.D.4.

Nonequilibrium quasiparticles. Microscopic insights into the nonequilibrium response and properties of photodoped systems can be obtained by analyzing the nature of photodoped quasiparticles; see Sec. VI. Typically, charge carriers are initially produced with excess kinetic energy and subsequently get dressed through their interaction with phonons (see Sec. VI.D.2) and spins (see Sec. VI.D.3), resulting in the previously described cooling. After the intraband relaxation, quasiparticle features or in-gap states can appear in the spectral function. They are similar to the case of chemically doped Mott insulators [see Fig. 2(a)], but now there are features associated with both electronlike and holelike charge excitations [compare the doped spectra of Fig. 2(a) to Fig. 2(c)(iv)]. Moreover, quasiparticles in Mott insulators can be bound into excitons by the nonlocal Coulomb interaction or by interactions mediated by bosonic fluctuations; see Sec. VI.E.

Photoinduced phase transitions. If photoexcited states of correlated electron systems are sustained for a sufficiently long time, excitations beyond some threshold can drive the system into new nonthermal phases. Experimental observations include the switching to hidden insulating (Onda *et al.*, 2008; Ichikawa *et al.*, 2011) and metallic phases (Stojchevska *et al.*, 2014) or metastable superconductinglike states (Budden *et al.*, 2021). While none of these experimental observations are completely understood, several pathways leading to nonthermal phases have been proposed for Mott systems. In a Mott insulator or charge-transfer insulator, excitations of electrons across the gap will induce changes in the electronic structure. This includes both band shifts resulting from the redistribution of electrons between different orbitals and possible modifications of the local interaction parameters via changes in the screening environment; see Sec. VI.F. Both effects play an important role in photoinduced insulator-metal transitions. As a second mechanism, the nonthermal melting of long-range order (in particular, in the presence of competing orders) can lead to the transient stabilization of nonthermal symmetry-broken phases; see Sec. VII.E.1. Finally, an interesting playground for novel photoinduced phases are the aforementioned long-lived photodoped states. For sufficiently cold charge carrier distributions, the liquid of photodoped carriers may become unstable toward the formation of new orders. Theoretical predictions include hidden η-pairing states, as well as nonthermal magnetic, orbital, spin-orbital, and odd-frequency orders that cannot be stabilized under equilibrium conditions; see Sec. VII.E. Often, the photoinduced electronic orders strongly couple to the lattice, which may further stabilize a hidden state.

C. Experiments on photoexcited Mott states

The aforementioned phenomena in nonequilibrium Mott systems have been experimentally explored in both materials and cold-atom simulators. The latter provide a platform that allows to experimentally realize the models typically considered in theoretical studies (Bloch, Dalibard, and Zwerger, 2008; Gross and Bloch, 2017). Materials investigations often involve pump-probe setups (Giannetti *et al.*, 2016; Boschini, Zonno, and Damascelli, 2024) in which one of the following spectroscopies is used to probe the electronic properties.

Time-resolved optics. Time-resolved optics measures the evolution of optical responses, such as the absorption, reflection, and transmission of the probe field. An insulating state is characterized by a gap in the absorption spectrum. From modifications of the linear optical spectrum, one can detect the metallization of the system, the renormalization of the gap, and the emergence of photoinduced in-gap structures. Moreover, nonlinear responses can provide additional insights. For example, the second harmonic signal is a sensitive probe of inversion symmetry breaking. The use of even-higher-order responses as a probe is a currently active research direction.

Time-resolved photoemission spectroscopy. Photoemission spectroscopy (PES) analyzes the electrons ejected from the

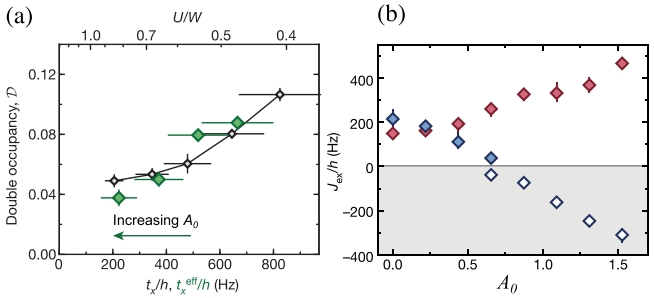

FIG. 3. Three-dimensional cold-atom system with driving frequency $\Omega \gg U, t_x, t_y, t_z$ and driving strength A_0. (a) Comparison of the double occupation $\mathcal{D}$ of the periodically driven system (open symbols) and the effective Floquet system (green symbols). (b) Exchange coupling in the limit of isolated dimers with $U > \Omega$ (red symbols) and $U < \Omega$ (blue symbols) that becomes negative for stronger driving (open symbols). $\Omega, U \gg t_x$, and the two dimer sites are along the x direction. From Görg *et al.*, 2018.

solid by the probe light. Time-resolved PES measures the evolution of the occupied part of the single-particle spectrum, and its angle-resolved version (ARPES) allows the dispersion of energy bands to be mapped out (Boschini, Zonno, and Damascelli, 2024). With this approach one can directly track the relaxation dynamics of photocarriers, as well as the renormalization of bands or gaps. However, owing to the charging effects, it is difficult to apply PES to large-gap insulators.

Time-resolved x-ray spectroscopy. Time-resolved x-ray absorption spectroscopy (XAS) and resonant inelastic x-ray scattering (RIXS) involve charge neutral excitations and are sensitive to the unoccupied states, which makes them particularly useful tools for nonequilibrium investigations of insulators. The absorption peaks in XAS can be used to identify the positions of bands, and the thermal or nonthermal population of different local states. In the RIXS process, a core electron is excited into a valence state, creating an intermediate state that lasts for a few femtoseconds, until the core hole is filled via emission of an x-ray photon (Ament *et al.*, 2011). The analysis of the emitted radiation provides information on single-particle and collective excitations within the valence manifold. Because of the large momentum of x-ray photons, the dispersions of spin, orbital, and charge excitations can be measured. Local transitions between multiplet states give rise to sharp excitation peaks, with energy splitting of the order of the Hund coupling, while inter-(Hubbard-)band excitations manifest themselves as broad charge-transfer features at higher energies. Time-resolved RIXS measurements have recently become possible thanks to the development of x-ray free-electron lasers (Bostedt *et al.*, 2016), which enable investigations of the dynamics of spin and charge correlations (Dean *et al.*, 2016; Mitrano *et al.*, 2019; Paris *et al.*, 2021).

In the following, we discuss a selection of nonequilibrium experiments on Mott systems to relate the measured phenomena to the concepts introduced in Sec. I.B. Additional experimental results are discussed in Secs. IV–VI.

1. Periodically driven systems

An example of Floquet engineering of strongly correlated fermion systems was demonstrated with cold-atom simulators. Görg *et al.* (2018) implemented the Hubbard model on a three-dimensional lattice with anisotropic hoppings $t_i(\equiv v_{0i})$, where $i \in \{x, y, z\}$, and, by shaking the optical lattice, mimicked the effect of a time-periodic electric field with frequency Ω along the x direction. The double occupation $\mathcal{D}$ was measured in the driven state. In the off-resonant regime ($\Omega \gg U, t_x, t_y, t_z$), the Floquet Hamiltonian predicts an effective reduction of t_x. This leads to a suppression of $\mathcal{D}$ (enhanced correlations), as shown in Fig. 3(a), and the results indeed match the prediction from Floquet theory. In the near-resonant regime with $\Omega, U \gg t_x, t_y, t_z$, the spin exchange coupling can be enhanced or reduced or can change the sign, depending on Ω and the field strength A_0 (Mentink, Balzer, and Eckstein, 2015); see Sec. V.D. The cold-atom experiments observed hints of an enhancement of antiferromagnetic correlations for $U > \Omega$, while the sign of the spin correlations changed at sufficiently strong fields for $U < \Omega$. The exchange coupling of isolated two-site systems behaves in a similar way under periodic driving; see Fig. 3(b).

2. Photodoped systems

The photocarrier generation and relaxation and the associated modifications of physical properties have been studied in solids using various time-resolved spectroscopic tools.

Carrier dynamics and heating. With time-resolved PES, one can monitor the dynamics of the photocarriers as well as changes in the band structure. An interesting example is the polaronic insulator $1T$-TaS_2, which is often described as a small-gap single-orbital Mott insulator, although the precise nature of the insulating state is under debate (Kratochvilova *et al.*, 2017; Butler *et al.*, 2020; Petocchi *et al.*, 2022). After a relatively weak excitation, the PES signal reveals the partial occupation of the upper Hubbard band (Ligges *et al.*, 2018), as illustrated by the feature inside the dashed box in Fig. 4(a). From the time evolution of this signal, the doublon lifetime

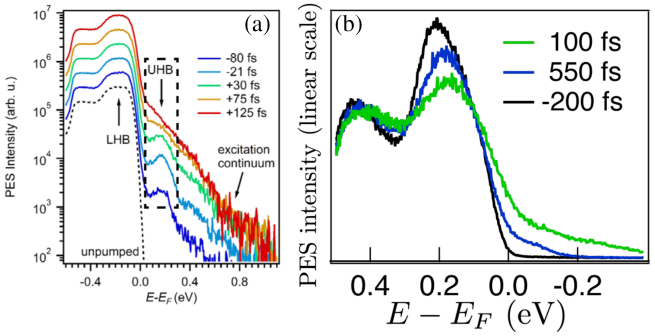

FIG. 4. (a) Time-resolved PES signal in the weak excitation limit shown with arbitrary offsets from the unpumped system (dashed line) with a fully occupied lower Hubbard band (LHB). The partial occupation of the upper Hubbard band (UHB) by doublons gives rise to the signal inside the dashed box. Adapted from Ligges *et al.*, 2018. (b) Photoexcitation with a strong pulse results in a rapid partial filling of the gap. Adapted from Perfetti *et al.*, 2006.

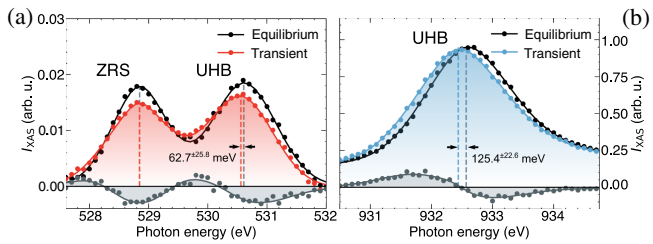

FIG. 5. Pump-induced change in the XAS signal at (a) the O K edge and (b) the Cu L_3 edge in $La_{2-x}Ba_xCuO_4$ ($x = 9.5\%$). The black lines show the equilibrium spectra before the pump pulse. The colored lines show the XAS signals of the pumped system at pump-probe delay $\Delta t \approx 0$ ps, and the gray lines show the difference between the photoexcited and equilibrium spectra. ZRS, Zhang-Rice singlet; UHB, upper Hubbard band. From Baykusheva *et al.*, 2022.

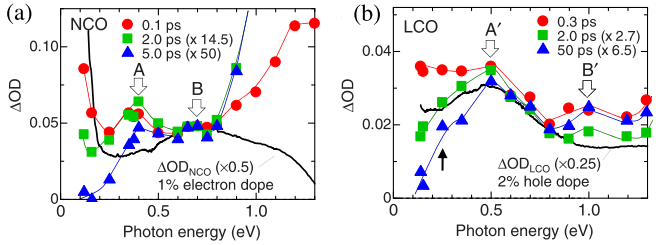

FIG. 6. Time-resolved change in the absorption spectra of photodoped (a) Nd_2CuO_4 (NCO) and (b) La_2CuO_4 (LCO) with midgap absorption peaks marked by empty arrows. The black lines show the change in the equilibrium absorption upon chemical doping. OD stands for optical density. Adapted from Okamoto *et al.*, 2010.

can be extracted. The surprisingly short (< 100 fs) lifetime, compared to theoretical predictions for half-filled Mott insulators (Eckstein and Werner, 2011), led Ligges *et al.* (2018) to conclude that the measured 1T-TaS_2 sample may have been intrinsically hole doped. Metallic low-energy states enable an efficient doublon-holon recombination and remove the thermalization bottleneck that is characteristic of Mott insulators; see Sec. VI.G. An alternative explanation for the short lifetime could be that 1T-TaS_2 is not a simple Mott insulator but features a bonding-antibonding gap associated with bilayer structures, especially in the bulk region (Petocchi *et al.*, 2023). Using a stronger pump pulse, Perfetti *et al.* (2006) observed a fast (< 100 fs) partial filling of the Mott gap; see Fig. 4(b). This was attributed to strong heating, which should induce a transition from the Mott insulator phase to the high-temperature incoherent metallic state in the metal-insulator crossover regime [thermalization in a hot metal state; see Fig. 2(c)]. This interpretation was supported by equilibrium dynamical mean-field theory (DMFT) calculations at high temperatures.

Dynamical screening and band shifts. In nonequilibrium states, photoinduced charge carriers can modify the electronic structure; see Fig. 2(c). Time-resolved XAS provides valuable insights into these modifications. For example, Baykusheva *et al.* (2022) studied a slightly hole-doped cuprate $La_{2-x}Ba_xCuO_4$ ($x = 9.5\%$) and revealed an almost instantaneous redshift of the feature associated with the upper Hubbard band, after a pump excitation with a 1.55 eV laser (Ω is approximately equal to the gap), while the peak associated with the Zhang-Rice singlet barely moves; see Fig. 5. Similar results were recently reported for above-gap excitations in NiO, where in addition to the shift of the upper Hubbard band, side peaks related to local many-body multiplet excitations could be resolved (Lojewski *et al.*, 2024). The observed band shifts have been interpreted as evidence for a photoinduced change in the on-site Hubbard interaction (Baykusheva *et al.*, 2022). While changes in dynamical screening can lead to reduced Mott gaps (Golež, Eckstein, and Werner, 2015; Tancogne-Dejean, Sentef, and Rubio, 2018), spectral shifts of the type reported in Fig. 5 could also result from photoinduced Hartree shifts, since the pump pulse redistributes charge between the orbitals; see Sec. VI.F.

Metallization and in-gap states. Photocarriers turn a Mott insulator into a nonthermal metal whose formation and decay can be investigated with time-resolved optics. As an example, Fig. 6 shows the change in the absorption ΔOD (OD stands for optical density) in Nd_2CuO_4 [(NCO), Fig. 6(a)] and La_2CuO_4 [(LCO), Fig. 6(b)] in the visible to infrared (IR) region (Okamoto *et al.*, 2010). In both materials a photoinduced metallic state with a Drude-like absorption peak is formed on a timescale much shorter than the 200 fs time resolution of the experiment, as seen in the low-energy upturn of the signal measured at 0.1 ps in Fig. 6(a). This upturn is similar to the change in the absorption that is induced in equilibrium NCO via 1% electron doping. Other noteworthy features are the midgap peaks indicated by A and B (A′ and B′) in NCO (LCO). These form on a somewhat slower timescale than the Drude peak and resemble the structures in chemically doped systems (Uchida *et al.*, 1991). Okamoto *et al.* (2010) associated the midgap features with (spin) polarons, but they could also be related to Mott excitons (Jeckelmann, 2003) or nonthermal state populations. The midgap features result from the intraband relaxation and are a manifestation of a photodoped quasisteady state [see Fig. 2(c)] since they persist up to long times on the order of 10 ps. The Drude feature itself disappears after a few picoseconds, presumably owing to trapping of the mobile charge carriers.

3. Strongly correlated photoinduced phases

Interest in nonthermal phases has been stimulated by noteworthy experiments indicating that long-lived states with novel properties can be photoinduced in certain correlated materials. Metastable states with nonthermal lattice structures were reported in manganite thin films ($Nd_{0.5}Sr_{0.5}MnO_3$) (Ichikawa *et al.*, 2011), $LaTe_3$ (Kogar *et al.*, 2020), and Ca_2RuO_4 subject to epitaxial strain (Verma *et al.*, 2023). Demonstrations that the correlated insulator 1T-TaS_2 can be switched into a long-lived hidden metallic state via 35 fs laser pulses (Stojchevska *et al.*, 2014) or slower voltage pulses (Hollander *et al.*, 2015) have triggered a large number of experimental studies and the development of the first ultrafast memory devices based on the switching between hidden and thermal states of matter (Vaskivskyi *et al.*, 2016). A similar photoinduced transition from an insulating to a hidden metallic state was also observed in manganite films

(Zhang *et al.*, 2016). The community has furthermore been captivated by reports of light-induced superconductinglike states in laser-driven cuprates (Fausti *et al.*, 2011; Hu *et al.*, 2014; Kaiser *et al.*, 2014b; Katsumi *et al.*, 2023), iron-based compounds (Suzuki *et al.*, 2019), and strongly correlated organic compounds (Mitrano *et al.*, 2016; Buzzi *et al.*, 2020). While the mechanisms underlying these phenomena are not yet fully understood, these and related experiments have motivated investigators to search for hidden phases, and, in particular, nonthermal electronic orders, in model systems.

II. MODELS

A. Models for strongly correlated lattice fermions

The theoretical discussions in this review are based mostly on simple but relevant models, which we list in this section. The most basic model for the study of Mott insulators is the single-band Hubbard model (Gutzwiller, 1963; Hubbard, 1963),

$$H_{\mathrm{Hub}} = -\sum_{i,j,\sigma} v_{ij} c^{\dagger}_{i\sigma} c_{j\sigma} - \mu \sum_{i,\sigma} n_{i\sigma} + U \sum_{i} n_{i\uparrow} n_{i\downarrow}, \quad (1)$$

which describes electrons on a lattice with hopping amplitude v_{ij}, chemical potential μ, and on-site repulsion U. In Eq. (1) $c_{i\sigma}$ denotes the annihilation operator for an electron on site i with spin σ and $n_{i\sigma} = c^{\dagger}_{i\sigma} c_{i\sigma}$ is the density operator. In the large-U regime, the spectral function of this model features upper and lower Hubbard bands separated by an energy U, as sketched in Fig. 2(a).

Relevant observables are the double occupation

$$\mathcal{D}(t) = \langle n_{\uparrow}(t) n_{\downarrow}(t) \rangle, \quad (2)$$

as well as the potential and kinetic energies

$$E_{\mathrm{pot}}(t) = N_{\mathrm{sites}} U \mathcal{D}(t), \quad (3)$$

$$E_{\mathrm{kin}}(t) = -\sum_{i,j,\sigma} v_{ij} \langle c^{\dagger}_{i\sigma}(t) c_{j\sigma}(t) \rangle = \sum_{\mathbf{k}\sigma} \epsilon_{\mathbf{k}}(t) n_{\mathbf{k}\sigma}(t), \quad (4)$$

where $n_{\mathbf{k}\sigma} = \langle c^{\dagger}_{\mathbf{k}\sigma} c_{\mathbf{k}\sigma} \rangle$ is the momentum occupation and $\epsilon_{\mathbf{k}}$ is the free-electron dispersion obtained as the lattice Fourier transform of $-v_{ij}$.

In the limit of large U and at half filling, the low-energy physics of Eq. (1) is described by the Heisenberg model. In the case of nearest-neighbor hopping v_0, it is given by

$$H_{\mathrm{J}} = \frac{J_{\mathrm{ex}}}{2} \sum_{\langle i,j \rangle} \mathbf{S}_i \cdot \mathbf{S}_j, \quad (5)$$

where $\mathbf{S}_i = (1/2) \sum_{\alpha,\beta} c^{\dagger}_{i\alpha} \boldsymbol{\sigma}_{\alpha,\beta} c_{i\beta}$ is the spin operator at site i, written with the vector $\boldsymbol{\sigma}$ of Pauli matrices. $\langle i,j \rangle$ denotes nearest-neighboring sites ($\langle i,j \rangle \neq \langle j,i \rangle$), and $J_{\mathrm{ex}} = 4v_0^2/U$ is the antiferromagnetic exchange coupling between neighboring spins induced by virtual doublon-holon fluctuations. In the hole-doped case, the low-energy physics is described by the t-J model (Chao, Spalek, and Oles, 1977; Gros, Joynt, and Rice, 1987),

$$H_{\mathrm{tJ}} = -v_0 \sum_{\langle i,j \rangle,\sigma} \tilde{c}^{\dagger}_{i\sigma} \tilde{c}_{j\sigma} - \mu \sum_{i,\sigma} \tilde{n}_{i\sigma} + \frac{J_{\mathrm{ex}}}{2} \sum_{\langle i,j \rangle} \mathbf{S}_i \cdot \mathbf{S}_j. \quad (6)$$

In Eq. (6) doubly occupied sites are projected out and $\tilde{c}^{\dagger}_{i\sigma} = c^{\dagger}_{i\sigma}(1 - n_{i\bar{\sigma}})$ and $\tilde{c}_{i\sigma} = c_{i\sigma}(1 - n_{i\bar{\sigma}})$ are projected creation and annihilation operators. An additional nearest-neighbor density-density term is omitted for simplicity.

A minimal model to describe the coupling of a Mott insulator to phonons is the Holstein-Hubbard model, which extends the Hubbard Hamiltonian in Eq. (1) by a local coupling (strength g) of the density $n_i = n_{i\uparrow} + n_{i\downarrow}$ to dispersionless phonons with frequency ω_0 (Holstein, 1959),

$$H_{\mathrm{HH}} = H_{\mathrm{Hub}} + \sum_{i} \left(\sqrt{2} g (n_i - 1) X_i + \frac{\omega_0}{2} (X_i^2 + P_i^2) \right). \quad (7)$$

In Eq. (7), X_i and P_i are canonical displacement and momentum operators of the oscillator ($[X_j, P_j] = i$). The effective electron-phonon coupling strength is often characterized by the parameter $\lambda = 2(g^2/\omega_0)$, which (up to the sign) corresponds to the phonon-induced static attraction.

Another relevant extension of the model in Eq. (1) is the U-V Hubbard model with local interaction U and nearest-neighbor interaction V,

$$H_{\mathrm{UV}} = H_{\mathrm{Hub}} + \frac{V}{2} \sum_{\langle i,j \rangle} n_i n_j, \quad (8)$$

which captures the effects of nonlocal screening and the formation of charge order.

Additional complexity is introduced by adding orbital degrees of freedom. The multiorbital extension of the Hubbard model combines a general hopping term H_{hop} with the Kanamori interaction (Kanamori, 1963),

$$H = H_{\mathrm{hop}} + U \sum_{i,\alpha} n_{i\alpha\uparrow} n_{i\alpha\downarrow} + U' \sum_{i,\alpha>\beta,\sigma} n_{i\alpha\sigma} n_{i\beta\bar{\sigma}} + (U' - J_{\mathrm{H}}) \sum_{i,\alpha>\beta,\sigma} n_{i\alpha\sigma} n_{i\beta\sigma} + H_{\text{sf-ph}}, \quad (9)$$

where α labels the orbitals, J_{H} is the Hund coupling, U denotes the intraorbital interaction, U' indicates the interorbital opposite-spin interaction, and $U' - J_{\mathrm{H}}$ denotes the interorbital same-spin interaction. An overline over the spin index σ marks the opposite spin. For a two- or three-orbital Hamiltonian that is rotationally invariant in spin and orbital space, one has to choose $U' = U - 2J_{\mathrm{H}}$ and add the spin-flip and pair-hopping terms $H_{\text{sf-ph}} = -J_{\mathrm{H}} \sum_{\alpha>\beta} (c^{\dagger}_{\alpha\downarrow} c^{\dagger}_{\beta\uparrow} c_{\beta\downarrow} c_{\alpha\uparrow} + c^{\dagger}_{\beta\uparrow} c^{\dagger}_{\beta\downarrow} c_{\alpha\uparrow} c_{\alpha\downarrow} + \mathrm{H.c.})$. Multiorbital Hubbard models can realize Mott-insulating phases with different integer fillings. The multiplet structure is reflected in substructures of the Hubbard bands, as well as J_{H}-related peaks in the metallic phase; see Fig. 2(a).

A different type of multiorbital setup describes systems with several atoms in the unit cell. A prominent example is the d-p model for cuprates, which treats strongly correlated transition metal (Cu) and more moderately correlated ligand (O) orbitals. This model is similar to H_{UV}, but with orbital-dependent interaction strengths.

B. Coupling to electric fields

To describe the laser excitation, the lattice models introduced in Sec. II.A need to incorporate the coupling to electromagnetic fields. There are different formulations of the light-matter coupling for general multiorbital systems (Boykin, Bowen, and Klimeck, 2001; Golež, Eckstein, and Werner, 2019; Li, Golez, Mazza *et al.*, 2020; Dmytruk and Schiró, 2021; Schüler *et al.*, 2021; Tai and Claassen, 2023). A convenient setting for tight-binding models with localized Wannier orbitals is the dipolar representation, which describes the coupling of electrons of charge q to the transverse vector potential $\mathbf{A}(t)$ and the transverse electric field $\mathbf{E}^T(t) = -\partial_t \mathbf{A}(t)$ in terms of dipolar matrix elements and a Peierls phase. The single-particle Hamiltonian becomes

$$H_{\mathrm{hop}}(t) = -\sum_{a,b} v_{ab} e^{i\chi_{ab}(t)} c_a^\dagger c_b - \mathbf{E}^T(t)\cdot\mathbf{P}(t), \tag{10}$$

where spin is omitted for simplicity. In Eq. (10), $c_a^\dagger$ creates an electron in a Wannier orbital $|a\rangle$ with center $\mathbf{R}_a$, and v_{ab} is a hopping matrix element. The fields enter through the Peierls phase (Peierls, 1933; Luttinger, 1951)

$$\chi_{ab}(t) = \frac{q}{\hbar}(\mathbf{R}_a - \mathbf{R}_b)\cdot\mathbf{A}(t) \tag{11}$$

and the polarization operator

$$\mathbf{P}(t) = \sum_{a,b} \mathbf{d}_{ab} e^{i\chi_{ab}(t)} c_a^\dagger c_b, \tag{12}$$

with the dipolar matrix elements $\mathbf{d}_{ab} = q\langle a|(\mathbf{r}-\mathbf{R}_a)|b\rangle = q\langle a|(\mathbf{r}-\mathbf{R}_b)|b\rangle$. Here we introduced shifts that make operators local with respect to the Wannier orbitals and assumed orthogonalized Wannier orbitals. Equations (10) and (11) are valid for spatially homogeneous fields (the dipole approximation). A straightforward extension to space-dependent fields is possible as long as they vary slowly on the scale of the unit cell. In the dipolar gauge, a static electric field E_0 corresponds to $A(t) = -tE_0$, and the Hamiltonian becomes time dependent in contrast to the corresponding Hamiltonian in the length gauge (Schüler *et al.*, 2021).

More generally, various unitary transformations of the minimal coupling Hamiltonian lead to different hybrid light-matter basis sets, with a modified dependence of the Hamiltonian $H[\mathbf{A}]$ on $\mathbf{A}$ and the polarization density $\mathbf{P}$ (Loudon, 1973). The resulting theory relates to the macroscopic Maxwell equation $\nabla\times\mathbf{B} = \mu_0(\mathbf{J}+\partial_t\mathbf{D})$, with current operator $\mathbf{J} = -\delta H[\mathbf{A}]/\delta\mathbf{A}$ and displacement field $\mathbf{D} = \epsilon_0\mathbf{E}+\mathbf{P}$. While the microscopic current density $\mathbf{j}$ always remains unique, its separation $\mathbf{j} = \mathbf{J}+\partial_t\mathbf{P}$ into a polarization contribution $\partial_t\mathbf{P}$ and the current $\mathbf{J}$ is representation dependent. The different representations are formally equivalent, but they differ after projection to a few-band model, which is important, in particular, for an accurate description of the nonlinear response (Li, Golez, Mazza *et al.*, 2020; Tai and Claassen, 2023). The dipolar Hamiltonian in Eq. (10) is obtained via a field-dependent basis rotation of the Wannier orbitals corresponding to a site-dependent Power-Zienau-Woolley transformation (Luttinger, 1951; Golež, Eckstein, and Werner, 2019; Schüler *et al.*, 2021). Several test calculations showed that a few-band model in the dipolar gauge is more accurate than a few-band model formulated in the velocity (Coulomb) gauge (Li, Golez, Mazza *et al.*, 2020; Schüler *et al.*, 2021).

In a single-band model with an inversion center, we have $\mathbf{P} = 0$, and Eq. (10) reduces to the well-known Peierls substitution (Peierls, 1933). The current, written in momentum space, is thus

$$\mathbf{J}(t) = q\sum_{\mathbf{k}} n_{\mathbf{k}} \mathbf{v}_{\mathbf{k}-\frac{q}{\hbar}\mathbf{A}(t)}, \tag{13}$$

with the velocity $\mathbf{v}_{\mathbf{k}} = (1/\hbar)\partial_{\mathbf{k}}\epsilon_{\mathbf{k}}$ determined by the lattice dispersion $\epsilon_{\mathbf{k}}$. Expressions for the current $\mathbf{J}$ in the multiband case can be obtained by taking the derivative $\delta H[\mathbf{A}]/\delta\mathbf{A}$ of Eq. (10). The additional contribution $\partial_t\mathbf{P}$ can be evaluated at the operator level, $\partial_t\mathbf{P} = i[H,\mathbf{P}]$; see Golež, Eckstein, and Werner (2019) and Schüler *et al.* (2021) for explicit expressions. However, because in general the commutator also has contributions from interaction terms, it may be easier in numerical studies to measure $\langle\mathbf{P}(t)\rangle$ and to calculate $\partial_t\mathbf{P}$ numerically.

In general, after the transformation to the light-matter basis, the interaction terms also depend on the field. In the dipolar representation, nonlocal Coulomb scattering matrix elements such as pair hoppings get multiplied with Peierls phases (Li, Golez, Mazza *et al.*, 2020) and thus contribute to the current operator. Coulomb scattering contributions to the current are particularly relevant for nonlinear responses in flat band systems (Tai and Claassen, 2023).

C. Spectroscopic observables

Optical conductivity. The optical conductivity $\sigma(t,t')$ defines the linear-response relation between the induced current $\delta\mathbf{j}$ and a weak probe electric field $\mathbf{E}_{\mathrm{probe}}(t)$,

$$\delta\mathbf{j}(t) = \int_{-\infty}^{t} dt'\sigma(t,t')\mathbf{E}_{\mathrm{probe}}(t'). \tag{14}$$

In general $\delta\mathbf{j}$ has contributions from the current $\mathbf{J}$ and the polarization $\mathbf{P}$, as discussed in Sec. II.B. $\sigma(t,t')$ can be expressed in terms of response functions $\chi(t,t')$ between $\mathbf{J}$ and/or $\mathbf{P}$ using the nonequilibrium Kubo formula; see Eckstein and Kollar (2008c), De Filippis *et al.* (2012), Lenarčič *et al.* (2014), and Shao *et al.* (2016) for single-band cases. In nonequilibrium simulations one can evaluate $\sigma(t,t')$ either by calculating $\chi(t,t')$ or by explicitly simulating a δ-function probe field [a steplike change of $\mathbf{A}(t)$] and measuring the induced current $\delta\mathbf{j}(t)$ (Lenarčič *et al.*, 2014; Shao *et al.*, 2016; Werner, Li *et al.*, 2019). In Green's-function-based approaches, the latter strategy automatically takes into account the vertex corrections in the diagrammatic expression of $\chi(t,t')$.

In experiments the nonequilibrium conductivity is measured using a pulse of nonzero duration $\mathbf{E}_{\mathrm{probe}}(t) = \mathbf{E}_{t_p}(t)$ centered at t_p. A possible working definition for the nonequilibrium conductivity is $\sigma_{\mathrm{meas}}(\omega,t_p) \equiv \delta\mathbf{j}(\omega)/\mathbf{E}_{t_p}(\omega)$, although other definitions may be more appropriate, depending on the experimental setup (Revelle, Kumar, and Kemper, 2019). In a quasiequilibrium situation, $\sigma_{\mathrm{meas}}(\omega,t_p) \simeq \int\sigma(t_p+s,t_p)e^{i(\omega+i\delta)s}ds$. However, in general the relation

between $\sigma_{\mathrm{meas}}(\omega, t_p)$ and $\sigma(t, t')$ depends on the shape of the probe (Shao *et al.*, 2016).

For the single-band Hubbard model in Eq. (1) under a pump field described by $\mathbf{A}_{\mathrm{pump}}(t)$,

$$\sigma_{\alpha\beta}(t, t') = \theta(t - t')\tau_{\alpha\beta}(t) + \int_{t'}^{t} d\bar{t}\chi_{J^\alpha, J^\beta}(t, \bar{t}). \quad (15)$$

In Eq. (15), $\tau_{\alpha\beta}(t) \equiv (q^2/\hbar^2)\sum_{\mathbf{k}}(\partial_{k_\beta}\partial_{k_\alpha}\epsilon_{\mathbf{k}-(q/\hbar)\mathbf{A}_{\mathrm{pump}}(t)})\langle n_{\mathbf{k}}(t)\rangle$ is the stress tensor, $\langle\cdots\rangle$ indicates the expectation value for a system with a pump field only, and $\chi_{J^\alpha, J^\beta}(t, t') \equiv -(i/\hbar)\theta(t - t')\langle[J^\alpha(t), J^\beta(t')]\rangle$. $J^\alpha(t)$ is the α component of the current operator in a Heisenberg representation with a pump field. The first term of Eq. (15) captures the modification of the current operator by the probe field and is called the diamagnetic term. The second term is the paramagnetic contribution.

Spectral functions. The time-dependent spectral function (A) and occupation function (N) provide useful information on the single-particle properties. They are related to the retarded (R) and lesser ($<$) parts of the single-particle Green's function $G(t, t') \equiv -i\langle\mathcal{T}_{\mathcal{C}}c(t)c^\dagger(t')\rangle$, where $\mathcal{T}_{\mathcal{C}}$ is the contour-ordering operator (Aoki *et al.*, 2014). For a mixed frequency-time representation, one can use the "forward" Fourier transforms

$$A(\omega, t') = -\frac{1}{\pi}\mathrm{Im}\int_{t'}^{\infty} dt e^{i\omega(t-t')}G^R(t, t'), \quad (16)$$

$$N(\omega, t') = \frac{1}{\pi}\mathrm{Im}\int_{t'}^{\infty} dt e^{i\omega(t-t')}G^<(t, t') \quad (17)$$

or the related "backward" or symmetric (Wigner) transforms. The occupation function is related to the time-resolved photoemission spectrum $I(\omega, t_p)$ via convolutions with the envelope function $S(t)$ of the probe pulse centered at probe time t_p (Eckstein and Kollar, 2008a; Freericks, Krishnamurthy, and Pruschke, 2009),

$$I(\omega, t_p) = -i\int dt dt' S(t)S(t')e^{i\omega(t-t')}G^<(t + t_p, t' + t_p). \quad (18)$$

In contrast to $A(\omega, t')$ and $N(\omega, t')$, this spectrum is guaranteed to be positive. Variants of Eq. (18), in particular, for momentum-resolved spectra or in the presence of fields also acting outside of the solid, were discussed in several reviews (Kemper *et al.*, 2017; Eckstein, 2021; Schüler and Sentef, 2021).

III. SIMULATION OF NONEQUILIBRIUM STRONGLY CORRELATED SYSTEMS

In this section, we explain relevant methods and concepts for the study of strongly correlated nonequilibrium systems, focusing predominantly on computational approaches. These numerical schemes can be classified into Green's function methods, such as various flavors of dynamical mean-field theory (see Sec. III.A), wave-function approaches such as exact diagonalization or matrix-product-state methods (see Sec. III.B), and density-functional theories (see Sec. III.C). We furthermore discuss the concept of quasisteady-state descriptions of photodoped large-gap Mott systems; see Sec. III.D. Valuable insights into driven strongly correlated systems can also be gained from analytical approaches, such as the perturbative Floquet analysis for periodically driven systems and the bosonization method for one-dimensional systems. Such results and analyses are discussed in connection with specific applications in Secs. IV.C, V.A, and VI.G.

A. Methods based on dynamical mean-field theory

1. General remarks

The Hubbard model and its extensions are generally not analytically solvable, and we have to resort to numerical techniques to study the strongly correlated regime. In the limit of infinite dimensions or infinite coordination number (Metzner and Vollhardt, 1989), an exact numerical solution is provided by DMFT (Georges *et al.*, 1996). If applied to finite-dimensional systems, DMFT neglects nonlocal correlations but provides a good description of the local correlation effects, which are important in Mott systems. DMFT has been widely used for studying the equilibrium properties of lattice models and materials (Kotliar *et al.*, 2006), and there are numerical methods and open-source libraries that enable efficient equilibrium simulations in the interesting parameter regimes (Parcollet *et al.*, 2015; Shinaoka, Gull, and Werner, 2017; Haule, 2018; Choi *et al.*, 2019; Melnick *et al.*, 2021). These tools, however, cannot be used to study nonequilibrium states in Mott insulators. In Secs. III.A.2–III.A.6, we introduce nonequilibrium DMFT (Aoki *et al.*, 2014) and various extensions of this formalism that provide access to such nonequilibrium states.

2. Nonequilibrium DMFT

DMFT maps a correlated lattice model onto a self-consistently determined single-site model, a so-called quantum impurity model (Georges and Kotliar, 1992). This approximate mapping identifies the momentum-dependent self-energy $\Sigma_{\mathbf{k}}^{\mathrm{latt}}$ of the lattice model with the local (momentum-independent) impurity self-energy Σ_{imp}. The bath properties of the impurity model are fixed via a self-consistency condition that demands that the local lattice Green's function be identical to the impurity Green's function, $G_{\mathrm{loc}}^{\mathrm{latt}} = \int(d\mathbf{k})G_{\mathbf{k}}^{\mathrm{latt}} \equiv G_{\mathrm{imp}}$; see Fig. 7. In the imaginary-time formalism, the bath is represented by a hybridization function $\Delta(\tau)$ that encodes how electrons hop in and out of the impurity site and thus plays the role of a dynamical mean field. To generalize DMFT to systems out of equilibrium (Schmidt and Monien, 2002; Freericks, Turkowski, and Zlatič, 2006), the equations are rewritten within the Kadanoff-Baym or Keldysh formalism. This generalization is also possible for cluster (Maier *et al.*, 2005), inhomogeneous (Potthoff and Nolting, 1999), and diagrammatic (Rohringer *et al.*, 2018) extensions of DMFT. In the following, the formalism for the real-time evolution from an equilibrium initial state is described. Nonequilibrium steady-state approaches are discussed in Sec. III.A.5.

In practice there are two main challenges. The first one is the solution of the impurity problem; see Sec. III.A.6. The

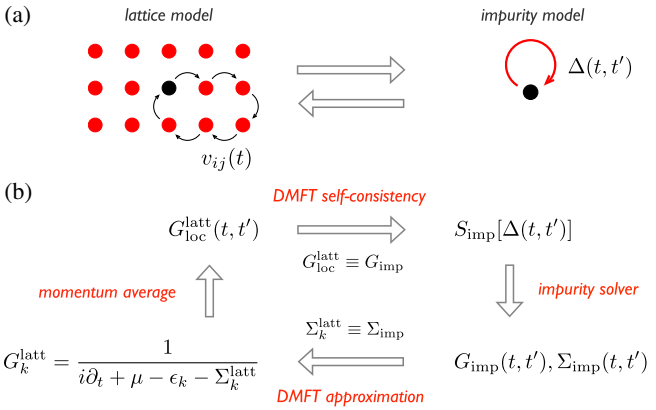

FIG. 7. (a) Self-consistent mapping of a correlated lattice model to an effective impurity problem with hybridization function Δ. (b) Sketch of the DMFT self-consistency loop with the lattice (impurity) Green's function $G_{\rm latt}$ ($G_{\rm imp}$), the lattice (impurity) self-energy $\Sigma_{\rm latt}$ ($\Sigma_{\rm imp}$), and the impurity action $S_{\rm imp}[\Delta]$.

second challenge is that in nonequilibrium DMFT, the functions $G(t,t')$, $\Sigma(t,t')$, and $\Delta(t,t')$ are defined on the Kadanoff-Baym or Keldysh time contour $\mathcal{C}$ instead of the imaginary-time axis. To evaluate G, one must solve the Dyson equation $G = G_0 + G_0 * \Sigma * G$, where an asterisk indicates the convolution on $\mathcal{C}$ and G_0 is the free-electron Green's function. When the system is in equilibrium or in a steady state, the Dyson equation can be solved via Fourier transformation with respect to the time difference $t - t'$. However, generic cases require the explicit solution of the equation on $\mathcal{C}$. A standard implementation using an equidistant time mesh can be found in the open-source library NESSi (Schüler *et al.*, 2020). With such a scheme, the required computer memory [CPU time] scales like $\mathcal{O}(N_t^2)$ [$\mathcal{O}(N_t^3)$] with the number of time points N_t, which makes simulations of the long-time behavior challenging. Several ideas have recently been put forward to overcome this computational bottleneck in simulations of Mott systems, including quasisteady-state approaches (see Sec. III.D) and compressed representations (Kaye and Golež, 2021; Shinaoka *et al.*, 2023). Systematic truncations of the memory kernel in the Dyson equation (Schüler, Eckstein, and Werner, 2018; Stahl *et al.*, 2022) also allow one to significantly extend the simulation time in certain parameter regimes (Dasari *et al.*, 2021; Picano and Eckstein, 2021).

DMFT provides direct access to single-particle observables and spectroscopic probes such as the time-resolved photoemission spectrum; see Sec. I.C. The time-resolved optical conductivity can be evaluated diagrammatically (Eckstein and Kollar, 2008c) or by simulating the probe process with a time-dependent electric field and computing the current; see Eq. (13). The latter approach includes vertex corrections originating from the two-particle irreducible vertex (functional derivative of the DMFT self-energy with respect to the probe field) (Stefanucci and Van Leeuwen, 2013; Murakami *et al.*, 2016; Golež, Eckstein, and Werner, 2019). Moreover, DMFT is well suited for predicting core-level x-ray photoemission spectroscopy and XAS data. These probes involve a localized core hole and the spectroscopic signal can be computed by considering an extended impurity model that contains the core level in addition to the valence orbitals (Cornaglia and Georges, 2007; Haverkort *et al.*, 2014; Hariki, Winder, and Kuneš, 2018). Within this extended impurity problem, the relevant interactions between the core hole and the valence electrons are treated exactly. Such a scheme has been used to calculate time-resolved XAS in a two-orbital Hubbard model (Werner, Golez, and Eckstein, 2022) and charge-transfer insulator (Lojewski *et al.*, 2024; Golež *et al.*, 2025). Similarly, DMFT can be used to predict the RIXS signal, although this approach only captures the dynamics of momentum-integrated excitations (Eckstein and Werner, 2021; Werner, Johnston, and Eckstein, 2021).

3. Cluster DMFT

The DMFT approximation neglects spatial fluctuations, which can qualitatively alter the physics in one-dimensional (1D) or 2D lattice models. Cluster extensions of DMFT have been developed to capture short-range correlations within small clusters, while longer-range correlations are treated at a mean-field level (Maier *et al.*, 2005). The dynamical cluster approximation (DCA) (Hettler *et al.*, 1998) approximates the self-energy $\Sigma^{\rm latt}_{\mathbf{k}}$ as constant within specific regions ("patches") of the Brillouin zone and associates it with the corresponding momentum component of the self-energy in a cluster impurity model, $\Sigma^{\rm latt}_{\mathbf{k}}(t,t') \approx \sum_{\mathbf{K}} \Sigma^{\rm imp}_{\mathbf{K}}(t,t') \phi_{\mathbf{K}}(\mathbf{k})$, where $\phi_{\mathbf{K}}(\mathbf{k}) = 1$ for $\mathbf{k}$ inside momentum patch $\mathbf{K}$ and 0 otherwise. The DCA self-consistency loop is analogous to Fig. 7 but with momentum averaging performed over the respective patch. The patch-averaged lattice Green's function $G^{\rm latt,av}_{\mathbf{K}}$ is identified with the cluster impurity Green's function $G^{\rm imp}_{\mathbf{K}}$ for momentum $\mathbf{K}$. For nonequilibrium simulations DCA is preferred over real-space cluster DMFT (CDMFT) (Lichtenstein and Katsnelson, 2000). Owing to its diagonal representation in momentum space, it avoids solving matrix-valued Dyson equations and leads to a linear (rather than quadratic) scaling of the memory requirement with the number of cluster sites (Tsuji *et al.*, 2014). Nonequilibrium DCA has been used to investigate several phenomena in photodoped Mott systems, such as the effects of spin-charge coupling (Eckstein and Werner, 2016), geometric frustration (Bittner *et al.*, 2020b), and Mott exciton formation (Bittner *et al.*, 2020a). A limitation is that DCA lacks gauge invariance (Lin, Gull, and Millis, 2009; Bittner *et al.*, 2020b), which could possibly be overcome via a nonequilibrium extension of periodized CDMFT (Kotliar *et al.*, 2001; Biroli, Parcollet, and Kotliar, 2004).

4. Extended DMFT and *GW* + EDMFT

Extended DMFT (EDMFT). The extended DMFT formalism (Sengupta and Georges, 1995; Si and Smith, 1996; Sun and Kotliar, 2002; Ayral, Biermann, and Werner, 2013; Golež, Eckstein, and Werner, 2015) enables the treatment of models with nonlocal interactions, like the U-V Hubbard model in Eq. (8), and incorporates dynamical screening effects on the local level (Werner and Casula, 2016). EDMFT maps the lattice system to a single-site impurity model but now includes both a fermionic dynamical mean field, corresponding to the hybridization function $\Delta(t,t')$, and a bosonic dynamical mean field, represented by a self-consistently computed retarded

impurity interaction $\mathcal{U}(t,t')$. Δ is determined by the usual fermionic self-consistency loop [see Fig. 7(b)], while $\mathcal{U}$ is calculated using an additional bosonic self-consistency loop that connects the screened interaction W to the polarization P. The fully screened interaction in the lattice is determined by the bosonic lattice Dyson equation $W_{\mathbf{k}} = V_{\mathbf{k}} + V_{\mathbf{k}} * P_{\mathbf{k}} * W_{\mathbf{k}}$, where $V_{\mathbf{k}}$ is the bare interaction and $P_{\mathbf{k}}$ is the momentum-dependent polarization function. Within EDMFT $P_{\mathbf{k}}$ is approximated via the local polarization function P_{imp} of the impurity model, which relates the fully screened impurity interaction W_{imp} and the "bare impurity interaction" $\mathcal{U}$ through $W_{\mathrm{imp}} = \mathcal{U} + \mathcal{U} * P_{\mathrm{imp}} * W_{\mathrm{imp}}$. The condition $\int (d\mathbf{k}) W_{\mathbf{k}} = W_{\mathrm{imp}}$ closes the self-consistency.

The impurity effective interaction $\mathcal{U}$ and the fully screened interaction W reflect the time-dependent modifications of the dynamically screened interactions out of equilibrium. The dominant peaks in the spectrum of $\mathcal{U}$,

$$-\frac{1}{\pi}\mathrm{Im}\,\mathcal{U}^{\mathrm{R}}(\omega,t) = -\frac{1}{\pi}\mathrm{Im}\int_t^\infty dt'\, e^{i\omega(t'-t)}\mathcal{U}^{\mathrm{R}}(t',t) \tag{19}$$

(and similarly for W), represent the screening modes associated with single-particle and collective charge fluctuations. By integrating over these modes, we can define an effective coupling strength between the electrons and charge fluctuations (Ayral, Biermann, and Werner, 2013),

$$\lambda(t) = -\frac{2}{\pi}\int_0^\infty d\omega \frac{\mathrm{Im}\,\mathcal{U}^{\mathrm{R}}(\omega,t)}{\omega}. \tag{20}$$

The EDMFT framework is also applicable to models with nonlocal spin interactions and has been used to study the t-J model in Eq. (6) (Haule *et al.*, 2002; Bittner *et al.*, 2018) and the Heisenberg model in Eq. (5) (Otsuki and Kuramoto, 2013). In this case the nonlocal magnetic interactions determine a retarded impurity spin-spin interaction $\mathcal{J}(t,t')$ whose modes describe the local magnetic excitations.

GW + EDMFT. To incorporate nonlocal correlation and screening effects into the single-site EDMFT formalism for the U-V Hubbard model, we can add nonlocal Σ and P components taken from the GW approximation (Hedin, 1965) and feed the resulting fermionic and bosonic self-energies back into the self-consistency loop (Biermann, Aryasetiawan, and Georges, 2003; Ayral, Biermann, and Werner, 2013; Golež *et al.*, 2017). In this so-called GW + DMFT formalism, we define

$$\Sigma^{\mathrm{latt}}_{ij} = \Sigma^{\mathrm{EDMFT}}\delta_{ij} + \Sigma^{GW}_{ij}(1-\delta_{ij}), \tag{21}$$

$$P^{\mathrm{latt}}_{ij} = P^{\mathrm{EDMFT}}\delta_{ij} + P^{GW}_{ij}(1-\delta_{ij}), \tag{22}$$

where the terms in brackets are the GW expressions for Σ and P, with the local contributions subtracted to avoid double counting. This formalism allows one to study nonlocal (charge) fluctuations in the Mott-insulating phase, and the inclusion of the nonlocal polarization substantially improves the description of the fluctuation spectrum (Ayral, Biermann, and Werner, 2013). GW + EDMFT can lead to noncausal behavior of the auxiliary fields Δ and $\mathcal{U}$ (Nilsson *et al.*, 2017). Recently, an alternative self-consistency scheme that ensures causality was proposed (Backes, Sim, and Biermann, 2022; Chen, Petocchi, and Werner, 2022), but the nonequilibrium implementation of this variant has not yet been realized.

The GW + EDMFT formalism can be extended to a multitier approach (Boehnke *et al.*, 2016; Nilsson *et al.*, 2017; Kang *et al.*, 2023) in which the weakly correlated bands are treated at the GW level, while the nonperturbative corrections Σ^{EDMFT} and P^{EDMFT} are obtained for a subset of strongly correlated orbitals from a self-consistently embedded impurity model. The nonequilibrium implementation of this formalism (Golež *et al.*, 2019; Golež, Eckstein, and Werner, 2019) provides a self-consistent description of the dynamically screened interactions and Hartree shifts in photoexcited Mott systems; see Sec. VI.F.

5. Steady-state DMFT and Floquet DMFT

If a system is connected to heat baths and is subjected to time-translation-invariant perturbations, the balance between the energy injection and dissipation leads to a nonequilibrium steady state (NESS). If the external perturbations are time periodic, the system reaches a time-periodic nonequilibrium state. Steady-state and Floquet DMFT enable one to describe such steady and time-periodic states without explicitly simulating the initial transient evolution (Schmidt and Monien, 2002; Joura, Freericks, and Pruschke, 2008; Tsuji, Oka, and Aoki, 2008; Qin and Hofstetter, 2017). For the heat baths, one typically considers either a bath of noninteracting fermions with a finite bandwidth, or a boson bath. The self-energy produced by these baths is added to the impurity self-energy in the DMFT self-consistency loop. Both steady-state and Floquet formalisms are implemented on the two-branch Keldysh contour using functions $\hat{G}(t,t')$, $\hat{\Sigma}(t,t')$, and $\hat{\Delta}(t,t')$, which depend on the real physical time and have a 2×2 Keldysh matrix structure (Tsuji, Oka, and Aoki, 2008; Aoki *et al.*, 2014). The transformation to average time $t_{\mathrm{av}} = (t+t')/2$ and relative time $t_{\mathrm{rel}} = (t-t')$ allows one to perform a Fourier transform with respect to t_{rel}, which introduces the frequency ω. In a NESS, two-time functions do not depend on t_{av} and the Dyson equation becomes a 2×2 matrix equation in Keldysh space, $\hat{G}(\omega)^{-1} = \hat{G}_0(\omega)^{-1} - \hat{\Sigma}(\omega)$. In a time-periodic state, we assume that all two-time quantities are periodic with respect to t_{av}, with a period $\mathcal{T} = 2\pi/\Omega$. The Floquet matrix representation is then defined by a continuous Fourier transform with respect to t_{rel} and the discrete transform

$$\underline{\hat{G}}_{mn}(\omega) = \frac{1}{\mathcal{T}}\int_0^{\mathcal{T}} dt_{\mathrm{av}}\, e^{i(m-n)\Omega t_{\mathrm{av}}}\hat{G}\left(\omega + \frac{m+n}{2}\Omega, t_{\mathrm{av}}\right), \tag{23}$$

where the continuous frequency ω is restricted to the Floquet Brillouin zone $[-\Omega/2, \Omega/2)$ and $\underline{\hat{G}}$ indicates a matrix with respect to the Floquet indices n and m. With this matrix representation, the Dyson equation can be expressed simply as a matrix equation, $\underline{\hat{G}}(\omega)^{-1} = \underline{\hat{G}}_0(\omega)^{-1} - \underline{\hat{\Sigma}}(\omega)$.

6. Impurity solvers

The main challenge for the implementation of nonequilibrium DMFT and its extensions is the solution of the effective

impurity model. In the case of the Hubbard model in Eq. (1) and paramagnetic single-site DMFT, this is the Anderson impurity model with action

$$S_{\mathrm{imp}} = \int_{\mathcal{C}} dt dt' \sum_{\sigma} c_{\sigma}^{\dagger}(t)\Delta(t,t')c_{\sigma}(t') + \int_{\mathcal{C}} dt H_{\mathrm{loc}}(t). \tag{24}$$

In Eq. (24), H_{loc} is the local Hamiltonian, which contains the interaction U. In equilibrium, the Anderson model can be solved efficiently using a variety of methods, like quantum Monte Carlo (QMC) (Gull *et al.*, 2011) and wave-function-based techniques (Schollwöck, 2005; Bulla, Costi, and Pruschke, 2008). For nonequilibrium studies of Mott systems, there exist a number of approximate solvers, while exact solvers are currently limited to short-time or steady-state simulations.

Self-consistent strong-coupling expansion. The self-consistent strong-coupling (hybridization) expansion is a systematic approach that starts from the atomic limit. Its formulation in the nonequilibrium context was discussed in detail by Eckstein and Werner (2010) and Aoki *et al.* (2014). In brief, by performing a power-series expansion in $\Delta(t,t')$, one can express the partition function of the impurity problem in Eq. (24), $Z = \mathrm{Tr}[T_{\mathcal{C}} e^{-iS_{\mathrm{imp}}}]$, as an infinite sum over strong-coupling diagrams. Up to prefactors the weight of a given diagram is given by the product of hybridization functions and atomic propagators $\tilde{g}_{\alpha,\beta}(t,t')$ with indices α and β in a basis of the local Hilbert space. Dressed propagators $\tilde{G}_{\alpha,\beta}(t,t')$, which include all hybridization events, then satisfy a Dyson equation with a self-energy $\tilde{\Sigma}[\tilde{G},\Delta]$ expressed in terms of $\tilde{G}$ and Δ. The impurity Green's function G can be evaluated from the converged $\tilde{G}$ and Δ. Most nonequilibrium DMFT simulations for Mott insulators to date have used the noncrossing approximation (NCA) (Keiter and Kimball, 1971; Eckstein and Werner, 2010) or the one-crossing approximation (OCA) (Pruschke and Grewe, 1989), where $\tilde{\Sigma}[\tilde{G},\Delta]$ is calculated to first or second order in Δ, respectively. This is a versatile approach that works for arbitrary local Hamiltonians and generic hybridizations. The constraint on the crossing of hybridization functions, however, introduces unphysical correlations, which can become problematic, especially in multiorbital or doped systems. A promising strategy for the development of efficient higher-order strong-coupling solvers is the combination with tensor cross interpolation (Núñez Fernández *et al.*, 2022), as implemented for steady states by Eckstein (2024) and Kim and Werner (2025).

A variant of the model in Eq. (24) that plays an important role in $(GW+)$EDMFT is the Anderson-Holstein model with additional local bosonic degrees of freedom. After integrating out the bosons, one obtains an additional retarded term in the action, $S = \int dt dt' n(t)\mathcal{B}(t,t')n(t')$, where $\mathcal{B}$ is the noninteracting boson propagator (Aoki *et al.*, 2014). Three complementary NCA and OCA impurity solvers have been developed to handle this term: (i) a combined strong- and weak-coupling expansion approach (Golež, Eckstein, and Werner, 2015; Chen *et al.*, 2016) where the partition function is expanded in both the hybridization Δ and the retarded interaction $\mathcal{B}$ [for a discussion of retarded spin-spin interactions, see Bittner *et al.* (2018)]; (ii) a method based on a Lang-Firsov decoupling (Lang and Firsov, 1962) of the electron-boson interaction and a transformation to polaron operators (Werner and Eckstein, 2013); and (iii) the direct inclusion of phonons into the local Hilbert space, which is then truncated (Grandi, Li, and Eckstein, 2021).

Monte Carlo-based solvers. The direct extension of continuous-time QMC algorithms from imaginary time to the Keldysh contour (Mühlbacher and Rabani, 2008; Werner, Oka, and Millis, 2009) leads to a severe dynamical sign problem, which restricts simulations to short times. Numerically exact nonequilibrium DMFT results have been obtained with the real-time implementation of the weak-coupling continuous-time Monte Carlo method (Werner *et al.*, 2010), but accessing the Mott regime with this solver is challenging (Eckstein, Kollar, and Werner, 2010). The inchworm algorithm is a more promising diagrammatic Monte Carlo algorithm that uses the causal structure of the self-consistent strong-coupling expansion while sampling the contributions to the propagation kernel in the Dyson equation (Cohen *et al.*, 2015; Chen, Cohen, and Reichman, 2017a, 2017b). Owing to the high numerical cost, this algorithm has not yet been used within nonequilibrium DMFT to simulate photoinduced dynamics. The more recent steady-state inchworm algorithm (Erpenbeck, Gull, and Cohen, 2023; Künzel *et al.*, 2024) can be used as a solver for steady-state techniques; see Sec. III.D. A possibly even more compact resummation of the diagrammatic series can be achieved with triangular vertices (Kim *et al.*, 2022, 2023).

Hamiltonian representation and auxiliary master equation approach. The action in Eq. (24) is equivalent to the Anderson impurity Hamiltonian $H_{\mathrm{imp}} = H_{\mathrm{loc}} + H_{\mathrm{bath}}$, where H_{bath} includes additional bath orbitals p with fermion annihilation operators $a_{p,\sigma}$ and a time-dependent hybridization $V_p(t)a_{p,\sigma}^{\dagger}c_{\sigma} + \mathrm{H.c.}$ between the impurity site and the bath orbitals. H_{imp} can be solved using exact diagonalization (Gramsch *et al.*, 2013) or matrix-product-state techniques (Wolf, McCulloch, and Schollwöck, 2014), but the main challenge is to represent the time-evolving bath. The technique developed thus far (Gramsch *et al.*, 2013) requires a number of bath sites that increases with time, leading to an exponential increase of the numerical cost.

Alternatively, one can represent the impurity action in Eq. (24) in terms of a Markovian open quantum system, which includes both explicit bath orbitals as in H_{bath} and Lindblad dissipators that add and remove particles from the bath (Arrigoni, Knap, and von der Linden, 2013; Chen *et al.*, 2019). This auxiliary master equation approach has been formulated for NESS simulations (Dorda *et al.*, 2014, 2015; Titvinidze *et al.*, 2015; Chen, Cohen, and Galperin, 2019) and also applied to Floquet DMFT (Sorantin *et al.*, 2018; Gazzaneo *et al.*, 2022; Mazzocchi *et al.*, 2022, 2023; Werner, Lotze, and Arrigoni, 2023). The Lindblad terms can be adapted to independently represent $\Delta^{<}(\omega)$ (occupied density of states of the bath) and $\Delta^{>}(\omega)$ (unoccupied density of states), which are not linked by the fluctuation-dissipation relation in a NESS.

B. Wave-function-based methods

1. Exact diagonalization

The time evolution of small systems, such as Hubbard clusters up to 20 sites, can be calculated using the time-dependent Lanczos method (Park and Light, 1986; Prelovšek and Bonča, 2013). Expanding the time evolution of the wave function over one time step δt into a power series, $e^{-iH(t)\delta t}|\psi(t)\rangle \approx \sum_{n=0}^{p-1}\{[-i\delta t H(t)]^n/n!\}|\psi(t)\rangle$, yields p independent vectors $H(t)^n|\psi(t)\rangle$ that define the so-called Krylov space. The Lanczos algorithm (Lanczos, 1950) recursively generates an orthonormal Krylov space basis $\{|\phi_l\rangle\}$, starting with $|\phi_0\rangle = |\psi(t)\rangle$, in which the Hamiltonian $H(t)$ becomes a tridiagonal matrix. The time evolution is calculated in this small space (typically $p \sim 10$, depending on the step δt), and transformed back to yield the state vector $|\psi(t+\delta t)\rangle$. The normalization of the wave function is thus preserved exactly. The main source of error are finite-size effects and artificial recurrences. Assuming that correlations spread with a characteristic light-cone velocity v_{lc}, finite-size artifacts can be expected for times $t \gtrsim L/(2v_{\mathrm{lc}})$, where L is the linear size of the system. Larger systems can in some cases be treated using the time-dependent Lanczos procedure within a suitable "limited functional space," which is iteratively constructed from a simple initial product state (Edwards and Miyazaki, 1987; Trugman, 1988; Inoue and Maekawa, 1990). This approach has been used to study the dynamics of one or two photodoped charge carriers forming spin (Bonča, Mierzejewski, and Vidmar, 2012; Golež *et al.*, 2014) or lattice polarons (Vidmar *et al.*, 2011; Golež, Bonča, and Vidmar, 2012).

2. Matrix-product-state approach

The time evolution of large one-dimensional systems can be calculated using numerical methods based on a matrix-product-state (MPS) representation of the wave function, such as the density-matrix renormalization group (DMRG) (White, 1992; White and Feiguin, 2004; Haegeman *et al.*, 2011) or the time-evolving block decimation (TEBD) (Daley *et al.*, 2004; Vidal, 2004; Vidal, 2007). In these methods the state vector $|\psi\rangle$ is expressed as an MPS,

$$|\psi\rangle \approx \sum_{\sigma_1\cdots\sigma_L} A^{\sigma_1}\cdots A^{\sigma_L}|\sigma_1\cdots\sigma_L\rangle, \tag{25}$$

where σ_i represent the local degrees of freedom at site i, A^{σ_i} are $m\times m$ matrices, and m is called the bond dimension. A truncation in m is implemented by decomposing the system into subsystems A and B, performing a Schmidt decomposition $|\psi\rangle = \sum_\alpha s_\alpha |\alpha\rangle_A|\alpha\rangle_B$ and keeping only the m largest coefficients s_α (Schollwöck, 2005, 2011). The efficiency of the MPS *Ansatz* depends on the scaling of the entanglement entropy $S_{\mathrm{vN}} = -\sum_\alpha s_\alpha^2 \log s_\alpha^2$ with system size. Ground states of gapped quantum systems satisfy an area law (Schollwöck, 2011; Stoudenmire and White, 2012). In dimension $D = 1$, the entanglement entropy of a large subsystem then becomes system-size independent, and the ground state wave function can be accurately described with a finite bond dimension.

In TEBD, the ground state is obtained by an imaginary-time evolution whose algorithm is essentially the same as for the real-time evolution (Vidal, 2004). A Suzuki-Trotter decomposition is used to split the time evolution operator $\exp(-iH\delta t)$ for a time step δt into a product of operators $\exp(-ih_{i,i+1}\delta t)$ that act on just two neighboring A matrices in Eq. (25). Then one applies $\exp(-ih_{i,i+1}\delta t)$ to the MPS and performs a singular value decomposition at the bond $[i, i+1]$ to update the MPS. In DMRG, the MPS for the ground state is evaluated (for a given m) using the variational principle for the energy. The real-time evolution is implemented either with the TEBD algorithm (White and Feiguin, 2004) or using the time-dependent variational principle for MPSs (Haegeman *et al.*, 2011; Shinjo *et al.*, 2021). After a global perturbation such as a global quench or a perturbation with a uniform field, one usually finds that the entropy grows linearly with time, which in turn implies an exponential growth of the bond dimension m needed to keep a given accuracy.

In analogy to exact diagonalization (ED), response functions can be evaluated either by using the time-dependent Kubo formalism or by simulating a small probe pulse. For example, the single-particle spectrum can be evaluated by introducing an auxiliary fermionic band and considering the excitations from the system to this auxiliary band (Bohrdt *et al.*, 2018; Zawadzki and Feiguin, 2019; Murakami *et al.*, 2021). By adding core levels to the Hamiltonian, it is possible to calculate x-ray spectra (Zawadzki and Feiguin, 2019).

The thermodynamic limit can be accessed using a translationally invariant MPS *Ansatz* (Vidal, 2007; Kjäll *et al.*, 2013). To treat nonequilibrium systems in dimensions $D > 1$, related tensor-network *Ansätze* such as projected entangled pair states have been developed (Phien *et al.*, 2015; Hubig *et al.*, 2020).

In the context of nonequilibrium DMFT, an interesting recent development is the representation of the impurity problem's influence functional as a temporal MPS (Feynman and Vernon, 1963). Different variants of this approach have been implemented and tested on transport problems and as a solver for DMFT (Thoenniss, Lerose, and Abanin, 2023; Thoenniss *et al.*, 2023; Chen and Guo, 2024; Nayak *et al.*, 2025).

3. Time-dependent variational techniques

Time-dependent Gutzwiller approach. A widely used variational approach for correlated electrons employs the Gutzwiller wave function (Gutzwiller, 1965) and the Gutzwiller approximation (GA), which becomes exact in the limit of infinite dimensions (Metzner and Vollhardt, 1989). This *Ansatz* has provided an early description of the Mott transition in the single-band Hubbard model (Brinkman and Rice, 1970) and was later generalized to multiband systems (Bünemann, Weber, and Gebhard, 1998) and time-dependent problems (Schiró and Fabrizio, 2010; Schiró and Fabrizio, 2011; Fabrizio, 2013). The idea is to use the *Ansatz*

$$|\psi(t)\rangle = \prod_j \mathcal{P}_j(t)|\psi_{\mathrm{sd}}(t)\rangle \tag{26}$$

for the time-evolving state vector, where $|\psi_{\rm sd}(t)\rangle$ is a time-dependent variational Slater determinant, and $\mathcal{P}_j(t)$ are time-dependent variational operators that change the weights of the local many-body configurations at lattice site j and depend on a set of variational parameters ϕ_j. In the simplest case, the operator $\mathcal{P}_j$ can be parametrized in terms of projectors $\hat{P}_{j,\alpha}$ on the local Fock states at each site (for example, $\alpha = 0, \uparrow, \downarrow, \uparrow\downarrow$ for the Hubbard model), $\mathcal{P}_j(t) = \sum[_\alpha \phi_{j,\alpha}(t)/(P^0_{j,\alpha})^{1/2}]\hat{P}_{j,\alpha}$, with $P^0_{j,\alpha} = \langle\psi_{\rm sd}|\hat{P}_{j,\alpha}|\psi_{\rm sd}\rangle$. The dynamics is determined by requesting stationarity of the real-time action $\mathcal{S}(t) = \int_0^t dt' \langle\psi(t')|[i\partial_{t'} - H(t')]|\psi(t')\rangle$. When evaluating this action, one uses the GA while assuming the two constraints $\langle\psi_{\rm sd}|\mathcal{P}_j^\dagger\mathcal{P}_j|\psi_{\rm sd}\rangle = 1$ and $\langle\psi_{\rm sd}|\mathcal{P}_j^\dagger\mathcal{P}_j c_{j,a}^\dagger c_{j,b}|\psi_{\rm sd}\rangle = \langle\psi_{\rm sd}|c_{j,a}^\dagger c_{j,b}|\psi_{\rm sd}\rangle$. With the GA the expectation value of the kinetic energy in the state $|\psi(t)\rangle$ can be evaluated from the Slater determinant $|\psi_{\rm sd}\rangle$ and a renormalized hopping Hamiltonian H_{0*} in which the operators $c_{j,a}$ are modified by a renormalization factor. The stationarity condition for the action translates into a set of coupled differential equations for the variational parameters $\phi_{j,\alpha}(t)$, while $|\psi_{\rm sd}(t)\rangle$ evolves according to a single-particle Schrödinger equation with the renormalized single-particle Hamiltonian H_{0*} (Fabrizio, 2013; Sandri and Fabrizio, 2013).

The time-dependent Gutzwiller approach yields qualitative agreement with nonequilibrium DMFT simulations for the short-time dynamics after an interaction quench in the Hubbard model (Schiró and Fabrizio, 2010). It has also been applied to open quantum systems (Lanatà and Strand, 2012), quenches in multiorbital systems (Oelsen, Seibold, and Bünemann, 2011; Behrmann, Fabrizio, and Lechermann, 2013), the dynamics of antiferromagnetic (Sandri and Fabrizio, 2013) and superconducting order (Mazza, 2017), and photoinduced metal-insulator transitions; see Sec. VI.F. A main drawback is that the time-dependent Gutzwiller approach cannot describe thermalization. Nevertheless, an extended method called the time-dependent ghost Gutzwiller approach offers a systematic way to improve the description and to capture relaxation dynamics (Guerci, Capone, and Lanatà, 2023).

Time-dependent variational quantum Monte Carlo. While the Gutzwiller approach is semianalytical, more general variational wave functions have been used in numerical studies of strongly correlated nonequilibrium systems. To propagate a wave function $|\psi(\theta)\rangle$ depending on a vector $\theta = \theta_1, \theta_2, \ldots$ of time-dependent variational parameters, one can use the variational equation (Carleo *et al.*, 2012; Haegeman, Osborne, and Verstraete, 2013; Ido, Ohgoe, and Imada, 2017)

$$\langle\delta\psi(\bar{\theta})|\left(1 - \frac{|\psi(\theta)\rangle\langle\psi(\bar{\theta})|}{\langle\psi(\bar{\theta})|\psi(\theta)\rangle}\right)(H - i\partial_t)|\psi(\theta)\rangle = 0, \tag{27}$$

where $\bar{\theta}$ is the complex conjugate of θ. This generates a norm-conserving time evolution by projecting the full evolution onto the variational manifold. The projected time evolution is equivalent to the coupled equations of motion $i\dot{\theta} = S(\theta)^{-1}g(\theta)$ for the parameters $\theta \equiv (\theta_j)$, where $S(\theta)_{ij} = \partial_{\bar{\theta}_i}\partial_{\theta_j}\ln\langle\psi(\bar{\theta})|\psi(\theta)\rangle$ and $g_j = \partial_{\bar{\theta}_j}[\langle\psi(\bar{\theta})|H|\psi(\theta)\rangle/\langle\psi(\bar{\theta})|\psi(\theta)\rangle]$.

This formulation has been used in variational QMC simulations. For the wave function, one typically considers an *Ansatz* similar to Eq. (26), where $|\psi_{\rm sd}\rangle$ is a pair-product wave function $\prod_{ij} e^{f_{ij}(t)c_i^\dagger c_j^\dagger}|0\rangle$ with variational parameters f_{ij} and $\mathcal{P}$ are operators of the Gutzwiller and Jastrow type. The differential equation for θ is then solved by Monte Carlo sampling the expectation values of S and g. Benchmarks of the short-time evolution in small Hubbard clusters after a quench have shown good agreement with exact diagonalization and MPS calculations (Ido, Ohgoe, and Imada, 2015), and the method has been used to study the dynamics of the Hubbard model (Ido, Ohgoe, and Imada, 2017; Orthodoxou, Zaïr, and Booth, 2021) and the Kondo lattice model (Fauseweh and Zhu, 2020).

C. DFT-based methods

Density-functional theory (DFT) in combination with the local density approximation (Kohn and Sham, 1965) is a highly successful theory for weakly correlated materials but fails to describe Mott insulators. The time-dependent version of DFT (TDDFT) represents the density $n(r,t) = \sum_j \rho_j |\langle r|\psi_j(t)\rangle|^2$ using a set of single-particle Kohn-Sham orbitals $|\psi_j\rangle$ (with occupations ρ_j) and solves the time-dependent Kohn-Sham equation (Runge and Gross, 1984)

$$i\partial_t|\psi_j(t)\rangle = H[n](t)|\psi_j(t)\rangle. \tag{28}$$

Besides the kinetic term, the Hamiltonian in Eq. (28) contains the external potential $V_{\rm ext}(t)$ describing the effects of the nuclei and possible external fields, the Hartree potential $V_H[n(r,t)]$, and the exchange-correlation potential $V_{\rm xc}[n(r,t)]$.

By adding a local Hubbard U to the most strongly correlated orbitals (DFT + U) (Liechtenstein, Anisimov, and Zaanen, 1995; Anisimov, Aryasetiawan, and Lichtenstein, 1997), a better description of strongly correlated materials can be obtained, although a frequency-dependent self-energy with an imaginary part would be needed for a proper modeling of paramagnetic Mott states. In conventional DFT + U studies, the parameters U and $J_{\rm H}$ (Hund coupling) are either determined for a given ground state or treated as empirical parameters, while out of equilibrium one can expect transient changes of the screening environment; see Sec. VI.F. A possible way to include this screening is the ACBN0 functional (Agapito, Curtarolo, and Buongiorno Nardelli, 2015), in which U and $J_{\rm H}$ are defined self-consistently in terms of the density. The $+U$ contribution has the standard form (Dudarev *et al.*, 1998) $E_U[\{\rho^\sigma_{mm'}\}] = (U - J_{\rm H}/2)\sum_{m,m',\sigma}(\delta_{mm'} - \rho^\sigma_{m'm})\rho^\sigma_{mm'}$, where the sum is over a set of localized orbitals $\{\phi^\sigma_m\}$ and ρ^σ is the density matrix of this subspace. As in DFT + U, this correction is constructed to match the local Hartree-Fock energy (modulo double counting corrections). However, while in DFT + U the Hartree-Fock energy is defined in terms of partially screened Coulomb matrix elements, the ACBN0 functional uses bare matrix elements and instead renormalizes the density matrix by a factor measuring the overlap of the occupied orbitals with the target space. This defines U and $J_{\rm H}$ as functionals of the density; for explicit expressions, see Agapito, Curtarolo, and Buongiorno Nardelli (2015). By taking the derivative of E_U

with respect to $\rho^{\sigma}_{mm'}$, one obtains an extra potential V^{σ}_{U} that is added to $H[n]$ in Eq. (28).

The ACBN0 functional improves the standard DFT results for transition metal oxides (Agapito, Curtarolo, and Buongiorno Nardelli, 2015). When used within TDDFT (Tancogne-Dejean, Oliveira, and Rubio, 2017), an additional approximation is the adiabatic approximation but results for equilibrium optical properties show an improvement over TDDFT + U. This approach has also been used to estimate the effective on-site screening after the excitation (Tancogne-Dejean, Sentef, and Rubio, 2018).

An alternative strategy for incorporating strong correlation effects into (TD)DFT calculations is to construct an exchange-correlation functional V_{xc} from equilibrium DMFT solutions of a lattice model. This functional and the adiabatic approximation can then be used to compute the time evolution of the model within TDDFT (Verdozzi, 2008; Karlsson, Privitera, and Verdozzi, 2011; Boström *et al.*, 2019).

D. Nonequilibrium quasisteady-state approaches

In large-gap Mott insulators, the recombination time of photogenerated charge carriers can be much longer than the time needed for intraband thermalization. Quasisteady-state approaches approximate the resulting slowly evolving state at a given instance of time as a true steady state. In band insulators, this steady state is often well described by a Gibbs state with separate chemical potentials for the holes in the valence band and the electrons in the conduction band (Keldysh, 1986; Haug and Koch, 2009). In large-gap Mott insulators, one can expect a similar situation, but with holons and doublons instead of holes and electrons.

More generally, we can assume that, in addition to the energy E_{tot} and particle number N, there are macroscopic quantities O (we write only one for simplicity) that are almost conserved. Among other possibilities, O could represent the conduction band occupation in a semiconductor or the doublon number in a Mott insulator. If O were exactly conserved, the steady state would be a universal function of E_{tot}, N, and $\langle O\rangle$, usually taken to be a generalized Gibbs ensemble with a generalized chemical potential μ_O conjugate to O (Jaynes, 1957; Rigol *et al.*, 2007). In situations where $\langle O(t)\rangle$ evolves sufficiently slowly, the dynamics can result in so-called prethermal states, which at a given time t still have a universal form depending only on the conserved quantities (E_{tot} and N) and the slow variable $\langle O(t)\rangle$; see also Sec. VII.A. For the Hubbard model, the emergence of such a universal description is seen explicitly in long-time DMFT simulations (Dasari *et al.*, 2021), which yield distribution functions that depend on only a few parameters (Fermi functions with separate chemical potentials in the range of the upper and lower Hubbard bands).

While the hypothesis of a universal time-evolving state is not new, the question is how to construct such a state for a strongly correlated quantum system. There are two complementary strategies, the quasiequilibrium approach and the quasi-NESS approach, which we discuss with a focus on photodoped Mott states in the Hubbard model.

Quasiequilibrium approach. The quasiequilibrium approach approximates the quasisteady state as an equilibrium state of an approximate Hamiltonian H_{eff}, which conserves O (Takahashi, Yoshikawa, and Aihara, 2002; Rosch *et al.*, 2008; Kanamori, Matsueda, and Ishihara, 2011; Murakami, Takayoshi *et al.*, 2022). In this description, $\langle O\rangle$ can be fixed by introducing a generalized chemical potential μ_O. For a Mott-Hubbard system with hopping $v_0 \ll U$, the slow variables are the doublon and holon numbers, which correspond to $\hat{N}_{\mathrm{doub}} = \sum_i \hat{n}_{i\uparrow}\hat{n}_{i\downarrow}$ and $\hat{N}_{\mathrm{holon}} = \sum_i (1-\hat{n}_{i\uparrow})(1-\hat{n}_{i\downarrow})$, respectively, dressed via virtual charge fluctuations. The effective Hamiltonian H_{eff} in terms of these dressed doublons and holons can be obtained via the unitary Schrieffer-Wolff (SW) transformation $\hat{H}_{\mathrm{SW}} = e^{i\hat{S}}\hat{H}e^{-i\hat{S}}$ (MacDonald, Girvin, and Yoshioka, 1988), where the generator $\hat{S}$ is chosen to eliminate from $\hat{H}_{\mathrm{SW}}$, up to a given order in v_0/U, all recombination terms that change the doublon or holon number. For the U-V Hubbard model in Eq. (8) with $U \gg v_0, V$, the effective Hamiltonian H_{eff} up to $\mathcal{O}(v_0^2/U)$ is given by (Murakami, Takayoshi *et al.*, 2022)

$$\hat{H}_{\mathrm{eff}} = \hat{H}_U + \hat{H}_{\mathrm{kin,holon}} + \hat{H}_{\mathrm{kin,doub}} + \hat{H}_V + \hat{H}_{\mathrm{spin,ex}} + \hat{H}_{\mathrm{dh,ex}} + \hat{H}_{U,\mathrm{shift}} + \hat{H}_{\text{3-site}}. \quad (29)$$

In Eq. (29), $\hat{H}_U = U\sum_i \hat{n}_{i\uparrow}\hat{n}_{i\downarrow}$, $\hat{H}_V = (V/2)\sum_{\langle i,j\rangle}\hat{n}_i\hat{n}_j$, and $\hat{H}_{\mathrm{kin,holon}}$ and $\hat{H}_{\mathrm{kin,doub}}$ describe the hopping of holons and doublons of $\mathcal{O}(v_0)$, respectively. The remaining terms are of $\mathcal{O}(v_0^2/U)$. $\hat{H}_{\mathrm{spin,ex}} = (J_{\mathrm{ex}}/2)\sum_{\langle i,j\rangle}\mathbf{S}_i\cdot\mathbf{S}_j$ is a Heisenberg spin exchange between singly occupied sites. $\hat{H}_{\mathrm{dh,ex}} = -(J_{\mathrm{ex}}/2)\sum_{\langle i,j\rangle}\boldsymbol{\eta}_i\cdot\boldsymbol{\eta}_j$ is the analogous exchange for doublons and holons. Here the η spins are defined as

$$\eta_i^{+} = (-)^i c_{i\downarrow}^{\dagger} c_{i\uparrow}^{\dagger}, \quad \eta_i^{-} = (-)^i c_{i\uparrow} c_{i\downarrow}, \quad \eta_i^{z} = \tfrac{1}{2}(n_i - 1), \quad (30)$$

$\hat{H}_{U,\mathrm{shift}}$ describes a shift of the local interaction, and $\hat{H}_{\text{3-site}}$ consists of three-site terms such as correlated doublon hoppings. The model in Eq. (29) is a natural extension of the t-J model in Eq. (6), which is obtained by restricting H_{eff} to the sector with $\hat{N}_{\mathrm{doub}} = 0$ (hole doping) or $\hat{N}_{\mathrm{holon}} = 0$ (electron doping) and ignoring $\hat{H}_{\text{3-site}}$. To explore the steady state, one can then study the equilibrium properties of Eq. (29) for a given density of doublons and holons. In the thermodynamic limit, this can be done by introducing separate chemical potentials for the doublons and holons. Some applications of this formalism are discussed in Sec. VII.E.

Quasi-NESS approach. An alternative approach is to approximate the quasisteady state by coupling suitable particle and energy reservoirs to the system with some overall coupling strength g. The resulting state is a NESS (i.e., its properties are time independent), while the spectral and distribution functions do not necessarily satisfy the universal fluctuation-dissipation relation. However, if O is conserved, the limit $g \to 0$ should give the universal Gibbs state, where the effect of the bath is merely to fix the thermodynamic quantities E_{tot}, N, and $\langle O\rangle$. For almost conserved O, a weak bath coupling is already sufficient to control $\langle O\rangle$ independently from the other thermodynamic variables.

The strategy of controlling the values of almost conserved quantities was developed as a general framework for systems

close to integrability (Lange, Lenarčič, and Rosch, 2017). In the context of photoexcited Mott insulators, Li and Eckstein (2021) proposed approximating the slowly evolving photodoped state by coupling the system to particle reservoirs. If fully occupied (empty) electron baths are weakly coupled to the upper (lower) Hubbard band, a NESS with a given E_{tot}, N, and density of doublons and holons is established. The nonthermal occupations in the system are maintained via a small current from occupied to unoccupied states, while energy can be dissipated to the electron baths or to additional bosonic heat baths. The NESS approach was applied to photoexcited Mott insulators, with reasonable agreement of the spectral and distribution functions to time-dependent simulations (Li and Eckstein, 2021; Ray, Eckstein, and Werner, 2025). In the phase diagram of the photodoped Hubbard model, the NESS approach predicts the emergence of η pairing (Li, Golez, Werner, and Eckstein, 2020), which is consistent with the quasiequilibrium approach; see Sec. VII.E.3.

IV. MOTT INSULATORS IN STATIC ELECTRIC FIELDS

In this section we discuss the effects of static electric fields on Mott insulators. On the one hand, strong fields modify the kinematics of the charge carries (see Sec. IV.A), which also affects the low-energy spin physics (see Sec. IV.B). On the other hand, they create charge carriers via quantum tunneling, which can result in a metallic state; see Sec. IV.C. We also discuss the mobility of charge carriers in strong fields, where the energy dissipation plays a crucial role; see Sec. IV.D.

A. Field-induced localization

In the presence of a static dc electric field E_0, a charge carrier with charge q (for example, a conventional band electron or a doublon in a Mott insulator) that hops n times the lattice spacing a in the direction of the field gains an energy nqE_0a. If this energy exceeds the width of the Hubbard band W, the energy absorbed from the field can no longer be converted into kinetic energy. Hence, the charge carrier cannot move farther in the direction of the field unless it can pass on energy to other degrees of freedom. For free-electron systems, this results in Bloch oscillations (Bloch, 1929; Zener, 1934; Kruchinin, Krausz, and Yakovlev, 2018) where carriers move back and forth over a distance $na \sim W/qE_0$ and thus get localized in the direction of the field. This explains the phenomenon of field-induced dimensional reduction (Aron, Kotliar, and Weber, 2012).

The energy of the localized state depends on its central position. Thus, the lattice system with a static field exhibits an infinite series of localized states whose energy is shifted by lqE_0a (the Wannier-Stark ladder), where l corresponds to the site at which the state is localized. This ladder structure is directly evident in the single-particle spectrum, which can split into a series of δ peaks separated by $\Omega = qE_0a$ for noninteracting systems. Analytic expressions can be obtained, for example, for the hypercubic lattice (Tsuji, Oka, and Aoki, 2008).

In Mott insulators, dc fields result in a similar localization of charge carriers (Eckstein and Werner, 2013a; Lee and Park, 2014; Murakami and Werner, 2018; Udono, Kaneko, and Sugimoto, 2023). Again, the localization effects can be observed in the spectral function. Figure 8(a) shows DMFT + NCA results for an initially Mott-insulating Hubbard model on the infinite-dimensional hypercubic lattice [with a Gaussian noninteracting density of states $\rho(\epsilon) = (1/\sqrt{\pi}v_*)\exp(-\epsilon^2/v_*^2)$], which is obtained by applying the Floquet DMFT formalism to this steady-state problem in the dipolar gauge. Although an approximate impurity solver is used in this study, we expect it to capture the correct spectral features. Owing to the localization, the Hubbard bands get narrowed compared to the field-free case and we notice the emergence of sidebands, which are split off from the original band center by $\pm lqaE_0$. The side peak at $\omega = U/2 \pm lqaE_0$ is associated with adding an electron at site i into a many-body Wannier-Stark state with a localized doublon at site $i \mp l$. In this interacting system, the charge carriers can transfer excess potential energy to other particles or spin excitations and the localization is not perfect. This is reflected in the width of the Wannier-Stark bands. In addition, the many-body system can produce signals that are absent in free systems. For example, the faint spectral weight at $(3/2)U - 2qaE_0$, highlighted by the arrow in Fig. 8(a), represents a process where the insertion of one electron at a given site leads to the creation of a doublon and the simultaneous creation of another doublon-holon (D-H) pair.

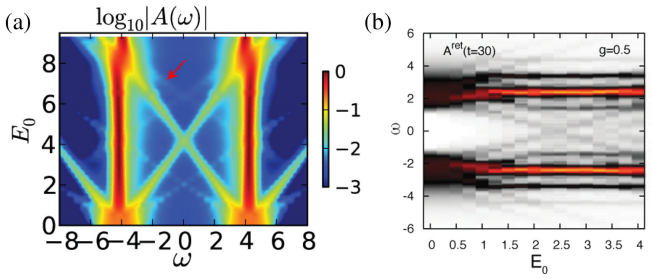

FIG. 8. (a) Spectral function of the Hubbard model with $U = 8$ under a static electric field with amplitude E_0 (hypercubic lattice, $v_* = 1$ and $q = a = 1$). The arrow marks the spectral weight at $(3/2)U - 2qaE_0$. (b) Corresponding result for the Holstein-Hubbard model with $U = 5$, $\omega_0 = 1$, and $g = 0.5$. Both results were obtained using DMFT + NCA. From Werner and Eckstein, 2015, and Murakami and Werner, 2018.

Recently, Udono, Kaneko, and Sugimoto (2023) studied the signature of the Wannier-Stark localization in the optical conductivity of the one-dimensional Hubbard model using the infinite time-evolving block decimation (iTEBD) algorithm. They demonstrated the emergence of multiple peaks in the optical conductivity and the reduction of the optical gap under the dc electric field. The latter can be regarded as the Franz-Keldysh effect in this Mott system.

Furthermore, since the dc field quenches the kinetic energy, it can enhance local interaction effects. Figure 8(b) illustrates the following three effects of a static electric field in the Holstein-Hubbard model: (i) the narrowing of the main Hubbard band for $qaE_0 \gtrsim W$, (ii) the appearance of Wannier-Stark sidebands that are split off from the main Hubbard bands by an energy $\pm lqaE_0$, and (iii) the appearance of phonon sidebands with an energy splitting $\pm n\omega_0$. In this

simulation, as is representative for typical electron-phonon systems, the ratio g/W between the phonon coupling and bandwidth is too small for the appearance of well-resolved phonon sidebands in equilibrium. However, if the field-induced localization narrows the bands, the relative coupling strength is enhanced and phonon sidebands can be clearly resolved in the nonequilibrium spectral function. The measurement of these sidebands would allow the phonon energy ω_0 to be extracted. Similarly, strong dc fields applied to multiorbital systems produce well-defined multiplet peaks in the single-particle spectrum, from which the Hund coupling J_H could be deduced (Dasari *et al.*, 2021).

B. Effective spin exchange

In Sec. IV.A, we showed that the energy levels of states with doublons and holons are strongly modified by a dc field. Since such states are involved in the virtual excitation processes underlying the spin exchange mechanism, the dc electric field also modifies the spin exchange couplings (Trotzky *et al.*, 2008; Takasan and Sato, 2019). The basic idea can be understood by considering the 1D Hubbard model in the length gauge,

$$H = -v_0 \sum_{\langle i,j\rangle\sigma} c^\dagger_{i\sigma} c_{j\sigma} + U \sum_i n_{i\uparrow} n_{i\downarrow} - qaE_0 \sum_i i n_i. \tag{31}$$

In this case the energy level difference between neighboring sites becomes $\Delta \equiv qaE_0$. If we assume a Mott-insulating phase and consider a Hilbert space consisting of states with only singlons, then second-order perturbation theory [see Fig. 9(a)] yields the spin Hamiltonian

$$H_{\text{spin}} = \sum_{\langle i,j\rangle} \left[\frac{v_0^2}{U-\Delta} + \frac{v_0^2}{U+\Delta} \right] \mathbf{S}_i \cdot \mathbf{S}_j. \tag{32}$$

The first (second) term is the contribution from the virtual excitation of an electron along (opposite to) the field direction; see Fig. 9(a). Equation (32) implies that for $U > \Delta$ the spin exchange coupling is enhanced, while for $U < \Delta$ its sign flips. The spin Hamiltonian in Eq. (32) describes the physics of the spin sector if the excitation of long-lived D-H pairs by the field can be neglected; see Sec. IV.C. In the dipolar gauge (see Sec. II.B), the vector potential for a dc field is $A(t) = -E_0 t$. Hence, the Hubbard model becomes time periodic with frequency $\Omega = qE_0 a$, and Eq. (32) can be obtained as a Floquet effective Hamiltonian; see Sec. V.

Similar ideas for modifying the spin exchange coupling have been discussed for both bosonic (Trotzky *et al.*, 2008; Dimitrova *et al.*, 2020; Sun *et al.*, 2021) and fermionic systems (Takasan and Sato, 2019; Furuya, Takasan, and Sato, 2021; Takasan and Tezuka, 2021). The bosonic case was considered in a cold-atom context, where the spin model can be derived from the two-component Bose-Hubbard model in the strong-coupling regime. It becomes ferromagnetic at $\Delta = 0$, unlike the fermionic Hubbard model, and it becomes antiferromagnetic for $\Delta > U$. For a two-site system, such a sign change of the spin exchange coupling has been demonstrated experimentally (Trotzky *et al.*, 2008). The experiment measured the spin imbalance $N_z = (n_{\uparrow L} + n_{\downarrow R} - n_{\uparrow R} - n_{\downarrow L})$ between the left

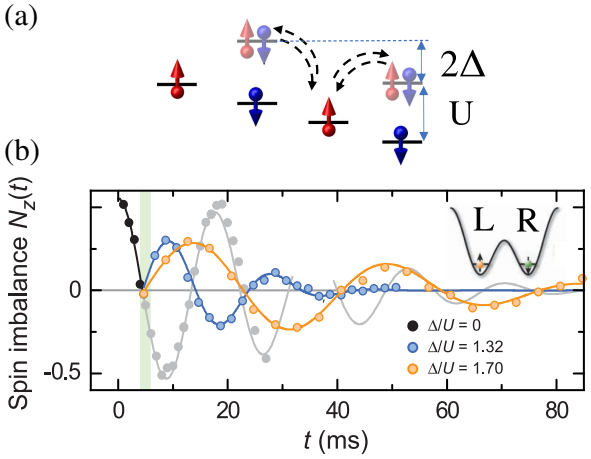

FIG. 9. (a) Real-space energy level structure of a Mott insulator with interaction strength U in a dc field corresponding to the nearest-neighbor energy difference Δ. The dashed arrows indicate second-order virtual hopping processes. (b) Time evolution of the spin imbalance $N_z(t)$ for different field strengths in a cold-atom experiment on a two-site Bose-Hubbard system. The oscillation of $N_z(t)$ can be related to the value of the spin exchange coupling. The hopping-to-interaction ratio is $v_0/U = 0.08$. Inset: initial state. From Trotzky *et al.*, 2008.

(L) and right (R) sites, starting with an initial product state, as shown in the inset of Fig. 9(b). The observed pseudospin precessional dynamics depends on the value of the exchange coupling. For $\Delta > U$, N_z exhibits the opposite dynamics of the system with $\Delta = 0$, which demonstrates the sign change of the exchange coupling; see Fig. 9(b). A modification of the exchange coupling based on this idea has also been experimentally realized in extended systems (Dimitrova *et al.*, 2020). For fermionic systems the modification of magnetic superexchange couplings using dc fields has been discussed in regard to the d-p model (Furuya, Takasan, and Sato, 2021). Control over the exchange couplings is helpful for realizing exotic spin phases that are hard to access in equilibrium, such as the antiferromagnetic state in bosonic systems (Sun *et al.*, 2021) or a chiral spin-liquid state in a frustrated fermionic system (Schultz *et al.*, 2023). In solids, heating effects for $\Delta \approx U$ may, however, limit the ability to significantly modify the exchange coupling.

C. Dielectric breakdown

The destruction of an insulating state by a static electric field is called dielectric breakdown. A well-studied scenario in the context of Mott insulators is the creation of charge carriers via quantum tunneling. In a Mott-insulating single-band Hubbard model, the tunneling induced by a static field E_0 produces D-H pairs. This process is illustrated in the length gauge in Fig. 10(a), which sketches the lower and upper Hubbard bands that are tilted by the potential $V(x) = -qE_0 x$ and separated in energy by the Mott gap Δ_{Mott}. If a D-H pair is created on neighboring sites and then separated by a distance na, the energy $nqE_0 a$ is absorbed from the field. If this energy exceeds the gap Δ_{Mott}, D-H pairs can be freely generated, similar to the Schwinger mechanism for electron-positron

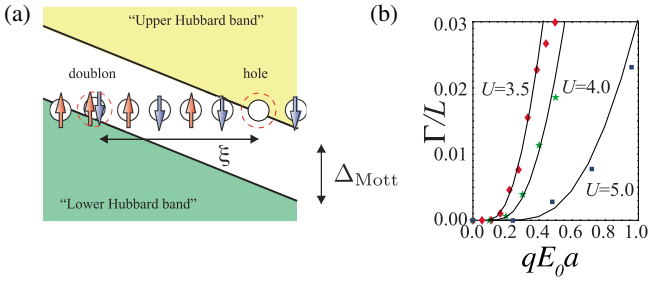

FIG. 10. (a) Dielectric breakdown of a Mott insulator in a static electric field E_0. The Hubbard bands are tilted because of the potential $V(x) = -qE_0x$. Δ_{Mott} denotes the Mott gap and ξ represents the characteristic size of a *D*-*H* pair. (b) Decay rate of the ground state Γ calculated with time-dependent DMRG (symbols) for a 1D system of length L. The solid lines indicate the analytical results from Eqs. (33) and (34). From Oka and Aoki, 2010, and Oka, 2012.

production (Schwinger, 1951) or the Zener breakdown of band insulators (Oka and Aoki, 2005).

Numerical and analytical calculations (Oka, Arita, and Aoki, 2003; Oka and Aoki, 2005, 2010; Eckstein, Oka, and Werner, 2010; Heidrich-Meisner *et al.*, 2010; Tanaka and Yonemitsu, 2011; Lenarčič and Prelovšek, 2012; Oka, 2012; Eckstein and Werner, 2013a; Takasan, Nakagawa, and Kawakami, 2019) demonstrated that the *D*-*H* production rate Γ follows a threshold behavior

$$\Gamma \propto E_0 \exp\left(-\frac{\pi E_{0,\mathrm{th}}}{E_0}\right) \tag{33}$$

with some threshold field $E_{0,\mathrm{th}}$. It is generally expected that the threshold field is related to the Mott gap Δ_{Mott} and the *D*-*H* correlation length ξ in equilibrium as

$$E_{0,\mathrm{th}} \sim \frac{\Delta_{\mathrm{Mott}}}{2q\xi}. \tag{34}$$

Equation (34) was analytically derived for the 1D Hubbard model (Oka and Aoki, 2010; Oka, 2012) by applying Landau-Dykhne tunneling theory for the *D*-*H* pair states and using the Bethe *Ansatz* solution for the non-Hermitian Hubbard model (Fukui and Kawakami, 1998). Equations (33) and (34) show that a field $qE_0\xi \sim \Delta_{\mathrm{Mott}}$ is required to turn the fluctuations of *D*-*H* pairs into real excitations.

In connection with experiments, the dependence of $E_{0,\mathrm{th}}$ on the gap is important. For the 1D Hubbard model with a small gap, $E_{0,\mathrm{th}} \propto \Delta_{\mathrm{Mott}}^2$, which is analogous to the Landau-Zener result (Oka, Arita, and Aoki, 2003). An intuitive understanding of the dielectric breakdown in a 1D Mott insulator can also be obtained by analytically treating the fully spin polarized limit (Lenarčič and Prelovšek, 2012). This calculation yields a different scaling, $E_{0,\mathrm{th}} \propto \Delta_{\mathrm{Mott}}^{3/2}$. For the infinite-dimensional case, a DMFT + NCA analysis showed $E_{0,\mathrm{th}} \to 0$ when the system approached the metal-insulator crossover regime, as expected from Eq. (34) (Eckstein, Oka, and Werner, 2010). Figure 10(b) shows the ground state decay rate, which is related to the *D*-*H* production rate ($|\langle\psi(t)|\psi(0)\rangle|^2 \sim e^{-\Gamma t}$), from time-dependent DMRG simulations of a 1D Mott insulator in a constant electric field switched on at $t = 0$ (Oka and Aoki, 2010). The decay rate shows a threshold behavior and matches the analytical results from Landau-Dykhne tunneling theory.

Strictly speaking, Eq. (33) is expected to hold asymptotically for small E_0. For large E_0 one should consider the reconstruction of the spectral function and the emergence of in-gap states owing to the development of the Wannier-Stark ladder, as discussed in Sec. IV.A. In particular, for large U, the resonant enhancement of the pair creation at $qE_0a = U/n$ (n integer) is clearly observed in the DMFT simulations (Eckstein and Werner, 2013a). A related enhancement of the doublon-holon density has also been reported in the steady state of a Mott insulator under dc fields (Aron, 2012; Lee and Park, 2014; Murakami and Werner, 2018).

Experimentally, the dielectric breakdown of Mott insulators induced by dc fields has been extensively studied (Taguchi, Matsumoto, and Tokura, 2000; Janod *et al.*, 2015). In many experiments dielectric breakdown is observed for much weaker electric fields than predicted by the quantum tunneling analysis. This low threshold has been attributed to other mechanisms, such as filament formation and avalanche effects (Guiot *et al.*, 2013), efficient carrier generation from impurity levels (Diener *et al.*, 2018; Kalcheim *et al.*, 2020), and a simultaneous structural phase transition (Nakamura *et al.*, 2013). Theoretical scenarios for a transition induced by weak fields consider the possibility of a gap collapse in the metal-insulator coexistence region (Mazza *et al.*, 2016) or the inhomogeneous properties of resistor networks (Stoliar *et al.*, 2013).

To study the physics induced by dc fields, one may in practice use terahertz to midinfrared fields that vary slowly on electronic timescales. Liu *et al.* (2012) considered the dielectric breakdown induced by strong terahertz fields in VO_2. The insulator-metal transition occurs on a timescale of several picoseconds and is associated with carrier generation from impurities and heating caused by carrier acceleration in the field. The midinfrared excitation of VO_2 also provides evidence of the dielectric breakdown of a Mott insulator via quantum tunneling (Mayer *et al.*, 2015). Further examples are terahertz excitation studies of 1D and 2D organic Mott-insulating compounds (Yamakawa *et al.*, 2017; Takamura *et al.*, 2023). Yamakawa *et al.* (2017) subjected the 2D system κ-$(ET)_2Cu[N(CN)_2]Br$ on a diamond substrate, with a Mott gap of approximately 30 meV, to a strong pump pulse with a frequency of about 1 THz. By observing changes in the OD in the midinfrared range, it was possible to trace the insulator-metal transition; see Fig. 11(a). The field-strength dependence of the change in the OD at $t = 0$ (at the peak of the terahertz pulse) was found to be consistent with the tunneling formula in Eq. (33), with $E_{0,\mathrm{th}} = 64\ \mathrm{kV\,cm^{-1}}$; see Fig. 11(b). The corresponding correlation length $\xi = \Delta_{\mathrm{Mott}}/2qE_{0,\mathrm{th}}$ is 23 Å, which is a reasonable value for this system. At $t = 0.7$ ps, the change in the OD no longer follows the tunneling formula, which was explained by the collapse of the Mott gap.

D. Mobility of charge carriers in strong fields

In this section, we discuss how the charge carriers contribute to the current in strong dc fields. In closed systems the

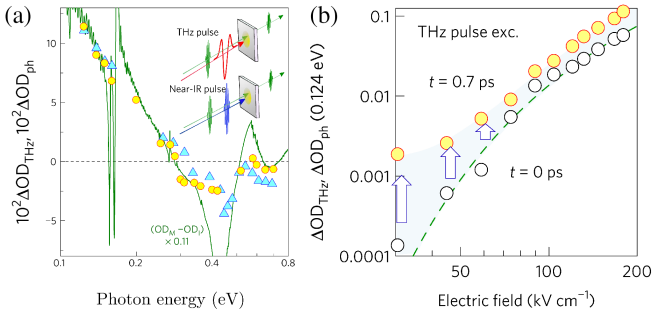

FIG. 11. (a) Transient absorption changes at $t = 0.7$ ps induced by a terahertz pulse ΔOD_{THz} (circles) and a near-IR light pulse ΔOD_{ph} (triangles) with a frequency of 0.93 eV. The solid green line shows the difference between the absorption spectra of the Mott-insulating and metallic phases in equilibrium. (b) Transient absorption change ΔOD_{THz} at delay $t = 0$ (empty circles) and 0.7 ps (yellow circles) at photon energy 0.124 eV versus electric-field strength $E_0 \equiv E_{THz}$ ($t = 0$). The green dashed line is a fit to Eq. (33). From Yamakawa *et al.*, 2017.

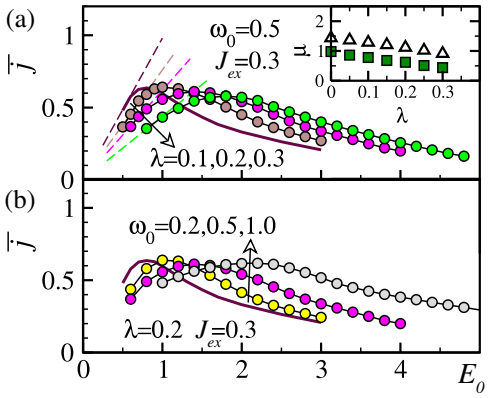

FIG. 12. ED results for the quasisteady current $\bar{j}$ of a single hole in the two-dimensional t-J-Holstein model with an electron-phonon coupling $\lambda = g^2/W\omega_0$ and an exchange coupling $J = J_{ex}$. Inset: sketch showing how the mobility scales with λ. Adapted from Vidmar *et al.*, 2011.

dc field in Mott insulators leads to a broad energy distribution (high temperature) of the generated doublons and holons (Oka, 2012; Eckstein and Werner, 2013a); see also Sec. V.F. Such "hot" doublons and holons hardly contribute to the current, which results in a small conductivity. This is in contrast to photodoped systems, where photodoped populations with a relatively narrow energy distribution and finite conductivity can be realized. Besides the temperature effect, recent studies emphasized that kinetic constraints due to the high fields can lead to a transient nonergodic evolution (Desaules *et al.*, 2021; Scherg *et al.*, 2021; Kohlert *et al.*, 2023) and reduced conductivity (Shinjo, Sota, and Tohyama, 2022). In the strong-field regime, the mobility of the carriers in the field direction is limited by their ability to dissipate the energy gained from the field, which leads to a negative differential resistivity (Mierzejewski *et al.*, 2011; Vidmar *et al.*, 2011). Thus, the coupling between the charge carriers and dissipation channels, which leads to cooling and the breaking of kinetic constraints, is crucial for understanding the current induced by dc fields.

Possible dissipation channels in the single-orbital case are the interaction of doublons and holons with an antiferromagnetic spin background (see Sec. VI.D.3) and their coupling to phonons. The effects of the spin and phonon baths have been considered in the ED study by Vidmar *et al.* (2011), which simulated a single hole in the two-dimensional t-J model with a static electric field and additional coupling to Holstein phonons. Because of the energy dissipation, the current reaches a quasisteady-state value $\bar{\mathbf{j}} \equiv \mathbf{J}(t_{max})$ at the longest propagation time t_{max} after an initial transient. Figure 12 plots the value of $\bar{j}$ as a function of the field strength E_0. In the small-field regime, $\bar{j}$ increases linearly with E_0 and the slope (conductivity) is plotted as a function of the electron-phonon coupling λ in the inset. The decrease in conductivity with increasing λ is due to stronger phonon scattering, which is consistent with the linear-response result (triangles). As the field strength is increased, the conventional positive differential resistivity gives way to a negative differential resistivity, i.e., the quasisteady-state current gets suppressed with increasing E_0. In this regime, the phonon coupling has the opposite effect: a stronger phonon coupling enables more efficient energy dissipation and hence higher hole mobility. Furthermore, for fixed λ the current is enhanced for larger ω_0 because the phonons can absorb larger energy quanta.

Comparing the effects of the phonons and the antiferromagnetic spin background on the dissipation, Vidmar *et al.* (2011) concluded that the spin cooling is more effective for realistic parameters as long as the antiferromagnetic correlations in the spin background remain significant. The energy transfer to the antiferromagnetic spin background is large because, in an antiferromagnetic state, each hopping breaks antiferromagnetic bonds and dissipates energy of the order of J_{ex}. In contrast, for small phonon coupling, there can be several hops before a phonon is emitted.

The nonlinear strong-field transport behavior can also be relevant for strong internal fields. Such internal electric fields appear in polar heterostructures, and the separation of photodoped doublons and holons in these fields has been discussed in connection with Mott-insulating solar cells (Assmann *et al.*, 2013; Eckstein and Werner, 2014; Petocchi *et al.*, 2019). Heterostructures can be simulated with the inhomogeneous extension of DMFT (Potthoff and Nolting, 1999; Okamoto and Millis, 2004; Eckstein and Werner, 2013b). In addition, in this setup a fast diffusion and hence separation of the charge carriers is possible only in the presence of an efficient dissipation mechanism, since otherwise the strong field will localize the charge carriers (Eckstein and Werner, 2014). Mott-insulating heterostructures with antiferromagnetic order have a built-in efficient dissipation channel (transfer of kinetic energy to the spin background) and are therefore particularly interesting for solar cell applications. The effect of the ordered spin background on the separation of doublons and holons is illustrated in Fig. 13, which plots the time evolution of a photoinduced doublon and holon population in a six-layer heterostructure. Figure 13(a) plots the evolution in a high-temperature paramagnetic structure. Here the doublons and holons, which are produced by the pulse in layer 1, remain confined close to this surface layer even though the heterostructure has a strong internal field that pushes the doublons in

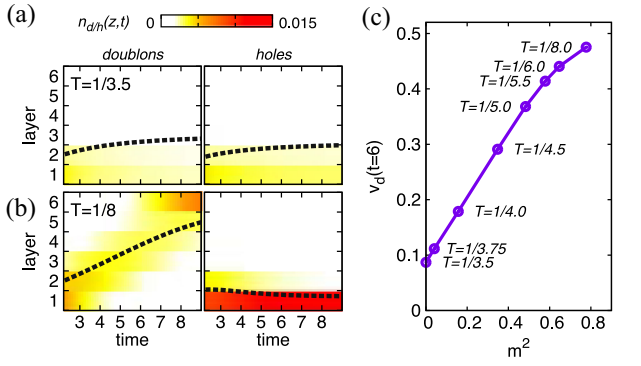

FIG. 13. Layer-dependent doublon and holon densities in a six-layer Mott-insulating polar heterostructure within (a) the high-temperature paramagnetic regime and (b) the low-temperature antiferromagnetic regime. (c) Plot of the drift velocity v_d measured at time $t = 6$ as a function of the staggered magnetization squared. The results were obtained via DMFT + NCA. From Eckstein and Werner, 2014.

the direction of layer 6. In the lower-temperature antiferromagnetic state [Fig. 13(b)], the mobility of the doublons is much higher because they can now dissipate their kinetic energy to the spin background. The holons remain confined near layer 1, so the doublons and holons are physically separated after just a few hopping times. The drift velocity of the doublons is plotted in Fig. 13(c) as a function of the squared staggered magnetization m. The quadratic scaling can be understood by considering that the spin energy is $\sim J_{\mathrm{ex}} m^2$ and the energy dissipation rate is $\sim J_{\mathrm{ex}} m(dm/dt)$ (Eckstein and Werner, 2014).

V. MOTT INSULATORS IN AC FIELDS

In this section, we discuss the ac driving of Mott insulators, which includes the engineering of effective Floquet Hamiltonians under periodic driving, photocarrier generation, nonlinear optical responses under strong driving fields (such as high-harmonic generation), and nonlinear phononics. For an overview of phenomena in periodically driven systems, see Sec. I.B.1.

A. Floquet Hamiltonian

The Floquet Hamiltonian provides useful insights into the effects of ac fields on Mott insulators. We assume that the Hamiltonian is time periodic with frequency Ω. Denoting the unitary time evolution operator from t_0 to t by $\mathcal{U}(t, t_0)$, one can define the Floquet Hamiltonian as the generator of the evolution $\mathcal{U}(t_0 + T_p, t_0) = e^{-iT_p \hat{H}_{\mathrm{Floq}}[t_0]}$ over one period $T_p \equiv 2\pi/\Omega$ (stroboscopic evolution). While this definition depends on the choice of t_0, the operators $\hat{H}_{\mathrm{Floq}}[t_0]$ for different t_0 are unitarily equivalent (Bukov, D'Alessio, and Polkovnikov, 2015). In general, it is difficult to evaluate $\hat{H}_{\mathrm{Floq}}$, and in solids or realistic optical lattice systems, excitations to higher bands complicate the analysis. However, in simple models, when Ω is large compared to the typical energy scales of the system, the effective Hamiltonian can be approximated via a perturbative high-frequency expansion that comes in three main flavors: (i) the Floquet-Magnus expansion, where the Floquet Hamiltonian depends on the gauge freedom inherent in $\hat{H}_{\mathrm{Floq}}[t_0]$ (Rahav, Gilary, and Fishman, 2003); (ii) the Van Vleck expansion, where the gauge freedom is removed by considering a nonstroboscopic Hamiltonian (Bukov, D'Alessio, and Polkovnikov, 2015); and (iii) the Brillouin-Wigner inverse frequency expansion (Mikami *et al.*, 2016). The latter is gauge invariant and often suitable for numerical studies, but it suffers from non-Hermitian high-order terms. Here we proceed with the description of the Van Vleck formalism, where the effective Floquet Hamiltonian is given by

$$\hat{H}_{\mathrm{eff}} = \hat{H}_0 + \sum_{l>0} \frac{[\hat{H}_l, \hat{H}_{-l}]}{l\Omega} + \mathcal{O}\left(\frac{1}{\Omega^2}\right), \tag{35}$$

where $\hat{H}_l$ is defined in terms of the Fourier expansion $\hat{H}(t) = \sum_l \hat{H}_l e^{il\Omega t}$. It describes the transition from n-photon-dressed states to $(n + l)$-photon-dressed states such that $\hat{H}_{\mathrm{eff}}$ takes into account virtual fluctuations to photo-dressed states.

As a simple example, we consider the single-band Hubbard model in Eq. (1) in the Mott regime, with a hopping amplitude $v_{ij}(t)$ that oscillates with frequency Ω. (This includes the driving with ac electric fields.) The high-frequency expansion can be used in two separate limits, leading to different effective Hamiltonians.

High-frequency regime ($\Omega \gg U, v_0$). When Ω is much larger than all system parameters, one can directly apply Eq. (35) to obtain the Floquet Hamiltonian. The lowest-order Hamiltonian becomes

$$\hat{H}_0 = -\sum_{\langle i,j\rangle,\sigma} \mathcal{A}_{ij}^{(0)} \hat{c}_{i\sigma}^\dagger \hat{c}_{j\sigma} + U \sum_j \hat{n}_{j\uparrow} \hat{n}_{j\downarrow}, \tag{36}$$

where $\mathcal{A}_{ij}^{(l)}$ is defined by $v_{ij}(t) = \sum_l \mathcal{A}_{ij}^{(l)} e^{il\Omega t}$. The higher-order terms are obtained from Eq. (35), with

$$\hat{H}_l = -\sum_{\langle i,j\rangle,\sigma} \mathcal{A}_{ij}^{(l)} \hat{c}_{i\sigma}^\dagger \hat{c}_{j\sigma}. \tag{37}$$

At this level of approximation, the main effect of the field is to modify the hopping terms, and the effective Hamiltonian remains of the Mott-Hubbard type.

High-frequency and large-U regime. When $\Omega, |U| \gg v_0$ but U and Ω are of comparable magnitudes, one can switch to a rotating frame to deal with U and Ω on an equal footing (Bukov, Kolodrubetz, and Polkovnikov, 2016). For this we introduce a common frequency Ω_0 such that $\Omega = k_0\Omega_0$ and $U \simeq l_0\Omega_0 (\equiv U_0)$, where k_0 and l_0 are coprime integers. The condition $U \simeq l_0\Omega_0$ assumes that the detuning $\Delta U (\equiv U - U_0)$ is much smaller than Ω_0. The rotating frame is defined by the unitary transformation $\hat{\mathcal{U}}(t) = \exp(-iU_0 t \sum_j \hat{n}_{j\uparrow}\hat{n}_{j\downarrow})$, so that the Hamiltonian in the rotating frame is given by $\hat{H}^{\mathrm{rot}}(t) = -\sum_{\langle i,j\rangle,\sigma}\{v_{ij}(t)\hat{g}_{ij\sigma} + [v_{ij}(t)e^{iU_0 t}\hat{h}_{ij\sigma}^\dagger + \mathrm{H.c.}]\} + \Delta U \sum_j \hat{n}_{j\uparrow}\hat{n}_{j\downarrow}$, where $\hat{g}_{ij\sigma} = (1 - \hat{n}_{i\bar{\sigma}})\hat{c}_{i\sigma}^\dagger \hat{c}_{j\sigma}(1 - \hat{n}_{j\bar{\sigma}}) + \hat{n}_{i\bar{\sigma}}\hat{c}_{i\sigma}^\dagger \hat{c}_{j\sigma}\hat{n}_{j\bar{\sigma}}$ conserves the number of holons and doublons and $\hat{h}_{ij\sigma}^\dagger = \hat{n}_{i\bar{\sigma}}\hat{c}_{i\sigma}^\dagger \hat{c}_{j\sigma}(1 - \hat{n}_{j\bar{\sigma}})$ generates a doublon. Then one

applies the high-frequency expansion (with respect to Ω_0) to $\hat{H}^{\rm rot}$. To lowest order

$$\hat{H}_0^{\rm rot} = -\sum_{\langle ij\rangle\sigma}\{\tilde{\mathcal{A}}_{ij}^{(0)}\hat{g}_{ij\sigma} + [\tilde{\mathcal{B}}_{ij}^{(0)}\hat{h}_{ij\sigma}^{\dagger} + \text{H.c.}]\} + \Delta U\sum_j \hat{n}_{j\uparrow}\hat{n}_{j\downarrow}, \tag{38}$$

where $\tilde{\mathcal{A}}$ and $\tilde{\mathcal{B}}$ are defined as $v_{ij}(t) = \sum_l \tilde{\mathcal{A}}_{ij}^{(l)} e^{il\Omega_0 t}$ and $\tilde{\mathcal{B}}_{ij}^{(l)} = \tilde{\mathcal{A}}_{ij}^{(l-l_0)}$. Higher-order terms are obtained with $\hat{H}_l^{\rm rot} = -\sum_{\langle ij\rangle\sigma}\{\tilde{\mathcal{A}}_{ij}^{(l)}\hat{g}_{ij\sigma} + [\tilde{\mathcal{B}}_{ij}^{(l)}\hat{h}_{ij\sigma}^{\dagger} + \tilde{\mathcal{B}}_{ij}^{(-l)*}\hat{h}_{ij\sigma}]\}$ from Eq. (35). The situation can be further categorized into the case $k_0 = 1$ ($U \simeq l_0\Omega$), corresponding to a driving in near resonance to single-photon or multiphoton absorption processes and the nonresonant case ($k_0 \neq 1$). In the former case, the *D*-*H* creation-annihilation terms in the low-order effective Hamiltonian [for example, $\tilde{\mathcal{B}}_{ij}^{(0)}$ in Eq. (38)] are nonzero, while they vanish in the nonresonant case. Nonresonant driving is relevant for the control of the low-energy physics, such as spin and orbital dynamics; see Sec. V.D.

B. Band renormalization

One of the most basic effects in a periodically driven lattice model is the renormalization of the hopping parameters, i.e., dynamical localization. This effect can be easily understood for noninteracting band electrons (Dunlap and Kenkre, 1986; Holthaus, 1992; Eckardt, Weiss, and Holthaus, 2005; Tsuji *et al.*, 2011), but it is equally relevant for the motion of doublons and holons in (photo)doped Mott insulators. In the Floquet Hamiltonians in Eqs. (36) and (38), this renormalization of the tunneling appears in the coefficients of the kinetic terms. For an ac electric field with peak amplitude E_0 and frequency Ω, the hopping along the direction of the field (and hence the corresponding $\mathcal{A}_{ij}^{(0)}$) is renormalized as

$$v_0 \to \mathcal{J}_0(A_0)v_0, \tag{39}$$

where $\mathcal{J}_0$ is the modified Bessel function of the first kind, $A_0 = qaE_0/\Omega$, and a is the bond length. When $\Omega \gg U$, there is no photon absorption in a single-band model and the main effect of the electric field is to drive the system into the strong-coupling regime. In such a case, a reduction of the doublon density is expected (Sandholzer *et al.*, 2019) and may tigger a metal-insulator transition (Ishikawa *et al.*, 2014). In addition, the directional dependence of the hopping renormalization may be used to control the dimensionality of the system.

The band renormalization effect is evident in the single-particle spectrum, as shown in Fig. 14 for an infinite-dimensional hypercubic lattice with a field along the body diagonal. In the noninteracting limit [Figs. 14(a) and 14(b)], the bandwidth shrinks to zero for the field strengths satisfying $\mathcal{J}_0(A_0) = 0$, in accordance with Eq. (39). A qualitatively similar evolution is seen in the spectral function of the Mott insulator with $U = 8$ [Figs. 14(c) and 14(d)], where the width of the main Hubbard bands shrinks and widens with increasing E_0.

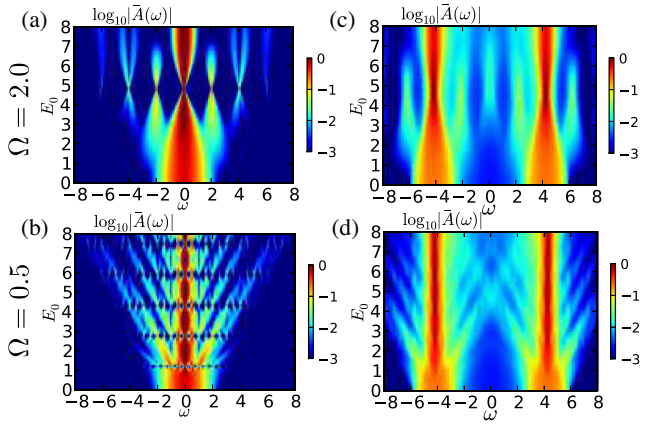

FIG. 14. Log scale plots of the time-averaged local (momentum-averaged) spectral function $A(\omega)$ of the Hubbard model on a hypercubic lattice driven by ac fields with $\Omega = 2.0$ or 0.5 as a function of the field amplitude E_0 (hypercubic lattice, $v_* = 1$). (a),(b) Noninteracting system. (c),(d) Floquet DMFT + NCA results for Mott-insulating systems with $U = 8$ coupled to a fermion bath to stabilize a time-periodic state. From Murakami and Werner, 2018.

C. Floquet sidebands

Periodic driving not only renormalizes the Hubbard bands but also leads to new features in the spectral function, so-called Floquet sidebands. These bands correspond to photodressed states and are split off from the center of the original band by multiples of the driving frequency Ω. Floquet bands have been observed experimentally in good metals (Wang *et al.*, 2013), even for few-cycle pulses (Ito *et al.*, 2023). However, the existence of Floquet sidebands depends on the electronic lifetime, as the electron-electron scattering prevents a coherent motion of Bloch electrons (Aeschlimann *et al.*, 2021). While doublons and holons in a Mott insulator move incoherently, theoretical simulations nevertheless show clear Floquet bands for sufficiently strong and high-frequency excitations. Again, it is instructive to compare the spectra for the Mott insulator and noninteracting system in Fig. 14. When the excitation frequency is high enough, one can identify clear Floquet sidebands with an energy splitting $\Delta\omega = m\Omega$ from the main band [Fig. 14(a)] or the Hubbard bands [Fig. 14(c)]. In particular, when $\mathcal{J}_0(A_0) = 0$, the Floquet bands in the noninteracting system [Fig. 14(a)] are clearly defined, with a position at $m\Omega$ regardless of the momentum. For the Mott insulator, the dynamical localization is not perfect, but nevertheless Floquet sidebands of the Hubbards bands are best defined at $\mathcal{J}_0(A_0) = 0$. For small Ω (compared to the bandwidth $\simeq 2v_*$), the sidebands overlap with each other and the spectrum shows structures resembling the Wannier-Stark ladders for a dc field; see Figs. 14(b) and 14(d) and Sec. IV.A.

D. Effective spin and orbital exchange

In Mott insulators, ac fields can be used to directly modify low-energy degrees of freedom related to magnetic and orbital orders. In particular, the optical manipulation of magnetism is potentially interesting for ultrafast magnetic memories (Kirilyuk, Kimel, and Rasing, 2010). Floquet spin

Hamiltonians can be engineered based on the linear coupling of spins to the magnetic field of light via the Zeeman term (Takayoshi, Aoki, and Oka, 2014; Takayoshi, Sato, and Oka, 2014; Sato, Takayoshi, and Oka, 2016). However, the stronger electric field of the laser can also be used, although it does not linearly couple to the spin. The underlying principle is general and extends to basically all low-energy degrees of freedom. Virtual transitions to photodressed states can modify the exchange couplings or even induce new terms in the Hamiltonian of spin and/or orbital degrees of freedom.

A fundamental example is the half-filled single-band repulsive Hubbard model with nearest-neighbor hopping v_0 exposed to a linearly polarized ac field with frequency Ω and vector potential amplitude A_0. The corresponding effective Hamiltonian can be obtained following the discussion in Sec. V.A for the case $\Omega, U \gg v_0$. For off-resonant driving ($U \neq l\Omega$), no doublons and holons are generated, and the leading term of the effective Hamiltonian becomes a spin Hamiltonian $\hat{H}_{\mathrm{J}} = (J_{\mathrm{ex}}/2)\sum_{\langle i,j\rangle}\hat{\mathbf{S}}_i \cdot \hat{\mathbf{S}}_j$ with a renormalized exchange coupling

$$J_{\mathrm{ex}} = \sum_l \frac{4v_0^2}{U - l\Omega}|\mathcal{J}_l(A_0)|^2. \tag{40}$$

Equation (40) shows that the exchange coupling contains the contributions from virtual creations of D-H pairs dressed with l photons [transition amplitudes $\mathcal{A}^{(-l)} = v_0\mathcal{J}_{-l}(A_0)$]. In addition to the Floquet Schrieffer-Wolff transformation (Bukov, Kolodrubetz, and Polkovnikov, 2016), the Floquet spin Hamiltonian in Eq. (40) has been obtained via a perturbation theory in v_0/U in the extended Floquet Hilbert space (Mentink, Balzer, and Eckstein, 2015), a time-dependent Schrieffer-Wolff transformation (Kitamura and Aoki, 2016), a variant of the high-frequency expansion (Itin and Katsnelson, 2015), and a time-dependent perturbation theory (Hejazi, Liu, and Balents, 2019).

Equation (40) implies that, by tuning the field strength and excitation frequency, one can switch the sign of the exchange coupling. In Fig. 15(a), we show J_{ex} for a Hubbard model with $U = 10v_0$. In the small-field regime, J_{ex} increases with drive amplitude for $\Omega < U$, while it decreases for $\Omega > U$. In both cases J_{ex} can be negative at certain field strengths. The perturbative prediction was compared with time-dependent DMFT simulations of the driven Hubbard model, where the modified exchange interaction was determined by analyzing the spin precession under a static magnetic field; see Fig. 15(c). The agreement with Eq. (40) is excellent away from the resonance $\Omega = U$. Close to the resonance, however, incoherent excitations dominate, and the perturbative treatment becomes unreliable (Mentink, Balzer, and Eckstein, 2015). Multicolor driving schemes can help to suppress unwanted excitations and to realize larger modifications in the effective exchange coupling (Viebahn *et al.*, 2021; Murakami, Schüler *et al.*, 2023).

The ac field-induced modification of J_{ex} was experimentally confirmed in a cold-atom setup (Görg *et al.*, 2018); see also Sec. I.C. Depending on the excitation frequency and the field strength, the spin correlations are either reduced or enhanced and in some cases can become ferromagnetic; see Fig. 15(b).

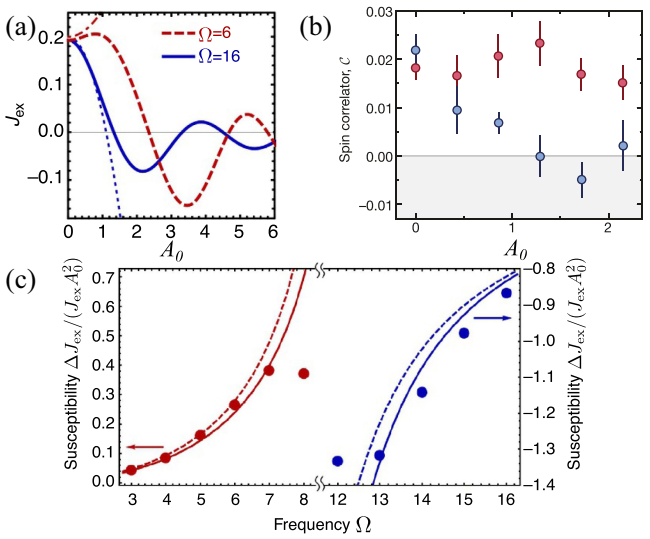

FIG. 15. (a) Superexchange for a two-site Hubbard model driven below ($\Omega < U$) and above ($\Omega > U$) the upper Hubbard band for $U/v_0 = 10$. (b) Change in the nearest-neighbor spin correlations in a cold-atom setup vs the driving strength A_0 for the red ($\Omega < U$) and blue ($\Omega > U$) detuned periodic drive. (c) Simulated change in the superexchange $\Delta J_{\mathrm{ex}}/(J_{\mathrm{ex}}A_0^2)$ in the weak-driving regime $A_0 \to 0$ from a two-site Hubbard cluster (solid lines), perturbative expansion (dashed lines), and time-dependent DMFT simulation (dots) for driving $\Omega < U$ (red lines) and $\Omega > U$ (blue lines). From Mentink, Balzer, and Eckstein, 2015, and Görg *et al.*, 2018.

Similar ideas can be applied to the attractive Hubbard model (Kitamura and Aoki, 2016; Fujiuchi *et al.*, 2020; Murakami, Schüler *et al.*, 2023). The low-energy physics of the system in the strong-coupling regime is described by a Heisenberg-type model of the η pseudospins [see Eq. (30)], which represent doublons and holons. The ac electric field can effectively modify the anisotropy and/or the sign of the exchange couplings between the pseudospins, which allows various phases with charge and s-wave superconducting orders to be induced. Other proposed applications involve the control of the exchange interaction in Kondo systems (Nakagawa and Kawakami, 2015; Iwahori and Kawakami, 2016; Eckstein and Werner, 2017; Müller, Eckstein, and Viola Kusminskiy, 2023). Going beyond linearly polarized light, it was shown that circularly polarized light applied to frustrated lattices, like the triangular or honeycomb lattices, induces a scalar spin chiral term $\propto \hat{\mathbf{S}}_i \cdot (\hat{\mathbf{S}}_j \times \hat{\mathbf{S}}_k)$, which breaks time reversal symmetry while preserving the SU(2) symmetry (Claassen *et al.*, 2017; Kitamura, Oka, and Aoki, 2017; Sur, Udupa, and Sen, 2022). The chirality originates from Floquet-induced virtual hoppings on three-site clusters, and it could potentially lead to a chiral spin-liquid state. Suggested candidate materials include herbertsmithite [$ZnCu_3(OH)_6Cl_2$], which is an antiferromagnet on a frustrated lattice, and $PdCrO_2$.

In multiorbital systems, the Floquet drive can be used to manipulate exchange couplings between spins and/or orbital degrees of freedom. Here dipolar light-matter coupling terms

and higher-order exchange paths via ligand orbitals may also have to be considered (Chaudhary, Hsieh, and Refael, 2019). Liu, Hejazi, and Balents (2018) and Hejazi, Liu, and Balents (2019) studied the partially filled three-band Hubbard model under time-periodic electric fields and discussed the conditions for modified or sign-inverted spin exchange couplings in ferromagnetic $YTiO_3$ and antiferromagnetic $LaTiO_3$. Eckstein, Mentink, and Werner (2017) demonstrated the electric-field control of the exchange couplings in the spin-orbital model (the Kugle-Khomskii model) obtained from the quarter-filled two-orbital Hubbard model.

A further extension of the aforementioned studies is to consider multiband Mott-Hubbard (Arakawa and Yonemitsu, 2021) or charge-transfer insulators (Sriram and Claassen, 2022) with strong spin-orbit coupling under circularly polarized light. On a honeycomb lattice, besides the manipulation of the Heisenberg exchange, one can modify a Kitaev interaction $KS_i^\gamma S_j^\gamma$ with $\gamma = x, y, z$ representing the three inequivalent bonds. Furthermore, circulary polarized light can effectively induce Zeeman terms, which results in the inverse Faraday effect (Banerjee, Kumar, and Lin, 2022; Sriram and Claassen, 2022; Yonemitsu, 2022). The competition between different magnetic instabilities leads to exotic phases within the Floquet prethermalized region, including a Kitaev spin-liquid state (Kitaev, 2006). The most prominent candidate material is α-$RuCl_3$ owing to the honeycomb lattice and the strong spin-orbit coupling. For this compound the relevant inverse Faraday effect has been experimentally observed (Amano *et al.*, 2022). Finally, Floquet engineering can be used to control fractionalized excitations in one-dimensional systems originating from spin-charge separation (Gao *et al.*, 2020) or spin-orbital separation (Müller, Grandi, and Eckstein, 2022).

Many proposals for real materials rely on driving with frequencies not too far from the Mott gap. Even though the Mott gap can protect the system from rapid laser heating, for strong pulses a substantial *D-H* production due to multiphoton processes is expected. An interesting proposal is therefore to observe the transient change of the interactions directly by motoring the spin or orbital dispersions during the Floquet pulse, which could be achieved using, for example, time-resolved RIXS (Mitrano and Wang, 2020; Wang *et al.*, 2021; Müller, Grandi, and Eckstein, 2022). In this context, it is important to note that an adiabatic Floquet Hamiltonian with a time-dependent amplitude parameter often provides an adequate description of the dynamics during a few-cycle pulse (Eckstein, Mentink, and Werner, 2017), while in the limit of a single cycle, there is a crossover to the description in terms of a dc-field modified exchange; see Sec. IV.B.

Another, more elaborate proposal for Floquet engineering is to replace the laser drive with a strongly coupled mode of the quantum electromagnetic field, such as a confined cavity mode (Bloch *et al.*, 2022; Schlawin, Kennes, and Sentef, 2022). At strong coupling Floquet Hamiltonians may be realized as photon-dressed Hamiltonians with few photons (Sentef *et al.*, 2020). Various cavity analogs of the aforementioned Floquet Hamiltonians have been proposed (Kiffner *et al.*, 2019; Li and Eckstein, 2020; Boström *et al.*, 2022), although the experimental realization of such cavity quantum materials is a largely open problem. Driving the cavity with an external laser might open yet another avenue for Floquet engineering of long-range spin interactions (Chiocchetta *et al.*, 2021).

E. Floquet prethermalization

A generic isolated system is expected to heat up to infinite temperature under periodic driving (D'Alessio and Rigol, 2014; Lazarides, Das, and Moessner, 2014). However, in some cases, such heating occurs only on relatively long timescales, while on shorter timescales the system is trapped in a so-called Floquet prethermalized state (D'Alessio and Polkovnikov, 2013; Abanin, De Roeck, and Huveneers, 2015; Citro *et al.*, 2015; Canovi, Kollar, and Eckstein, 2016; Mori, Kuwahara, and Saito, 2016; Weidinger and Knap, 2017; Howell *et al.*, 2019; Kuhlenkamp and Knap, 2020; Rubio-Abadal *et al.*, 2020; Ikeda and Polkovnikov, 2021; Pizzi, Nunnenkamp, and Knolle, 2021; Torre and Dentelski, 2021). For example, this behavior is observed in the high-frequency limit, where the prethermal state can last for exponentially long times in Ω and can be described by the effective Hamiltonian obtained from the high-frequency expansion. This partially justifies the analysis of equilibrium states of such effective Hamiltonians. The suppression of heating in the high-frequency limit is mathematically related to conventional prethermalization owing to constraints arising from a large energy gap in closed quantum systems (Abanin *et al.*, 2017). Another strategy for the suppression of heating, demonstrated in the integrable quantum Ising chain (Das, 2010), is called dynamical freezing (Bhattacharyya, Das, and Dasgupta, 2012). It relies on approximately conserved quantities that emerge because of the strong drive beyond some threshold for the drive amplitude (Haldar, Moessner, and Das, 2018; Haldar *et al.*, 2021).

In the context of Mott insulators, Floquet prethermalization has been numerically observed in a wide parameter range, even close to resonant conditions. Prominent examples are time-dependent DMFT results for the single-band Hubbard model. Figure 16(a) shows the evolution of the kinetic energy in a system with $U = 8$ and $W = 4$ under periodic modulations of the Coulomb interaction (Peronaci, Schiró, and Parcollet, 2018). At infinite temperature the kinetic energy should be zero. The system quickly approaches this state for

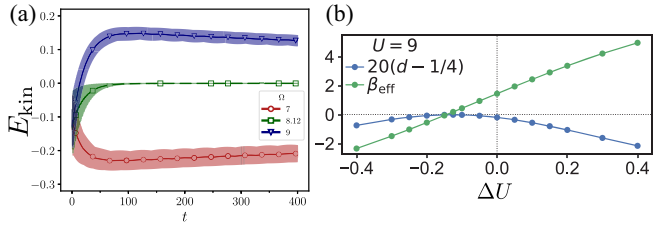

FIG. 16. (a) Kinetic energy $E_{\rm kin}$ during a periodic interaction modulation with frequency Ω close to the resonance (Bethe lattice, $U = 8$, $W = 4$). (b) Doublon number (d) and inverse temperature ($\beta_{\rm eff} = 1/T_{\rm eff}$) of the ac-field-driven Hubbard model at the symmetric point (see the text), with interaction $U + \Delta U$ and $\Omega = U/2$ (hypercubic lattice, $v_* = 1$, $U = 9$). From Herrmann *et al.*, 2017, and Peronaci, Schiró, and Parcollet, 2018.

the excitation frequency $\Omega = \Omega^* \equiv 8.12$, but even for slightly off-resonant conditions, the kinetic energy shows a nonthermal plateau. In the case of an electric-field-driven system, this prethermal state would correspond to a thermal state of H_0^{rot} [Eq. (38)] up to corrections of order $1/\Omega$. This has been analyzed explicitly for the case where E_0 is tuned to the symmetric point $\tilde{\mathcal{A}}_{ij}^{(0)} = \tilde{\mathcal{B}}_{ij}^{(0)}$, such that H_0^{rot} becomes the Hubbard model with renormalized hopping and the interaction given by the detuning ΔU (Herrmann *et al.*, 2017). This condition allows the dynamics of the driven system and the equilibrium state of the effective Floquet Hamiltonian within DMFT to be directly compared. For a sudden switch-on of the driving, the effective temperature T_{eff} of the Floquet state is obtained from the expectation value of H_0^{rot}, which is conserved under the stroboscopic time evolution and can be evaluated from the initial Mott state. Based on this prediction, one expects a positive (negative) T_{eff} for $\Delta U > 0$ ($\Delta U < 0$), which is confirmed by the simulation up to deviations of $\mathcal{O}(1/\Omega)$; see Fig. 16(b).

F. Single-photon or multiphoton absorption

Another important effect of the ac field is the creation of photocarriers. In the weak-field (perturbative) regime, this can be described as single-photon or multiphoton absorption. If $n\Omega \gtrsim \Delta_{\mathrm{Mott}} > (n-1)\Omega$, the probability for creating a D-H pair via n-photon absorption is proportional to E_0^{2n}. The effective Floquet Hamiltonian introduced in Sec. V.A captures the single-photon or multiphoton absorption in the D-H creation terms. The multiphoton absorption is complementary to the quantum tunneling mechanism discussed in Sec. IV.C.

For the 1D Hubbard model, the production rate of D-H pairs can be analytically obtained using a combination of the Landau-Dykhne method and the Bethe *Ansatz* (Oka, 2012). The crossover between the quantum tunneling and multiphoton absorption regime is controlled by the Keldysh parameter $\gamma \equiv \Omega/qE_0\xi$, where the length ξ characterizes the spatial extent of the D-H pairs. The multiphoton absorption (tunneling) regime corresponds to $\gamma \gg 1$ ($\gamma \ll 1$). The value $\gamma = 1$ defines the Keldysh line (Keldysh, 1965); see Fig. 17(a). In the multiphoton absorption regime, the creation probability of the D-H pairs is given by

$$\mathcal{P}_{D\text{-}H} \simeq \left(\frac{qE_0\xi}{2\pi\Omega}\right)^{2(\Delta_{\mathrm{Mott}}/\Omega)}, \tag{41}$$

which should be compared with Eq. (33) in the tunneling case. These two D-H creation mechanisms lead to a different energy distribution of the charge carriers, as sketched in Fig. 17(c). In the case of tunneling, the D-H distribution becomes momentum independent, i.e., the created doublons and holons are effectively hot. Using multiphoton processes, the doublons and holons can instead be created near the edges of the Mott gap.

The crossover from the multiphoton (power-law) to the tunneling (exponential) behavior was experimentally observed in Ca_2RuO_4, an antiferromagnetic Mott insulator

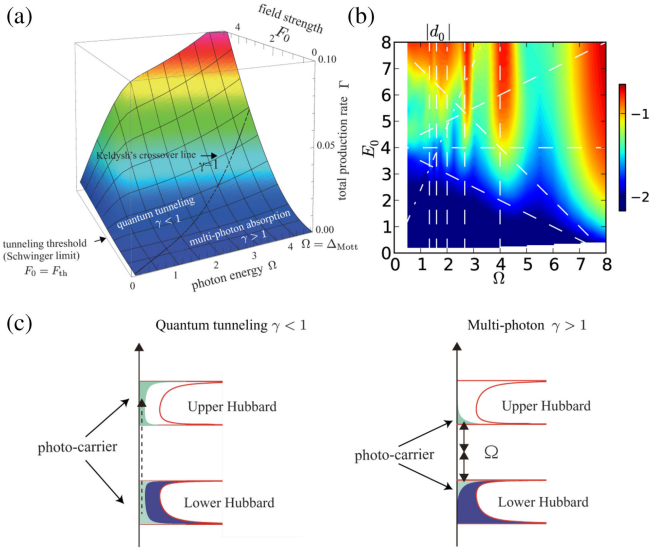

FIG. 17. (a) Production rate of doublon-holon pairs for the 1D Hubbard model with $U = 8$ and $W = 4$ in an ac field obtained with the Landau-Dykhne method. (b) Time-averaged double occupancy d_0 (on a log scale) in the plane of field amplitude E_0 and frequency Ω, in a Mott-insulating system with $U = 8$, analyzed with Floquet DMFT and attached fermion bath (hypercubic lattice, $v_* = 1$). The vertical dashed lines at $\Omega = U/n$ mark the resonances associated with n-photon absorption. (c) Schematics of the doublon-holon distribution for different excitations. From Oka, 2012, and Murakami and Werner, 2018.

with a 0.6 eV gap (Li *et al.*, 2022). The nonthermal distribution of charge carriers was investigated by analyzing the photoinduced reflectivity change $\Delta R(\omega)$ for a subgap excitation. With increasing excitation strength one observes a shift of the characteristic frequency defined by $\Delta R(\omega) = 0$, which was linked to the change in the D-H distribution associated with the Keldysh crossover.

A systematic numerical analysis of the generation of D-H pairs has been conducted using Floquet DMFT + NCA in a hypercubic system (Murakami and Werner, 2018). Figure 17(b) shows the number of photogenerated doublons as a function of Ω and E_0. One can identify the resonant excitations around $\Omega = U/n$ ($n = 1 \sim 6$), which are associated with n-photon absorption. In the perturbative regime, the n-photon absorption probability is proportional to $|E_0|^{2n}$, which is consistent with the fact that higher-order peaks become more prominent with larger E_0 for $E_0 \lesssim U/2$. When the field strength is increased beyond $E_0 \approx U/2$, some higher-order resonances disappear or emerge at off-resonant conditions, which reflects nonperturbative effects.

G. Nonlinear optical responses

Nonlinear optical responses reveal excited states beyond the reach of linear responses and thus provide a means to extract detailed information on the system's excitation spectrum (Boyd, 2008). Strongly correlated systems can host excited states whose properties are significantly different from those of conventional semiconductors and thus can show characteristic nonlinear optical signals.

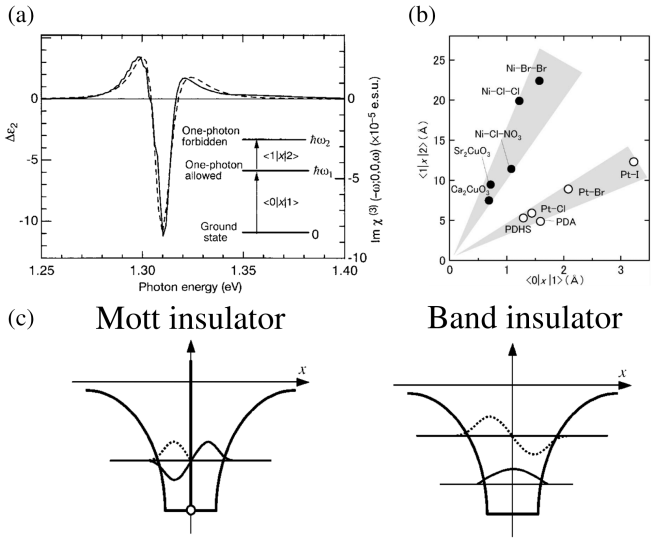

FIG. 18. (a) Third-order nonlinear susceptibility spectra $\mathrm{Im}\chi^{(3)}(-\omega;0,0,\omega)$ of $[\mathrm{Ni(chxn)_2Br}]\mathrm{Br_2}$ at 77 K. The solid line is the experimental result, and the dashed line shows the results of the three-level model illustrated in the inset. (b) Relation between the transition dipole moments for various 1D materials, where the filled circles and open circles correspond to 1D Mott insulators and 1D semiconductors, respectively. (c) Schematic of the wave function of odd- and even-parity excitons in a 1D Mott insulator and a 1D band insulator. From Kishida *et al.*, 2000, and Ono *et al.*, 2004.

1. Third-order responses

One-dimensional Mott insulators are known to show large third-order nonlinear optical (TNLO) responses owing to the characteristic features of excited states (in particular, excitons), originating from spin-charge separation (Kishida *et al.*, 2000, 2001; Ono *et al.*, 2004; Ono, Kishida, and Okamoto, 2005). In general, the TNLO response is characterized by the susceptibility $\chi^{(3)}$ defined as $P(\omega_\sigma) \propto \epsilon_0\chi^{(3)}(-\omega_\sigma;\omega_a,\omega_b,\omega_c)E(\omega_a)E(\omega_b)E(\omega_c)$, where $P(\omega_\sigma)$ is the nonlinear polarization, $E(\omega_i)$ is the electric field, ϵ_0 is the vacuum permittivity, and energy conservation implies that $\omega_\sigma = \omega_a + \omega_b + \omega_c$. The nonlinear susceptibility $\mathrm{Im}\chi^{(3)}(-\omega;0,0,\omega)$ was measured by electroreflectance experiments for 1D charge-transfer insulators, like the Ni-halogen and CuO chains, for ω around the band gap; see Fig. 18(a). In these materials $\chi^{(3)}(-\omega;0,0,\omega)$ reaches 10^{-8}–10^{-5} esu (Kishida *et al.*, 2000; Ono *et al.*, 2004), which is much larger than values in semiconductors such as silicon polymers and Peierls insulators (10^{-12}–10^{-7} esu). The third-order response $\chi^{(3)}(-\omega;0,0,\omega)$ can also be measured using strong terahertz fields (Yada, Miyamoto, and Okamoto, 2013). In addition, a large third-harmonic generation, which corresponds to $\chi^{(3)}(-3\omega;\omega,\omega,\omega)$, was reported for 1D Mott insulators (Kishida *et al.*, 2001; Ono, Kishida, and Okamoto, 2005).

The observed spectral features of the nonlinear susceptibilities can be described by a three-level model (Kishida *et al.*, 2000; Ono *et al.*, 2004) that considers the ground state ($|0\rangle$), an optically active parity-odd state ($|1\rangle$), and an optically forbidden parity-even state ($|2\rangle$). $|1\rangle$ and $|2\rangle$ are associated with Mott excitons (see Sec. VI.E) or with low-lying states in the D-H continuum. Within the three-level model, the main term in $\chi^{(3)}(-\omega;0,0,\omega)$ becomes

$$\chi^{(3)}(-\omega;0,0,\omega) \propto \frac{|\langle 0|x|1\rangle|^2|\langle 1|x|2\rangle|^2}{(E_1-\omega-i\gamma_1)^2(E_2-\omega-i\gamma_2)}. \quad (42)$$

Fitting the experimental results to this model [Fig. 18(a)] provides information on the dipole moments $\langle i|x|j\rangle$ and the energies E_i of the excited states $|i\rangle$. The main origin of the large TNLO responses in 1D Mott insulators turns out to be a large dipole moment between $|1\rangle$ and $|2\rangle$ [see Fig. 18(b)] and the energy differences between the excited states, which are small compared to conventional semiconductors.

The peculiar properties of the excited states in the 1D Mott insulator were clarified by the "holon-doublon" model, which is based on spin-charge separation and focuses only on the charge degrees of freedom (doublons and holons). In this model doublons and holons are treated as hard-core particles. Owing to the combination of a hard-core nature and a 1D lattice structure, the odd-party and even-parity excitons are degenerate and have the same form of wave function [see Fig. 18(c)], which explains the large transition dipole moment (Mizuno *et al.*, 2000). In conventional semiconductors the lack of a hard-core nature makes the energy difference between the odd-parity and even-parity states large and the dipole moment between them small (Ono *et al.*, 2004). The special features of 1D Mott excitons also lead to efficient and controllable terahertz light generation (Miyamoto *et al.*, 2023) and enable the exploration of photodressed states (Yamakawa *et al.*, 2023).

In higher dimensions, owing to the lack of spin-charge separation, the excitation spectrum is different. TNLO responses become weaker in ladders or 2D systems compared to 1D systems (Mizuno *et al.*, 2000). Nevertheless, TNLO signals provide a useful spectroscopy of Mott excitons. For example, the contribution of the spin-charge coupling to the formation of Mott excitons has been detected using TNLO responses; see Sec. VI.E.

2. High-harmonic generation

Optical excitations with even stronger fields result in high-harmonic generation (HHG), i.e., the emission of higher harmonics of the injected light from matter. HHG was initially studied in gases (Ferray *et al.*, 1988), but it has also been observed in solids, in particular, semiconductors (Ghimire *et al.*, 2011; Schubert *et al.*, 2014). In a semiconductor, the light emission is associated with the independent dynamics of electrons and holes under the ac field. Both intraband and interband currents contribute to HHG (Vampa *et al.*, 2014). The latter contribution can be analyzed by the three-step model (Corkum, 1993; Lewenstein *et al.*, 1994; Vampa, McDonald *et al.*, 2015), which describes (i) the creation of an electron-hole pair, (ii) the electron-hole dynamics in the bands, and (iii) the recombination via light emission. Since both the intraband and interband contributions depend on the band structure, HHG spectroscopy of semiconductors

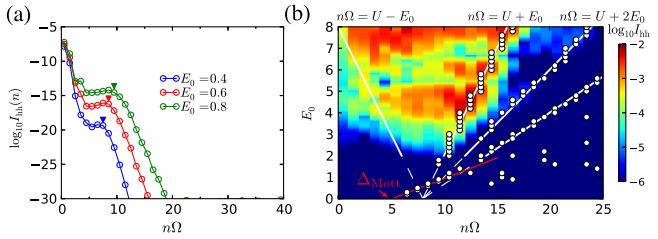

FIG. 19. (a) HHG spectrum $I_{\rm HHG}(\omega)$ of a paramagnetic Mott-insulating Hubbard model for different field amplitudes E_0. Arrows indicate the cutoff energies of the plateaus. (b) $I_{\rm HHG}(\omega)$ as a function of E_0 and the harmonic energy ($n\Omega$). The white circles show cutoff energies. The red and white lines indicate the linear scaling of the cutoff energy with E_0. Results obtained with Floquet DMFT + NCA on a hypercubic lattice with $v_*=1$ for $U=8$ ($\Delta_{\rm Mott}\simeq 5$), $\beta=2$, and $\Omega=0.5$. From Murakami, Eckstein, and Werner, 2018.

(Luu *et al.*, 2015; Vampa, Hammond *et al.*, 2015) allows band information to be revealed.

More recently, the scope of HHG research has been extended to strongly correlated solids (Murakami, Eckstein, and Werner, 2018; Silva *et al.*, 2018; Tancogne-Dejean, Sentef, and Rubio, 2018), where the excitations cannot be explained by independent electrons and holes. The relevant questions are the physical origin of HHG, its relation to many-body excitations, and potential application as a spectroscopic tool. Basic features of HHG in Mott insulators have been revealed by analyzing the Hubbard model with Floquet DMFT (Murakami, Eckstein, and Werner, 2018). Figures 19(a) and 19(b) show the HHG spectrum $I_{\rm HHG}(\omega)$, which is evaluated from the current $j(\omega)$ as $I_{\rm HHG}(\omega)=|\omega j(\omega)|^2$ for a paramagnetic Mott insulator exposed to a strong subgap excitation. The HHG features change qualitatively depending on the field strength E_0. When E_0 is relatively weak, the HHG spectrum is characterized by a single plateau, as in atomic gases; see Fig. 19(a). However, for stronger fields the HHG spectrum shows multiple plateaus. The cutoff frequencies ($\omega_{\rm cut}$) of the plateaus scale linearly with E_0, i.e., $\omega_{\rm cut}=\Delta+\alpha E_0$. In particular, in the strong-field regime, the cutoff follows $\omega_{\rm cut}=U+mE_0$ with integer m; see Fig. 19(b). In both cases the HHG signal is dominated by the recombination of *D*-*H* pairs, and the three-step picture applies to these *D*-*H* pairs. The qualitative change in the HHG spectra reflects the switch from the itinerant nature of the *D*-*H* pairs in the weaker-field regime to a localized nature of the pairs in the stronger-field regime; see Sec. IV.A. The Floquet-DMFT study (Murakami, Eckstein, and Werner, 2018) also revealed that, in contrast to semiconductors, the HHG spectrum of Mott insulators is not directly related to the dispersion reflected in the single-particle spectrum.

Further insights into the relation between HHG and the excitation spectrum of Mott insulators have been obtained by studying the 1D Hubbard model with iTEBD (Murakami *et al.*, 2021). This system shows spin-charge separation and at half filling hosts many-body elementary excitations called doublons, holons, and spinons whose dispersion relations are known from the Bethe *Ansatz*. Figure 20(a) plots the subcycle

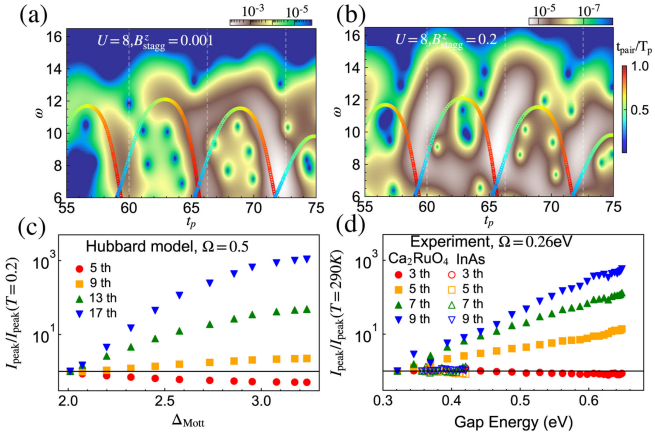

FIG. 20. (a),(b) Subcycle analysis of $I_{\rm HHG}(\omega,t_p)$ for the 1D Hubbard model with staggered magnetic field $B^z_{\rm stagg}$ analyzed with iTEBD for the pump parameters $\Omega=0.5$ and $E_0=0.8$. The colored markers show the prediction from the three-step model combined with the *D*-*H* dispersion, with the color indicating the time interval $t_{\rm pair}$ between pair creation and recombination in units of $T_p=2\pi/\Omega$. The larger staggered field $B^z_{\rm stagg}$ in (b) mimics the spin-charge coupling. The vertical dashed lines indicate the times when $A(t)=0$. (c) Intensity of the HHG peaks as a function of the Mott gap $\Delta_{\rm Mott}$ for the single-band Hubbard model within DMFT + NCA. (d) Experimental HHG intensity as a function of the optical gap for Ca_2RuO_4 (Mott insulator) and InAs (semiconductor). From Murakami, Uchida *et al.*, 2022, and Uchida *et al.*, 2022.

signal $I_{\rm HHG}(\omega,t_p)\equiv|\omega j(\omega,t_p)|^2$ (the frequency profile of the light emitted at time t_p), where $j(\omega,t_p)=\int dt e^{i\omega t}F_{\rm window}(t-t_p)j(t)$ is a windowed Fourier transform of the current with $F_{\rm window}(t)$ a window function centered at $t=0$. This subcycle signal is well explained by the light emission from the recombination of the *D*-*H* pair predicted by the semiclassical three-step model combined with the *D*-*H* dispersion determined by the many-body theory; see the colored line. This is in stark contrast to semiconductors, where HHG directly reflects the dispersions of the single-particle bands. These results suggest that HHG could be used to detect the information of elementary excitations emerging out of many-body interactions (Imai, Ono, and Ishihara, 2022). Beyond this, an interesting proposal is to measure subcycle-resolved nonlinear processes in correlated electron systems using ideas from multidimensional spectroscopy (Valmispild *et al.*, 2023).

In higher dimensions, the dynamics of doublons and holons disturbs the spin background (see Sec. VI.D.3), resulting in strong spin-charge coupling with profound effects on HHG. Murakami, Uchida *et al.* (2022) showed that spin-charge coupling efficiently reduces the coherence time of the *D*-*H* pairs [see Fig. 20(b)], which leads to a strong temperature dependence of the HHG signal. Although the band gap increases with decreasing temperature, which suppresses the *D*-*H* production, the change in the coherence time dominates this effect and leads to a drastic enhancement of HHG with increasing gap size; see Fig. 20(c). A similar behavior has been experimentally reported in the Mott insulator Ca_2RuO_4 (Uchida *et al.*, 2022), where the HHG

intensity is exponentially enhanced with increasing gap size [see Fig. 20(d)] following a peculiar phenomenological scaling. This behavior was not observed in the conventional semiconductor InAs. A similar temperature dependence was also reported in $Pr_{0.6}Ca_{0.4}MnO_3$ for midinfrared excitations (Nakano *et al.*, 2023) and in $RNiO_3$ (R is a rare-earth atom) for terahertz excitations (Prajapati *et al.*, 2024). The analysis of the two-leg ladder Hubbard model further revealed the multifaceted effects of the spin-charge couplings on HHG, such as unique dephasing mechanisms and signal fractionalization (Murakami *et al.*, 2025).

Doping and edge effects on HHG in the 1D Hubbard models have been studied with ED (Hansen, Jensen, and Madsen, 2022; Hansen and Madsen, 2022; Huang and Du, 2023; Pooyan and Bauer, 2024). Going beyond the single-band Hubbard model, strongly correlated systems can host various types of elementary excitations, such as solitons in dimer systems (Imai, Ono, and Ishihara, 2020), string states in multiorbital systems (Lysne, Murakami, and Werner, 2020), Mott excitons (Udono *et al.*, 2022; Yamakawa *et al.*, 2023), magnons in magnetic insulators (Ikeda and Sato, 2019; Takayoshi, Murakami, and Werner, 2019), and renormalized electrons coupled to local spins in Kondo lattice systems (Zhu *et al.*, 2021; Ono *et al.*, 2024). The relation between HHG and the dynamics of these excitations has been investigated, which may open a path to HHG spectroscopy.

Another direction for HHG research in correlated materials is to use HHG as a spectroscopic tool for phase transitions. The analysis of the Hubbard model revealed significant changes in the transient HHG signal during a photoinduced insulator-metal transition (Silva *et al.*, 2018; Orthodoxou, Zaïr, and Booth, 2021). Experimental work on VO_2 by Bionta *et al.* (2021) tested this idea. They analyzed the photoinduced transition to two types of metallic phases by monitoring the time evolution of the HHG intensity. In addition, the detection of equilibrium phase transitions using HHG was theoretically studied in the Hubbard model (Shao *et al.*, 2022) and experimentally reported in $YBa_2Cu_3O_{7-d}$ (Alcala *et al.*, 2022).

H. Nonlinear phononics

Terahertz laser fields allow certain IR active phonon modes to be selectively excited. The coherent oscillation of the IR mode can significantly affect the electronic properties through its nonlinear coupling to other lattice modes or through a direct coupling to the electrons. For both mechanisms the term *nonlinear phononics* is used. In the former case, owing to a third-order nonlinear coupling between the IR mode and a Raman mode, the excitation of the IR mode distorts the lattice along the coordinate of the Raman mode, which changes the electronic properties (Först *et al.*, 2011; Subedi, Cavalleri, and Georges, 2014). Nonlinear phononics has been used to induce insulator-metal transitions (Rini *et al.*, 2007), melt a spin-Peierls phase (Sakai *et al.*, 2024), and manipulate ferroelectric order (Mankowsky *et al.*, 2017; Nova *et al.*, 2019; Henstridge *et al.*, 2022), magnetic states (Nova *et al.*, 2017; Disa *et al.*, 2020, 2023), and superconductinglike states (Fausti *et al.*, 2011; Mankowsky *et al.*, 2014; Mitrano *et al.*, 2016; Buzzi *et al.*, 2020), as reviewed by Mankowsky, Först, and Cavalleri (2016), Nicoletti and Cavalleri (2016), Cavalleri (2018), Disa, Nova, and Cavalleri (2021), and Subedi (2021). In the case of a direct coupling between the lattice and the electrons, we focus on the modification of the electron-electron interactions by nonlinear phononics, which is also relevant for Mott systems. A modulation of the Hubbard interaction due to a coherent phonon and nonlinear electron-lattice couplings was experimentally reported in the 1D Mott insulator ET-F_2TCNQ (Kaiser *et al.*, 2014a; Singla *et al.*, 2015). After a vibrational excitation, one observes a redshift of the optical charge-transfer gap, and the appearance of midgap peaks with a separation of twice the phonon frequency. The redshift was connected with a strong asymmetry in the coupling of the lattice modes to holons and doublons. In systems with coupled lattice and orbital order, optical driving of the IR active phonon can modify orbital order and induce an insulator-metal transition (Esposito *et al.*, 2017). These experiments show the importance of nonlinear electron-lattice couplings in photoexcited systems. Nevertheless, their relevance for photoinduced phase transitions in systems like K_3C_{60} (Mitrano *et al.*, 2016) or κ-$(ET)_2Cu[N(CN)_2]Br$ (Buzzi *et al.*, 2020) remain to be understood. Note that when we regard the phonon oscillations as an external field for the electronic system, nonlinear phononics shares aspects with Floquet engineering (Hübener, De Giovannini, and Rubio, 2018; Sono *et al.*, 2022).

On the theory side, Kennes *et al.* (2017) proposed that in systems with quadratic electron-phonon coupling, which can be dominant owing to the crystal symmetry, intense external driving leads to an attractive contribution to the electronic interaction, which could overcome the Hubbard repulsion and induce either a metal-to-superconductor or insulator-to-metal transition. The induction of the attractive interaction was confirmed by ED studies on small clusters (Sentef, 2017) and in the dilute limit of an extended system (Kovač *et al.*, 2023). For half-filled systems, an iTEBD study starting from a direct product state of a metal and coherent phonons showed that the final state is rather dynamically localized (Sous *et al.*, 2021). A transition between a Mott insulator and a coherent metal was demonstrated in a model with nonlinear electron-phonon coupling using time-dependent DMFT (Grandi, Li, and Eckstein, 2021).

Another proposed mechanism for inducing or enhancing an attractive (static) electron-electron interaction is the parametric excitation of a phonon linearly coupled to electrons (Knap *et al.*, 2016; Babadi *et al.*, 2017). The effect is most prominent at the resonance, where heating is also strong, so the pairing susceptibility can be reduced in the driven state in spite of an enhanced attraction (Murakami *et al.*, 2017). In general, it is numerically challenging to take into account the effects of both heating and modified interactions, but such results are important for understanding the conditions under which nonthermal phase transitions can be induced.

VI. PHOTODOPED MOTT INSULATORS

In this section, we explore processes that control the evolution of photodoped charge carriers in Mott insulators. After an electronic excitation across the Mott gap, depending on the type of system, we can expect two fundamentally different scenarios; see Fig. 2. In small-gap Mott insulators

(or correlated metals), the electrons thermalize quickly. Conversely, in large-gap Mott insulators, the dynamics can be described in terms of nonthermal populations of electronlike and holelike carriers (doublons and holons in a single-band Mott insulator). The central questions are how these carriers interact with other degrees of freedom, how they develop into dressed quasiparticles or bind into excitons, how the presence of these carriers modifies the band structure and interactions, whether the nonthermal carrier populations can stabilize new types of electronic orders, and how the photodoped carriers ultimately recombine to restore the original Mott phase. Note that the overall evolution of photodoped charge carriers is analogous to the well-studied physics of photodoped semiconductors (Haug and Koch, 2009), at least when photoinduced lattice displacements do not play an important role. However, the details of each step can differ significantly owing to strong correlation effects, such as spin-charge coupling. In the following we discuss the different stages in the evolution of a photodoped Mott system and the underlying physical phenomena.

A. Excitation across the Mott gap

Intraband acceleration. The easiest way to electronically excite a Mott insulator is to apply a light pulse with a frequency comparable to the Mott gap. What distinguishes Mott insulators from conventional band insulators is the possibility of optical transitions between the lower and upper Hubbard bands, which originate from a single orbital. These transitions result from the intraband acceleration of the electrons that is induced by the Peierls phases of the hopping terms; see Sec. II.B. For low amplitudes the absorbed energy is proportional to the pump intensity ($\propto E_0^2$, linear optical absorption), while in the strong-field regime a significant increase in double occupancy can be generated within just a few cycles.

Interband dipole transitions. In generic multiband systems, the light-matter interaction contains both dipolar transition matrix elements between orbitals of different symmetry and Peierls phases; see Sec. II.B. Hence, both intraband and interband transitions need to be considered. For sufficiently high frequency, excitations may occur also outside the valence band manifold and, in the absence of particle-hole asymmetry, transiently change the particle number in the valence band. This effect can be important for the initial stage of photoinduced insulator-metal transitions (Stojchevska *et al.*, 2014) and can be exploited in tailored excitation protocols; see Sec. VI.D.4.

Nonlinear mechanisms. Strong laser pulses enable nonresonant excitations across a Mott or charge-transfer gap. The underlying mechanisms are discussed in Secs. V.F (multiphoton absorption) and IV.C (Zener-type tunneling).

Considering these different mechanisms, we expect that targeted pump field excitations can create specific states. For instance, in the single-band simulation result shown in Fig. 21, the distribution function of electrons after the excitation differs for pulses with frequency $\Omega > U$ and $\Omega < U$, even if these pulses inject the same amount of energy. Similarly, multiphoton and tunneling processes lead to distinct doublon populations; see Sec. V.F and Fig. 17. However, intraband relaxation processes can quickly erase the information on the excitation pathway. For example, in a study of La_2CuO_4 based on the *d*-*p* model for charge-transfer insulators (Golež *et al.*, 2019; Golež, Eckstein, and Werner, 2019), excitations producing holes in the lower Hubbard band or holes with mixed *d*-*p* character (Zhang-Rice singlets) (Zhang and Rice, 1988) were explored. It was shown that the rapid hole transfer between the Zhang-Rice band and the lower Hubbard band erases the information on the initial excitation on the femtosecond timescale if electron-electron interactions and nonlocal charge fluctuations are taken into account.

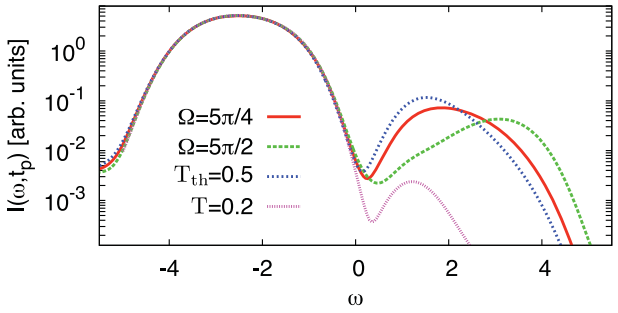

FIG. 21. Time-resolved photoemission spectrum $I(\omega, t_p)$ after a resonant pump excitation in a single-band Mott insulator for two different pump energies Ω. The pink (blue) dotted lines indicate the results for the initial (thermalized) system. The pulse amplitudes E_0 for the two driving frequencies Ω were chosen to be compatible with $T_{\rm th}$. Calculations based on DMFT + NCA on the hypercubic lattice ($v_* = 1$) with interaction $U = 5$. Adapted from Eckstein and Werner, 2011.

B. Thermalization of correlated electrons

An isolated interacting many-particle quantum system is expected to eventually thermalize. The final state will then be indistinguishable from the Gibbs density matrix $\rho_{\rm th} \sim e^{-(H-\mu N)/T_{\rm th}}$, with parameters μ and $T_{\rm th}$ that depend only on the total energy and particle number. In addition, correlation functions will satisfy a universal fluctuation-dissipation relation with temperature $T_{\rm th}$. Understanding the timescale on which this ergodic behavior is established is a fundamental problem of nonequilibrium quantum physics (Polkovnikov *et al.*, 2011; D'Alessio *et al.*, 2016) and crucial for determining whether laser excitations can lead to nonthermal electronic phases.

In the absence of symmetry breaking, correlated electrons can exist in three regimes: conventional Fermi-liquid states, strongly correlated unconventional metals, and robust Mott or charge-transfer insulators. In ideal Fermi liquids, the phase space for quasiparticle scattering is restricted, causing thermalization to slow down as the temperature approaches zero. The relaxation proceeds in two stages, where the rapid formation of a prethermal phase (Berges, Borsányi, and Wetterich, 2004; Moeckel and Kehrein, 2008; Eckstein, Kollar, and Werner, 2009; Eckstein *et al.*, 2009; Hackl and Kehrein, 2009) is followed by a slower thermalization described by a Boltzmann equation (Haug and Jauho, 2008; Kollar, Wolf, and Eckstein, 2011). Nevertheless, even in good metals this second stage is often fast enough that the electronic subsystem thermalizes on femtosecond timescales, and thus before a significant amount of energy is transferred to the lattice. This assumption underlies widely used

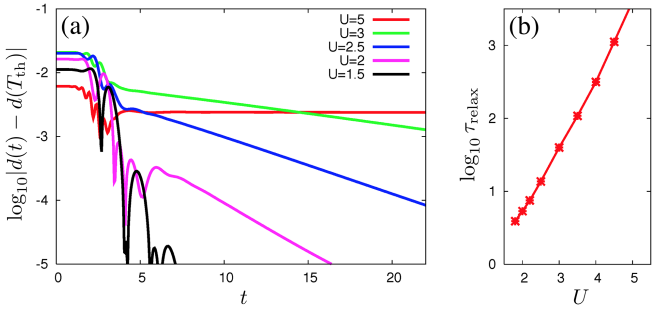

FIG. 22. (a) Thermalization of the double occupancy in a photodoped Hubbard model with indicated values of U in the metal-insulator crossover region. (b) Thermalization time as a function of interaction strength. The setting is the same as in Fig. 21, with a resonant excitation $\Omega = U\pi/2$. The pulse amplitudes E_0 are adjusted such that $T_{\rm th} = 0.5$ for all values of U. Adapted from Eckstein and Werner, 2011.

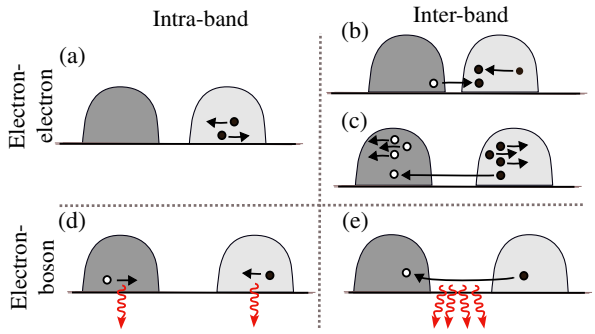

FIG. 23. Different scattering processes in Mott insulators, as discussed in the text. Depending on the initial state, these processes can go in either direction. The solid (empty) dots represent excited multiplets with negative (positive) charge such as doublons (holons), and the wavy red lines represent energetic couplings to bosonic modes.

phenomenological few-temperature models (Allen, 1987), which describe photoexcited electrons as quasithermal hot electrons.

Stronger interactions do not necessarily lead to faster thermalization. In particular, a large-gap Mott insulator exhibits a thermalization bottleneck, as observed in interaction quenches of the Hubbard model in both one and infinite dimensions (Kollath, Läuchli, and Altman, 2007; Eckstein, Kollar, and Werner, 2009). Further simulations for the isolated single-band Hubbard model (Eckstein and Werner, 2011) revealed a crossover from rapid thermalization at intermediate interactions (in the insulator-to-metal crossover regime) to an exponential slowdown in the Mott state. Figure 22(a) illustrates this behavior by plotting the absolute value of the difference between the double occupancy $d(t)$ and the thermalized double occupancy $d(T_{\rm th})$ after a resonant photoexcitation. Here $d(T_{\rm th})$ is obtained from a Gibbs state with the final state temperature $T_{\rm th}$ determined by the absorbed energy. The exponential decay of $|d(t) - d(T_{\rm th})|$ provides an estimate for the thermalization time τ, which is plotted in Fig. 22(b). Deep in the Mott insulator ($U = 5$), the relaxation time is hundreds of inverse hoppings, while it becomes faster as we approach the insulator-metal crossover region [$U_{\rm crossover}/v_* \approx 2.6$ for the present setting (Werner, Held, and Eckstein, 2014)]. In the strongly correlated metal ($U = 1.5$), the system thermalizes within a few inverse hopping times.

In the following we separately discuss these two cases of fast thermalization and exponential slowdown.

Fast thermalization in the correlated metal. At intermediate interactions the thermalized state can become a bad metal with a temperature $T_{\rm th}$ above the Fermi-liquid coherence temperature. In this state quasiparticles are not well defined (Deng *et al.*, 2013), and rapid thermalization, as observed in Fig. 22, cannot be understood within conventional Boltzmann scattering theory. Sachdev-Ye-Kitaev models (Chowdhury *et al.*, 2022), which can be solved with equations that are closely related to DMFT, capture rapid thermalization in a bad metallic non-Fermi-liquid regime (Eberlein *et al.*, 2017). Here one finds a universal thermalization rate determined solely by the temperature T. However, a comprehensive understanding of thermalization in strongly correlated unconventional metals is still lacking. The previous discussion pertains to single-particle quantities, while two-particle quantities like spin and charge correlation functions may thermalize on different timescales (Matveev *et al.*, 2019; Sayyad *et al.*, 2019; Simard and Werner, 2022). Multiorbital systems, which already show unconventional slow behavior such as spin freezing in equilibrium (Werner *et al.*, 2008), have not yet been systematically explored. In disordered metals thermalization can be delayed as shown in the analyses of the Falicov-Kimball model (Eckstein and Kollar, 2008b, 2008c). The interplay of strong disorder and interactions in a nonequilibrium context and the possible relations to many-body localization (Abanin *et al.*, 2019) remain largely unexplored.

The rapid electronic thermalization in a correlated metal or a small-gap insulator may appear as an obstacle to the realization of nonthermal electronic phases. However, it provides a unique opportunity to study electronic states and their properties at effective temperatures that are much higher than those achievable in equilibrium, while the lattice remains frozen. An early example of such an exploration is a time-resolved photoemission experiment on the correlated insulator $1T$-TaS_2 (Perfetti *et al.*, 2006); see Sec. I.C. Another more recent example is a time-resolved ARPES (trARPES) study on $SrIrO_4$. Choi *et al.* (2024) argued that the specific behavior of the spectral function in the high-temperature regime, which can be accessed by ultrafast laser excitations, allows one to identify antiferromagnetic correlations rather than Mott physics as the primary origin of the insulating state.

Thermalization bottleneck in the Mott regime. In large-gap Mott insulators, the relaxation and thermalization dynamics can be understood by considering the scattering of carriers (doublons and holons in the single-band case) among themselves and with bosonic excitations, such as spin or charge excitations and phonons. Figure 23 illustrates different processes. On the one hand, one can distinguish electron-electron scattering processes that can thermalize the electrons (upper panels) from electron-boson scattering processes where the energy is transferred to other degrees of freedom (lower panels). On the other hand, there are processes that change the occupation in the upper band (recombination and

excitation; see the right panels of Fig. 23), and intraband processes which keep this number constant (left panels of Fig. 23). The intraband relaxation modifies the distribution of photoexcited doublons and holons by either electron-electron scattering [see Fig. 23(a)] or electron-boson scattering [see Fig. 23(d)]. The interband relaxation by single-particle scattering, i.e., impact ionization and its inverse [see Fig. 23(b)], is possible only in small-gap insulators; see Sec. VI.C. As the Mott gap Δ_{Mott} (or the local interaction U) becomes large compared to other energy scales, the remaining high-order interband processes [see Figs. 23(c) and 23(e)] become exponentially suppressed with increasing gap size (Rosch *et al.*, 2008; Sensarma *et al.*, 2010; Strohmaier *et al.*, 2010). This is because the recombination (creation) of charge carries releases (requires) an energy of order U that must be transferred simultaneously to (from) many low-energy excitations with a smaller energy $\epsilon_0 \ll U$. Here ϵ_0 can be the kinetic energy of the carriers (v_0, hopping), as in Fig. 23(c), or the energy of the bosonic excitation, as in Fig. 23(e). For this reason, an asymptotic estimate of how the rate Γ for these processes depends on the gap U can be obtained from a high-order perturbation theory (Sensarma *et al.*, 2010),

$$\Gamma \sim \exp[-\alpha(U/\epsilon_0)\log(U/v_0)]. \tag{43}$$

The coefficient α in Eq. (43) is a phase space factor that depends on the number of available scattering partners, similar to the density of doublons and holons in the final thermal state. While Eq. (43) gives the functional form of the decay time, numerical simulations are necessary to fix the free parameters. For example, the U dependence of the thermalization time of the DMFT results in Fig. 22(b) can be well fitted using Eq. (43) with α close to 1.

The slowdown of interband processes explains the electronic thermalization bottleneck in large-gap Mott systems because thermalization of the electronic single-particle properties requires that the change in the number of doublons is compensated by a change in the kinetic energy, as illustrated in Figs. 23(b), 23(c), and 23(e). In Secs. VI.C, VI.D, and VI.G, we discuss the processes depicted in Fig. 23 for the thermalization of Mott insulators. In particular, in open systems with a robust Mott gap, the photocarrier generation is followed by intraband relaxation of the carriers (see Sec. VI.D), and subsequently by the recombination of carriers (see Sec. VI.G), as shown in Fig. 2(c). We also discuss phenomena that are directly related to the presence of nonthermal charge carriers, such as Mott exciton formation (see Sec. VI.E) and the renormalization of the interactions and band structure by the photocarriers (see Sec. VI.F).

C. Impact ionization

Impact ionization is a process where a high-energy charge carrier loses kinetic energy by creating other charge carriers; see Fig. 23(b). This process is well understood in semiconductors (Bhattacharya, 1997) and finds applications in avalanche photodiodes. It has also been discussed as a potential mechanism to overcome the Shockley-Queisser limit for the efficiency of semiconductor solar cells (Werner, Kolodinski, and Queisser, 1994; Spirkl and Ries, 1995). Analogous processes play a role in Mott insulators if the Mott gap is smaller than the width of the Hubbard bands. Here the injection of doublons and holons with high kinetic energy can lead to a multiplication of charge carriers (Manousakis, 2010; Werner, Held, and Eckstein, 2014). In impact ionization a doublon near the upper edge of the upper Hubbard band scatters to the lower edge, exciting an additional D-H pair with low kinetic energy: $\mathrm{doublon}_{\mathrm{high}} \rightarrow \mathrm{doublon}_{\mathrm{low}} + \mathrm{doublon}_{\mathrm{low}} + \mathrm{holon}_{\mathrm{low}}$; see Fig. 23(b). A similar process occurs when a holon with high kinetic energy scatters within the lower Hubbard band. In a particle-hole symmetric situation, the net effect of these impact ionization processes is that each high-energy D-H pair produces three low-energy D-H pairs.

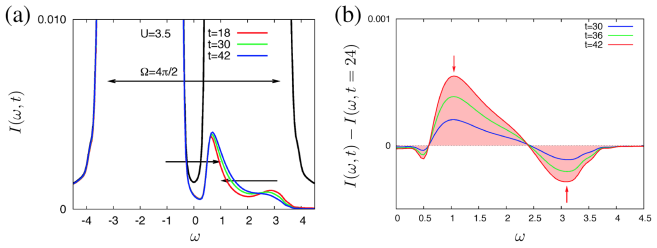

FIG. 24. (a) Time evolution of the photoemission spectrum $I(\omega,t)$ after a pulse excitation with energy $\Omega = 4\pi/2$ and amplitude $E_0 = 0.5$. (b) Time-dependent change of the photoemission spectrum relative to time $t = 24$. DMFT + NCA results for a single-band Hubbard model on a hypercubic lattice with $U = 3.5$ and $v_* = 1$. Adapted from Werner, Held, and Eckstein, 2014.

The multiplication of charge carriers and the associated changes in their energy distribution are evident in the short-time dynamics of the photoemission spectrum, as shown in Fig. 24 for a single-band Hubbard model. Figure 24(a) plots $I(\omega,t)$ at three times after a photodoping pulse that inserted doublons (holons) near the upper (lower) edge of the upper (lower) Hubbard band. It is evident that the spectral weight associated with high-energy doublons decreases over time, while the spectral weight near the lower band edge increases. To analyze the redistribution of spectral weight, we display in Fig. 24(b) the change in the photoemission spectrum relative to the result at time $t = 24$. This clearly reveals how spectral weight disappears at an energy $\omega \approx 3$, while there is an approximately 2.3 times larger increase in spectral weight near $\omega \approx 1$. If impact ionization were the only process responsible for this reshuffling of spectral weight, we would expect a 3 times larger increase in low-energy spectral weight. The observed number is somewhat smaller due to intraband scattering processes; see Fig. 23(a). In systems with coupling to bosonic modes, the effect would be further reduced. Similar results for impact ionization were obtained using a quantum Boltzmann description without momentum conservation (Wais *et al.*, 2018). Impact ionization in Mott insulators has also been studied using a steady-state Floquet setup (Sorantin *et al.*, 2018). For real materials the impact ionization in VO_2 was theoretically proposed and experimentally reported (Coulter, Manousakis, and Gali, 2014; Holleman *et al.*, 2016).

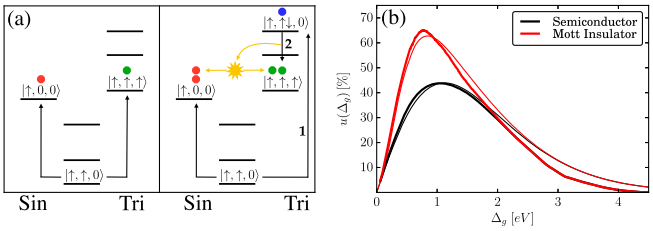

FIG. 25. (a) Excitation of a low-energy singlon (Sin) and triplon (Tri) pair in a three-orbital Mott insulator with average occupation $n = 2$ by a low-energy field pulse (left panel), and excitation of a high-energy triplon (1), with subsequent Hund impact ionization creating an additional low-energy pair (2). (b) Ultimate quantum efficiency $u(\Delta_g)$ of the Mott-insulating system compared to that of a semiconductor solar cell. The thin (thick) lines show the results for a blackbody (solar) spectrum. Inhomogeneous DMFT + NCA results for the three-orbital Slater-Kanamori Hamiltonian. From Petocchi *et al.*, 2019.

Following initial proposals by Manousakis (2010), Assmann *et al.* (2013), and Werner, Held, and Eckstein (2014), several studies exploited the carrier multiplication due to impact ionization in Mott systems to design efficient photovoltaic devices. A strategy based on combining heterostructures and magnetic materials was presented in Sec. IV.D. Further enhancements may be realized in multiorbital systems, where the Hund coupling leads to subbands in the Hubbard bands, corresponding to local spin excitations (Hund excitations). Their energy separation is U, $U - 2J_{\mathrm{H}}$, and $U - 3J_{\mathrm{H}}$ in the case of the model in Eq. (9) with density-density interactions. If the splitting between these Hubbard subbands is comparable to the gap, transitions between Hund excitations can produce additional charge carriers (Petocchi *et al.*, 2019). For example, a three-band Mott insulator with two electrons per site and positive J_{H} is dominated by high-spin doublon states of the type $|\uparrow,\uparrow,0\rangle$. A photodoping pulse with sufficiently high energy can produce a singlon-triplon pair, with the triplon in the low-spin configuration $|\uparrow,\uparrow\downarrow,0\rangle$ (corresponding to the highest-energy subband in the upper Hubbard band); see step 1 in the right panel of Fig. 25(a). Such a low-spin triplon can be converted into a high-energy triplon plus an additional low-energy singlon-triplon pair (step 2) if the gap size is comparable to or smaller than $3J_{\mathrm{H}}$, which in typical transition metal compounds can be as large as 2 to 3 eV. Impact ionization by Hund excitations is conceptually related to singlet fission in molecular systems or semiconductor quantum dots (Nozik *et al.*, 2010).

Figure 25(b) compares the ultimate quantum efficiency of a Mott insulator with impact ionization to that of a semiconductor. The Shockley-Queisser estimate of the ultimate quantum efficiency (Shockley and Queisser, 1961) assumes that charge excitations across a gap Δ_g in semiconductors contribute an energy Δ_g. For the Mott insulator estimate, it was assumed that photons with frequency $\Omega > 2\Delta_g$ ($\Omega > 3\Delta_g$) produce 2 times (3 times) as many charge carriers than photons with frequency $\Delta_g < \Omega < 2\Delta_g$. This comparison suggests that the efficiency of a Mott system that fully exploits impact ionization can be larger than 60% and that the optimal gap size of a Mott solar cell is smaller than that of a semiconductor solar cell.

D. Intraband relaxation and cooling of charge carriers

If the Mott gap is large, intraband relaxation processes [see Fig. 23(d)] can precede electron thermalization and carrier recombination. These processes lead to a reduced kinetic energy and are called carrier cooling in this review. Cooling before recombination is a typical prerequisite for the realization of novel nonthermal phases. Moreover, the processes behind the carrier cooling describe the formation of dressed quasiparticles, such as spin and lattice polarons, and are therefore important for understanding the properties of the long-lived photodoped state.

1. Weak-coupling scenario

Generic aspects of carrier cooling can be understood within a weak-coupling scenario. In Green's function methods, electron-boson scattering can be described by a self-energy contribution Σ_B given by the Migdal diagram $\Sigma_k(t,t') = \sum_q i|g_q|^2 G_{k-q}(t,t') D_q(t,t')$, where $G(t,t')$ is the electron Green's function, $D_q(t,t')$ is the equilibrium bosonic propagator, and different types of bosons (phonons, magnons, and plasmons) are distinguished only by their couplings g_q and dispersions. This formalism is closely related to a kinetic description of population dynamics, where relaxation rates are determined by scattering matrix elements $\propto g_q$ and the available phase space for the bosons and electrons. This theory can be used to numerically simulate the carrier cooling rate (see later discussion), and a reverse argument can be applied to extract information on the bosons (spectrum and couplings g_q) from the relaxation times (Conte *et al.*, 2012; Novelli *et al.*, 2014; Giannetti *et al.*, 2016; Golež *et al.*, 2022). For example, gapped bosonic modes relevant for the relaxation can be identified with a bottleneck effect since electrons with energy $\epsilon - E_F < \omega_0$ cannot relax further via the emission of bosons of energy ω_0 at sufficiently low temperature (Sentef *et al.*, 2013; Murakami *et al.*, 2015; Rameau *et al.*, 2016; Kemper *et al.*, 2017).

The weak-coupling approach has been used to simulate the intraband relaxation of photoexcited carriers in Mott insulators (Eckstein and Werner, 2013c). In large-gap systems, the kinetic energy of the photodoped doublons and holons is transferred to the boson bath, while the density of doublons and holons is approximately conserved. This cooling effect manifests itself in the accumulation of spectral weight of the doublons (holons) at the lower (upper) edge of the respective Hubbard band. Recent long-time DMFT simulations up to $t \approx 2000$ inverse hoppings (corresponding to picoseconds in realistic materials) explicitly demonstrated the formation of a quasistationary state in which the distribution function $N(\omega,t)/A(\omega,t)$ within the upper and lower Hubbard bands is well approximated by Fermi functions $f(\omega - \mu, T_{\mathrm{eff}})$ with separate chemical potentials for the doublons and holons (Dasari *et al.*, 2021). For a sufficiently low temperature T_{eff} in the quasisteady state, one observes the emergence of narrow bands close to the band edges, which shows that both the doublons and the holons behave as strongly renormalized

quasiparticles in the cold photodoped state. Moreover, a comparison of different excitation protocols (such as laser excitations and "temperature quenches," in which the initial carrier distribution is thermally excited) revealed that in the quasisteady state the spectral function does not depend on details of the excitation protocol, but only on the effective temperature T_{eff} and the two effective chemical potentials. This numerical observation justifies the quasisteady description of photodoped states with a few generalized thermodynamic variables, as explained in Sec. III.D. Nevertheless, a detailed understanding of the formation time of this universal state is presently lacking. DMFT simulations indicate that the transfer of energy to the bath becomes less efficient close to the onset of the quasiparticle formation (Sayyad and Eckstein, 2016; Dasari *et al.*, 2021), so for a remarkably long time after the excitation, a photodoped metal state can still be less coherent than a doped Mott insulator with a comparable density of carriers and the temperature of the bosonic bath (Eckstein and Werner, 2013c).

2. Electron-phonon interactions

The coupling to phonons is a natural mechanism for carrier cooling and is qualitatively captured by the weak-coupling description of Sec. VI.D.1. The simplest relevant model is the Holstein-Hubbard model in Eq. (7), which describes the linear coupling of the electronic density to the displacement of an Einstein phonon mode. The dynamics for a wide range of couplings was studied using ED for a single Holstein polaron by Golež *et al.* (2012) and using MPS simulations by Dorfner *et al.* (2015). At weak couplings the relaxation rate of photoexcited charge carriers is consistent with the rate expected from Fermi's golden rule, $1/\tau(\omega) \propto g^2\rho(\omega-\omega_0)$, where ρ is the electronic density of states, ω_0 is the boson frequency, and g is the coupling constant. At stronger couplings the relaxation timescales deviate from this simple scaling and the feedback of the excited lattice modes to the electronic dynamics is eventually strong enough that the system oscillates in a self-formed potential trap.

The properties of the photodoped Mott insulator described via the Holstein-Hubbard model have been systematically studied using DMFT combined with a variant of NCA based on the Lang-Firsov decoupling of the electron-phonon term (Werner and Eckstein, 2015). The cooling rate $1/\tau$ of the kinetic energy, as determined from an exponential fit to the time-dependent kinetic energy, was found to be proportional to g^2/ω_0 in the weak-coupling limit, in contrast to the scaling for a single polaron or in a metallic system. In particular, the decay rate of the kinetic energy in metallic states is expected to be proportional to $g^2\omega_0/v_0^2$ (Inayoshi, 2023). For stronger couplings the DMFT simulations help clarify the effects of polaron formation on the electronic properties. Figure 26 compares the spectral functions [Figs. 26(a) and 26(c)] and occupation functions [Figs. 26(b) and 26(d)] of the Hubbard and Holstein-Hubbard models. In the Hubbard model [Figs. 26(a) and 26(b)], the photodoping pulse centered near $t = 6$ has little effect on the spectral function, and there are no in-gap states generated by the photodoping. The result is very different in the Holstein-Hubbard case [Figs. 26(c) and 26(d)]. The effect is demonstrated with an artificially large phonon

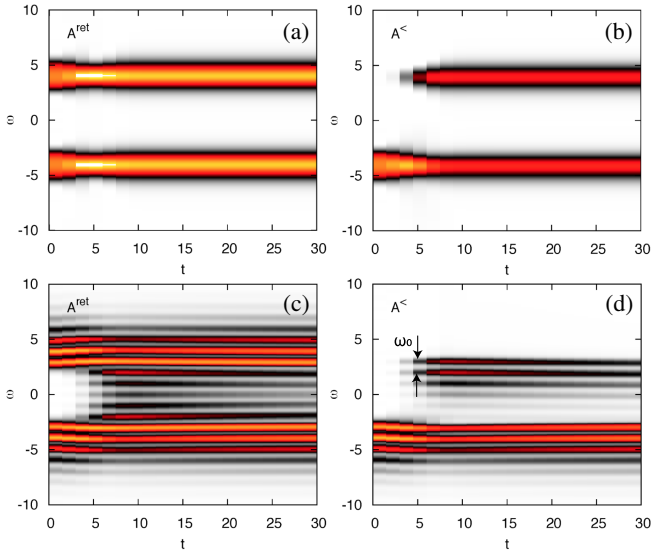

FIG. 26. Spectral function $A(\omega,t)$ (A^{ret}) and occupied states $N(\omega,t)$ ($A^{<}$) of (a),(b) the photodoped Mott-insulating Hubbard model and (c),(d) the Holstein-Hubbard model. *D-H* pairs are produced via a few-cycle pulse with frequency $\Omega = U = 8$, centered around $t = 6$. DMFT + NCA calculations for a hypercubic lattice with $v_* = 1$, $\omega_0 = 1$, and $g = 1$. Adapted from Werner and Eckstein, 2015.

coupling $g = 1$, which splits the Hubbard bands into phonon sidebands separated by an energy $\omega_0 = 1$. During the pulse, additional phonon sidebands corresponding to electron insertion or removal processes with simultaneous emission or absorption of phonons emerge in the gap; cf. Fig. 2. They appear in the spectrum because, in a dynamical phonon calculation, photodoped doublons and holons get dressed via lattice excitations. The occupied part of the spectrum ($A^{<}$) shows that in the Holstein-Hubbard case, the photodoped doublons and holons mainly occupy these induced in-gap states, which significantly affects the *D-H* recombination rate and thermalization process; see Sec. VI.G.

3. Electron-spin interactions

An efficient cooling mechanism for photodoped doublons and holons is their interaction with antiferromagnetically ordered spins (Takahashi, Gomi, and Aihara, 2002; Werner, Tsuji, and Eckstein, 2012; Golež *et al.*, 2014; Iyoda and Ishihara, 2014; Dal Conte *et al.*, 2015; Eckstein and Werner, 2016; Bohrdt, Grusdt, and Knap, 2020). In a half-filled Mott insulator with Néel order and dimension $D \geq 2$, each hopping of a doublon or holon flips a spin against the antiferromagnetically ordered surroundings, which costs energy of the order of the exchange coupling J_{ex}; see Fig. 27. The moving doublon or holon thus leaves behind a string of flipped spins and exhausts its kinetic energy after just a few hoppings. This mechanism is also relevant for systems with only short-range antiferromagnetic correlations, such as high-temperature superconductors in the pseudogap phase (Lee, Nagaosa, and Wen, 2006).

Detailed investigations of the coupled charge-spin dynamics have been conducted in the small-doping regime either by exciting a single holon in the AFM background or by inserting

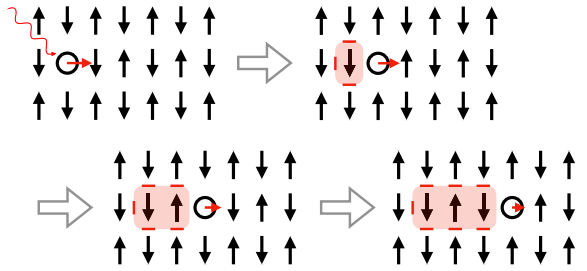

FIG. 27. Formation of a string state by a holon moving in an antiferromagnetic spin background. The red bars indicate broken antiferromagnetic bonds, which cost an energy J_{ex}, and the red arrows denote the holon's motion (kinetic energy).

a holon into the t-J model using ED (Takahashi, Gomi, and Aihara, 2002; Golež *et al.*, 2014; Dal Conte *et al.*, 2015; Hahn, Bohrdt, and Grusdt, 2022), real-time QMC calculations at high temperatures (Kanász-Nagy *et al.*, 2017), and MPS approaches (Bohrdt, Grusdt, and Knap, 2020; Hubig *et al.*, 2020). These studies revealed a two-stage dynamics that was recently confirmed using a cold-atom simulator (Ji *et al.*, 2021); see Fig. 28. At short times the initially localized holon spreads ballistically with the maximal group velocity. The root-mean-square of the position in units of lattice spacing grows as $d_{\mathrm{rms}} = (2v_0/\hbar)t$, where v_0 is the hopping parameter, as in a noninteracting quantum walk; see the dashed line in Fig. 28(a). The subsequent stage exhibits a slowdown and diffusivelike spreading ($d_{\mathrm{rms}} \propto \sqrt{t}$) with a sensitive temperature dependence. The slowdown can be analytically understood by considering a free-particle walk on the Bethe lattice in a spinful environment (Golež *et al.*, 2014; Kanász-Nagy *et al.*, 2017). In the low-temperature regime ($T < J_{ex}$), the spreading scales with the superexchange J_{ex} (Kogoj *et al.*, 2014; Ji *et al.*, 2021). At early times holes leave behind a string of antiferromagnetic correlations with the opposite sign, similar to Fig. 27, although at later times spin fluctuations restore the antiferromagnetic correlations; see Fig. 28(b). The high-temperature regime was modeled by assuming no quantum interference between paths leading to the same holon position, while different paths leave behind a different spin background (Kanász-Nagy *et al.*, 2017). A recent t-J_z model study showed that near the Néel temperature there is a temperature-driven confinement-deconfiment transition between the two regimes (Hahn, Bohrdt, and Grusdt, 2022).

DMFT-based approaches were used to discuss the effects of larger photodoping densities. Single-site DMFT allows one to study photodoping in a Hubbard model with long-range antiferromagnetic order, such as Néel order on a bipartite lattice (Werner, Tsuji, and Eckstein, 2012). Figure 29(a) plots the occupied density of states $N(\omega, t) \equiv A^<(\omega, t)$ for a half-filled antiferromagnetically ordered Mott insulator (upper Hubbard band). The "photodoping" is mimicked here by a quench from a moderately correlated initial state $U = 4 \to 12$, but the excitation with a short electric-field pulse yields similar results. In the antiferromagnetically ordered system [the lines in Fig. 29(a)], the spectral weight rapidly accumulates near the bottom of the Hubbard band (around $\omega \approx 2$) owing to the energy dissipation to the spin background. In a paramagnetic calculation [the crosses in Fig. 29(a)], this dissipation mechanism is absent, and there is no significant change in the energy distribution on the timescale of the calculation. The carrier cooling is accompanied by a reduction of the antiferromagnetic order; see Fig. 29(b). At low photodoping concentrations, the order decreases only slightly and the system is trapped in a long-lived prethermal antiferromagnetic state. As the photodoping concentration increases, the system undergoes a dynamical phase transition with a critical slowdown; see Fig. 29(c). An analogous slowdown has been reported in Slater antiferromagnets with weaker interaction strengths ($U < W$) (Tsuji, Eckstein, and Werner, 2013), although with a different lifetime of the prethermal phase (Picano, Li, and Eckstein, 2021).

A related intraband carrier relaxation is observed in systems without long-range order but with strong short-range antiferromagnetic correlations, which can be realized either by heating above the Néel temperature (Eckstein and Werner, 2016; Gillmeister *et al.*, 2020) or by chemical doping (Bittner *et al.*, 2018). DMFT simulations fail to capture these correlations, resulting in inefficient carrier cooling in the paramagnetic phase, as shown in Fig. 29(a). Fast cooling in the paramagnetic phase has been demonstrated in the

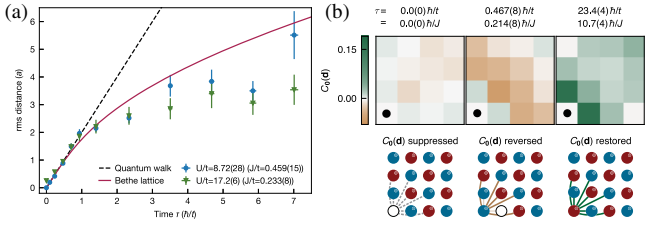

FIG. 28. (a) Time evolution of the root-mean-square distance for a holon (hole) suddenly inserted into the 2D square lattice Hubbard model, where time is measured in units of inverse hopping $\hbar/v_0 \equiv \hbar/t$. Results obtained with a cold-atom simulator (dots) for two values of the Coulomb repulsion, $U/v_0 = 8.72$ and 17.2, are compared with a quantum walk model and the Bethe lattice evolution; see the text. (b) Time evolution of the spin correlation function $C_0(d)$ with brown (green) marking ferromagnetic (antiferromagnetic) correlations with respect to the Néel background. Adapted from Ji *et al.*, 2021.

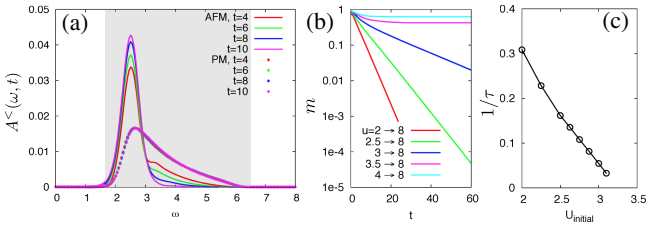

FIG. 29. (a) Occupied part of the spectral function within the upper Hubbard band (shaded area) for an antiferromagnetically ordered Hubbard model after an interaction quench from $U = 4 \to 12$. Crosses show the paramagnetic results. (b) Time evolution of the staggered magnetization m after an interaction quench from the indicated values of the initial U to $U_{\mathrm{final}} = 8$. (c) Inverse relaxation time as a function of the initial U. DMFT + NCA calculations on the Bethe lattice ($W = 4$) for an initial temperature $T = 0.1$. Adapted from Werner, Tsuji, and Eckstein, 2012.

Mott-insulating half-filled square lattice Hubbard model using the four-site DCA description (Eckstein and Werner, 2016). Here spin correlations within a four-site cluster are considered, while longer-range correlations are neglected. The cooling rate was determined from the decrease of the photoemission spectral weight near the upper edge of the upper Hubbard band and was shown to scale quadratically with the nearest-neighbor spin correlations S_{NN}. This scaling can be rationalized by a simple rate equation argument. Since the antiferromagnetic energy E_{AFM} is quadratic in the short-range order m, and the rate of generation of spin flips is proportional to m, one finds that $dE_{\mathrm{AFM}}/dt \propto m(dm/dt) \propto m^2$. With increasing temperature S_{NN} decreases, leading to a slower dissipation of kinetic energy to the spin background. Similarly, a saturation of the cooling rate occurs at high photodoping density, where S_{NN} is reduced by the effect of the pulse. The fragility of the cooling via electron-spin interactions should be contrasted with the cooling via phonons, which is more robust against the excitation intensity (Eckstein and Werner, 2016; Kogoj, Mierzejewski, and Bonča, 2016). In nonbipartite lattices, the intraband relaxation due to scattering with the spin background can be reduced as a result of magnetic frustration (Bittner *et al.*, 2020b).

The effect of chemical doping on the photoinduced dynamics was studied in the t-J model using EDMFT (Bittner *et al.*, 2018). The fastest cooling occurs at low temperatures in the weakly doped regime, where antiferromagnetic spin correlations are strong, while the cooling rate decreases with increasing temperature or doping. Bittner *et al.* (2018) also revealed oscillations in the time evolution of the kinetic energy and the antiferromagnetic spin correlations, but only in the regime where pseudogap signatures are present in equilibrium. Similar short-lived oscillations (several femtoseconds) were detected in cuprates by Miyamoto *et al.* (2018), who connected the presence of the oscillations with the two-magnon excitation signal in Raman scattering.

In multiorbital systems with Hund coupling, an additional highly efficient cooling mechanism based on local spin excitations exists even in the paramagnetic state (Strand *et al.*, 2017; Rincón, Dagotto, and Feiguin, 2018). The Hund coupling J_{H} favors high-spin configurations if the filling is $n > 1$ electrons per site. As photodoped charge carriers (for example, singlons or triplons in a half-filled two-orbital system) move through this background of predominantly high-spin states, they induce local spin excitations into lower-spin states at an energy cost of $O(J_{\mathrm{H}})$. Since J_{H} is large (of the order of eV) in transition metal compounds, this allows the photodoped carriers to release kinetic energy and cool down to an effective temperature of the order of J_{H} within a few hopping times. This cooling mechanism is expected to dominate over antiferromagnetic spin-flip scattering in the first stage of the relaxation process.

An experimental two-photon photoemission (2PPE) study of the multiorbital Mott insulator NiO with long-range antiferromagnetic order revealed how the aforementioned effects cooperate (Gillmeister *et al.*, 2020). The fast initial relaxation of the photodoped spectral weight (on a timescale < 80 fs) and the generation of photoinduced in-gap states was assigned to local spin (Hund) excitations. The subsequent dynamics is governed by long-lived oscillations of the in-gap state intensity whose lifetime exhibits a critical damping close to the Néel temperature [extracted from low-energy electron diffraction (LEED)], which was interpreted as evidence for the strong coupling between the charge carriers and the magnetic background; see Fig. 30.

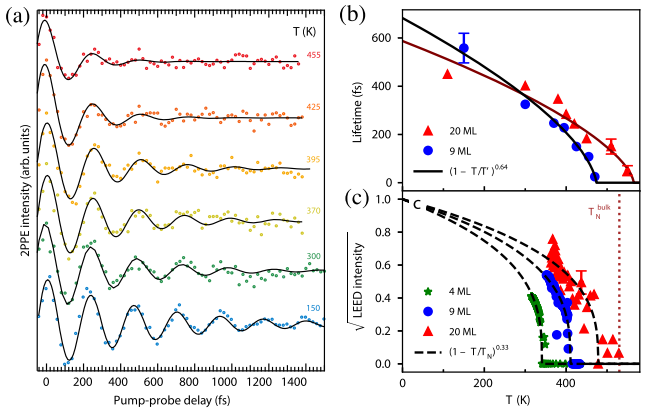

FIG. 30. (a) Time evolution of the two-photon photoemission (2PPE) signal for a photoinduced in-gap state in NiO at various temperatures. (b) Lifetime of the oscillations as a function of temperature for 9 and 20 monolayer thin films. The solid line indicates critical behavior with an exponent $\nu = 0.64$. (c) Antiferromagnetic scattering amplitude extracted from superstructure spots in low-energy electron diffraction (LEED) as a function of temperature. The dashed lines indicate the critical behavior with an exponent $\beta = 0.33$. From Gillmeister *et al.*, 2020.

4. Entropy cooling

Carrier cooling before recombination through interactions with bosonic degrees of freedom is a natural mechanism for generating effectively cold photodoped states. Alternatively, one can try to design targeted excitation protocols that allow photodoped states to be directly generated without excess kinetic energy. In this section, we discuss proposals along these lines suggesting that photoexcitation can lead to a reduced effective temperature in the valence band.

A general strategy for cooling down a system, denoted by *entropy cooling* in the following, involves exchanging particles or energy with another subsystem that is initially prepared in a state of low entropy. This concept is utilized in various contexts, such as evaporative cooling, adiabatic demagnetization (Pecharsky and Gschneidner, 1999), and protocols in cold-atom setups where the two subsystems are prepared using an inhomogeneous potential (Bernier *et al.*, 2009; Chiu *et al.*, 2018). Interband photoexcitation can be viewed as a similar process. Two bands are transiently coupled by light, and the transfer of electrons between different bands also implies a flow of entropy; see Fig. 31(a). To understand the possible cooling effects in this setup, it is useful to consider the ideal situation where the charge transfer is adiabatic (isentropic with respect to the entire system). Within DMFT the Mott-insulating Hubbard model has a large entropy of $S_{\mathrm{Mott}} = \ln 2$ per site down to the lowest temperatures, while the entropy of a Fermi-liquid metal is $S_{\mathrm{FL}} = \gamma T$, with $\gamma = \lim_{T\to 0} C/T$ and C the specific heat. In a

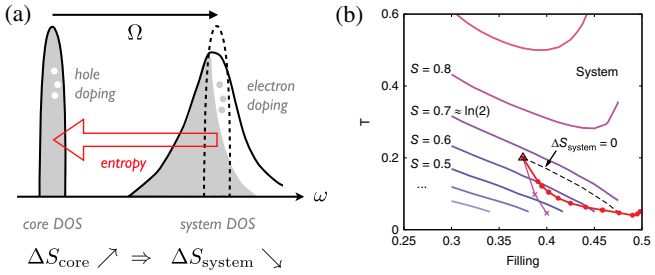

FIG. 31. (a) Basic principle of the entropy reshuffling from a partially filled valence or Hubbard band (*system*) to an initially filled band (*core*). (b) Isentropy lines of a single-band Hubbard model with bandwidth $W = 4$ and $U = 6$, where S denotes the entropy per spin. The violet line with crosses shows the temperatures and fillings realized by an isentropic charge transfer from an initially full and narrow band. The red dots indicate the temperatures and fillings that can be obtained with realistic short (chirped) pulses. Adapted from Werner, Eckstein *et al.*, 2019.

doped Mott insulator, the γ factor diverges as $1/|1/2 - n_\sigma|$ near half filling (Werner and Millis, 2007a), but the Fermi-liquid coherence temperature also drops. Figure 31(b) shows that the isentropy lines of the doped Mott insulator for $S \lesssim \ln 2$ decrease to 0 as $|n_\sigma| \to 1/2$ but increase for $S \gtrsim \ln 2$. If we assume that the isentropy lines of photodoped states as a function of the total number of carriers (doublons and holons) have a similar form, the isentropic generation of doublons and holons always leads to a high temperature (corresponding to $S \gtrsim \ln 2$ at nonzero doping). This is consistent with the observation that the photodoped metal states obtained by exciting charge carriers across the Mott gap typically have a broad energy distribution [see the PM solution in Fig. 29(a)], and characteristic features of low-temperature strongly correlated metal states, such as narrow quasiparticle peaks, are not observed in simulations of isolated single-band systems.

In a multiband context, entropy considerations suggest that photodoping can substantially cool the electronic state (Werner, Eckstein *et al.*, 2019). Consider a two-band set-up with an initially completely filled, narrow low-energy band (such as a core level or ligand band in a charge-transfer insulator) and a partially filled, wider band near the Fermi level, as sketched in Fig. 31(a). For the cooling effect, it does not make a qualitative difference if this partially filled band is weakly (Glazman, 1981) or strongly interacting (Werner, Eckstein *et al.*, 2019), but in the following we discuss the case of a Mott insulator with a partially filled lower Hubbard band. For simplicity, we assume that the initially filled narrow band is noninteracting such that the entropy of this band, above a temperature scale determined by its bandwidth, is given by the infinite-T (or atomic limit) result $S_\infty = 2n_\sigma^{\rm core} \ln n_\sigma^{\rm core} + 2(1 - n_\sigma^{\rm core}) \ln(1 - n_\sigma^{\rm core})$. In the initial state, $n_\sigma^{\rm core} = 1$ and $S_\infty = 0$, while the entropy grows rapidly with hole doping. An isentropic photodoping process, which conserves the total entropy of the system while electrons are transferred between the core and valence bands, therefore results in a reduced entropy and temperature of the valence band electrons.

The violet curve with crosses in Fig. 31(b) shows the effective temperature achieved by such an isentropic photodoping process when one starts at the initial filling and temperature marked by the black triangle. Even a small charge transfer (a few percent photodoping) can produce a significant cooling. In reality, the photodoping by a short and strong pulse may not be isentropic. Nevertheless, using suitably optimized chirped pulses (Werner, Eckstein *et al.*, 2019), it is possible to achieve a net cooling down to a temperature that is essentially limited by the width of the low-energy band, as indicated by the red dots in Fig. 31(b).

Similar cooling effects can be produced by exciting electrons from the system into an initially empty narrow high-energy state. Such a process was proposed for K_3C_{60}, where the high-energy localized spin-triplet exciton visible in the midinfrared absorption spectrum can be populated by light (Nava *et al.*, 2018). Motivated by this, Fabrizio (2018) studied the cooling dynamics in a minimal exactly solvable model consisting of two infinitely connected transverse-field Ising models. It was shown that one of them can be cooled down from the disordered into the ordered phase by switching on a transient coupling between the two subsystems. In systems coupled to an environment, it was shown that the entropy-cooled state can lead to a long-lived metastable state (Nava and Fabrizio, 2022). Moreover, a generalized photodoping setup involving both full and empty narrow bands can be used to create an effectively cold strongly photodoped Hubbard model and to realize the η-pairing state (Werner, Li *et al.*, 2019). These minimal models are useful for understanding the underlying mechanism, which should generically play a role in systems involving photoexcitations from or into narrow bands. More realistic modeling will be needed to understand competing relaxation channels that may destabilize the photodoped state and result in heating to estimate whether (and on which timescales) cooling by photodoping can be realized in experiments.

E. Mott excitons

Excitons in photodoped Mott insulators are bound pairs of photogenerated multiplets (holons and doublons in the single-band case). Like excitons in semiconductors, these states can be detected using linear or nonlinear optical responses, and the photogenerated carriers can relax into such exciton states. In this section, we focus on excitons that are bound by the nonlocal Coulomb interaction and/or the exchange of spin and orbital fluctuations.

Excitons from nonlocal Coulomb interactions. In any spatial dimension, strong nonlocal Coulomb interactions can naturally lead to bound excitons. Their properties are well understood in 1D systems thanks to the study of effective models (Gallagher and Mazumdar, 1997; Gebhard *et al.*, 1997) and numerical DMRG investigations of the extended Hubbard model; see Eq. (8) (Jeckelmann, 2003; Matsueda, Tohyama, and Maekawa, 2004; Essler *et al.*, 2005). The bosonization approach provides further insights into the formation of Mott excitons in the small Mott gap regime (Essler, Gebhard, and Jeckelmann, 2001). For sufficiently strong nonlocal interactions, one finds excitons of odd and even parity, where the former (latter) corresponds to a subgap

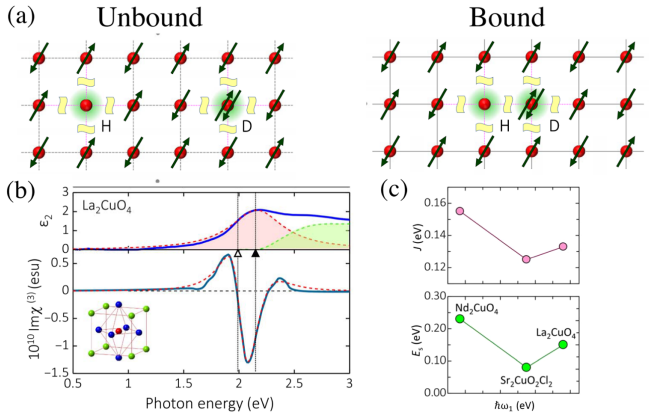

FIG. 32. (a) Sketch of an exciton pair stabilized by the shared disturbance of the antiferromagnetic background, with broken bonds marked by wavy lines. (b) Imaginary part of the dielectric function ϵ_2 (solid blue line) and nonlinear optical response $\chi^{(3)}$ (solid black line) for La_2CuO_4. The red (green) regions correspond to the optical transitions to the odd-parity exciton (holon-doublon continuum). The solid (empty) triangle indicates the energy of the odd-parity (even-parity) exciton. (c) Exchange interaction $J_{ex} \equiv J$ and splitting of the odd-parity and even-parity excitons E_s as a function of the odd-parity exciton energy $\hbar\omega_1$. From Terashige *et al.*, 2019.

optically active (forbidden) mode. In one dimension, the energy levels of odd and even excitons are close, and the transition dipole matrix element is large as a result of spin-charge separation (Mizuno *et al.*, 2000). Linear optical measurements can directly access the optically allowed excitons, while the nonlinear optical response allows the dark excitons to be detected, as explained in Sec. V.G.1. Related to this is a modification of the optical response by strong excitations, for example, the emergence of in-gap signals and/or the renormalization of the exciton energy (Novelli *et al.*, 2012; Lu *et al.*, 2015; Rincón and Feiguin, 2021). In addition, analogous to the observation of excitons in two-dimensional materials (Madéo *et al.*, 2020; Dong *et al.*, 2021; Schmitt *et al.*, 2022), Mott excitons should be observable in pump-probe PES. This has been demonstrated in a nonequilibrium DCA study of excitons in a two-dimensional extended Hubbard model in which small excitons are bound by a sufficiently strong nonlocal Coulomb interaction (Bittner *et al.*, 2020a). If the binding energy decreases, the excitons merge into the particle-hole continuum and become short-lived resonances. A similar excitonic signal in PES has been observed in the photodoped 1D Mott insulator simulated with iTEBD (Sugimoto and Ejima, 2023). Experimentally, long-lived Mott excitons with a lifetime of more than several hundred picoseconds have been detected using trARPES in α-$RuCl_3$ (Nevola *et al.*, 2021).

Exchange coupling assisted excitons. An alternative binding force of charge carriers originates from the energy gain due to the shared distortion of the background order, as illustrated in the case of a spin system in Fig. 32(a). This mechanism is characteristic of strongly correlated systems in dimensions $D \geq 2$ and acts on both chemically doped and photodoped charge carriers. Spin-mediated excitons have been extensively studied owing to their relevance for high-temperature superconductors. Theoretical studies concluded that, while the wave function of a pair of two holons has a d-wave symmetry, the wave function of a bound holon-doublon pair is s (p) wave for even (odd) parity excitons (Takahashi, Tohyama, and Maekawa, 2002; Tohyama, 2006; Lenarčič and Prelovšek, 2013). Furthermore, it has been pointed out that the even exciton can have lower energy than the odd exciton owing to the spin contribution, unlike in the 1D case (Mizuno *et al.*, 2000; Takahashi, Tohyama, and Maekawa, 2002).

To relate the Mott exciton binding with the spin-charge coupling, the exciton energies were extracted by measuring the third-order response using a terahertz pump and an optical probe to detect the electric-field-induced changes in the optical response of cuprates (Terashige *et al.*, 2019); see Fig. 32(b) and Sec. V.G.1. The characteristic plus-minus-plus structure originates from a transition between the ground state and an even-parity and odd-parity exciton. The exciton energies were extracted by fitting the nonlinear spectrum. It was found that the even-parity exciton is below the odd-parity exciton and that their energy difference scales with the superexchange J_{ex}. Theoretical calculations based on the t-J model using ED (Terashige *et al.*, 2019), DMRG (Shinjo *et al.*, 2021), and the self-consistent Born approximation (Huang *et al.*, 2023) confirmed this scaling and showed that the presence of the Coulomb interaction further enhances the binding energy (Lenarčič and Prelovšek, 2013; Terashige *et al.*, 2019). In pump-probe setups, direct transitions between excitons with different symmetries are allowed and have been observed by ultrafast terahertz optical spectroscopy in Sr_2IrO_4, showing a transfer of weight from the short-lived Drude response to a longer-lived intraexcitonic peak (Mehio *et al.*, 2023). This type of exciton formation is not limited to spin pairing but can instead originate as well from a mixture of spin and orbital pairing, as was demonstrated in an analysis of the transient optical conductivity of $LaVO_3$ thin films (Lovinger *et al.*, 2020).

Biexcitons. There are also bound objects that are composites of several excitons (Jeckelmann, 2003). The simplest example is the biexciton, which consists of two bound excitons. Coulomb-bound biexcitons were identified in an ED analysis of the square lattice U-V-V' Hubbard model (nearest-neighbor interaction V, next-nearest-neighbor interaction V') by simulating the optical conductivity in a laser-excited system where one-exciton states are produced by the pump (Shinjo and Tohyama, 2017). Experimental observations of biexcitons using pump-probe experiments have been reported for ET-F_2TCNQ (Miyamoto *et al.*, 2019). In addition, the in-gap states identified in photodoped La_2CuO_4 and Nd_2CuO_4 (Okamoto *et al.*, 2010) or the blueshift of the Mott gap feature in the experiment by Novelli *et al.* (2014) could be related to photoinduced biexcitons.

F. Dynamical screening and band-gap renormalization

The photodoping of charge carriers into a Mott insulator almost instantaneously transforms the insulator into a conductor, which can have significant effects on the screening of the interactions. In the context of semiconductors, a similar screening due to the photoinduced electrons and holes has

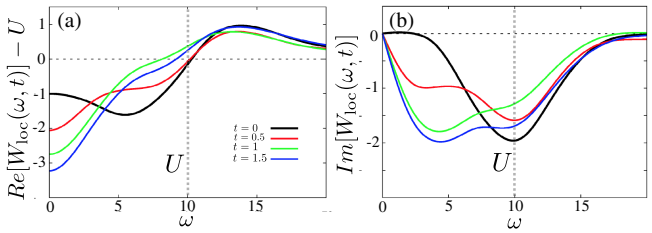

FIG. 33. Change of (a) the real part (shifted by U) and (b) the imaginary part of the local screened interaction $W_{\mathrm{loc}}(\omega,t)$ after a photoexcitation in the 2D extended Hubbard model. The calculations are based on EDMFT + NCA with $W=8$, $U=10$, and $V=2$. Adapted from Golež, Eckstein, and Werner, 2015.

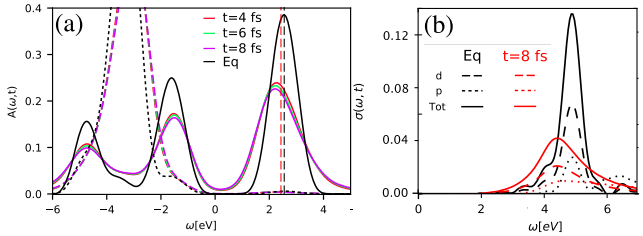

FIG. 34. Time evolution of the (a) spectral function $A(\omega,t)$ and (b) optical conductivity $\sigma(\omega,t)$ of the photodoped d-p model. The black lines show the results for the initial equilibrium state, and the colored lines the evolution during and after a photodoping pulse with $\Omega=7.5$ eV, which creates about 5% photodoping. The solid lines in (a) are for the d orbital, while the dashed lines pertain to the p orbitals. The vertical lines indicate the center of the upper Hubbard band. Adapted from Golež, Eckstein, and Werner, 2019.

been discussed using the GW method (El Sayed *et al.*, 1994; Bányai *et al.*, 1998; Rossi and Kuhn, 2002; Golež *et al.*, 2022; Perfetto, Pavlyukh, and Stefanucci, 2022). In the case of Mott insulators, dynamical screening effects can be captured via EDMFT and GW + EDMFT. In addition, TDDFT + U simulations based on the ACBN0 functional yield interactions that depend on the nonequilibrium population and thus capture some form of screening (Tancogne-Dejean, Sentef, and Rubio, 2018). Within EDMFT and GW + EDMFT, the screening modes, which originate from single-particle and collective charge excitations, are encoded in the frequency-dependent screened local interaction $W_{\mathrm{loc}}(\omega,t')=-(1/\pi)\int_{t'}^{\infty}dt e^{i\omega(t-t')}W^{R}_{\mathrm{loc}}(t,t')$ or in the effective local interaction $\mathcal{U}(\omega,t)$, which is related to the screened interaction and the local charge susceptibility χ_{loc} through $W_{\mathrm{loc}}=\mathcal{U}-\mathcal{U}*\chi_{\mathrm{loc}}*\mathcal{U}$.

Figure 33 illustrates the photo-doping-induced modifications in the real and imaginary parts of $W_{\mathrm{loc}}(\omega,t)$ for an initially Mott-insulating U-V Hubbard model with bandwidth $W=8$, $U=10$, $V=2$, and inverse temperature $\beta=5$ [EDMFT results from Golež, Eckstein, and Werner (2015)]. The black line shows $W_{\mathrm{loc}}(\omega)$ for the equilibrium Mott insulator. In the imaginary part, we see a broad peak centered at $\omega=U$ (the dashed vertical line), which indicates that screening in the Mott state is associated with charge excitations across the Mott gap. Below this energy, $\mathrm{Re}[W_{\mathrm{loc}}(\omega)]$ is reduced, but the static value $W_{\mathrm{loc}}(\omega=0)$ is still close to the bare interaction U.

Photodoping introduces additional screening channels and results in substantial changes in $W_{\mathrm{loc}}(\omega,t)$. In particular, as soon as doublons and holons are generated by the pulse, an additional low-energy peak appears in $\mathrm{Im}[W_{\mathrm{loc}}(\omega,t)]$ and grows with increasing density of the photodoped carriers. This peak is associated with excitations of doublons and holons within the Hubbard bands and represents low-energy photoinduced metallic screening. As seen in Fig. 33(a), this screening reduces the static value of W_{loc} significantly. One consequence of the modified screening environment is a rapid shrinking of the Mott gap on the timescale of the electron hopping (Golež, Eckstein, and Werner, 2015). Similar changes occur in the effective local interaction $\mathcal{U}(\omega,t)$, and the dominant peaks in $\mathrm{Im}\,\mathcal{U}(\omega,t)$ define the screening modes. From the integral over these modes [see Eq. (20)], we can extract the effective electron-boson coupling strength, which is typically large. The coupling to charge fluctuations can thus lead to a substantial broadening of the Hubbard bands and to the appearance of high-energy "plasmon" satellites in the spectral function (Golež *et al.*, 2017).

In multiband setups, where the photoexcitation transfers charge between different bands, there is a second pronounced effect that occurs on the timescale of the photodoping pulse, namely, a relative shift of the bands due to changes in the electrostatic interaction energy (Hartree shifts). These shifts were initially studied in the context of photoinduced insulator-metal transitions; see Sec. VII.B.2. The combined effect of Hartree shifts and dynamical screening has been studied in a photodoped d-p model using GW + EDMFT (Golež, Eckstein, and Werner, 2019). The two effects cooperate to increase the band-gap renormalization and lead to substantial shifts in the optical conductivity and photoemission spectrum, as shown in Fig. 34. In addition to the aforementioned broadening, we see that the photodoping results in a shift of the upper Hubbard band to lower energies [the dashed vertical red line in Fig. 34(a)]. This photoinduced shift also manifests itself as a redshift of the charge-transfer peak in the optical conductivity; see Fig. 34(b). Similar conclusions were reached using TDDFT + U based on the ACBN0 functional in the case of strong driving below the gap. In these simulations, incoherent processes led to a modification of the optical gap and a reduced effective interaction (Tancogne-Dejean, Sentef, and Rubio, 2018).

The renormalization of the gap edge and position of the upper Hubbard band leads to shifts in experimental probes that are sensitive to the unoccupied states, such as the optical conductivity or x-ray absorption. Novelli *et al.* (2014) reported a redshift in the optical response after a photoexcitation of La_2CuO_4, which may be explained by ultrafast changes in the screening. Recently, a band-gap renormalization was also observed with x-ray absorption spectroscopy on $La_{2-x}Ba_xCuO_4$ ($x=9.5\%$) (Baykusheva *et al.*, 2022) and NiO (Wang *et al.*, 2022; Lojewski *et al.*, 2024; Golež *et al.*, 2025). The response strongly depends on the frequency of the pump pulse. Above-gap excitations in NiO lead to a long-lived renormalization (Lojewski *et al.*, 2024), while below-gap excitations can result in an observable (Wang *et al.*, 2022) or nonobservable (Grånäs *et al.*, 2022) band-gap

renormalization. As these experiments were performed below the Néel temperature, the gap renormalization can be a combination of screening effects and a partial melting of the antiferromagnetic order. A clear separation of the two effects has not yet been achieved. In addition, further experiments are needed to understand whether the aforementioned relation between the pump frequency and the renormalization of the gap is specific to NiO or a generic phenomenon.

Complementary information can be extracted from experiments that measure the occupied part of the spectrum, such as photoemission spectroscopy. Cilento *et al.* (2018) reported a nonthermal renormalization and strong broadening of the oxygen band (in the antinodal direction) in optimally doped Y-Bi2212 that is extremely similar to the theoretical results shown in Fig. 34.

G. Recombination of charge carriers

In this subsection, we discuss the recombination of photodoped carriers; see Figs. 23(c) and 23(e). These processes are also important for understanding the lifetime of nontrivial quasistationary phases; see Sec. VII. As mentioned in Sec. VI.B, for large-gap Mott systems, the recombination times associated with electron-electron and electron-boson scatterings are expected to be exponentially long; see Eq. (43). Nevertheless, compared to conventional band insulators, where the nonradiative recombination of electrons and holes via phonon emission can take nanoseconds or even microseconds, the recombination times in Mott insulators are typically short.

Electron-electron scattering. Photocarriers can recombine as a result of electron-electron scattering processes; see Fig. 23(c). In this case the released energy of order U is transferred to the kinetic energy of the remaining charge carriers, and ϵ_0 in Eq. (43) corresponds to the hopping v_0. The exponential scaling of the doublon lifetime was confirmed in a cold-atom experiment (Sensarma *et al.*, 2010; Strohmaier *et al.*, 2010); see Fig. 35. In the experiment, a nonthermal state with excess doublons was created via a 10% modulation in the depth of the lattice with a frequency close to U. The subsequent dynamics of the double occupancy follows an exponential relaxation, from which the doublon lifetime was extracted.

Electron-boson scattering. An alternative recombination pathway is provided by electron-boson scatterings; see Fig. 23(e). An explicit theoretical description of carrier recombination through electron-spin interactions has been developed for the decay of bound D-H pairs (excitons) in the strongly repulsive two-dimensional Hubbard model (Lenarčič and Prelovšek, 2013). One starts with a Schrieffer-Wolff transformation to separate the Hilbert subspaces with fixed numbers of D-H pairs (t-J model) and focuses on the subspace with a single pair; see also Sec. III.D. Within the t-J model, the doublon-holon pair can form an exciton that is bound by spin fluctuations. The recombination rate of this pair can be described using Fermi's golden rule, $\Gamma = 2\pi \sum_m |\langle \Psi_m | H_3 | \Psi_{\rm hd} \rangle|^2 \delta(E_m - E_{\rm dh})$, where $\Psi_{\rm dh}$ is the initial state (s-wave Mott exciton) with energy $E_{\rm dh}$ and Ψ_m are final states with energy E_m and no doublons and holons. The relevant transition operator is the leading three-site correction to the t-J Hamiltonian, $H_3 = (J/2)\sum_{\langle ijk \rangle ss'} [h_{is} d_{ks'} \boldsymbol{\sigma}_{ss'} \cdot \mathbf{S}_j]$, where h_{is} (d_{is}) denotes the holon (doublon) annihilation operator for spin s at site i and $\boldsymbol{\sigma}$ are the Pauli matrices. Fermi's golden rule expression was evaluated using ED; see Fig. 36(b). The decay rate Γ essentially follows Eq. (43), where ϵ_0 is now the exchange energy $J_{\rm ex}$. For realistic parameters for cuprates ($J_{\rm ex}/v_0 \approx 0.4$), the decay rate Γ is large despite the considerable number of emitted magnons. This is a consequence of the strong spin-charge coupling in doped AFM insulators, which implies that the wave function of the initial exciton already contains configurations with many spin excitations; see Fig. 36(a). The modeling was extended to charge-transfer insulators (Lenarčič and Prelovšek, 2014), and fairly good agreement was obtained with observed recombination times in the picosecond range for photodoped cuprates; see Sec. I.C. A similar argument has been developed for 1D organic systems (Lenarčič, Eckstein, and Prelovšek, 2015), where the decay of the exciton via spin scattering is inefficient because of

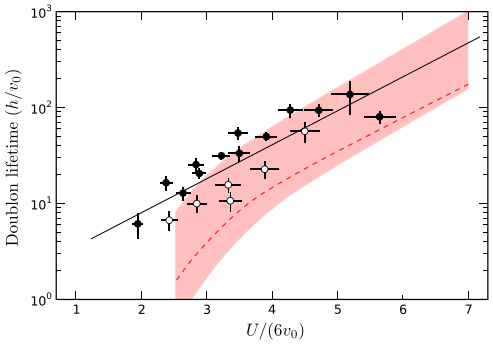

FIG. 35. Lifetime of doublons measured in a cold-atom simulation of the Hubbard model on a cubic lattice with hopping v_0 for two different mixtures of spin states (solid and open circles). The black line indicates the asymptotic behavior in Eq. (43) without the logarithmic correction. The shaded region was obtained by varying the filling factor in the theoretical calculations by 0.3. Adapted from Strohmaier *et al.*, 2010.

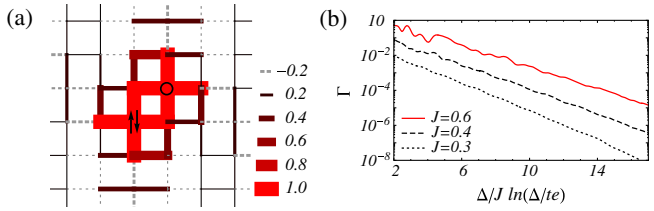

FIG. 36. (a) The most probable configuration leading to doublon-holon recombination in the 2D t-J model with a three-site term. The bond thickness represents the deviation of the bond energy relative to the AFM ground state for $J \equiv J_{\rm ex} = 0.4$. (b) Recombination rate Γ vs the expected scaling $\Delta/J_{\rm ex} \log(\Delta/v_0)$ for a gap Δ, different superexchanges $J_{\rm ex} \equiv J$, and a hopping $v_0 \equiv t$. Adapted from Lenarčič and Prelovšek, 2013.

spin-charge separation, but a decay on the timescale of a few hundred femtoseconds is possible owing to the large frequency of the relevant local vibrations of the molecular crystal (Mitrano *et al.*, 2014).

Besides spin fluctuations, nonlocal charge fluctuations can provide a high-energy bosonic mode that is relevant for the recombination. In models with nonlocal interactions, such as the U-V Hubbard model in Eq. (8), the coupling to single-particle and collective charge excitations leads to modifications in the local interaction $\mathcal{U}(\omega)$; see Sec. VI.F. The frequency dependence can be interpreted as a coupling to a continuum of bosonic modes (plasmons), with frequency ω and coupling strength $g_\omega^2 = -(1/\pi)\,\mathrm{Im}\,\mathcal{U}(\omega)$ (Ayral, Biermann, and Werner, 2013; Werner and Casula, 2016). For moderate values of V, the effective electron-boson coupling can become strong compared to typical electron-phonon couplings and can therefore lead to a considerably faster recombination (Golež *et al.*, 2017).

An interesting question concerns the dependence of the recombination time on the excitation density. While the decay of the exciton is exponential (similar to the approach of the thermal state in Fig. 22), the recombination of two particles out of the continuum is a bimolecular process. It should therefore be described by a nonlinear rate equation where the scattering is determined by the probability at which a doublon encounters a holon. Specifically, $(d/dt)\mathcal{D} \propto -(\mathcal{D}-\mathcal{D}_{\mathrm{eq}})^2$, where $\mathcal{D}_{\mathrm{eq}}$ is the double occupancy in the equilibrium state and it is assumed that the doublons and holons have the same density. This equation, which implies a nonexponential decay, fits the DMFT solution of a Holstein-Hubbard model with strong electron-phonon coupling well, with the relaxation occurring via phonon emission (Werner and Eckstein, 2015). However, at least in the low photodoping regime, experiments seem compatible with an exponential relaxation (Okamoto *et al.*, 2011). This hints at a two-stage process where initially an exciton is formed that then annihilates via a much slower recombination mechanism (Lenarčič and Prelovšek, 2013). Deviations from the exponential behavior at higher photodoping in insulating cuprates (Sahota *et al.*, 2019) have been interpreted as Auger-type processes; see Sec. VI.C. However, the recombination rate at high photodoping concentration is not yet understood, and theoretical considerations should also take into account possible band-gap renormalizations due to photodoping; see Sec. VI.F.

Within DMFT simulations, the gap in the photodoped state remains relatively robust (i.e., the Mott state can sustain a high density of photodoped carriers), which can be important for the stabilization of new phases; see Sec. VII. In iTEBD simulations of 1D Mott insulators, one observes a more pronounced shrinking and filling of the gap with photodoping (Murakami, Takayoshi *et al.*, 2022), but nevertheless the state can sustain large photodoping. The robustness of the Mott gap distinguishes this state from situations where the gap is opened by long-range orders, as in weak-coupling antiferromagnets (Tsuji, Eckstein, and Werner, 2013) or excitonic insulators (Mor *et al.*, 2017). If the gap is due to long-range order, recombination can lead to a melting of the order and the closing of the gap, which potentially results in a highly nonlinear dynamics or even an avalanche breakdown of the insulator (Picano, Li, and Eckstein, 2021).

VII. NONTHERMAL PHASES AND NONEQUILIBRIUM PHASE TRANSITIONS

A. Nonthermal and hidden phases: General remarks

Mott insulators provide an interesting platform to control the physical properties of materials with short laser pulses. In particular, *nonthermal phases*, i.e., states that allow for an approximate steady-state description but exhibit properties distinct from thermal equilibrium states, may emerge. Because of the complexity of correlated materials, there are various types of nonthermal phases and pathways toward them, as we discuss in this section. Nonthermal phases are also sometimes called *hidden phases* to emphasize that they cannot be reached along thermodynamic pathways.

We can distinguish among three categories of nonthermal phases.

(i) *Prethermal steady states*. A prethemal quasisteady state (or "trapped" state) emerges when the dynamics is constrained by approximate conservation laws. Prethermalization (Berges, Borsányi, and Wetterich, 2004) and its relation to almost conserved quantities has been widely discussed for systems close to integrability (Langen, Gasenzer, and Schmiedmayer, 2016; Moeckel and Kehrein, 2008; Kollar, Wolf, and Eckstein, 2011; Polkovnikov *et al.*, 2011). In strongly correlated electron systems, the main constraint is imposed by the Mott gap (see Sec. VI.B), and the quasiconserved quantities correspond to the density of photodoped carriers, such as doublons and holons or more general local spin-orbital multiplets. Within the prethermal category, nonthermal charge carriers can stabilize existing orders or lead to the emergence of new orders.

(ii) *Classical metastability.* In this case the quasisteady state corresponds to a free-energy minimum in the space of emergent classical variables. The emergent variables can be extensive thermodynamic variables, as in the case of metastable phases close to a first-order phase transition, or local fields, as in the presence of defects in an ordered state. An example is the stabilization of photoinduced states via a lattice deformation.

(iii) *Dissipative steady states associated with energy and particle flows*. Such a state arises, for example, if a flow of energy from the electronic sector transiently supports a dissipative driven state within some subset of low-energy degrees of freedom. These emergent nonthermal steady states can also be related to nonthermal criticality (Berges, Rothkopf, and Schmidt, 2008; Nowak, Sexty, and Gasenzer, 2011; Mikheev, Siovitz, and Gasenzer, 2023) and turbulence, with energy and particle flow between different length scales. In photoexcited correlated systems, this scenario has been investigated much less than prethermal or metastable states. Theoretical predictions include a nonequilibrium phase transition in a quantum antiferromagnet (Kalthoff *et al.*, 2022) and a population inversion in the charge sector that is maintained by D-H recombination energy (Werner and Eckstein, 2016; Golež *et al.*, 2017).

From a phenomenological perspective, both prethermal and metastable phases fit the traditional description of photoinduced phase transitions (Nasu, 2004) in terms of a nonthermal free-energy surface for a small set of nonequilibrium order parameters. However, in the case of strongly correlated systems, it remains an outstanding challenge for microscopic theory to determine such nonthermal free energies or even to identify the relevant coarse-grained degrees of freedom. The quasisteady description of photodoped states (see Sec. III.D) provides a possible starting point. In this section, we review nonthermal phases in Mott insulators that belong to the prethermal and metastable category, pathways to reach such states via the ultrafast melting of order, and protocols to switch between different phases.

B. Photoinduced insulator-metal transitions

Photoinduced insulator-metal transitions are among the most common examples of photoinduced phase transitions. While the injection of charge carriers into an insulator is expected to metallize the system, the possible coexistence of multiple types of charge carriers and their nonthermal nature distinguish photoinduced metals from their chemically doped counterparts. The following discussion covers the emergence of metallic phases, their characteristics, and the possible origins of their metastability.

1. Metallic properties of photodoped states

Time-resolved optical pump-probe experiments generally lead to an almost instantaneous appearance of a low-energy conductivity signal (Drude peak) in photodoped Mott insulators; see Iwai *et al.* (2003), Okamoto *et al.* (2007, 2010), Giannetti *et al.* (2016), and Fig. 6. The Drude peak indicates that the photoinduced charge carriers (for example, holons and doublons) are highly mobile and support a transient metallic state. In large-gap Mott insulators, owing to the thermalization bottleneck (see Sec. VI.B), such photodoped metallic phases fall into the category of trapped states.

The experimental observation of a Drude peak is in agreement with theoretical simulations for Hubbard-type models based on ED (Maeshima and Yonemitsu, 2005; Shao *et al.*, 2016; Shinjo and Tohyama, 2017), DMFT (Eckstein and Werner, 2013c; Werner, Li *et al.*, 2019), and DMRG (Rincón and Feiguin, 2021). As an illustration, Fig. 37(a) shows results from the ED study by Maeshima and Yonemitsu (2005) on the 1D Hubbard model. In equilibrium, the real part of the conductivity [the thin line in Fig. 37(a)] exhibits a gap and a "continuum" of excitations (up to finite-size effects) in the range $U - W \lesssim \omega \lesssim U + W$ set by the bandwidth W. In the photodoped state (mimicked here by the first optically allowed excited state), the conductivity has a Drude peak [the bold line in Fig. 37(a)]. In addition, negative spectral weight at the lower edge of the continuum indicates energy gain in optical deexcitation processes due to a partially inverted population. Qualitatively similar results were also found for the infinite-dimensional Hubbard model within DMFT (Werner, Li *et al.*, 2019), as exemplified in Fig. 37(c). In the conductivity of the photodoped state, one again observes a dip near the lower edge of the continuum (that would develop into negative weight for larger photodoping) and a prominent photoinduced Drude peak. The continuum of excitations across the Mott gap (near $U \approx 9$) is hardly modified by the photodoping, apart from a slight bleaching.

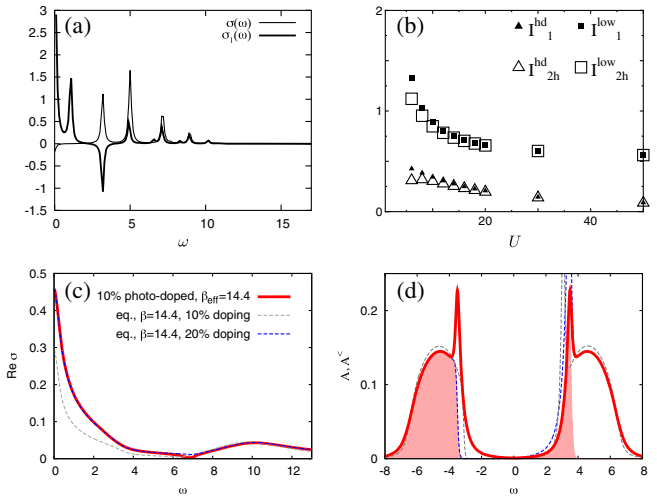

FIG. 37. Optical conductivity and spectral function of photodoped Mott-insulating Hubbard models. (a) One-dimensional Hubbard model with $U = 6$ and bandwidth $W = 4$. $\sigma(\omega)$ and $\sigma_1(\omega)$ show the conductivity in equilibrium and for a photodoped state, respectively. (b) Weight of the Drude peak (squares) and of the continuum (triangles) for the photodoped state (solid symbols) and an equilibrium system with two holons (empty symbols). (c) Optical conductivity and (d) spectral function of the photodoped Hubbard model on the Bethe lattice with $U = 9$ and $W = 4$ (10% doublons and holons, effective inverse temperature $\beta_{\mathrm{eff}} = 14.4$). The gray (blue) dashed lines show equilibrium results for the indicated chemical doping. In (d) the equilibrium spectra are shifted to match the positions of the Hubbard bands in nonequilibrium. Adapted from Maeshima and Yonemitsu, 2005, and Werner, Li *et al.*, 2019.

A basic question is to what extent the photodoped system with $x\%$ doublons and $x\%$ holons resembles a chemically doped Mott insulator with doping concentration $2x\%$. Maeshima and Yonemitsu (2005) compared the weight of the Drude peak (I^{low}) and the continuum feature (I^{hd}) for a photodoped system with a single D-H pair and a chemically doped system with two holons and found good agreement; see Fig. 37(b). In addition, in the DMFT simulations, the Drude peak of the photodoped state corresponding to $x = 10\%$ is well reproduced by $2x\%$ chemical doping, which means that doublons and holons independently contribute to the low-energy conductivity; see Fig. 37(c). In contrast, the spectral function of the photodoped system shows a quasiparticle peak for both holons and doublons and cannot be directly compared to that of the chemically doped state; see Fig. 37(d).

Another relevant question is the lifetime of the Drude peak and the dynamics of its buildup. Consistent with the sum rule $\int d\omega \mathrm{Re}\sigma(\omega, t) = -E_{\mathrm{kin}}(t)$ for a single-band model, the buildup of the Drude peak requires a cooling of the photoinduced carriers. Consequently, in the DMFT simulations, the Drude peak grows as the photodoped carriers dissipate energy

to bosonic excitations (see Sec. VI.D), while it remains broad and of small weight if the coupling to the bath is inefficient (Eckstein and Werner, 2013c). In experiments, the Drude peak can emerge within a few femtoseconds, such as in the cuprate Mott insulator Nd_2CuO_4 (Miyamoto *et al.*, 2018). However, at longer times the Drude peak can disappear even before the recombination of the charge carriers (see Fig. 6), as the latter may get trapped by impurity states (Okamoto *et al.*, 2010), may be dressed into lattice polarons (Yonemitsu and Maeshima, 2009; Golež *et al.*, 2012; Matsueda *et al.*, 2012; Tohyama, 2013; Vitalone *et al.*, 2022) and spin polarons (Lenarčič *et al.*, 2014), or may form (bi)excitons; see Sec. VI.E.

2. Photoinduced changes in the electronic structure

In correlated electron systems, an insulator-metal transition can be induced not only through the generation of mobile carriers (transfer of population across the gap) but also by changing the electronic structure, i.e., the generation of new states within the gap or the closing of the gap. In particular, photoinduced changes in the electronic structure may occur as a result of dynamical screening effects (see Sec. VI.F) and the electrostatic interaction energy between electrons in different bands (Hartree shifts). The latter can already have interesting consequences in metals, such as a change in the Fermi surface topology (Beaulieu *et al.*, 2021). A gap closing resulting from changes in the screening environment has been proposed to explain the observation of a short-lived metallic phase in VO_2 (Wegkamp *et al.*, 2014) that was also detected with time-resolved electron diffraction (Morrison *et al.*, 2014). DMFT-based simulations instead suggest a gap filling scenario (Chen *et al.*, 2024a).

Especially in multiband systems, a restructuring of the density of states provides a promising pathway for photo-induced insulator-metal transitions. Studies within the Hartree-Fock approximation (He and Millis, 2016) predict that a carrier redistribution between bands can lead to metastable metallic states. A photoinduced metastable state has also been found within the time-dependent Gutzwiller approximation for a quarter-filled two-band Hubbard model (Sandri and Fabrizio, 2015) near a first-order insulator-metal transition. For certain intermediate excitations, the charge gap can be closed, while spin correlations survive. Similar features were observed in time-resolved x-ray and photoemission studies on V_2O_3, which reported an induced metallic state with a lifetime of several picoseconds (Lantz *et al.*, 2017), although its nonthermal nature is still under debate (Moreno-Mencía *et al.*, 2019; Chen *et al.*, 2024b).

Note that in the presence of strong electron-lattice coupling, charge excitations can modify the lattice structure, which can subsequently affect the electronic parameters. This effect can also result in photoinduced phase transitions. For example, a photoinduced insulator-metal transition reported in the dimer-Mott insulator κ-$(BEDT\text{-}TTF)_2Cu[N(CN)_2]Br$ can be attributed to a reduction of the effective Coulomb interaction (in the dimer basis) by such a mechanism (Kawakami *et al.*, 2009). In dimer-Mott systems, the effective Coulomb interaction is related to the intradimer hopping, which can be modified by changing the distance between dimers through the charge excitations (Yonemitsu, Miyashita, and Maeshima, 2011).

3. Metastable phases and inhomogeneities

External driving can also induce novel metastable phases that are absent in equilibrium. Such phenomena can be observed in various systems, particularly in Mott insulators coupled to lattice distortions and near first-order phase transitions. A paradigmatic example is the photoinduced insulator-metal transition in VO_2 (Cavalleri *et al.*, 2001; Hilton *et al.*, 2007; Kübler *et al.*, 2007). The entangled motion of the electrons and lattice makes it difficult to decide whether transitions in VO_2 are electronically or lattice driven. Experiments indicate an ultrafast transition from the insulator to an isostructural metallic state, which can be reached by optical excitation (Wall *et al.*, 2013; Morrison *et al.*, 2014; Wegkamp *et al.*, 2014), strong-field tunneling breakdown (see Sec. IV.C) (Gray *et al.*, 2018), or short voltage pulses (Sood *et al.*, 2021) but has also been interpreted within a thermal scenario (Vidas *et al.*, 2020). A metastable photoinduced metallic phase was also reported in Ca_2RuO_4. Supported by DMFT simulations, Verma *et al.* (2023) proposed that photo-doped charge carriers can quickly reduce the orbital order that stabilizes the equilibrium Mott phase. The coupling of the orbital order to the lattice leads to a slow evolution into a nonthermal metallic phase, with a distinct lattice configuration compared to the high-temperature metallic phase (revealed by time-resolved x-ray diffraction).

In the conventional picture of ultrafast structural phase transitions, atoms move in a slowly varying free-energy landscape determined by the fast electrons, as qualitatively captured by a time-dependent Ginzburg-Landau theory for few global lattice displacement coordinates. However, heterogeneities [of both extrinsic (O'Callahan *et al.*, 2015) and intrinsic natures] can have a profound effect on the dynamics of the transient state. On a timescale of tens of picoseconds, nucleation and growth dynamics of metallic domains has been reported for thin films of V_2O_3 (Abreu *et al.*, 2015) and nickelates (Abreu *et al.*, 2020). In addition, the long-lived hidden metallic states in 1*T*-TaS_2 (Stojchevska *et al.*, 2014) have distinct nanoscale patterns (Gerasimenko *et al.*, 2019; Ravnik *et al.*, 2021). Intrinsic disorder can emerge on shorter timescales. Within the so-called ultrafast disordering scenario, as proposed for the photoinduced transition in VO_2 (Wall *et al.*, 2018; de la Peña Muñoz *et al.*, 2023) and in a layered manganite (Perez-Salinas *et al.*, 2022), the nonequilibrium dynamics leads to strong disorder on the atomic scale such that the mean value of the order parameter is no longer representative of the local environment.

Disorder may lead to nonergodic behavior on long time-scales, known as glassy behavior. This is evident, for example, in the phenomenon of aging, where the correlation function after a quench never becomes stationary (Bouchaud *et al.*, 1997). Glasses are found in systems with quenched disorder, such as in disordered spin systems (Weissman, 1993; Mydosh, 2015; Cugliandolo and Müller, 2023; King *et al.*, 2023) or electronic systems (Miranda and Dobrosavljević, 2005), and also in classical translationally invariant liquids (Berthier and Biroli, 2011). This has led to the idea that disorder may also emerge dynamically in quantum systems with a disorder-free Hamiltonian. Such behavior is observed in ideal models with a mixture of particles with a large mass ratio, where heavy

particles can localize in the presence of an almost frozen configuration of the lighter particles (De Roeck and Huveneers, 2014; Grover and Fisher, 2014; Schiulaz and Müller, 2014). An extreme case is the Falicov-Kimball model, where heavy particles are immobile, and DMFT studies show nonergodic behavior of the mobile particles (Eckstein and Kollar, 2008b; Moritz, Devereaux, and Freericks, 2010). In addition to glassy dynamics, the combination of electronic correlations and disorders can yield interesting dynamical features even near equilibrium, as exemplified by non-Fermi-liquid behavior, as well as electronic Griffiths phases close to the Mott transition (Miranda and Dobrosavljević, 2005). Given these findings, it is an interesting but largely open question whether correlated systems, after photoexcitation, transition into a glassy phase that gives rise to such long-lived nonergodic behavior. Theoretically, ultrafast disordering has been studied in the Holstein model (Sous *et al.*, 2021; Picano, Grandi, and Eckstein, 2023) and for the evolution of magnetic domains in the Hubbard model (Bakshi and Majumdar, 2024). Within DMFT disorder can be incorporated in a statistical framework (Dobrosavljević and Kotliar, 1997; Miranda and Dobrosavljević, 2012). The dynamical variant of statistical DMFT, though computationally challenging, could offer a path toward a better understanding of the role of dynamically generated disorder in photoinduced phase transitions of correlated electrons.

Recent experimental progress is opening new avenues for studying this spatiotemporal dynamics in correlated systems with femtosecond temporal resolution and nanometer spatial resolution. Diffuse electron scattering can map out phonon occupations (Seiler *et al.*, 2021), ultrafast electron diffraction has revealed defects and transient subdominant orders in a charge density wave (CDW) phase (Zong *et al.*, 2019b, 2021), while free-electron-laser-based ultrafast x-ray imaging has been used to study inhomogeneities in the photoinduced transition of VO_2 with a time resolution of 150 fs (Johnson *et al.*, 2023). Further useful information on the spatial distribution can be obtained by monitoring collective excitations in ordered systems using time-resolved RIXS. In the case of doped lanthanum barium copper oxide, such measurements revealed diffusivelike charge dynamics (Mitrano *et al.*, 2019). Electron microscopy (Vogelgesang *et al.*, 2018; Danz, Domröse, and Ropers, 2021) has revealed the evolution of CDW domains and topological defects in the unconventional CDW in $1T$-TaS_2. Finally, an interesting development is ultrafast scanning tunneling microscopy (Plankl *et al.*, 2021; Roelcke *et al.*, 2024). Applications of these techniques to correlated insulators should further clarify the role of spatial patterns in nonequilibrium transitions.

C. Melting and trapping of electronic orders

Owing to the delayed thermalization, electronic orders in large-gap Mott insulators can persist for extended periods even if the injected energy is sufficient to disorder the thermalized state (Werner, Tsuji, and Eckstein, 2012; Tsuji, Eckstein, and Werner, 2013). Nevertheless, the injected mobile carriers can disrupt the ordered state at early times after the excitation. This ultrafast melting dynamics is important for understanding relaxation pathways toward nonthermal hidden phases.

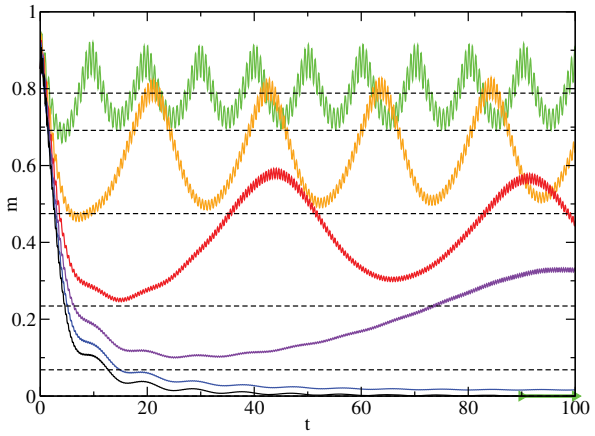

FIG. 38. Time evolution of the staggered magnetization m in a Hubbard model with a bandwidth $W = 4$ for interaction quenches $U_i = 4 \rightarrow U_f = 12$, 14, 16, 18, 20, and 22 (from top to bottom). For all cases the thermalized state would be disordered ($m = 0$). From Sandri and Fabrizio, 2013.

As a simple example, we discuss the dynamics of AFM order in the Hubbard model after an interaction quench. (For the purpose of this discussion, the quench acts like a photodoping pulse, as it produces a state with a nonthermal doublon-holon population.) As shown in Fig. 29, the generation of doublons and holons by the quench does not always lead to a melting of the staggered magnetization on numerically accessible timescales, even when the fully thermalized state is expected to be paramagnetic. The behavior of the order changes from trapped to exponentially decaying at a sharply defined excitation threshold. This transition was also studied by Sandri and Fabrizio (2013) using the time-dependent Gutzwiller variational approach; see Sec. III.B.3. Figure 38 shows the time evolution of the staggered magnetization m in a Hubbard model for interaction quenches from an initial interaction U_i in the AFM phase to larger final interactions. For the smallest quench, the thermalized system would already be paramagnetic, but the staggered magnetization oscillates around a large value $m \approx 0.8$. The frequency ω_2 shows a critical slowdown with increasing U_f and vanishes at $U_f^c \approx 21$, where the dynamics switches to an exponential decay.

These transitions are examples of dynamical phase transitions between ordered and disordered phases that are both prethermal. Such transitions have been widely discussed for systems close to integrability (Marino *et al.*, 2022), including the quench dynamics of superconducting and antiferromagnetic states in the weakly correlated regime (Barankov and Levitov, 2006; Yuzbashyan and Dzero, 2006; Tsuji, Eckstein, and Werner, 2013). A critical slowdown, as predicted for such dynamical phase transitions [see also Fig. 29(c)], has been observed for the melting of a CDW (Zong *et al.*, 2019a). A dynamical phase transition in a strongly correlated electron system has been reported for the photoinduced melting of AFM order in Sr_2IrO_4 (de la Torre *et al.*, 2022). In this case one finds separate fluence thresholds for the ultrafast melting

of AFM order and for the critical slowdown of the recovery dynamics. This indicates that the lower threshold, which is for the melting of AFM order, corresponds to a dynamical phase transition, which is consistent with the aforementioned numerical predictions.

In the presence of coexisting order parameters, the ultrafast partial melting of orders can provide an interesting pathway leading to hidden states. An important aspect is that an order parameter that is dominant in equilibrium can be less robust in the nonequilibrium setting. For example, the signatures of light-induced superconductivity appearing within the stripe phase of high-T_c cuprates (Fausti *et al.*, 2011; Nicoletti *et al.*, 2014) may be explained by the melting of the initially dominant stripe order. From a more general perspective, Sun and Millis (2020) proposed that in a system with intertwined orders, after a partial melting of both orders, the system can preferentially relax into a subdominant metastable free-energy minimum. This rather generic pathway to reach hidden states was demonstrated within a time-dependent Ginzburg-Landau theory for a multicomponent order parameter (assuming an overdamped, so-called model A dynamics) (Hohenberg and Halperin, 1977). A somewhat related theoretical prediction is discussed in Sec. VII.E.1, where one order parameter (orbital order) is more robust against thermal fluctuations than another (magnetic order) but nevertheless melts more efficiently upon photodoping (Li *et al.*, 2018).

D. Switching on electronic timescales

While Sec. VII.C pointed out pathways to hidden states through the incoherent melting of orders, one can also ask whether more coherent switching pathways can be realized. This is particularly interesting for systems with a discrete manifold of long-lived states, including (i) phases close to a first-order transition and (ii) equivalent realizations of the order under the breaking of a discrete symmetry. Such switching pathways may also be relevant for possible ultrafast memory devices. In this section, we mainly review proposals where the switching relies on electronic mechanisms and happens on correspondingly fast timescales.

Optical access to competing states. Close to a first-order transition, states featuring a competing order can appear as low-lying excited states that may be reached by optical excitation. A proposal for controlled optical switching based on this scenario was made for the extended Hubbard model [Eq. (8)] on a 1D chain (Lu *et al.*, 2012). At half filling, a first-order phase transition occurs around $U \simeq 2V$ between a conventional Mott insulator characterized by singly occupied sites and AFM spin correlations and a CDW phase. As shown in Fig. 39, the charge order correlations are enhanced by a few-cycle electric-field pulse when the system is in the Mott-insulating phase but close to the phase boundary. This photoinduced charge order can be realized only if the excitation pulse is resonant with an excited state with large CDW correlations. A related switching mechanism has been discussed for the competing charge orders in the extended Hubbard model on a frustrated lattice (Hashimoto *et al.*, 2014) and for those in the Peierls-Hubbard model (Yonemitsu and Miyashita, 2003).

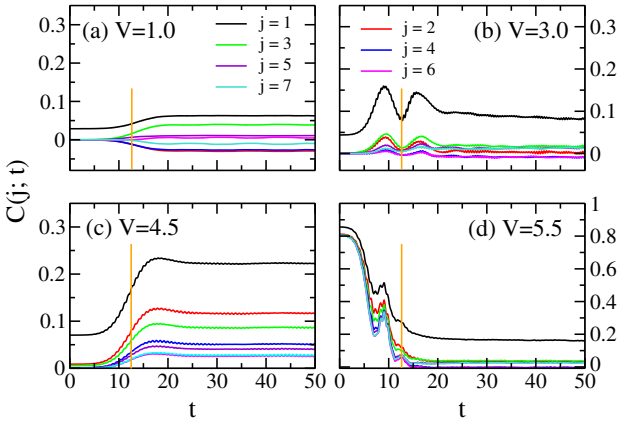

FIG. 39. ED results for the time evolution of the charge correlations $C(j,t)$ at distance j in a photoexcited half-filled extended Hubbard model on a 14-site chain. V is the nearest-neighbor interaction, and the Gaussian laser pulse is centered at $t = 12.5$ (vertical lines). The pump frequencies match the resonance peaks of the optical absorption spectrum. Parameters: $U = 10$, (a) $\omega_{\text{pump}} = 7.1$ and $E_0 = 0.10$, (b) $\omega_{\text{pump}} = 6.1$ and $E_0 = 0.30$, (c) $\omega_{\text{pump}} = 4.0$ and $E_0 = 0.07$, and (d) $\omega_{\text{pump}} = 4.1$ and $E_0 = 0.60$. From Lu *et al.*, 2012.

Experimentally, such an optical switching was demonstrated in a bromine-bridged Pd-chain compound (Matsuzaki *et al.*, 2014), although the electron-phonon coupling also matters there. The material shows a first-order transition from a CDW phase to a Mott insulator with decreasing temperature. Exciting the low-temperature phase resonantly with the Mott exciton leads to a transition to the CDW phase, while above-gap excitations induce a metallic state. Somewhat related transitions were reported in the organic molecular compound $(\text{EDO-TTF})_2\text{PF}_6$ for near-infrared excitations (Onda *et al.*, 2008) and in κ-$(\text{ET})_2\text{Cu}[\text{N}(\text{CN})_2]\text{Cl}$ for terahertz excitations (Yamakawa *et al.*, 2021). The opposite effect was observed in the iodine-bridged platinum compound, where the equilibrium CDW is transformed into the Mott-insulating phase (Kimura *et al.*, 2009).

Switching by periodic driving. As an alternative to resonant optical transitions between competing states, one can try to use the effective time-averaged forces arising from a periodic drive to transfer a system between different free-energy minima. Experimentally, the most established pathway along these lines is the switching via nonlinear phononics (see Sec. V.H), as recently demonstrated for ferromagnetic order in $YTiO_3$ (Disa *et al.*, 2023) and ferroelectric order in $LiNbO_3$ (Mankowsky *et al.*, 2017). Theoretical proposals include a switching of the lattice structure in $ErFeO_3$ (Juraschek, Fechner, and Spaldin, 2017) and a modification of the spin configuration in Cr_2O_3 via the transient modification of the exchange interaction (Fechner *et al.*, 2018). An obvious question is whether related switching protocols can be realized using a transient Floquet engineering of the electronic structure and interactions. Promising materials for the investigation of this physics are systems with orbital order of electronic origin that feature a discrete set of equivalent orders. An example is the switching of composite order, which has been theoretically discussed in the context of the

fulleride compounds A_3C_{60} (Werner *et al.*, 2017). These half-filled three-orbital systems exhibit a Mott transition and a nearby peculiar Jahn-Teller metal state with coexisting metallic and Mott-insulating orbitals (Zadik *et al.*, 2015); see Fig. 1. This state has been identified as a spontaneous orbital-selective Mott phase (Hoshino and Werner, 2017), where two orbitals are in a paired Mott state and the third one is metallic. There are therefore three equivalent ordered states with different metallic orbitals. Because of the orbital-dependent spatial anisotropy of the hopping, one can selectively modify the hoppings for the three orbitals through dynamical localization with a suitable choice of the polarization of an applied laser field; see Sec. V.B. This enables the controlled switching between the three order realizations on electronic timescales.

Similarly, conventional orbital order due to the Kugel-Khomskii orbital exchange mechanisms has discrete domains, and laser control of the orbital exchange (see Sec. V.D) along selected crystallographic directions can be used to rotate the order parameter (Grandi and Eckstein, 2021). In such switching protocols, relevant forces can also arise as a result of anharmonic interactions and a transient modification of the order parameter fluctuations.

E. Hidden phases

In this section, we discuss examples of hidden states in Mott insulators, with a focus on those supported by the presence of long-lived charge carriers. There are various pathways to possible hidden phases that involve the melting of orders, prethermal dynamics, or the activation of new degrees of freedom and new types of correlations.

1. Magnetic and orbital order

Strongly correlated multiorbital systems with spin and orbital degrees of freedom display competition or coexistence between magnetic and orbital orders, which provides a rich playground for the study of hidden phases. Photogenerated charge carriers can trigger transitions in these systems through the partial melting of spin and orbital orders. Relevant examples include the metal-insulator transition (Miyano *et al.*, 1997; Esposito *et al.*, 2017) and transient hidden orders in manganites (Ichikawa *et al.*, 2011). Beaud *et al.* (2014) identified the energy density as the main nonequilibrium order parameter for a transition in a manganite. In combination with strain in thin films, even a single optical pulse can initiate a transition to a long-lived metastable hidden metallic phase (Zhang *et al.*, 2016; Teitelbaum *et al.*, 2019).

Because the excitation of orbital order is often strongly coupled to the lattice dynamics (Wall *et al.*, 2009), a microscopic theory of these photoinduced transitions is challenging. However, if the initial step of the switching toward a hidden state involves the perturbation of orbital orders by the photodoped carriers, typically on the femtosecond timescale (Singla *et al.*, 2013), relevant aspects of the switching can be captured by simple models. For example, a transient hidden state with intertwined spin and orbital orders can be realized in the three-quarter-filled two-band Hubbard model on a cubic lattice (Li *et al.*, 2018).

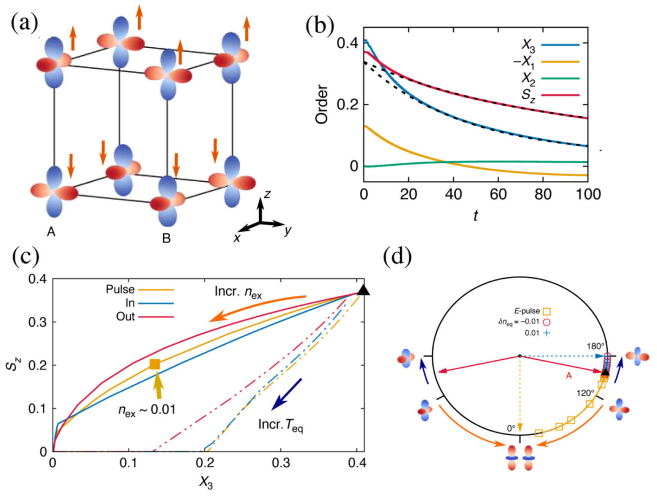

FIG. 40. (a) Spin and orbital order of a two-orbital Hubbard model with three electrons per site in equilibrium. The unoccupied orbital is shown, as is the total electron-spin moment (arrows). (b) DMFT evolution of spin and orbital order after an electric-field pulse that creates a photodoping $n_{ex} = 0.015$. (c) Order parameter in the S_z-X_3 plane for the prethermal photodoped state at different n_{ex} (solid lines), in equilibrium with increasing temperature at integer filling (dotted yellow line), and for chemically doped systems with $\delta n = \pm 0.01$ (dotted red and blue lines). (d) Normalized orbital-order components X_1 and X_3 in the trapped state shown on the pseudospin compass. From Li *et al.*, 2018.

The two orbitals could represent partially filled e_g orbitals ($d_{y^2-z^2}$ and $d_{3x^2-r^2}$), as in $KCuF_3$ (Pavarini *et al.*, 2004). The low-temperature equilibrium state features *A*-type AFM spin order (antiferromagnetically aligned ferromagnetic planes) and *G*-type antiferro-orbital order (alternating orbital occupations in all directions); see Fig. 40(a). The order is characterized by the ordered magnetic moment S_z and the orbital pseudospin-1/2 moment $\mathbf{X} = (X_1, X_2, X_3)$ in the basis $(d_{y^2-z^2}, d_{3x^2-r^2})$. The excitation of the system by an electric-field pulse induces a partial melting of the spin and orbital order; see Fig. 40(b). The prethermal trapped photodoped state is obtained by extrapolating the curves to long times. Figure 40(c) locates the corresponding order in the (X_3, S_z) plane for different photodoping densities n_{ex} and various excitation protocols (solid lines) and compares it to the equilibrium behavior for different temperatures (dashed lines). Upon photodoping one can realize a state with dominant magnetic order, while in equilibrium, with increasing temperature, the magnetic order melts before the orbital order. In addition, the change in the direction of the orbital pseudospin is opposite in equilibrium and in the photodoped case; see Fig. 40(d). Hence, the photodoped state realizes a nonthermal hidden order. This can be understood by considering how the photodoping melts the two orders. The efficient melting of *G*-type orbital order originates from the motion of the injected charge carriers, which leave behind strings of defects in the ordered background (analogous to the case of *G*-type AFM order in Sec. VI.D.3). The magnetic order, in contrast, is ferromagnetic in the planes and therefore perturbed only by the out-of-plane motion of the carriers. This difference in the effect

of the charge motion explains the faster melting of the orbital order, in spite of the fact that this is the more robust order in equilibrium.

A related theoretical proposal for a hidden state realized through the partial melting of orders in multiband systems has been made for the half-filled three-band Hubbard model with negative Hund coupling (Werner and Murakami, 2021), which describes the alkali-doped fullerides A_3C_{60} (Fabrizio and Tosatti, 1997; Capone *et al.*, 2009). At low temperatures the strongly correlated system shows an AFM spin order and a composite ferro-type orbital order (Hoshino and Werner, 2017). As in the previous example, photoexcitation of electrons across the gap rapidly melts the AFM order, while the ferro-type order is only moderately perturbed. This allows a pure composite orbital order (that does not occur in equilibrium upon increasing temperature) to be realized. After an initial relaxation, the composite order is favored by the presence of photodoped doublons or holons, similar to the stabilization of ferromagnetic order by itinerant carriers in the double-exchange model (Zener, 1951; de Gennes, 1960); see also Sec. VII.E.2. Similarly, the emergence of ferromagnetism upon photodoping of a half-filled two-orbital Mott insulator with orbital-dependent bandwidths was discussed by Ray and Werner (2024).

2. Hidden phases near a spin state transition

Another interesting playground for hidden states exists near spin state transitions, which arise from the competition between crystal field splitting and Hund coupling. The dynamics of the photoinduced high-spin (HS) to low-spin (LS) transitions has been experimentally studied in molecular spin crossover compounds (Bertoni *et al.*, 2015) and spin crossover complexes (Ogawa *et al.*, 2000; Tayagaki and Tanaka, 2001; Ohkoshi *et al.*, 2011). Related physics in Mott systems can be described by the two-band Hubbard model with Hund coupling [see Eq. (9)] and crystal field splitting $H_{\mathrm{cf}} = \Delta_{\mathrm{cf}}(n_1 - n_2)$ (Werner and Millis, 2007b). For $\Delta_{\mathrm{cf}} \gtrsim \sqrt{2}J_{\mathrm{H}}$ the system favors the LS doublon configuration, while for $\Delta \lesssim \sqrt{2}J_{\mathrm{H}}$ the HS doublon configuration is dominant; see Fig. 41(a) for a representation of the local states.

Photoinduced high-spin states. The photodoped two-orbital Hubbard model with orbital-dependent hopping features a hidden phase stabilized by a nonthermal population of local multiplets. Using ED, Kanamori, Matsueda, and Ishihara (2011) studied the nonequilibrium phase diagram of the half-filled Mott system by fixing the photodoping density (the number of singlons and triplons) in a generalized strong-coupling model, as discussed in Sec. III.D. They found that the LS-HS coexistence region expands in the photodoped case; compare the green and dashed black lines in Fig. 41(b). The additional stabilization of the HS doublon state can be understood within a double-exchange mechanism, which can give rise to a bound state between a singlon and a HS state; see the bottom part of Fig. 41(c). The singlon-HS bound state induces a new absorption peak at $\omega \simeq 2v_1$, which corresponds to the excitation of the electron in orbital 1 from a bonding to an antibonding state. These results explain the experimental observations from femtosecond pump-probe spectroscopy on a series of cobaltites $R\mathrm{BaCo_2O_{6-\delta}}$ (R = Sm, Gd, and Tb)

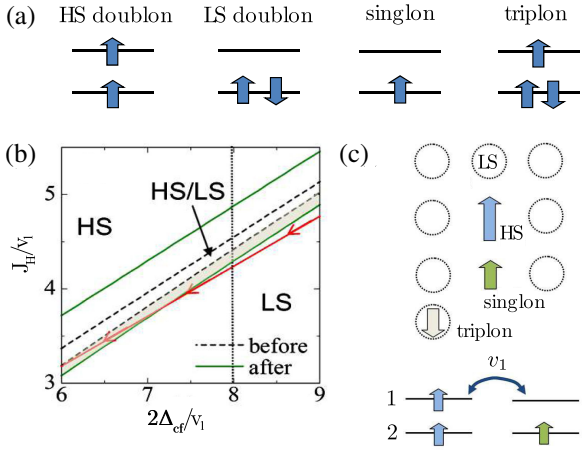

FIG. 41. Two-orbital model with crystal field splitting Δ_{cf}, Hund coupling J_{H}, and nearest-neighbor orbital-dependent hopping v_1 and v_2 ($v_1 > v_2$). (a) Sketch of the HS doublon, LS doublon, singlon, and triplon configurations. (b) Phase diagrams before and after photodoping, obtained using ED, showing the boundaries of the HS-LS coexistence region in equilibrium (dashed lines) and in the photodoped state with one additional singlon-triplon pair (bold green lines). (c) Illustration of the singlon-HS bound state and the double-exchange mechanism that stabilizes this state. Adapted from Kanamori, Matsueda, and Ishihara, 2011.

(Okimoto *et al.*, 2011), which show distinct in-gap spectra in the photodoped state and the high-temperature equilibrium state, as well as an increase of the in-gap spectral weight with increasing ionic radius of R.

Transient excitonic order. The initial dynamics after an excitation can sometimes be qualitatively described by the mean-field dynamics. Mean-field theory has many conserved quantities, which results in prethermal (trapped) orders, and phenomena related to this trapping can survive in more accurate treatments. Near a spin state transition, one finds an interesting example of a hidden phase associated with such a trapping. In the two-orbital Hubbard model [Eq. (9)] with orbital-independent hopping, the system near the HS-LS transition is susceptible to excitonic (spin-orbital) order (Kuneš, 2015); see the DMFT + NCA phase diagram in Fig. 42(a). The spin-triplet excitonic order parameters can be defined as $\phi^{\lambda} = \sum_{\sigma\sigma'} \sigma^{\lambda}_{\sigma\sigma'} \langle c^{\dagger}_{1\sigma} c_{2\sigma'} \rangle$, where σ^{λ} denotes the Pauli matrix for $\lambda = X, Y, Z$. (The Y component is selected for the forthcoming realization of the order.) Werner and Murakami (2020) studied the dynamics after a quench of the crystal field Δ_{cf}, starting with a normal metallic state in the low-spin regime above the highest excitonic transition temperature. In an adiabatic ramp of Δ_{cf}, the system would follow the isentropic line [the dashed gray line in Fig. 42(a)]. Along this line the formation of disordered HS moments leads to entropy reshuffling from the electronic to the spin sector, and the electronic temperature can drop below the excitonic transition temperature. The expected thermalized temperature after a sudden quench of Δ_{cf} is higher than it is after an adiabatic ramp (see the filled dots in Fig. 42), but it can still drop below the transition temperature. The dynamics after such quenches shows a dynamical phase transition, as seen in the trace of the

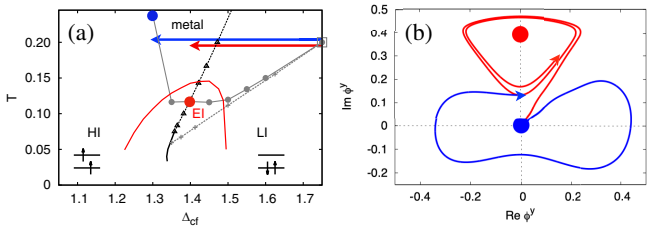

FIG. 42. (a) Phase diagram of the half-filled two-orbital Hubbard model with solid (dashed) black lines indicating the high-spin (HI) insulator to low-spin (LI) insulator transition (crossover). The boundary of the excitonic insulator (EI) phase is shown by the red line. The dashed gray line marks the isentropic line and the solid gray line indicates with dots the thermalized results after quenches starting with the open square. (b) Order parameter trajectories after crystal field quenches from $\Delta_{cf} = 1.75$ and $T = 0.2$ to $\Delta_{cf} = 1.4$ (red line) and $\Delta_{cf} = 1.3$ (blue line). The red and blue dots indicate the corresponding thermalized states. $U = 6$, $J_H = 1$, $W = 4$, and a small seed field is applied in the imaginary ϕ^Y direction. From Werner and Murakami, 2020.

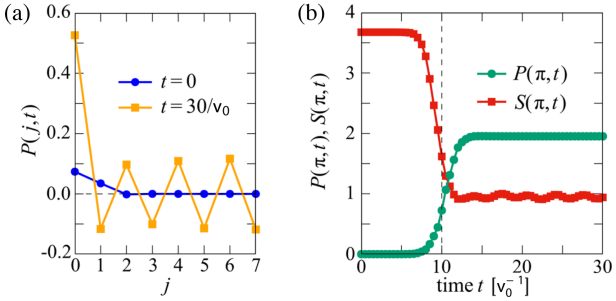

FIG. 43. (a) Real-space profile of the pair correlations $P(j,t)$ before ($t = 0$) and after ($t = 30/v_0$) an electric-field excitation. (b) Time evolution of the pair and spin correlations at $q = \pi$. These ED results are for a Hubbard chain with $N = 14$ sites and $U = 8v_0$. From Kaneko *et al.*, 2019.

order parameter ϕ^Y in Fig. 42(b). For quenches to the ordered regime ($\Delta_{cf} \geq 1.35$), the order parameter oscillates counterclockwise around the expected equilibrium value indicated by the colored dot. For quenches to $\Delta_{cf} \leq 1.3$, where the thermalized state is disordered, one observes the transient emergence of order with trajectories that rotate clockwise around zero. This is a distinctly nonthermal type of symmetry breaking. The existence of the two qualitatively different dynamical regimes can be reproduced by a strong-coupling mean-field theory whose dynamics is restricted by the conservation of the local entropy. The model thus exhibits a dynamical phase transition (Marino *et al.*, 2022) between a thermal-like and nonthermal symmetry breaking.

3. Superconductivity and η-pairing states

While the enhancement of the superconducting gap by microwave radiation (the Eliashberg effect) was predicted long ago (Eliashberg, 1970) and experimentally confirmed even in cuprates (Vedeneev, Maude, and Byrne, 2008), recent research on nonequilibrium superconducting orders has been strongly motivated by experimental works reporting superconductinglike phases induced far above the equilibrium T_c by strong mid-IR or terahertz pulses (Fausti *et al.*, 2011; Hu *et al.*, 2014; Kaiser *et al.*, 2014b; Mitrano *et al.*, 2016; Buzzi *et al.*, 2020). On the theory side, significant efforts have been made in the exploration of nonequilibrium superconducting states. In the context of nonlinear phononics, various scenarios for the enhancement of pairing interactions have been discussed, for example, parametric phonon excitations (Knap *et al.*, 2016; Komnik and Thorwart, 2016; Babadi *et al.*, 2017; Murakami *et al.*, 2017), nonlinear electron-phonon couplings (Kennes *et al.*, 2017; Sentef, 2017), and excitations of phonons coupled to interband transitions (Chattopadhyay *et al.*, 2023; Eckhardt *et al.*, 2023). As in the Eliashberg effect, the possibility of an effective cooling of the system has been considered (Nava *et al.*, 2018; Grunwald, Passetti, and Kennes, 2023). In Mott insulators photodoping leads to a metallization of the system and naturally enhances the correlations for Cooper pairs of various types (Wang *et al.*, 2018; Werner *et al.*, 2018).

In the following, we review mechanisms that are unique to photodoped states and arise from activated correlations between photoexcited carriers. To begin, we consider the single-band Hubbard model on a bipartite lattice. By analyzing the time evolution of the 1D Hubbard model using ED, Kaneko *et al.* (2019) showed that electric-field excitations strongly enhance the η-pairing correlations. Specifically, they measured the pair-correlation function $P(j,t) = (1/N)\sum_i \langle\Psi(t)|(\hat{\Delta}^\dagger_{i+j}\hat{\Delta}_i + \text{H.c.})|\Psi(t)\rangle$ and the spin correlation function $S(j,t) = (1/N)\sum_i \langle\Psi(t)|\hat{m}^z_{i+j}\hat{m}^z_i|\Psi(t)\rangle$, where $\hat{\Delta}_i = \hat{c}_{i,\uparrow}\hat{c}_{i,\downarrow}$ and $\hat{m}^z_i = \hat{n}_{i,\uparrow} - \hat{n}_{i,\downarrow}$ and the corresponding Fourier transforms $P(q,t)$ and $S(q,t)$. After an electric-field excitation, the staggered component of the pair-correlation function $P(q = \pi, t)$ is strongly enhanced, while the spin correlations $S(q = \pi, t)$ are suppressed; see Fig. 43. The pump frequency dependence of the enhancement of the pair correlations matches the linear optical spectrum. The staggered nature of the photoinduced $P(j,t)$ indicates that the momentum of the corresponding pairs is peaked at π, in contrast to conventional s-wave condensation of zero-momentum pairs. The photoexcited state reported by Kaneko *et al.* (2019) and Kaneko, Yunoki, and Millis (2020) can therefore be associated with the η-pairing states originally introduced by Yang (1989) as exact eigenstates of the Hubbard model on a bipartite lattice. This model has a SU(2) symmetry with respect to the η spins [$\hat{\eta}^+ = \sum_i (-)^i c^\dagger_{i\downarrow} c^\dagger_{i\uparrow}$, $\hat{\eta}^- = \sum_i (-)^i c_{i\uparrow} c_{i\downarrow}$, and $\hat{\eta}^z = (1/2)\sum_i (n_i - 1)$]. Energy eigenstates can be expressed as simultaneous eigenstates $|\eta, \eta_z\rangle$ of $\hat{\eta}^2$ and $\hat{\eta}^z$, with a direct relation to the pair-correlation function, $P(q = \pi) = 2\langle\eta, \eta_z|\hat{\eta}^+\hat{\eta}^-|\eta, \eta_z\rangle = 2[\eta(\eta+1) - \eta^z(\eta^z - 1)]/N$. The equilibrium states are $|\eta, \eta_z = -\eta\rangle$ and exhibit no $P(q = \pi)$ correlations (Essler, Korepin, and Schoutens, 1992; Essler *et al.*, 2005). However, the electric field breaks the SU(2) symmetry and states $|\eta, \eta_z \neq -\eta\rangle$ are created during the excitation (Kaneko *et al.*, 2019). (This follows from the Wigner-Eckart theorem and the fact that the current operator is a rank-1 operator in terms of the $\hat{\eta}$ operators.) After the pulse, the evolution is again constrained by the SU(2) symmetry such that the enhancement of $P(q = \pi)$ due to the photogenerated admixture of $|\eta, \eta_z \neq -\eta\rangle$ states is long lived. While the results reported in Fig. 43 are for a finite chain, an enhancement of η pairing correlations was also reported in the thermodynamic limit and at nonzero temperatures

using iTEBD (Ejima *et al.*, 2020). A related enhancement of pairing was found in a steady-state nonequilibrium system realized via the selective excitation of spin degrees of freedom (Tindall *et al.*, 2019). Because of the η-SU(2) symmetry, the pairing correlations were enhanced despite strong heating. A similar phenomenon was also reported in the Kondo lattice model (Shirakawa, Miyakoshi, and Yunoki, 2020) as well as in the two-leg Hubbard model (Ueda, Kuroki, and Kaneko, 2024).

The emergence of the η-pairing phase was also predicted for quasisteady states of photodoped Mott insulators (large-gap Hubbard model). Motivated by cold-atom experiments, Rosch *et al.* (2008) studied the effective model obtained from the SW transformation for a system consisting of only doublons and holons, i.e., the SU(2) ferromagnetic Heisenberg model for η spins; see $\hat{H}_{\mathrm{dh,ex}}$ in Eq. (29). The ground state of this model corresponds to the η-pairing state characterized by staggered off-diagonal long-range order. This result raised the question of whether long-lived η pairings can also be realized away from this fully photodoped limit. For the photodoped Hubbard model, this has been numerically studied using nonequilibrium DMFT. Li, Golez, Werner, and Eckstein (2020) prepared and stabilized a quasisteady state with a given photodoping density by attaching electron baths (the NESS approach discussed in Sec. III.D). The η-pairing phase was found to be stable over a wide range of photodoping densities and up to inverse effective temperatures β_{eff} comparable to the Néel temperature in the undoped Mott phase; see Fig. 44(a). The same phase was also realized with the entropy-cooling protocol discussed in Sec. VI.D.4 (Werner, Li *et al.*, 2019). The imaginary part of the optical conductivity in the η-pairing phase has the $1/\omega$ behavior that is characteristic of superconducting states, and the behavior of the superfluid density is well explained within a strong-coupling model derived from the SW transformation. The real part of the conductivity generically features a Drude peak (instead of a gap) since the condensed doublons and holons coexist with normal singlons (Li, Golez, Werner, and Eckstein, 2020).

For 1D systems with on-site interaction U and nearest-neighbor interaction V, further physical insights into the photodoped states have been obtained in an analysis of the effective model in Eq. (29) based on the quasiequilibrium approach discussed in Sec. III.D (Murakami, Takayoshi *et al.*, 2022, 2023). For these systems the wave function of the metastable photodoped state at large U can be factorized as

$$|\Psi\rangle = |\Psi_{\mathrm{charge}}\rangle|\Psi_{\mathrm{spin}}\rangle|\Psi_{\eta\text{-spin}}\rangle. \tag{44}$$

In Eq. (44), $|\Psi_{\mathrm{charge}}\rangle$ represents the configuration of the singlons and is ruled by the free Hamiltonian of spinless fermions. $|\Psi_{\mathrm{spin}}\rangle$ represents the configuration of spins and is ruled by the isotropic Heisenberg model in the "squeezed spin space" where the doubly occupied or empty sites are eliminated. $|\Psi_{\eta\text{-spin}}\rangle$ represents the configuration of the doublons and holons and is ruled by the XXZ model of the η spins in the squeezed space where the singly occupied sites are eliminated. For example, for a state $|\Psi\rangle = |\uparrow, d, h, \downarrow, d\rangle$, we have $|\Psi_{\mathrm{charge}}\rangle = |1,0,0,1,0\rangle$, $|\Psi_{\mathrm{spin}}\rangle = |\uparrow,\downarrow\rangle$, and $|\Psi_{\eta\text{-spin}}\rangle = |d,h,d\rangle$. The wave function in Eq. (44) is a natural extension

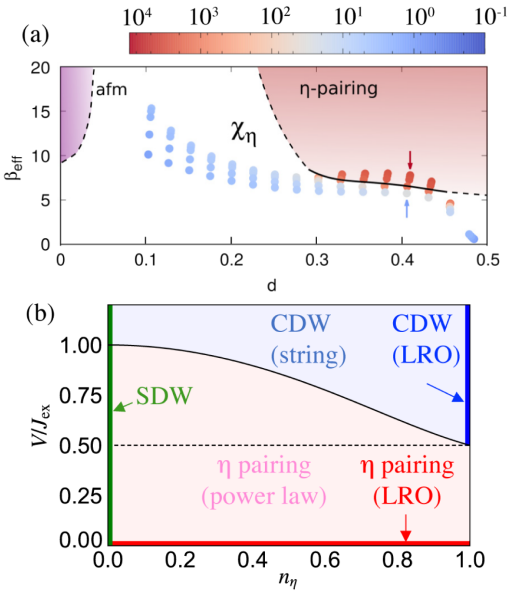

FIG. 44. (a) Nonequilibrium phase diagram of the photodoped steady state of a Mott insulator with doublon density d and effective inverse temperature β_{eff}, obtained using the steady-state DMFT formalism (infinitely coordinated Bethe lattice; $W = 4$ and $U = 8$). The data points show the η-pairing susceptibility χ_η, while the phase boundary is a guide for the eye (defined by $\chi_\eta \simeq 10^3$). (b) Ground state ($T_{\mathrm{eff}} = 0$) phase diagram of the photodoped 1D Mott insulator described by Eq. (29) in the limit $J_{\mathrm{ex}} \to 0$ (keeping V/J_{ex} constant) at half filling for D-H density n_η and nearest-neighbor interaction V. From Li, Golez, Werner, and Eckstein, 2020, and Murakami, Takayoshi *et al.*, 2023.

of the Ogata-Shiba state for the doped Hubbard model in equilibrium (Ogata and Shiba, 1990) and indicates the presence of spin, charge, and η-spin separation in the 1D metastable state (Woynarovich, 1982). In particular, the XXZ model of the η spins in the squeezed space is described as $\hat{H}^{(SQ)}_{\eta\text{-spin}} = -J^\eta_X \sum_j (\hat{\eta}^x_{j+1}\hat{\eta}^x_j + \hat{\eta}^y_{j+1}\hat{\eta}^y_j) + J^\eta_Z \sum_j \hat{\eta}^z_{j+1}\hat{\eta}^z_j$, where J^η_X and J^η_Z are functions of the density of the η spins, V, and J_{ex}. The XXZ model explains the origin and nature of the photodoped metastable states. The gapless state of the XXZ model for $J^\eta_X > |J^\eta_Z|$ corresponds to the η-pairing phase, while the gapful state of the XXZ model for $J^\eta_X < J^\eta_Z$ corresponds to the CDW phase; see Fig. 44(b). The photoinduced CDW phase exhibits a hidden long-range order (LRO) in the squeezed space (string order) that is similar to the Haldane phase of the spin chain.

The development of pairing correlations associated with η spins has also been studied for geometrically frustrated systems and multiorbital systems. In an analysis of a Hubbard model on a chain with tunable frustration, the time evolution of the system has been simulated using an MPS (Tindall *et al.*, 2020). While the presence of frustration removes the η-SU(2) symmetry, a transient enhancement of η-pairing correlations has nevertheless been observed for frustrations below a critical value. Li *et al.* (2023) studied photodoped Mott insulators on triangular, kagome, and similar three-colorable lattices using nonequilibrium DMFT and ED simulations. They found metastable superconducting

phases with a 120° phase twist between the different sublattices. These are chiral superconducting states that are stabilized by the frustrated η-spin correlations. Because of the phase twist, there are persistent loop currents in the symmetry-broken phase that lead to a peculiar transverse supercurrent response to external fields applied in certain directions. In a two-orbital system, the existence of η-pairing-type phases of the spin or orbital triplet type (depending on the sign of J_H) has been demonstrated in the strongly photodoped regime (Ray, Murakami, and Werner, 2023). In the presence of orbital-dependent bandwiths, a variety of nonthermal superconducting states (η-type spin-triplet and spin-singlet pairings, coexistence of ferromagnetism with a η spin-singlet pairing) can be realized (Ray and Werner, 2024).

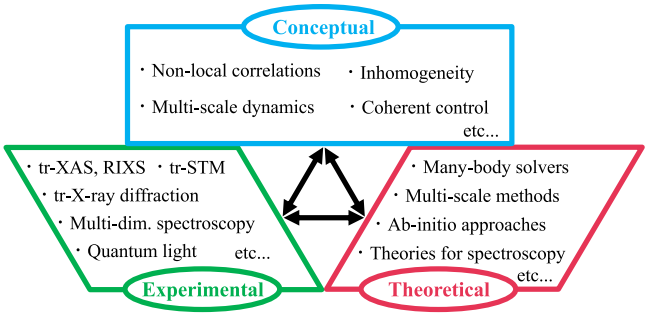

FIG. 45. Conceptual challenges in the field of nonequilibrium control of strongly correlated lattice systems and experimental or theoretical developments that will help to address these challenges.

VIII. OUTLOOK

The intricate nature of strongly correlated systems, in particular, states near a Mott phase, results in notable physical phenomena whose underlying mechanisms are often not yet fully understood. Driving such systems out of equilibrium can provide new perspectives on correlation phenomena and reveal effects or properties that are not accessible in equilibrium. This review discussed the responses of Mott insulators to various driving protocols, including ac and dc fields and photodoping excitations, and the resulting transient or long-lived nonthermal phases. The significant recent progress in the development of experimental and theoretical tools has created a situation where the cross-fertilization between theory and experiment is driving further progress in this field. As experimental techniques evolve and more subtle effects are revealed, the comparison to reliable theoretical calculations becomes essential for understanding microscopic mechanisms. At the same time, model studies and theoretical insights into nonlinear responses or nonthermal phases can suggest further experiments with refined control over the relevant microscopic degrees of freedom.

An ultimate goal in the field is the on-demand nonequilibrium control of material properties, meaning controlled access to or dynamic stabilization of nonthermal states with specific characteristics. Achieving this requires a comprehensive understanding of the multiscale physics in space and time that governs the nonequilibrium dynamics of the active degrees of freedom, along with a robust classification framework for the various types of nonthermal states. In the following we summarize conceptual questions related to these challenges, as illustrated in Fig. 45, discuss relevant experimental techniques, and provide perspectives on theoretical developments that will help to address these challenges.

A. Conceptual questions

Local and nonlocal correlations. Spatial correlations can be classified into local and nonlocal correlations. The latter are essential for describing complex orders like *d*-wave superconductivity or the dynamics of collective excitations such as plasmons and magnons. Most theories used for the study of Mott systems, in particular, (cluster) DMFT, however, treat only local or short-range correlations and fluctuations (Georges *et al.*, 1996; Maier *et al.*, 2005), which are expected to primarily influence the short-time dynamics (Aoki *et al.*, 2014). Apart from dynamical screening (Golež *et al.*, 2017), the effects of long-range nonlocal correlations on the nonequilibrium dynamics remain largely unexplored. To predict the long-term evolution of a correlated system, it is crucial to account for the effects of long-range spin, charge, and orbital fluctuations and to consider their mutual feedback. Nonlocal correlations also influence the dynamics of order parameters since spatial fluctuations can modify the potential landscape for nonthermal states (Grandi *et al.*, 2024).

Inhomogeneity. A potentially significant aspect of ultrafast photoinduced dynamics that has received relatively little attention is the role of inhomogeneities and disorder; see Sec. VII.B.3. The sources of inhomogeneity can be categorized as follows: (i) microscopic defects inherent to a given sample; (ii) extrinsic factors from the experimental setup, such as the laser spot size and the penetration depth; and (iii) intrinsic inhomogeneity that spontaneously emerges in a homogeneous sample owing to thermal or quantum fluctuations. Microscopic defects presumably play a role in phenomena such as filament formation (Guiot *et al.*, 2013) and explain the discrepancy between predicted and measured threshold fields for dielectric breakdown. Intrinsic inhomogeneity can manifest itself on a variety of scales, ranging from atomic-scale disorder (Wall *et al.*, 2018; Johnson *et al.*, 2022) to domain growth and coarsening during photoinduced phase transitions. Key questions include how and on what timescale inhomogeneities develop or disappear and which microscopic properties govern these characteristic timescales.

Strong disorder can lead to nonergodic behavior over long timescales driven by different physical mechanisms. For example, many-body localization in one-dimensional systems with strong disorder and correlations (Abanin *et al.*, 2019; Sierant *et al.*, 2025) can result in long-lived nonthermal states. Dynamically generated disorder in an otherwise clean correlated system can also have strong effects and can potentially result in a glass phase (Picano, Grandi, and Eckstein, 2023; Rammal *et al.*, 2024); see Sec. VII.B.3. Understanding the role of these intrinsically or dynamically emergent disorders in long-lived nonthermal phases of solids remains an open challenge requiring further theoretical and experimental studies, for example, investigations involving x-ray scattering and nanoscale imaging techniques.

Multiscale dynamics. The nonequilibrium evolution of correlated materials involves physical processes spanning different spatial and temporal (or energy) scales, each associated with specific active degrees of freedom. A typical scenario is a laser-excited system where the initial coherent dynamics is followed by incoherent scattering or relaxation processes (Yonemitsu and Nasu, 2008; Aoki *et al.*, 2014). The subsequent evolution of low-energy modes, which affect electronic states in a quasistatic manner, governs the long-term dynamics. In addition, the emergence of spatial inhomogeneities introduces new timescales that further influence the long-term behavior.

To achieve a comprehensive description of the nonequilibrium dynamics of correlated systems, it is crucial to bridge the physics across different scales and understand the crossovers between various stages of the dynamics. This goal requires systematic experimental analyses combined with theoretical advancements. In particular, it is important to clarify the range of applicability of specific approximate approaches tailored to certain scales, such as generalized quantum kinetic equations and time-dependent Ginzburg-Landau theory, and to develop methods for connecting these different approaches.

Coherent and incoherent dynamics. Photoinduced phase transitions (PIPTs) can be broadly categorized into coherent and incoherent mechanisms with respect to the "slow" degrees of freedom (Yonemitsu and Nasu, 2008; Koshihara *et al.*, 2022). The primary distinction between the two lies in whether the "fast" degrees of freedom lead to slow or rapid damping on the characteristic timescales for the dynamics of the slow modes. A process can also be incoherent with respect to the fast degrees of freedom but can initiate partially coherent dynamics of slow variables, such as lattice distortions or various order parameters. For example, in the case of an incoherent electronic excitation, the excess energy injected into the electronic system can suddenly deform the free-energy landscape associated with the slow degrees of freedom. Subsequent relaxation and dissipation processes may then lead to the formation of hidden states. To comprehensively understand and control incoherent PIPTs, it is crucial to clarify the relationship between microscopic descriptions and the free-energy surfaces considered in phenomenological models. Fully coherent mechanisms aim to realize a PIPT by preserving and utilizing the system's coherence without injecting excessive energy. This approach has gained significant attention with the development of strong lasers with tunable frequencies. Compared to incoherent mechanisms, coherent mechanisms offer the potential for faster, more energy-efficient, and highly controlled pathways for PIPTs. Notable examples discussed in this review include Floquet engineering using off-resonant excitations and nonlinear phononics. A key challenge is to establish photoexcitation protocols that enable on-demand coherent control. In addition to phonons, correlated materials and ordered phases exhibit unique many-body excitations such as magnons and Higgs modes. Strong excitations of such many-body modes may provide a fruitful avenue for coherent control (Yoshikawa *et al.*, 2021; Gassner, Weber, and Claassen, 2024).

B. Experimental techniques

To address the aforementioned conceptual questions, it is essential to employ a variety of experimental techniques to gather multifaceted information and to explore new pathways for nonequilibrium control. Currently, we are witnessing an era of rapid advancements in spectroscopic and device technologies (Giannetti *et al.*, 2016; de la Torre *et al.*, 2021).

Expanding time-resolved spectroscopies. Recently, various spectroscopic techniques that have been developed for equilibrium studies have been used as a probe in pump-probe experiments, and their resolutions are rapidly improving. Prominent examples include x-ray spectroscopy (Mitrano *et al.*, 2024), time-of-flight-based photoelectron spectroscopy (Maklar *et al.*, 2020; Boschini, Zonno, and Damascelli, 2024), near-field optical spectroscopy, scanning tunneling spectroscopy, and time-resolved electron microscopy. The construction of x-ray free-electron laser facilities around the world has significantly advanced time-resolved x-ray spectroscopy techniques such as XAS and RIXS, enabling the observation of the dynamics of local charge excitations, collective modes, nonlocal correlations, and fluctuations. The wealth of spectroscopic information obtained by combining various techniques provides an increasingly precise picture of the nonequilibrium evolution.

Nonlinear optical spectroscopies. Optical spectroscopy has been the most fundamental probe for studying systems both in and out of equilibrium. Beyond the basic linear response, nonlinear optical responses can provide deeper insights into a system, thereby revealing properties such as topology and many-body correlations. Notable examples include nth order responses, multidimensional spectroscopy, high-harmonic generation, and optical rectification. For instance, third-harmonic generation can be used to detect the Higgs mode in superconductors (Shimano and Tsuji, 2020). Multidimensional spectroscopy (Hamm and Zanni, 2011) employs multiple probe pulses to uncover cross-correlations between different excitations, to measure the coherence times of excited states, or to distinguish extrinsic disorder from intrinsic lifetime effects (Liu *et al.*, 2024). High-harmonic generation offers a unique window into ultrafast charge dynamics, elementary excitations, and many-body interactions, thus enabling the exploration of the interplay between strong-field effects and electronic correlations in solids (Ghimire and Reis, 2019; Heide *et al.*, 2024). In general, however, nonlinear responses involve various processes, which complicates the interpretation of the signals and makes the comparison with theoretical models essential for insightful analyses. In addition, it is crucial to develop a deeper understanding of how nonlinear optical responses can serve as probes for nonequilibrium states.

On-chip devices and cavities. The development of on-chip transport measurements and terahertz spectroscopy has introduced powerful tools capable of generating strong pulses that can act as both manipulators and probes of low-energy collective excitations (Auston, 1975; McIver *et al.*, 2020). In addition, cavity-based setups offer a promising route for controlling material properties through enhanced light-matter interactions. Experimental platforms such as microcavities, split-ring resonators, and plasmonic cavities are increasingly

being utilized. An interesting route is the integration of spatially confined terahertz waveguide modes in on-chip devices (Kipp *et al.*, 2024). Several theoretical proposals for manipulating Mott insulators with quantum light have been developed (Schlawin, Kennes, and Sentef, 2022), but there have been few experiments to date (Jarc *et al.*, 2023). The quantum nature of light can also enrich the nonequilibrium physics in correlated materials. Specifically, nonclassical strong light, such as bright squeezed light, can serve as a unique source for triggering nonequilibrium phenomena (Even Tzur *et al.*, 2023). Moreover, leveraging the quantum properties of emitted light in spectroscopy could enable the probing of topological and many-body properties that are not accessible via classical light (Grunwald *et al.*, 2024; Nambiar, Grankin, and Hafezi, 2024).

C. Theoretical and methodological developments

To tackle the aforementioned conceptual questions and aid in the interpretation of experimental results, further theoretical developments are necessary. We briefly outline potentially relevant directions.

Many-body solvers. For reliable and realistic descriptions of nonequilibrium correlated systems, we need to develop more accurate and efficient many-body solvers. In the coming years, we can expect to see progress in various directions. In the context of Green's function methods, it is important to develop (i) new approximate schemes, (ii) numerically exact solvers, and (iii) efficient propagation schemes.

As for (i), naively speaking, the accuracy and applicability of a certain Green's function technique is determined by the diagrams that are taken into account. For example, DMFT takes into account local self-energy diagrams and thus captures only the local correlations. It is important to develop novel approximate schemes that also provide an economical description of the essential nonlocal physics. For strongly correlated systems, DMFT is a suitable starting point for systematically including nonlocal correlations. A prominent example discussed in this review is $GW + \mathrm{EDMFT}$, which captures the screening from nonlocal correlations. Similarly, nonequilibrium DMFT can be combined with the fluctuation-exchange (FLEX) approximation (Bickers and Scalapino, 1989) or the two-particle self-consistent approach (Vilk and Tremblay, 1997) to build in effects of nonlocal spin and charge correlations. However, such schemes are currently limited to "one-shot" combinations (Geng, Yan, and Werner, 2025). An alternative route is to switch from a local self-energy to a local three- or four-point vertex function, as is done in diagrammatic techniques like the triply irreducible local expansion (TRILEX), DΓA, and the dual fermion-boson approach (Rohringer *et al.*, 2018). Self-energy and polarization diagrams built with these local vertex functions capture different types of long-range correlations. These methods have yet to be implemented for nonequilibrium problems and require both accurate DMFT solvers and memory efficient representations of the three- and four-point functions.

As for (ii), various highly accurate impurity solvers have recently emerged, including the inchworm Monte Carlo formalism (Cohen *et al.*, 2015), solvers based on tensor cross interpolation (TCI) (Núñez Fernández *et al.*, 2022), and influence functional-based tensor-train techniques (Thoenniss, Lerose, and Abanin, 2023). These solvers can be employed within the context of DMFT, but applying them to real-world problems beyond the reach of perturbative approaches and extending them to multiband systems and dynamically screened interactions remains an important challenge.

As for (iii), several time propagation schemes with significantly reduced computational cost have recently been proposed based on memory truncation (Schüler, Eckstein, and Werner, 2018; Stahl *et al.*, 2022), memory compression (Kaye and Golež, 2021), and approximate quantum kinetic equations (Lipavský, Špička, and Velický, 1986; Schlünzen, Joost, and Bonitz, 2020). Furthermore, in realistic setups one often must deal with correlation functions with multidimensional indices, including time, space, spins, and orbitals. Applying modern tensor-based compression techniques such as quantics tensor trains (Shinaoka *et al.*, 2023) and TCI in this context will enable new and more efficient implementations. These techniques should make it possible to realize long-time simulations that capture nonlocal correlations.

Besides Green's function methods, promising variational many-body solvers based on tensor-networks (Schollwöck, 2011) and neural networks (Carleo and Troyer, 2017) have been developed. Although these methods can properly take into account nonlocal dynamics in principle, further progress is needed to simulate long time dynamics in large systems. This may require the exploration of new network architectures adapted to the aforementioned multiscale dynamics.

Ab initio simulations. In equilibrium, material-specific simulations of strongly correlated systems have been achieved by combining downfolding schemes with appropriate many-body solvers (Kotliar *et al.*, 2006; Nilsson *et al.*, 2017). Here the low-energy effective model is derived through an *ab initio* framework using an appropriate multitier downfolding procedure, and the model is solved with many-body approaches such as DMFT, $GW + \mathrm{EDMFT}$, or variational QMC. This is a hierarchical description in orbital space where higher-lying orbitals are treated within a simpler and numerically more efficient approximation.

In principle, the same procedure can be applied to study material-specific nonequilibrium dynamics. In this review, we discussed the nonequilibrium extension of $GW + \mathrm{EDMFT}$ for the d-p model of cuprates (Golež, Eckstein, and Werner, 2019), which represents a first step in the direction of material-specific nonequilibrium simulations. However, at the current stage, we still lack powerful and versatile many-body solvers that can handle the complexity of realistic models. Another challenge is that the downfolding results in interaction parameters with very high energy scales (Aryasetiawan *et al.*, 2004). This is difficult to treat unless the simulation can resolve attosecond dynamics. To avoid this complication, a truncation in energy space or some sort of "freezing" of high-energy scales may be needed.

An alternative route is to employ the framework of TDDFT. To describe the time evolution of strongly correlated systems, new functionals that can capture strong correlation effects and relaxation or thermalization are necessary. First steps in this direction are the ACBN0 functional (Agapito, Curtarolo, and Buongiorno Nardelli, 2015), which provides a $(\mathrm{DFT} + U)$-like description, and attempts to derive functionals for Mott

systems from equilibrium DMFT solutions (Karlsson, Privitera, and Verdozzi, 2011; Boström *et al.*, 2019).

Multiscale methods. The diversity in temporal and spatial scales gives rise to complex dynamics in correlated materials. Several microscopic and phenomenological approaches enable investigations of the physics at some specific scale. To achieve unified and efficient descriptions of nonequilibrium dynamics, it is crucial to develop multiscale methods that combine techniques tailored for different scales. A particularly relevant situation is the separation of timescales. Notable examples include the slow dynamics of phonons or order parameters, which should be contrasted with the fast relaxation of photocarriers, or the potentially even slower recombination of doublons and holons in large-gap Mott systems. In such cases one can devise methods combining a quasisteady-state description of the fast degrees of freedom with quantum kinetic or semiclassical descriptions of the slowly evolving quantities (Lange, Lenarčič, and Rosch, 2018; Marini and Calandra, 2021).

A related question is how to connect the microscopic descriptions of nonequilibrium strongly correlated systems with the time-dependent Ginzburg-Landau (GL) theory for low-energy degrees of freedom (Hohenberg and Halperin, 1977). A key issue in this context is understanding how the free-energy landscape is modified by the nonequilibrium dynamics of the electrons. Since the GL theory is often used to interpret experimental results, a systematically extended framework incorporating proper microscopic information would enable a closer comparison between theory and experiment. Furthermore, establishing a clear connection between microscopic theory and GL theory would enable more reliable GL-based descriptions of spatial inhomogeneities and help identify the conditions under which a time-dependent "free-energy" landscape remains a valid concept.

Nonequilibrium spectroscopy. As pointed out, the interpretation of time-resolved spectra is often nontrivial, creating a need for theoretical support. For example, time-resolved XAS measurements of pump-excited Mott insulators reveal shifts in the absorption peaks (Baykusheva *et al.*, 2022; Lojewski *et al.*, 2024) that could originate from changes in the screening environment or from band shifts associated with the reshuffling of charge between the orbitals. Such shifts can also partially overlap with photoinduced features from nonthermally populated multiplets. Recently developed DMFT techniques based on an extended impurity model with a core level (Hariki, Uozumi, and Kuneš, 2017; Werner, Golez, and Eckstein, 2022) can provide useful information. Similar approaches (Eckstein and Werner, 2021) have been used to compute the local RIXS spectra of photoexcited Mott insulators (Werner, Johnston, and Eckstein, 2021). Exact diagonalization of small clusters provides some momentum resolution (Wang *et al.*, 2020). Extending such calculations from simplified model setups to realistic materials simulations, however, will require more work.

Besides observing the evolution of various spectroscopic features, it will also be important to consider what kind of quantum information can be extracted from experimental data. For example, from correlation functions one can evaluate the quantum Fisher information, which provides bounds on multipartite entanglement (Baykusheva *et al.*, 2023).

D. Concluding remarks

Strongly correlated systems provide an interesting platform for exploring exotic nonequilibrium phenomena arising from the intricate interplay of different degrees of freedom and the multiscale nature of these systems. However, their inherent complexity is both a blessing and a challenge. While it gives rise to a wealth of rich and interesting physics, it also poses significant difficulties for theoretical analyses and the interpretation of experiments. Indeed, a considerable gap remains between the complexity of real materials and the relative simplicity of numerically accessible models. We hope that the future advancements discussed in this outlook will help to narrow this gap, thereby enabling more precise predictions, a closer link between theory and experiment, the discovery of novel nonequilibrium phenomena, and ultimately a better control of nonthermal phases.

LIST OF SYMBOLS AND ABBREVIATIONS

Different components of the propagators are marked by superscripts, namely, R for the retarded component, $<$ for the lesser component, and M for the Matsubara component.

$\mathbf{A}$	vector potential
$A(\omega, \mathrm{t})$	time-dependent spectral function
$A(\omega)$	spectral function
$c_{i\sigma}$	annihilation operator at site i for spin σ
$\mathbf{d}_{ab}$	dipolar matrix element (a and b Wannier orbitals)
$\mathcal{D}$	double occupation
$D_{\mathbf{k}}(t, t')$	two-time bosonic propagator for momentum $\mathbf{k}$
$\mathbf{E}$	electric field
E_0	electric-field amplitude
g	electron-boson (phonon) interaction
$G_i(t, t')$	two-time Green's function for flavor i
H	Hamiltonian
$\hbar$	Planck constant$/2\pi$ (sometimes set to unity)
$\mathbf{J}$	current $-\delta H[\mathbf{A}]/\delta\mathbf{A}$
$\mathbf{j}$	microscopic current density $\mathbf{j} = \mathbf{J} + \partial_t\mathbf{P}$
J_{H}	Hund coupling
J_{ex}	superexchange interaction
$N(\omega, t)$	time-dependent occupation function
$\mathbf{P}$	polarization density
$P_{\mathbf{k}}(t, t')$	two-time polarization for momentum $\mathbf{k}$
q	electric charge
$\mathbf{S}$	vector of spin operators
S	entropy
$\mathcal{S}$	action
$\mathcal{T}_{\mathcal{C}}$	time-ordering operator on the contour $\mathcal{C}$
U	Hubbard interaction
$\mathcal{U}$	effective bare impurity interaction
v_{ij}	hopping integral between sites i and j
v_0	nearest-neighbor hopping integral

v_*	rescaled hopping integral on the hypercubic lattice
W	bandwidth
$W_{\mathbf{k}}(t,t')$	two-time retarded interaction for momentum $\mathbf{k}$
X (P)	lattice distortion (momentum)
$\Delta(t,t')$	two-time hybridization function
Δ_{cf}	crystal field splitting
$\epsilon_{\mathbf{k}}$	noninteracting dispersion
$\boldsymbol{\eta}$	vector of η operators
λ	effective electron-boson coupling
μ	chemical potential
$\sigma(t,t')$	two-time optical conductivity
$\Sigma_{\mathbf{k}}(t,t')$	two-time self-energy for momentum $\mathbf{k}$
$\chi(t,t')$	two-time charge susceptibility
ω_0	phonon frequency

ACKNOWLEDGMENTS

We thank H. Aoki, R. Arita, N. Bittner, L. Boehnke, J. Bonča, U. Bovensiepen, J. Chen, D. Choi, N. Dasari, T. Esslinger, N. Gedik, A. Georges, F. Grandi, K. Held, S. Hoshino, K. Inayoshi, S. Ishihara, M. Ivanov, S. Iwai, S. Johnson, T. Kaneko, J. Kaye, A. Kim, S. Kitamura, A. Koga, A. Läuchli, Z. Lenarčič, J. Li, M. Mierzejewski, D. Mihailović, A. Millis, M. Mitrano, C. Monney, M. Müller, C. Nicholson, T. Oka, H. Okamoto, O. Parcollet, F. Petocchi, A. Picano, P. Prelovšek, S. Ray, G. Refael, K. Sandholzer, M. Schüler, M. Sentef, H. Shinaoka, K. Shinjo, C. Stahl, U. Staub, H. Strand, K. Sugimoto, Z. Sun, S. Takayoshi, K. Tanaka, T. Tohyama, N. Tsuji, K. Uchida, L. Vidmar, W. Widdra, and K. Yonemitsu for stimulating discussions and collaborations on topics related to this review. D. G. acknowledges the hospitality of the College de France, and P. W. acknowledges the hospitality of the Aspen Center for Physics. Y. M. was supported by a Grant-in-Aid for Scientific Research from JSPS; KAKENHI Grants No. JP20K14412 No. JP21H05017, No. JP24H00191, and No. JP25K07235; and JST CREST Grant No. JPMJCR1901. D. G. acknowledges the support from Programs No. P1-0044 and No. J1-2455 of the Slovenian Research Agency (ARRS). P. W. was supported by ERC Consolidator Grant No. 724103 and by the Swiss National Science Foundation through Grant No. 200021-19696 and NCCR Marvel.

REFERENCES

Abanin, D., W. De Roeck, W. W. Ho, and F. Huveneers, 2017, Commun. Math. Phys. **354**, 809.
Abanin, D. A., E. Altman, I. Bloch, and M. Serbyn, 2019, Rev. Mod. Phys. **91**, 021001.
Abanin, D. A., W. De Roeck, and F. Huveneers, 2015, Phys. Rev. Lett. **115**, 256803.
Abreu, E., D. Meyers, V. K. Thorsmølle, J. Zhang, X. Liu, K. Geng, J. Chakhalian, and R. D. Averitt, 2020, Nano Lett. **20**, 7422.
Abreu, E., S. Wang, J. G. Ramírez, M. Liu, J. Zhang, K. Geng, I. K. Schuller, and R. D. Averitt, 2015, Phys. Rev. B **92**, 085130.
Aeschlimann, S., *et al.*, 2021, Nano Lett. **21**, 5028.
Agapito, L. A., S. Curtarolo, and M. Buongiorno Nardelli, 2015, Phys. Rev. X **5**, 011006.
Alcala, J., *et al.*, 2022, Proc. Natl. Acad. Sci. U.S.A. **119**, e2207766119.
Allen, P. B., 1987, Phys. Rev. Lett. **59**, 1460.
Amano, T., *et al.*, 2022, Phys. Rev. Res. **4**, L032032.
Ament, L. J. P., M. van Veenendaal, T. P. Devereaux, J. P. Hill, and J. van den Brink, 2011, Rev. Mod. Phys. **83**, 705.
Anisimov, V. I., F. Aryasetiawan, and A. I. Lichtenstein, 1997, J. Phys. Condens. Matter **9**, 767.
Aoki, H., N. Tsuji, M. Eckstein, M. Kollar, T. Oka, and P. Werner, 2014, Rev. Mod. Phys. **86**, 779.
Arakawa, N., and K. Yonemitsu, 2021, Phys. Rev. B **103**, L100408.
Aron, C., 2012, Phys. Rev. B **86**, 085127.
Aron, C., G. Kotliar, and C. Weber, 2012, Phys. Rev. Lett. **108**, 086401.
Arrigoni, E., M. Knap, and W. von der Linden, 2013, Phys. Rev. Lett. **110**, 086403.
Aryasetiawan, F., M. Imada, A. Georges, G. Kotliar, S. Biermann, and A. I. Lichtenstein, 2004, Phys. Rev. B **70**, 195104.
Assmann, E., P. Blaha, R. Laskowski, K. Held, S. Okamoto, and G. Sangiovanni, 2013, Phys. Rev. Lett. **110**, 078701.
Auston, D. H., 1975, Appl. Phys. Lett. **26**, 101.
Ayral, T., S. Biermann, and P. Werner, 2013, Phys. Rev. B **87**, 125149.
Babadi, M., M. Knap, I. Martin, G. Refael, and E. Demler, 2017, Phys. Rev. B **96**, 014512.
Backes, S., J.-H. Sim, and S. Biermann, 2022, Phys. Rev. B **105**, 245115.
Bakshi, S. S., and P. Majumdar, 2024, arXiv:2407.00558.
Banerjee, S., U. Kumar, and S.-Z. Lin, 2022, Phys. Rev. B **105**, L180414.
Bányai, L., Q. T. Vu, B. Mieck, and H. Haug, 1998, Phys. Rev. Lett. **81**, 882.
Barankov, R. A., and L. S. Levitov, 2006, Phys. Rev. Lett. **96**, 230403.
Basov, D. N., R. D. Averitt, and D. Hsieh, 2017, Nat. Mater. **16**, 1077.
Baykusheva, D. R., M. H. Kalthoff, D. Hofmann, M. Claassen, D. M. Kennes, M. A. Sentef, and M. Mitrano, 2023, Phys. Rev. Lett. **130**, 106902.
Baykusheva, D. R., *et al.*, 2022, Phys. Rev. X **12**, 011013.
Beaud, P., *et al.*, 2014, Nat. Mater. **13**, 923.
Beaulieu, S., *et al.*, 2021, Sci. Adv. **7**, eabd9275.
Behrmann, M., M. Fabrizio, and F. Lechermann, 2013, Phys. Rev. B **88**, 035116.
Berges, J., S. Borsányi, and C. Wetterich, 2004, Phys. Rev. Lett. **93**, 142002.
Berges, J., A. Rothkopf, and J. Schmidt, 2008, Phys. Rev. Lett. **101**, 041603.
Bernier, J.-S., C. Kollath, A. Georges, L. De Leo, F. Gerbier, C. Salomon, and M. Köhl, 2009, Phys. Rev. A **79**, 061601.
Berthier, L., and G. Biroli, 2011, Rev. Mod. Phys. **83**, 587.
Bertoni, R., M. Lorenc, A. Tissot, M.-L. Boillot, and E. Collet, 2015, Coord. Chem. Rev. **282–283**, 66.
Bhattacharya, P., 1997, *Semiconductor Optoelectronic Devices*, 2nd ed. (Prentice-Hall, Upper Saddle River, NJ).
Bhattacharyya, S., A. Das, and S. Dasgupta, 2012, Phys. Rev. B **86**, 054410.
Bickers, N., and D. Scalapino, 1989, Ann. Phys. (N.Y.) **193**, 206.

Biermann, S., F. Aryasetiawan, and A. Georges, 2003, Phys. Rev. Lett. **90**, 086402.

Bionta, M. R., *et al.*, 2021, Phys. Rev. Res. **3**, 023250.

Biroli, G., O. Parcollet, and G. Kotliar, 2004, Phys. Rev. B **69**, 205108.

Bittner, N., D. Golež, M. Eckstein, and P. Werner, 2020a, Phys. Rev. B **101**, 085127.

Bittner, N., D. Golež, M. Eckstein, and P. Werner, 2020b, Phys. Rev. B **102**, 235169.

Bittner, N., D. Golež, H. U. R. Strand, M. Eckstein, and P. Werner, 2018, Phys. Rev. B **97**, 235125.

Bloch, F., 1929, Z. Phys. **52**, 555.

Bloch, I., J. Dalibard, and W. Zwerger, 2008, Rev. Mod. Phys. **80**, 885.

Bloch, J., A. Cavalleri, V. Galitski, M. Hafezi, and A. Rubio, 2022, Nature (London) **606**, 41.

Boehnke, L., F. Nilsson, F. Aryasetiawan, and P. Werner, 2016, Phys. Rev. B **94**, 201106.

Bohrdt, A., D. Greif, E. Demler, M. Knap, and F. Grusdt, 2018, Phys. Rev. B **97**, 125117.

Bohrdt, A., F. Grusdt, and M. Knap, 2020, New J. Phys. **22**, 123023.

Bonča, J., M. Mierzejewski, and L. Vidmar, 2012, Phys. Rev. Lett. **109**, 156404.

Boschini, F., M. Zonno, and A. Damascelli, 2024, Rev. Mod. Phys. **96**, 015003.

Bostedt, C., S. Boutet, D. M. Fritz, Z. Huang, H. J. Lee, H. T. Lemke, A. Robert, W. F. Schlotter, J. J. Turner, and G. J. Williams, 2016, Rev. Mod. Phys. **88**, 015007.

Boström, E. V., P. Helmer, P. Werner, and C. Verdozzi, 2019, Phys. Rev. Res. **1**, 013017.

Boström, E. V., A. Sriram, M. Claassen, and A. Rubio, 2022, arXiv:2211.07247.

Bouchaud, J.-P., L. F. Cugliandolo, J. Kurchan, and M. Mézard, 1997, *Out of Equilibrium Dynamics in Spin-Glasses and Other Glassy Systems* (World Scientific, Singapore), pp. 161–223.

Boyd, R. W., 2008, *Nonlinear Optics*, 3rd ed. (Academic Press, New York).

Boykin, T. B., R. C. Bowen, and G. Klimeck, 2001, Phys. Rev. B **63**, 245314.

Brinkman, W. F., and T. M. Rice, 1970, Phys. Rev. B **2**, 4302.

Budden, M., *et al.*, 2021, Nat. Phys. **17**, 611.

Bukov, M., L. D'Alessio, and A. Polkovnikov, 2015, Adv. Phys. **64**, 139.

Bukov, M., M. Kolodrubetz, and A. Polkovnikov, 2016, Phys. Rev. Lett. **116**, 125301.

Bulla, R., T. A. Costi, and T. Pruschke, 2008, Rev. Mod. Phys. **80**, 395.

Bünemann, J., W. Weber, and F. Gebhard, 1998, Phys. Rev. B **57**, 6896.

Butler, C. J., M. Yoshida, T. Hanaguri, and Y. Iwasa, 2020, Nat. Commun. **11**, 2477.

Buzzi, M., *et al.*, 2020, Phys. Rev. X **10**, 031028.

Canovi, E., M. Kollar, and M. Eckstein, 2016, Phys. Rev. E **93**, 012130.

Capone, M., M. Fabrizio, C. Castellani, and E. Tosatti, 2009, Rev. Mod. Phys. **81**, 943.

Carleo, G., F. Becca, M. Schiró, and M. Fabrizio, 2012, Sci. Rep. **2**, 243.

Carleo, G., and M. Troyer, 2017, Science **355**, 602.

Cavalleri, A., 2018, Contemp. Phys. **59**, 31.

Cavalleri, A., C. Tóth, C. W. Siders, J. A. Squier, F. Ráksi, P. Forget, and J. C. Kieffer, 2001, Phys. Rev. Lett. **87**, 237401.

Chao, K. A., J. Spalek, and A. M. Oles, 1977, J. Phys. C **10**, L271.

Chattopadhyay, S., C. J. Eckhardt, D. M. Kennes, M. A. Sentef, D. Shin, A. Rubio, A. Cavalleri, E. A. Demler, and M. H. Michael, 2023, arXiv:2303.15355.

Chaudhary, S., D. Hsieh, and G. Refael, 2019, Phys. Rev. B **100**, 220403.

Chen, F., G. Cohen, and M. Galperin, 2019, Phys. Rev. Lett. **122**, 186803.

Chen, H.-T., G. Cohen, A. J. Millis, and D. R. Reichman, 2016, Phys. Rev. B **93**, 174309.

Chen, H.-T., G. Cohen, and D. R. Reichman, 2017a, J. Chem. Phys. **146**, 054105.

Chen, H.-T., G. Cohen, and D. R. Reichman, 2017b, J. Chem. Phys. **146**, 054106.

Chen, J., F. Petocchi, V. Christiansson, and P. Werner, 2024a, Phys. Rev. B **109**, L201101.

Chen, J., F. Petocchi, V. Christiansson, and P. Werner, 2024b, Phys. Rev. B **110**, 045117.

Chen, J., F. Petocchi, and P. Werner, 2022, Phys. Rev. B **105**, 085102.

Chen, R., and C. Guo, 2024, Phys. Rev. B **110**, 165114.

Chen, Y., Y. Wang, C. Jia, B. Moritz, A. M. Shvaika, J. K. Freericks, and T. P. Devereaux, 2019, Phys. Rev. B **99**, 104306.

Chiocchetta, A., D. Kiese, C. P. Zelle, F. Piazza, and S. Diehl, 2021, Nat. Commun. **12**, 5901.

Chiu, C. S., G. Ji, A. Mazurenko, D. Greif, and M. Greiner, 2018, Phys. Rev. Lett. **120**, 243201.

Choi, D., *et al.*, 2024, Proc. Natl. Acad. Sci. U.S.A. **121**, e2323013121.

Choi, S., P. Semon, B. Kang, A. Kutepov, and G. Kotliar, 2019, Comput. Phys. Commun. **244**, 277.

Chowdhury, D., A. Georges, O. Parcollet, and S. Sachdev, 2022, Rev. Mod. Phys. **94**, 035004.

Cilento, F., *et al.*, 2018, Sci. Adv. **4**, eaar1998.

Citro, R., E. G. Dalla Torre, L. D'Alessio, A. Polkovnikov, M. Babadi, T. Oka, and E. Demler, 2015, Ann. Phys. (Amsterdam) **360**, 694.

Claassen, M., H.-C. Jiang, B. Moritz, and T. P. Devereaux, 2017, Nat. Commun. **8**, 1192.

Cohen, G., E. Gull, D. R. Reichman, and A. J. Millis, 2015, Phys. Rev. Lett. **115**, 266802.

Conte, S. D., *et al.*, 2012, Science **335**6076, 1600.

Corkum, P. B., 1993, Phys. Rev. Lett. **71**, 1994.

Cornaglia, P. S., and A. Georges, 2007, Phys. Rev. B **75**, 115112.

Coulter, J. E., E. Manousakis, and A. Gali, 2014, Phys. Rev. B **90**, 165142.

Cugliandolo, L. F., and M. Müller, 2023, *Quantum Glasses* (World Scientific, Singapore), pp. 353–374.

Dagotto, E., 1994, Rev. Mod. Phys. **66**, 763.

Dagotto, E., 2005, Science **309**, 257.

Dal Conte, S., *et al.*, 2015, Nat. Phys. **11**, 421.

D'Alessio, L., Y. Kafri, A. Polkovnikov, and M. Rigol, 2016, Adv. Phys. **65**, 239.

D'Alessio, L., and A. Polkovnikov, 2013, Ann. Phys. (Amsterdam) **333**, 19.

D'Alessio, L., and M. Rigol, 2014, Phys. Rev. X **4**, 041048.

Daley, A. J., C. Kollath, U. Schollwöck, and G. Vidal, 2004, J. Stat. Mech. P04005.

Danz, T., T. Domröse, and C. Ropers, 2021, Science **371**6527, 371.

Das, A., 2010, Phys. Rev. B **82**, 172402.

Dasari, N., J. Li, P. Werner, and M. Eckstein, 2021, Phys. Rev. B **103**, L201116.

Dean, M. P. M., *et al.*, 2016, Nat. Mater. **15**, 601.

De Filippis, G., V. Cataudella, E. A. Nowadnick, T. P. Devereaux, A. S. Mishchenko, and N. Nagaosa, 2012, Phys. Rev. Lett. **109**, 176402.

de Gennes, P. G., 1960, Phys. Rev. **118**, 141.

de la Peña Muñoz, G. A., *et al.*, 2023, Nat. Phys. **19**, 1489.

de la Torre, A., D. M. Kennes, M. Claassen, S. Gerber, J. W. McIver, and M. A. Sentef, 2021, Rev. Mod. Phys. **93**, 041002.

de la Torre, A., *et al.*, 2022, Commun. Phys. **5**, 35.

de' Medici, L., J. Mravlje, and A. Georges, 2011, Phys. Rev. Lett. **107**, 256401.

Deng, X., J. Mravlje, R. Žitko, M. Ferrero, G. Kotliar, and A. Georges, 2013, Phys. Rev. Lett. **110**, 086401.

De Roeck, W., and F. Huveneers, 2014, Commun. Math. Phys. **332**, 1017.

Desaules, J.-Y., A. Hudomal, C. J. Turner, and Z. Papic, 2021, Phys. Rev. Lett. **126**, 210601.

Diener, P., *et al.*, 2018, Phys. Rev. Lett. **121**, 016601.

Dimitrova, I., N. Jepsen, A. Buyskikh, A. Venegas-Gomez, J. Amato-Grill, A. Daley, and W. Ketterle, 2020, Phys. Rev. Lett. **124**, 043204.

Disa, A. S., M. Fechner, T. F. Nova, B. Liu, M. Först, D. Prabhakaran, P. G. Radaelli, and A. Cavalleri, 2020, Nat. Phys. **16**, 937.

Disa, A. S., T. F. Nova, and A. Cavalleri, 2021, Nat. Phys. **17**, 1087.

Disa, A. S., *et al.*, 2023, Nature (London) **617**, 73.

Dmytruk, O., and M. Schiró, 2021, Phys. Rev. B **103**, 075131.

Dobrosavljević, V., and G. Kotliar, 1997, Phys. Rev. Lett. **78**, 3943.

Dong, S., *et al.*, 2021, Nat. Sci. **1**, e10010.

Dorda, A., M. Ganahl, H. G. Evertz, W. von der Linden, and E. Arrigoni, 2015, Phys. Rev. B **92**, 125145.

Dorda, A., M. Nuss, W. von der Linden, and E. Arrigoni, 2014, Phys. Rev. B **89**, 165105.

Dorfner, F., L. Vidmar, C. Brockt, E. Jeckelmann, and F. Heidrich-Meisner, 2015, Phys. Rev. B **91**, 104302.

Dudarev, S. L., G. A. Botton, S. Y. Savrasov, C. J. Humphreys, and A. P. Sutton, 1998, Phys. Rev. B **57**, 1505.

Dunlap, D. H., and V. M. Kenkre, 1986, Phys. Rev. B **34**, 3625.

Eberlein, A., V. Kasper, S. Sachdev, and J. Steinberg, 2017, Phys. Rev. B **96**, 205123.

Eckardt, A., 2017, Rev. Mod. Phys. **89**, 011004.

Eckardt, A., C. Weiss, and M. Holthaus, 2005, Phys. Rev. Lett. **95**, 260404.

Eckhardt, C. J., S. Chattopadhyay, D. M. Kennes, E. A. Demler, M. A. Sentef, and M. H. Michael, 2023, arXiv:2303.02176.

Eckstein, M., 2021, J. Electron Spectrosc. Relat. Phenom. **253**, 147108.

Eckstein, M., 2024, arXiv:2410.19707.

Eckstein, M., A. Hackl, S. Kehrein, M. Kollar, M. Moeckel, P. Werner, and F. A. Wolf, 2009, Eur. Phys. J. Special Topics **180**, 217.

Eckstein, M., and M. Kollar, 2008a, Phys. Rev. B **78**, 245113.

Eckstein, M., and M. Kollar, 2008b, Phys. Rev. Lett. **100**, 120404.

Eckstein, M., and M. Kollar, 2008c, Phys. Rev. B **78**, 205119.

Eckstein, M., M. Kollar, and P. Werner, 2009, Phys. Rev. Lett. **103**, 056403.

Eckstein, M., M. Kollar, and P. Werner, 2010, Phys. Rev. B **81**, 115131.

Eckstein, M., J. H. Mentink, and P. Werner, 2017, arXiv:1703.03269.

Eckstein, M., T. Oka, and P. Werner, 2010, Phys. Rev. Lett. **105**, 146404.

Eckstein, M., and P. Werner, 2010, Phys. Rev. B **82**, 115115.

Eckstein, M., and P. Werner, 2011, Phys. Rev. B **84**, 035122.

Eckstein, M., and P. Werner, 2013a, J. Phys. Conf. Ser. **427**, 012005.

Eckstein, M., and P. Werner, 2013b, Phys. Rev. B **88**, 075135.

Eckstein, M., and P. Werner, 2013c, Phys. Rev. Lett. **110**, 126401.

Eckstein, M., and P. Werner, 2014, Phys. Rev. Lett. **113**, 076405.

Eckstein, M., and P. Werner, 2016, Sci. Rep. **6**, 21235.

Eckstein, M., and P. Werner, 2017, arXiv:1704.02300.

Eckstein, M., and P. Werner, 2021, Phys. Rev. B **103**, 115136.

Edwards, D. M., and M. Miyazaki, 1987, J. Phys. F **17**, L311.

Ejima, S., T. Kaneko, F. Lange, S. Yunoki, and H. Fehske, 2020, Phys. Rev. Res. **2**, 032008.

Eliashberg, G. M., 1970, JETP Lett. **11**, 134.

El Sayed, K., S. Schuster, H. Haug, F. Herzel, and K. Henneberger, 1994, Phys. Rev. B **49**, 7337.

Erpenbeck, A., E. Gull, and G. Cohen, 2023, Phys. Rev. Lett. **130**, 186301.

Esposito, V., *et al.*, 2017, Phys. Rev. Lett. **118**, 247601.

Essler, F. H., F. Gebhard, and E. Jeckelmann, 2001, Phys. Rev. B **64**, 125119.

Essler, F. H., V. E. Korepin, and K. Schoutens, 1992, Nucl. Phys. **B372**, 559.

Essler, F. H. L., H. Frahm, F. Göhmann, A. Klümper, and V. E. Korepin, 2005, *The One-Dimensional Hubbard Model* (Cambridge University Press, Cambridge, England).

Even Tzur, M., M. Birk, A. Gorlach, M. Krüger, I. Kaminer, and O. Cohen, 2023, Nat. Photonics **17**, 501.

Fabrizio, M., 2013, in *New Materials for Thermoelectric Applications: Theory and Experiment*, edited by V. Zlatic and A. Hewson (Springer Netherlands, Dordrecht), pp. 247–273.

Fabrizio, M., 2018, Phys. Rev. Lett. **120**, 220601.

Fabrizio, M., and E. Tosatti, 1997, Phys. Rev. B **55**, 13465.

Fauseweh, B., and J.-X. Zhu, 2020, Phys. Rev. B **102**, 165128.

Fausti, D., R. I. Tobey, N. Dean, S. Kaiser, A. Dienst, M. C. Hoffmann, S. Pyon, T. Takayama, H. Takagi, and A. Cavalleri, 2011, Science **331**6014, 189.

Fechner, M., A. Sukhov, L. Chotorlishvili, C. Kenel, J. Berakdar, and N. A. Spaldin, 2018, Phys. Rev. Mater. **2**, 064401.

Ferray, M., A. L'Huillier, X. F. Li, L. A. Lompre, G. Mainfray, and C. Manus, 1988, J. Phys. B **21**, L31.

Feynman, R., and F. Vernon, 1963, Ann. Phys. (N.Y.) **24**, 118.

Först, M., C. Manzoni, S. Kaiser, Y. Tomioka, Y. Tokura, R. Merlin, and A. Cavalleri, 2011, Nat. Phys. **7**, 854.

Freericks, J. K., H. R. Krishnamurthy, and T. Pruschke, 2009, Phys. Rev. Lett. **102**, 136401.

Freericks, J. K., V. M. Turkowski, and V. Zlatič, 2006, Phys. Rev. Lett. **97**, 266408.

Fujiuchi, R., T. Kaneko, K. Sugimoto, S. Yunoki, and Y. Ohta, 2020, Phys. Rev. B **101**, 235122.

Fukui, T., and N. Kawakami, 1998, Phys. Rev. B **58**, 16051.

Furuya, S. C., K. Takasan, and M. Sato, 2021, Phys. Rev. Res. **3**, 033066.

Gallagher, F. B., and S. Mazumdar, 1997, Phys. Rev. B **56**, 15025.

Gao, H., J. R. Coulthard, D. Jaksch, and J. Mur-Petit, 2020, Phys. Rev. Lett. **125**, 195301.

Gassner, S., C. S. Weber, and M. Claassen, 2024, Nat. Commun. **15**, 1776.

Gazzaneo, P., T. M. Mazzocchi, J. Lotze, and E. Arrigoni, 2022, Phys. Rev. B **106**, 195140.

Gebhard, F., K. Born, M. Scheidler, P. Thomas, and S. Koch, 1997, Philos. Mag. B **75**, 13.

Geng, L., J. Yan, and P. Werner, 2025, Phys. Rev. B **111**, 115143.

Georges, A., and G. Kotliar, 1992, Phys. Rev. B **45**, 6479.

Georges, A., G. Kotliar, W. Krauth, and M. J. Rozenberg, 1996, Rev. Mod. Phys. **68**, 13.

Georges, A., L. de' Medici, and J. Mravlje, 2013, Annu. Rev. Condens. Matter Phys. **4**, 137.

Gerasimenko, Y. A., I. Vaskivskyi, M. Litskevich, J. Ravnik, J. Vodeb, M. Diego, V. Kabanov, and D. Mihailovic, 2019, Nat. Mater. **18**, 1078.

Ghimire, S., A. D. DiChiara, E. Sistrunk, P. Agostini, L. F. DiMauro, and D. A. Reis, 2011, Nat. Phys. **7**, 138.

Ghimire, S., and D. A. Reis, 2019, Nat. Phys. **15**, 10.

Giannetti, C., M. Capone, D. Fausti, M. Fabrizio, F. Parmigiani, and D. Mihailovic, 2016, Adv. Phys. **65**, 58.

Gillmeister, K., D. Golez, C.-T. Chiang, N. Bittner, Y. Pavlyukh, J. Berakdar, P. Werner, and W. Widdra, 2020, Nat. Commun. **11**, 4095.

Glazman, L., 1981, Zh. Eksp. Teor. Fiz. **80**, 349.

Golež, D., L. Boehnke, M. Eckstein, and P. Werner, 2019, Phys. Rev. B **100**, 041111.

Golež, D., L. Boehnke, H. U. R. Strand, M. Eckstein, and P. Werner, 2017, Phys. Rev. Lett. **118**, 246402.

Golež, D., J. Bonča, M. Mierzejewski, and L. Vidmar, 2014, Phys. Rev. B **89**, 165118.

Golež, D., J. Bonča, and L. Vidmar, 2012, Phys. Rev. B **85**, 144304.

Golež, D., J. Bonča, L. Vidmar, and S. A. Trugman, 2012, Phys. Rev. Lett. **109**, 236402.

Golež, D., M. Eckstein, and P. Werner, 2015, Phys. Rev. B **92**, 195123.

Golež, D., M. Eckstein, and P. Werner, 2019, Phys. Rev. B **100**, 235117.

Golež, D., E. Paprotzki, P. Werner, and M. Eckstein, 2025, Phys. Rev. B **111**, 045147.

Golež, D., *et al.*, 2022, Phys. Rev. B **106**, L121106.

Görg, F., M. Messer, K. Sandholzer, G. Jotzu, R. Desbuquois, and T. Esslinger, 2018, Nature (London) **553**7689, 481.

Gramsch, C., K. Balzer, M. Eckstein, and M. Kollar, 2013, Phys. Rev. B **88**, 235106.

Grånäs, O., *et al.*, 2022, Phys. Rev. Res. **4**, L032030.

Grandi, F., and M. Eckstein, 2021, Phys. Rev. B **103**, 245117.

Grandi, F., J. Li, and M. Eckstein, 2021, Phys. Rev. B **103**, L041110.

Grandi, F., A. Picano, R. Thomale, D. M. Kennes, and M. Eckstein, 2024, arXiv:2412.02616.

Gray, A. X., *et al.*, 2018, Phys. Rev. B **98**, 045104.

Gros, C., R. Joynt, and T. M. Rice, 1987, Phys. Rev. B **36**, 381.

Gross, C., and I. Bloch, 2017, Science **357**6355, 995.

Grover, T., and M. P. A. Fisher, 2014, J. Stat. Mech. P10010.

Grunwald, L., E. V. Boström, M. K. Svendsen, D. M. Kennes, and A. Rubio, 2024, arXiv:2410.21515.

Grunwald, L., G. Passetti, and D. M. Kennes, 2023, arXiv:2307.09935.

Guerci, D., M. Capone, and N. Lanatà, 2023, Phys. Rev. Res. **5**, L032023.

Guiot, V., L. Cario, E. Janod, B. Corraze, V. T. Phuoc, M. Rozenberg, P. Stoliar, T. Cren, and D. Roditchev, 2013, Nat. Commun. **4**, 1722.

Gull, E., A. J. Millis, A. I. Lichtenstein, A. N. Rubtsov, M. Troyer, and P. Werner, 2011, Rev. Mod. Phys. **83**, 349.

Gutzwiller, M. C., 1963, Phys. Rev. Lett. **10**, 159.

Gutzwiller, M. C., 1965, Phys. Rev. **137**, A1726.

Hackl, A., and S. Kehrein, 2009, J. Phys. Condens. Matter **21**, 015601.

Haegeman, J., J. I. Cirac, T. J. Osborne, I. Pižorn, H. Verschelde, and F. Verstraete, 2011, Phys. Rev. Lett. **107**, 070601.

Haegeman, J., T. J. Osborne, and F. Verstraete, 2013, Phys. Rev. B **88**, 075133.

Hahn, L., A. Bohrdt, and F. Grusdt, 2022, Phys. Rev. B **105**, L241113.

Haldar, A., R. Moessner, and A. Das, 2018, Phys. Rev. B **97**, 245122.

Haldar, A., D. Sen, R. Moessner, and A. Das, 2021, Phys. Rev. X **11**, 021008.

Hamm, P., and M. Zanni, 2011, *Concepts and Methods of 2D Infrared Spectroscopy* (Cambridge University Press, Cambridge, England).

Hansen, T., S. V. B. Jensen, and L. B. Madsen, 2022, Phys. Rev. A **105**, 053118.

Hansen, T., and L. B. Madsen, 2022, Phys. Rev. B **106**, 235142.

Hariki, A., T. Uozumi, and J. Kuneš, 2017, Phys. Rev. B **96**, 045111.

Hariki, A., M. Winder, and J. Kuneš, 2018, Phys. Rev. Lett. **121**, 126403.

Hashimoto, H., H. Matsueda, H. Seo, and S. Ishihara, 2014, J. Phys. Soc. Jpn. **83**, 123703.

Haug, H., and A.-P. Jauho, 2008, *Quantum Kinetics in Transport and Optics of Semiconductors*, 2nd ed. (Springer, Berlin).

Haug, H., and S. W. Koch, 2009, *Quantum Theory of the Optical and Electronic Properties of Semiconductors* (World Scientific, Singapore).

Haule, K., 2018, J. Phys. Soc. Jpn. **87**, 041005.

Haule, K., A. Rosch, J. Kroha, and P. Wölfle, 2002, Phys. Rev. Lett. **89**, 236402.

Haverkort, M. W., G. Sangiovanni, P. Hansmann, A. Toschi, Y. Lu, and S. Macke, 2014, Europhys. Lett. **108**, 57004.

He, Z., and A. J. Millis, 2016, Phys. Rev. B **93**, 115126.

Hedin, L., 1965, Phys. Rev. **139**, A796.

Heide, C., Y. Kobayashi, S. R. U. Haque, and S. Ghimire, 2024, Nat. Phys. **20**, 1546.

Heidrich-Meisner, F., I. González, K. A. Al-Hassanieh, A. E. Feiguin, M. J. Rozenberg, and E. Dagotto, 2010, Phys. Rev. B **82**, 205110.

Hejazi, K., J. Liu, and L. Balents, 2019, Phys. Rev. B **99**, 205111.

Henstridge, M., M. Först, E. Rowe, M. Fechner, and A. Cavalleri, 2022, Nat. Phys. **18**, 457.

Herrmann, A., Y. Murakami, M. Eckstein, and P. Werner, 2017, Europhys. Lett. **120**, 57001.

Hettler, M. H., A. N. Tahvildar-Zadeh, M. Jarrell, T. Pruschke, and H. R. Krishnamurthy, 1998, Phys. Rev. B **58**, R7475.

Hilton, D. J., R. P. Prasankumar, S. Fourmaux, A. Cavalleri, D. Brassard, M. A. El Khakani, J. C. Kieffer, A. J. Taylor, and R. D. Averitt, 2007, Phys. Rev. Lett. **99**, 226401.

Hohenberg, P. C., and B. I. Halperin, 1977, Rev. Mod. Phys. **49**, 435.

Hollander, M. J., Y. Liu, W.-J. Lu, L.-J. Li, Y.-P. Sun, J. A. Robinson, and S. Datta, 2015, Nano Lett. **15**, 1861.

Holleman, J., M. M. Bishop, C. Garcia, J. S. R. Vellore Winfred, S. Lee, H. N. Lee, C. Beekman, E. Manousakis, and S. A. McGill, 2016, Phys. Rev. B **94**, 155129.

Holstein, T., 1959, Ann. Phys. (N.Y.) **8**, 325.

Holthaus, M., 1992, Phys. Rev. Lett. **69**, 351.

Hoshino, S., and P. Werner, 2016, Phys. Rev. B **93**, 155161.

Hoshino, S., and P. Werner, 2017, Phys. Rev. Lett. **118**, 177002.

Howell, O., P. Weinberg, D. Sels, A. Polkovnikov, and M. Bukov, 2019, Phys. Rev. Lett. **122**, 010602.

Hu, W., S. Kaiser, D. Nicoletti, C. R. Hunt, I. Gierz, M. C. Hoffmann, M. Le Tacon, T. Loew, B. Keimer, and A. Cavalleri, 2014, Nat. Mater. **13**, 705.

Huang, K., and T.-Y. Du, 2023, Phys. Rev. B **108**, 155125.

Huang, T.-S., C. L. Baldwin, M. Hafezi, and V. Galitski, 2023, Phys. Rev. B **107**, 075111.

Hubbard, J., 1963, Proc. R. Soc. A **276**, 238.

Hübener, H., U. De Giovannini, and A. Rubio, 2018, Nano Lett. **18**, 1535.

Hubig, C., A. Bohrdt, M. Knap, F. Grusdt, and J. I. Cirac, 2020, SciPost Phys. **8**, 021.

Ichikawa, H., *et al.*, 2011, Nat. Mater. **10**, 101.
Ido, K., T. Ohgoe, and M. Imada, 2015, Phys. Rev. B **92**, 245106.
Ido, K., T. Ohgoe, and M. Imada, 2017, Sci. Adv. **3**, e1700718.
Ihara, Y., H. Alloul, P. Wzietek, D. Pontiroli, M. Mazzani, and M. Riccò, 2011, Europhys. Lett. **94**, 37007.
Ikeda, T. N., and A. Polkovnikov, 2021, Phys. Rev. B **104**, 134308.
Ikeda, T. N., and M. Sato, 2019, Phys. Rev. B **100**, 214424.
Imada, M., A. Fujimori, and Y. Tokura, 1998, Rev. Mod. Phys. **70**, 1039.
Imai, S., A. Ono, and S. Ishihara, 2020, Phys. Rev. Lett. **124**, 157404.
Imai, S., A. Ono, and S. Ishihara, 2022, Phys. Rev. Res. **4**, 043155.
Inayoshi, K., 2023 (private communication).
Inoue, J.-i., and S. Maekawa, 1990, J. Phys. Soc. Jpn. **59**, 2110.
Ishikawa, T., *et al.*, 2014, Nat. Commun. **5**, 5528.
Itin, A. P., and M. I. Katsnelson, 2015, Phys. Rev. Lett. **115**, 075301.
Ito, S., *et al.*, 2023, Nature (London) **616**7958, 696.
Iwahori, K., and N. Kawakami, 2016, Phys. Rev. A **94**, 063647.
Iwai, S., M. Ono, A. Maeda, H. Matsuzaki, H. Kishida, H. Okamoto, and Y. Tokura, 2003, Phys. Rev. Lett. **91**, 057401.
Iyoda, E., and S. Ishihara, 2014, Phys. Rev. B **89**, 125126.
Jaklič, J., and P. Prelovšek, 2000, Adv. Phys. **49**, 1.
Janod, E., *et al.*, 2015, Adv. Funct. Mater. **25**, 6287.
Jarc, G., *et al.*, 2023, Nature (London) **622**, 487.
Jaynes, E. T., 1957, Phys. Rev. **106**, 620.
Jeckelmann, E., 2003, Phys. Rev. B **67**, 075106.
Ji, G., *et al.*, 2021, Phys. Rev. X **11**, 021022.
Johnson, A. S., D. Moreno-Mencía, E. B. Amuah, M. Menghini, J.-P. Locquet, C. Giannetti, E. Pastor, and S. E. Wall, 2022, Phys. Rev. Lett. **129**, 255701.
Johnson, A. S., *et al.*, 2023, Nat. Phys. **19**, 215.
Jotzu, G., M. Messer, R. Desbuquois, M. Lebrat, T. Uehlinger, D. Greif, and T. Esslinger, 2014, Nature (London) **515**, 237.
Joura, A. V., J. K. Freericks, and T. Pruschke, 2008, Phys. Rev. Lett. **101**, 196401.
Juraschek, D. M., M. Fechner, and N. A. Spaldin, 2017, Phys. Rev. Lett. **118**, 054101.
Kaiser, S., *et al.*, 2014a, Sci. Rep. **4**, 3823.
Kaiser, S., *et al.*, 2014b, Phys. Rev. B **89**, 184516.
Kalcheim, Y., A. Camjayi, J. del Valle, P. Salev, M. Rozenberg, and I. K. Schuller, 2020, Nat. Commun. **11**, 2985.
Kalthoff, M. H., D. M. Kennes, A. J. Millis, and M. A. Sentef, 2022, Phys. Rev. Res. **4**, 023115.
Kanamori, J., 1963, Prog. Theor. Phys. **30**, 275.
Kanamori, Y., H. Matsueda, and S. Ishihara, 2011, Phys. Rev. Lett. **107**, 167403.
Kanász-Nagy, M., I. Lovas, F. Grusdt, D. Greif, M. Greiner, and E. A. Demler, 2017, Phys. Rev. B **96**, 014303.
Kane, C. L., P. A. Lee, and N. Read, 1989, Phys. Rev. B **39**, 6880.
Kaneko, T., T. Shirakawa, S. Sorella, and S. Yunoki, 2019, Phys. Rev. Lett. **122**, 077002.
Kaneko, T., S. Yunoki, and A. J. Millis, 2020, Phys. Rev. Res. **2**, 032027.
Kang, B., P. Semon, C. Melnick, G. Kotliar, and S. Choi, 2023, arXiv:2310.04613.
Karlsson, D., A. Privitera, and C. Verdozzi, 2011, Phys. Rev. Lett. **106**, 116401.
Katsumi, K., M. Nishida, S. Kaiser, S. Miyasaka, S. Tajima, and R. Shimano, 2023, Phys. Rev. B **107**, 214506.
Kawakami, Y., S. Iwai, T. Fukatsu, M. Miura, N. Yoneyama, T. Sasaki, and N. Kobayashi, 2009, Phys. Rev. Lett. **103**, 066403.
Kaye, J., and D. Golež, 2021, SciPost Phys. **10**, 091.
Keiter, H., and J. C. Kimball, 1971, Int. J. Magn. **1**, 233.
Keldysh, L. V., 1965, Zh. Eksp. Teor. Fiz. **20**, 1307 [Sov. Phys. JETP **20**, 1307 (1965)].
Keldysh, L. V., 1986, Contemp. Phys. **27**, 395.
Kemper, A. F., M. A. Sentef, B. Moritz, T. P. Devereaux, and J. K. Freericks, 2017, Ann. Phys. (Berlin) **529**, 1600235.
Kennes, D. M., E. Y. Wilner, D. R. Reichman, and A. J. Millis, 2017, Nat. Phys. **13**, 479.
Kiffner, M., J. R. Coulthard, F. Schlawin, A. Ardavan, and D. Jaksch, 2019, Phys. Rev. B **99**, 085116.
Kim, A. J., K. Lenk, J. Li, P. Werner, and M. Eckstein, 2023, Phys. Rev. Lett. **130**, 036901.
Kim, A. J., J. Li, M. Eckstein, and P. Werner, 2022, Phys. Rev. B **106**, 085124.
Kim, A. J., and P. Werner, 2025, Phys. Rev. B **111**, 125120.
Kimura, K., H. Matsuzaki, S. Takaishi, M. Yamashita, and H. Okamoto, 2009, Phys. Rev. B **79**, 075116.
King, A. D., *et al.*, 2023, Nature (London) **617**, 61.
Kipp, G., *et al.*, 2024, arXiv:2403.19745.
Kirilyuk, A., A. V. Kimel, and T. Rasing, 2010, Rev. Mod. Phys. **82**, 2731.
Kishida, H., H. Matsuzaki, H. Okamoto, T. Manabe, M. Yamashita, Y. Taguchi, and Y. Tokura, 2000, Nature (London) **405**, 929.
Kishida, H., *et al.*, 2001, Phys. Rev. Lett. **87**, 177401.
Kitaev, A., 2006, Ann. Phys. (Amsterdam) **321**, 2.
Kitagawa, T., T. Oka, A. Brataas, L. Fu, and E. Demler, 2011, Phys. Rev. B **84**, 235108.
Kitamura, S., and H. Aoki, 2016, Phys. Rev. B **94**, 174503.
Kitamura, S., T. Oka, and H. Aoki, 2017, Phys. Rev. B **96**, 014406.
Kjäll, J. A., M. P. Zaletel, R. S. K. Mong, J. H. Bardarson, and F. Pollmann, 2013, Phys. Rev. B **87**, 235106.
Knap, M., M. Babadi, G. Refael, I. Martin, and E. Demler, 2016, Phys. Rev. B **94**, 214504.
Kogar, A., *et al.*, 2020, Nat. Phys. **16**, 159.
Kogoj, J., Z. Lenarčič, D. Golež, M. Mierzejewski, and P. Prelovšek, and J. Bonča, 2014, Phys. Rev. B **90**, 125104.
Kogoj, J., M. Mierzejewski, and J. Bonča, 2016, Phys. Rev. Lett. **117**, 227002.
Kohlert, T., S. Scherg, P. Sala, F. Pollmann, B. Hebbe Madhusudhana, I. Bloch, and M. Aidelsburger, 2023, Phys. Rev. Lett. **130**, 010201.
Kohn, W., and L. J. Sham, 1965, Phys. Rev. **140**, A1133.
Kollar, M., F. A. Wolf, and M. Eckstein, 2011, Phys. Rev. B **84**, 054304.
Kollath, C., A. M. Läuchli, and E. Altman, 2007, Phys. Rev. Lett. **98**, 180601.
Komnik, A., and M. Thorwart, 2016, Eur. Phys. J. B **89**, 244.
Koshihara, S., T. Ishikawa, Y. Okimoto, K. Onda, R. Fukaya, M. Hada, Y. Hayashi, S. Ishihara, and T. Luty, 2022, Phys. Rep. **942**, 1.
Kotliar, G., S. Y. Savrasov, K. Haule, V. S. Oudovenko, O. Parcollet, and C. A. Marianetti, 2006, Rev. Mod. Phys. **78**, 865.
Kotliar, G., S. Y. Savrasov, G. Pálsson, and G. Biroli, 2001, Phys. Rev. Lett. **87**, 186401.
Kovač, K., D. Golež, M. Mierzejewski, and J. Bonča, 2023, arXiv:2305.09238.
Kratochvilova, M., A. D. Hillier, A. R. Wildes, L. Wang, S.-W. Cheong, and J.-G. Park, 2017, npj Quantum Mater. **2**, 42.
Kruchinin, S. Y., F. Krausz, and V. S. Yakovlev, 2018, Rev. Mod. Phys. **90**, 021002.
Kübler, C., H. Ehrke, R. Huber, R. Lopez, A. Halabica, R. F. Haglund, and A. Leitenstorfer, 2007, Phys. Rev. Lett. **99**, 116401.
Kuhlenkamp, C., and M. Knap, 2020, Phys. Rev. Lett. **124**, 106401.
Kuneš, J., 2015, J. Phys. Condens. Matter **27**, 333201.

Künzel, F., A. Erpenbeck, D. Werner, E. Arrigoni, E. Gull, G. Cohen, and M. Eckstein, 2024, Phys. Rev. Lett. **132**, 176501.
Lanatà, N., and H. U. R. Strand, 2012, Phys. Rev. B **86**, 115310.
Lanczos, C., 1950, J. Res. Natl. Bur. Stand. **45**, 255.
Lang, I. G., and Y. A. Firsov, 1962, Sov. Phys. JETP **16**, 1301.
Lange, F., Z. Lenarčič, and A. Rosch, 2017, Nat. Commun. **8**, 15767.
Lange, F. and Z. Lenarčič, and A. Rosch, 2018, Phys. Rev. B **97**, 165138.
Langen, T., T. Gasenzer, and J. Schmiedmayer, 2016, J. Stat. Mech. 064009.
Lantz, G., *et al.*, 2017, Nat. Commun. **8**, 13917.
Lazarides, A., A. Das, and R. Moessner, 2014, Phys. Rev. E **90**, 012110.
Lee, P. A., N. Nagaosa, and X.-G. Wen, 2006, Rev. Mod. Phys. **78**, 17.
Lee, W.-R., and K. Park, 2014, Phys. Rev. B **89**, 205126.
Lenarčič, Z., M. Eckstein, and P. Prelovšek, 2015, Phys. Rev. B **92**, 201104.
Lenarčič, Z., D. Golež, J. Bonča, and P. Prelovšek, 2014, Phys. Rev. B **89**, 125123.
Lenarčič, Z., and P. Prelovšek, 2012, Phys. Rev. Lett. **108**, 196401.
Lenarčič, Z., and P. Prelovšek, 2013, Phys. Rev. Lett. **111**, 016401.
Lenarčič, Z., and P. Prelovšek, 2014, Phys. Rev. B **90**, 235136.
Lewenstein, M., P. Balcou, M. Y. Ivanov, A. L'Huillier, and P. B. Corkum, 1994, Phys. Rev. A **49**, 2117.
Li, J., and M. Eckstein, 2020, Phys. Rev. Lett. **125**, 217402.
Li, J., and M. Eckstein, 2021, Phys. Rev. B **103**, 045133.
Li, J., D. Golez, G. Mazza, A. J. Millis, A. Georges, and M. Eckstein, 2020, Phys. Rev. B **101**, 205140.
Li, J., D. Golez, P. Werner, and M. Eckstein, 2020, Phys. Rev. B **102**, 165136.
Li, J., M. Müller, A. J. Kim, A. M. Läuchli, and P. Werner, 2023, Phys. Rev. B **107**, 205115.
Li, J., H. Strand, P. Werner, and M. Eckstein, 2018, Nat. Commun. **9**, 4581.
Li, X., H. Ning, O. Mehio, H. Zhao, M.-C. Lee, K. Kim, F. Nakamura, Y. Maeno, G. Cao, and D. Hsieh, 2022, Phys. Rev. Lett. **128**, 187402.
Lichtenstein, A. I., and M. I. Katsnelson, 2000, Phys. Rev. B **62**, R9283.
Liechtenstein, A. I., V. I. Anisimov, and J. Zaanen, 1995, Phys. Rev. B **52**, R5467.
Ligges, M., *et al.*, 2018, Phys. Rev. Lett. **120**, 166401.
Lin, N., E. Gull, and A. J. Millis, 2009, Phys. Rev. B **80**, 161105.
Lipavský, P., V. Špička, and B. Velický, 1986, Phys. Rev. B **34**, 6933.
Liu, A., *et al.*, 2024, Nat. Phys. **20**, 1751.
Liu, J., K. Hejazi, and L. Balents, 2018, Phys. Rev. Lett. **121**, 107201.
Liu, M., *et al.*, 2012, Nature (London) **487**, 345.
Lojewski, T., *et al.*, 2024, Phys. Rev. B **110**, 245120.
Loudon, R., 1973, *The Quantum Theory of Light* (Oxford University Press, Oxford).
Lovinger, D. J., M. Brahlek, P. Kissin, D. M. Kennes, A. J. Millis, R. Engel-Herbert, and R. D. Averitt, 2020, Phys. Rev. B **102**, 115143.
Lu, H., C. Shao, J. Bonča, D. Manske, and T. Tohyama, 2015, Phys. Rev. B **91**, 245117.
Lu, H., S. Sota, H. Matsueda, and J. Bonča, and T. Tohyama, 2012, Phys. Rev. Lett. **109**, 197401.
Luttinger, J. M., 1951, Phys. Rev. **84**, 814.
Luu, T. T., M. Garg, S. Y. Kruchinin, A. Moulet, M. T. Hassan, and E. Goulielmakis, 2015, Nature (London) **521**, 498.
Lysne, M., Y. Murakami, and P. Werner, 2020, Phys. Rev. B **101**, 195139.
MacDonald, A. H., S. M. Girvin, and D. Yoshioka, 1988, Phys. Rev. B **37**, 9753.
Madéo, J., *et al.*, 2020, Science **370**, 1199.
Maeshima, N., and K. Yonemitsu, 2005, J. Phys. Soc. Jpn. **74**, 2671.
Maier, T., M. Jarrell, T. Pruschke, and M. H. Hettler, 2005, Rev. Mod. Phys. **77**, 1027.
Maklar, J., S. Dong, S. Beaulieu, T. Pincelli, M. Dendzik, Y. W. Windsor, R. P. Xian, M. Wolf, R. Ernstorfer, and L. Rettig, 2020, Rev. Sci. Instrum. **91**, 123112.
Mankowsky, R., M. Först, and A. Cavalleri, 2016, Rep. Prog. Phys. **79**, 064503.
Mankowsky, R., A. von Hoegen, M. Först, and A. Cavalleri, 2017, Phys. Rev. Lett. **118**, 197601.
Mankowsky, R., *et al.*, 2014, Nature (London) **516**, 71.
Manousakis, E., 2010, Phys. Rev. B **82**, 125109.
Marini, G., and M. Calandra, 2021, Phys. Rev. B **104**, 144103.
Marino, J., M. Eckstein, M. S. Foster, and A. M. Rey, 2022, Rep. Prog. Phys. **85**, 116001.
Matsueda, H., S. Sota, T. Tohyama, and S. Maekawa, 2012, J. Phys. Soc. Jpn. **81**, 013701.
Matsueda, H., T. Tohyama, and S. Maekawa, 2004, Phys. Rev. B **70**, 033102.
Matsuzaki, H., *et al.*, 2014, Phys. Rev. Lett. **113**, 096403.
Matveev, O. P., A. M. Shvaika, T. P. Devereaux, and J. K. Freericks, 2019, Phys. Rev. Lett. **122**, 247402.
Mayer, B., *et al.*, 2015, Phys. Rev. B **91**, 235113.
Mazza, G., 2017, Phys. Rev. B **96**, 205110.
Mazza, G., A. Amaricci, M. Capone, and M. Fabrizio, 2016, Phys. Rev. Lett. **117**, 176401.
Mazzocchi, T. M., P. Gazzaneo, J. Lotze, and E. Arrigoni, 2022, Phys. Rev. B **106**, 125123.
Mazzocchi, T. M., D. Werner, P. Gazzaneo, and E. Arrigoni, 2023, Phys. Rev. B **107**, 155103.
McIver, J. W., B. Schulte, F.-U. Stein, T. Matsuyama, G. Jotzu, G. Meier, and A. Cavalleri, 2020, Nat. Phys. **16**, 38.
Mehio, O., X. Li, H. Ning, Z. Lenarčič, Y. Han, M. Buchhold, Z. Porter, N. J. Laurita, S. D. Wilson, and D. Hsieh, 2023, Nat. Phys. **19**, 1876.
Melnick, C., P. Sémon, K. Yu, N. D'Imperio, A.-M. Tremblay, and G. Kotliar, 2021, Comput. Phys. Commun. **267**, 108075.
Mentink, J. H., K. Balzer, and M. Eckstein, 2015, Nat. Commun. **6**, 6708.
Metzner, W., and D. Vollhardt, 1989, Phys. Rev. Lett. **62**, 324.
Mierzejewski, M., L. Vidmar, J. Bonča, and P. Prelovšek, 2011, Phys. Rev. Lett. **106**, 196401.
Mikami, T., S. Kitamura, K. Yasuda, N. Tsuji, T. Oka, and H. Aoki, 2016, Phys. Rev. B **93**, 144307.
Mikheev, A. N., I. Siovitz, and T. Gasenzer, 2023, arXiv:2304.12464.
Miranda, E., and V. Dobrosavljević, 2005, Rep. Prog. Phys. **68**, 2337.
Miranda, E., and V. Dobrosavljević, 2012, *1616 Dynamical Mean-Field Theories of Correlation and Disorder* (Oxford University Press, New York).
Mitrano, M., S. Johnston, Y.-J. Kim, and M. P. M. Dean, 2024, Phys. Rev. X **14**, 040501.
Mitrano, M., and Y. Wang, 2020, Commun. Phys. **3**, 184.
Mitrano, M. *et al.*, 2014, Phys. Rev. Lett. **112**, 117801.
Mitrano, M., *et al.*, 2016, Nature (London) **530**, 461.
Mitrano, M., *et al.*, 2019, Sci. Adv. **5**, eaax3346.
Miyamoto, T., A. Kondo, T. Inaba, T. Morimoto, S. You, and H. Okamoto, 2023, Nat. Commun. **14**, 6229.
Miyamoto, T., *et al.*, 2018, Nat. Commun. **9**, 3948.
Miyamoto, T., *et al.*, 2019, Commun. Phys. **2**, 131.

Miyano, K., T. Tanaka, Y. Tomioka, and Y. Tokura, 1997, Phys. Rev. Lett. **78**, 4257.

Mizuno, Y., K. Tsutsui, T. Tohyama, and S. Maekawa, 2000, Phys. Rev. B **62**, R4769.

Moeckel, M., and S. Kehrein, 2008, Phys. Rev. Lett. **100**, 175702.

Mor, S., *et al.*, 2017, Phys. Rev. Lett. **119**, 086401.

Moreno-Mencía, D., A. Ramos-Álvarez, L. Vidas, S. M. Koohpayeh, and S. Wall, 2019, Nat. Commun. **10**, 4034.

Mori, T., T. Kuwahara, and K. Saito, 2016, Phys. Rev. Lett. **116**, 120401.

Moritz, B., T. P. Devereaux, and J. K. Freericks, 2010, Phys. Rev. B **81**, 165112.

Morrison, V. R., R. P. Chatelain, K. L. Tiwari, A. Hendaoui, A. Bruhá, M. Chaker, and B. J. Siwick, 2014, Science **346**6208, 445.

Mühlbacher, L., and E. Rabani, 2008, Phys. Rev. Lett. **100**, 176403.

Müller, A., F. Grandi, and M. Eckstein, 2022, Phys. Rev. B **106**, L121107.

Müller, H., M. Eckstein, and S. Viola Kusminskiy, 2023, Phys. Rev. Lett. **130**, 106905.

Murakami, Y., M. Eckstein, and P. Werner, 2018, Phys. Rev. Lett. **121**, 057405.

Murakami, Y., T. Hansen, S. Takayoshi, L. B. Madsen, and P. Werner, 2025, Phys. Rev. Lett. **134**, 096504.

Murakami, Y., M. Schüler, R. Arita, and P. Werner, 2023, Phys. Rev. B **108**, 035151.

Murakami, Y., S. Takayoshi, T. Kaneko, A. M. Läuchli, and P. Werner, 2023, Phys. Rev. Lett. **130**, 106501.

Murakami, Y., S. Takayoshi, T. Kaneko, Z. Sun, D. Golez, A. J. Millis, and P. Werner, 2022, Commun. Phys. **5**, 23.

Murakami, Y., S. Takayoshi, A. Koga, and P. Werner, 2021, Phys. Rev. B **103**, 035110.

Murakami, Y., N. Tsuji, M. Eckstein, and P. Werner, 2017, Phys. Rev. B **96**, 045125.

Murakami, Y., K. Uchida, A. Koga, K. Tanaka, and P. Werner, 2022, Phys. Rev. Lett. **129**, 157401.

Murakami, Y., and P. Werner, 2018, Phys. Rev. B **98**, 075102.

Murakami, Y., P. Werner, N. Tsuji, and H. Aoki, 2015, Phys. Rev. B **91**, 045128.

Murakami, Y., P. Werner, N. Tsuji, and H. Aoki, 2016, Phys. Rev. B **93**, 094509.

Mydosh, J. A., 2015, Rep. Prog. Phys. **78**, 052501.

Nakagawa, M., and N. Kawakami, 2015, Phys. Rev. Lett. **115**, 165303.

Nakamura, F., M. Sakaki, Y. Yamanaka, S. Tamaru, T. Suzuki, and Y. Maeno, 2013, Sci. Rep. **3**, 2536.

Nakano, A., K. Uchida, Y. Tomioka, M. Takaya, Y. Okimoto, and K. Tanaka, 2023, arXiv:2309.06537.

Nambiar, G., A. Grankin, and M. Hafezi, 2024, arXiv:2410.24215.

Nasu, K., 2004, *Photoinduced Phase Transitions* (World Scientific, Singapore).

Nava, A., and M. Fabrizio, 2022, SciPost Phys. **12**, 014.

Nava, A., C. Giannetti, A. Georges, E. Tosatti, and M. Fabrizio, 2018, Nat. Phys. **14**, 154.

Nayak, M., J. Thoenniss, M. Sonner, D. Abanin, and P. Werner, 2025, arXiv:2503.02848.

Nevola, D., *et al.*, 2021, Phys. Rev. B **103**, 245105.

Nicoletti, D., E. Casandruc, Y. Laplace, V. Khanna, C. R. Hunt, S. Kaiser, S. S. Dhesi, G. D. Gu, J. P. Hill, and A. Cavalleri, 2014, Phys. Rev. B **90**, 100503.

Nicoletti, D., and A. Cavalleri, 2016, Adv. Opt. Photonics **8**, 401.

Nilsson, F., L. Boehnke, P. Werner, and F. Aryasetiawan, 2017, Phys. Rev. Mater. **1**, 043803.

Nova, T. F., A. Cartella, A. Cantaluppi, M. Först, D. Bossini, R. V. Mikhaylovskiy, A. V. Kimel, R. Merlin, and A. Cavalleri, 2017, Nat. Phys. **13**, 132.

Nova, T. F., A. S. Disa, M. Fechner, and A. Cavalleri, 2019, Science **364**6445, 1075.

Novelli, F., D. Fausti, J. Reul, F. Cilento, P. H. M. van Loosdrecht, A. A. Nugroho, T. T. M. Palstra, M. Grüninger, and F. Parmigiani, 2012, Phys. Rev. B **86**, 165135.

Novelli, F., *et al.*, 2014, Nat. Commun. **5**, 5112.

Nowak, B., D. Sexty, and T. Gasenzer, 2011, Phys. Rev. B **84**, 020506.

Nozik, A. J., M. C. Beard, J. M. Luther, M. Law, R. J. Ellingson, and J. C. Johnson, 2010, Chem. Rev. **110**, 6873.

Núñez Fernández, Y., M. Jeannin, P. T. Dumitrescu, T. Kloss, J. Kaye, O. Parcollet, and X. Waintal, 2022, Phys. Rev. X **12**, 041018.

O'Callahan, B. T., A. C. Jones, J. Hyung Park, D. H. Cobden, J. M. Atkin, and M. B. Raschke, 2015, Nat. Commun. **6**, 6849.

Oelsen, E. v., G. Seibold, and J. Bünemann, 2011, Phys. Rev. Lett. **107**, 076402.

Ogata, M., and H. Shiba, 1990, Phys. Rev. B **41**, 2326.

Ogawa, Y., S. Koshihara, K. Koshino, T. Ogawa, C. Urano, and H. Takagi, 2000, Phys. Rev. Lett. **84**, 3181.

Ohkoshi, S.-i., K. Imoto, Y. Tsunobuchi, S. Takano, and H. Tokoro, 2011, Nat. Chem. **3**, 564.

Oka, T., 2012, Phys. Rev. B **86**, 075148.

Oka, T., and H. Aoki, 2005, Phys. Rev. Lett. **95**, 137601.

Oka, T., and H. Aoki, 2009, Phys. Rev. B **79**, 081406.

Oka, T., and H. Aoki, 2010, Phys. Rev. B **81**, 033103.

Oka, T., R. Arita, and H. Aoki, 2003, Phys. Rev. Lett. **91**, 066406.

Oka, T., and S. Kitamura, 2019, Annu. Rev. Condens. Matter Phys. **10**, 387.

Okamoto, H., H. Matsuzaki, T. Wakabayashi, Y. Takahashi, and T. Hasegawa, 2007, Phys. Rev. Lett. **98**, 037401.

Okamoto, H., T. Miyagoe, K. Kobayashi, H. Uemura, H. Nishioka, H. Matsuzaki, A. Sawa, and Y. Tokura, 2010, Phys. Rev. B **82**, 060513.

Okamoto, H., T. Miyagoe, K. Kobayashi, H. Uemura, H. Nishioka, H. Matsuzaki, A. Sawa, and Y. Tokura, 2011, Phys. Rev. B **83**, 125102.

Okamoto, S., and A. J. Millis, 2004, Phys. Rev. B **70**, 241104.

Okimoto, Y., *et al.*, 2011, Phys. Rev. B **84**, 121102.

Onda, K., *et al.*, 2008, Phys. Rev. Lett. **101**, 067403.

Ono, A., S. Okumura, S. Imai, and Y. Akagi, 2024, Phys. Rev. B **110**, 125111.

Ono, M., H. Kishida, and H. Okamoto, 2005, Phys. Rev. Lett. **95**, 087401.

Ono, M., K. Miura, A. Maeda, H. Matsuzaki, H. Kishida, Y. Taguchi, Y. Tokura, M. Yamashita, and H. Okamoto, 2004, Phys. Rev. B **70**, 085101.

Orthodoxou, C., A. Zaïr, and G. H. Booth, 2021, npj Quantum Mater. **6**, 76.

Otsuki, J., and Y. Kuramoto, 2013, Phys. Rev. B **88**, 024427.

Parcollet, O., M. Ferrero, T. Ayral, H. Hafermann, I. Krivenko, L. Messio, and P. Seth, 2015, Comput. Phys. Commun. **196**, 398.

Paris, E., *et al.*, 2021, npj Quantum Mater. **6**, 51.

Park, T. J., and J. C. Light, 1986, J. Chem. Phys. **85**, 5870.

Pavarini, E., S. Biermann, A. Poteryaev, A. I. Lichtenstein, A. Georges, and O. K. Andersen, 2004, Phys. Rev. Lett. **92**, 176403.

Pecharsky, V. K., and K. A. Gschneidner, Jr., 1999, J. Magn. Magn. Mater. **200**, 44.

Peierls, R., 1933, Z. Phys. **80**, 763.

Perez-Salinas, D., A. S. Johnson, D. Prabhakaran, and S. Wall, 2022, Nat. Commun. **13**, 238.

Perfetti, L., P. A. Loukakos, M. Lisowski, U. Bovensiepen, H. Berger, S. Biermann, P. S. Cornaglia, A. Georges, and M. Wolf, 2006, Phys. Rev. Lett. **97**, 067402.

Perfetto, E., Y. Pavlyukh, and G. Stefanucci, 2022, Phys. Rev. Lett. **128**, 016801.

Peronaci, F., M. Schiró, and O. Parcollet, 2018, Phys. Rev. Lett. **120**, 197601.

Petocchi, F., S. Beck, C. Ederer, and P. Werner, 2019, Phys. Rev. B **100**, 075147.

Petocchi, F., J. Chen, J. Li, M. Eckstein, and P. Werner, 2023, Phys. Rev. B **107**, 165102.

Petocchi, F., C. W. Nicholson, B. Salzmann, D. Pasquier, O. V. Yazyev, C. Monney, and P. Werner, 2022, Phys. Rev. Lett. **129**, 016402.

Phien, H. N., J. A. Bengua, H. D. Tuan, P. Corboz, and R. Orús, 2015, Phys. Rev. B **92**, 035142.

Picano, A., and M. Eckstein, 2021, Phys. Rev. B **103**, 165118.

Picano, A., F. Grandi, and M. Eckstein, 2023, Phys. Rev. B **107**, 245112.

Picano, A., J. Li, and M. Eckstein, 2021, Phys. Rev. B **104**, 085108.

Pizzi, A., A. Nunnenkamp, and J. Knolle, 2021, Phys. Rev. Lett. **127**, 140602.

Plankl, M., *et al.*, 2021, Nat. Photonics **15**, 594.

Polkovnikov, A., K. Sengupta, A. Silva, and M. Vengalattore, 2011, Rev. Mod. Phys. **83**, 863.

Pooyan, S., and D. Bauer, 2024, arXiv:2406.04114.

Potthoff, M., and W. Nolting, 1999, Phys. Rev. B **59**, 2549.

Prajapati, G. L., *et al.*, 2024, arXiv:2410.01424.

Prelovšek, P., and J. Bonča, 2013, in *Strongly Correlated Systems*, Springer Series in Solid-State Sciences Vol. 176, edited by A. Avella and F. Mancini (Springer, Berlin), pp. 1–30.

Pruschke, T., and N. Grewe, 1989, Z. Phys. B **74**, 439.

Qin, T., and W. Hofstetter, 2017, Phys. Rev. B **96**, 075134.

Rahav, S., I. Gilary, and S. Fishman, 2003, Phys. Rev. A **68**, 013820.

Rameau, J. D., *et al.*, 2016, Nat. Commun. **7**, 13761.

Rammal, H., A. Ralko, S. Ciuchi, and S. Fratini, 2024, Phys. Rev. Lett. **132**, 266502.

Ravnik, J., M. Diego, Y. Gerasimenko, Y. Vaskivskyi, I. Vaskivskyi, T. Mertelj, J. Vodeb, and D. Mihailovic, 2021, Nat. Commun. **12**, 2323.

Ray, S., M. Eckstein, and P. Werner, 2025, Phys. Rev. B **111**, 174309.

Ray, S., Y. Murakami, and P. Werner, 2023, Phys. Rev. B **108**, 174515.

Ray, S., and P. Werner, 2024, Phys. Rev. B **110**, L041109.

Revelle, J. P., A. Kumar, and A. F. Kemper, 2019, Condens. Matter **4**, 79.

Rigol, M., V. Dunjko, V. Yurovsky, and M. Olshanii, 2007, Phys. Rev. Lett. **98**, 050405.

Rincón, J., E. Dagotto, and A. E. Feiguin, 2018, Phys. Rev. B **97**, 235104.

Rincón, J., and A. E. Feiguin, 2021, Phys. Rev. B **104**, 085122.

Rini, M., R. Tobey, N. Dean, J. Itatani, Y. Tomioka, Y. Tokura, R. W. Schoenlein, and A. Cavalleri, 2007, Nature (London) **449**, 72.

Roelcke, C., L. Z. Kastner, M. Graml, A. Biereder, J. Wilhelm, J. Repp, R. Huber, and Y. A. Gerasimenko, 2024, Nat. Photonics **18**, 595.

Rohringer, G., H. Hafermann, A. Toschi, A. A. Katanin, A. E. Antipov, M. I. Katsnelson, A. I. Lichtenstein, A. N. Rubtsov, and K. Held, 2018, Rev. Mod. Phys. **90**, 025003.

Rosch, A., D. Rasch, B. Binz, and M. Vojta, 2008, Phys. Rev. Lett. **101**, 265301.

Rossi, F., and T. Kuhn, 2002, Rev. Mod. Phys. **74**, 895.

Rubio-Abadal, A., M. Ippoliti, S. Hollerith, D. Wei, J. Rui, S. L. Sondhi, V. Khemani, C. Gross, and I. Bloch, 2020, Phys. Rev. X **10**, 021044.

Runge, E., and E. K. U. Gross, 1984, Phys. Rev. Lett. **52**, 997.

Sahota, D. G., R. Liang, M. Dion, P. Fournier, H. A. Dabkowska, G. M. Luke, and J. S. Dodge, 2019, Phys. Rev. Res. **1**, 033214.

Sakai, D., T. Yamakawa, H. Ueda, R. Ikeda, T. Miyamoto, and H. Okamoto, 2024, Commun. Phys. **7**, 40.

Sandholzer, K., Y. Murakami, F. Görg, J. Minguzzi, M. Messer, R. Desbuquois, M. Eckstein, P. Werner, and T. Esslinger, 2019, Phys. Rev. Lett. **123**, 193602.

Sandri, M., and M. Fabrizio, 2013, Phys. Rev. B **88**, 165113.

Sandri, M., and M. Fabrizio, 2015, Phys. Rev. B **91**, 115102.

Sangiovanni, G., *et al.*, 2006, Phys. Rev. B **73**, 205121.

Sato, M., S. Takayoshi, and T. Oka, 2016, Phys. Rev. Lett. **117**, 147202.

Sayyad, S., and M. Eckstein, 2016, Phys. Rev. Lett. **117**, 096403.

Sayyad, S., R. Žitko, H. U. R. Strand, P. Werner, and D. Golež, 2019, Phys. Rev. B **99**, 045118.

Scherg, S., T. Kohlert, P. Sala, F. Pollmann, B. Hebbe Madhusudhana, I. Bloch, and M. Aidelsburger, 2021, Nat. Commun. **12**, 4490.

Schiró, M., and M. Fabrizio, 2010, Phys. Rev. Lett. **105**, 076401.

Schiró, M., and M. Fabrizio, 2011, Phys. Rev. B **83**, 165105.

Schiulaz, M., and M. Müller, 2014, AIP Conf. Proc. **1610**, 11.

Schlawin, F., D. M. Kennes, and M. A. Sentef, 2022, Appl. Phys. Rev. **9**, 011312.

Schlünzen, N., J.-P. Joost, and M. Bonitz, 2020, Phys. Rev. Lett. **124**, 076601.

Schmidt, P., and H. Monien, 2002, arXiv:cond-mat/0202046.

Schmitt, D., *et al.*, 2022, Nature (London) **608**, 499.

Schollwöck, U., 2005, Rev. Mod. Phys. **77**, 259.

Schollwöck, U., 2011, Ann. Phys. (Amsterdam) **326**, 96.

Schubert, O., *et al.*, 2014, Nat. Photonics **8**, 119.

Schüler, M., M. Eckstein, and P. Werner, 2018, Phys. Rev. B **97**, 245129.

Schüler, M., D. Golez, Y. Murakami, N. Bittner, A. Herrmann, H. U. Strand, P. Werner, and M. Eckstein, 2020, Comput. Phys. Commun. **257**, 107484.

Schüler, M., J. A. Marks, Y. Murakami, C. Jia, and T. P. Devereaux, 2021, Phys. Rev. B **103**, 155409.

Schüler, M., and M. A. Sentef, 2021, J. Electron Spectrosc. Relat. Phenom. **253**, 147121.

Schultz, D. J., A. Khoury, F. Desrochers, O. Tavakol, E. Z. Zhang, and Y. B. Kim, 2023, arXiv:2309.00037.

Schwinger, J., 1951, Phys. Rev. **82**, 664.

Seiler, H., *et al.*, 2021, Nano Lett. **21**, 6171.

Sengupta, A. M., and A. Georges, 1995, Phys. Rev. B **52**, 10295.

Sensarma, R., D. Pekker, E. Altman, E. Demler, N. Strohmaier, D. Greif, R. Jördens, L. Tarruell, H. Moritz, and T. Esslinger, 2010, Phys. Rev. B **82**, 224302.

Sentef, M., A. F. Kemper, B. Moritz, J. K. Freericks, Z.-X. Shen, and T. P. Devereaux, 2013, Phys. Rev. X **3**, 041033.

Sentef, M. A., 2017, Phys. Rev. B **95**, 205111.

Sentef, M. A., J. Li, F. Künzel, and M. Eckstein, 2020, Phys. Rev. Res. **2**, 033033.

Shao, C., H. Lu, X. Zhang, C. Yu, T. Tohyama, and R. Lu, 2022, Phys. Rev. Lett. **128**, 047401.

Shao, C., T. Tohyama, H.-G. Luo, and H. Lu, 2016, Phys. Rev. B **93**, 195144.

Shen, K. M., and J. S. Davis, 2008, Mater. Today **11**, 14.

Shimano, R., and N. Tsuji, 2020, Annu. Rev. Condens. Matter Phys. **11**, 103.

Shinaoka, H., E. Gull, and P. Werner, 2017, Comput. Phys. Commun. **215**, 128.

Shinaoka, H., M. Wallerberger, Y. Murakami, K. Nogaki, R. Sakurai, P. Werner, and A. Kauch, 2023, Phys. Rev. X **13**, 021015.

Shinjo, K., S. Sota, and T. Tohyama, 2022, Phys. Rev. Res. **4**, L032019.

Shinjo, K., Y. Tamaki, S. Sota, and T. Tohyama, 2021, Phys. Rev. B **104**, 205123.

Shinjo, K., and T. Tohyama, 2017, Phys. Rev. B **96**, 195141.

Shirakawa, T., S. Miyakoshi, and S. Yunoki, 2020, Phys. Rev. B **101**, 174307.

Shockley, W., and H. J. Queisser, 1961, J. Appl. Phys. **32**, 510.

Si, Q., and J. L. Smith, 1996, Phys. Rev. Lett. **77**, 3391.

Sierant, P., M. Lewenstein, A. Scardicchio, L. Vidmar, and J. Zakrzewski, 2025, Rep. Prog. Phys. **88**, 026502.

Silva, R. E. F., I. V. Blinov, A. N. Rubtsov, O. Smirnova, and M. Ivanov, 2018, Nat. Photonics **12**, 266.

Simard, O., and P. Werner, 2022, Phys. Rev. B **106**, L241110.

Singla, R., A. Simoncig, M. Först, D. Prabhakaran, A. L. Cavalieri, and A. Cavalleri, 2013, Phys. Rev. B **88**, 075107.

Singla, R., *et al.*, 2015, Phys. Rev. Lett. **115**, 187401.

Sono, N., T. Otaki, T. Kitao, T. Yamakawa, D. Sakai, T. Morimoto, T. Miyamoto, and H. Okamoto, 2022, Commun. Phys. **5**, 72.

Sood, A., *et al.*, 2021, Science **373**, 352.

Sorantin, M. E., A. Dorda, K. Held, and E. Arrigoni, 2018, Phys. Rev. B **97**, 115113.

Sous, J., B. Kloss, D. M. Kennes, D. R. Reichman, and A. J. Millis, 2021, Nat. Commun. **12**, 5803.

Spirkl, W., and H. Ries, 1995, Phys. Rev. B **52**, 11319.

Sriram, A., and M. Claassen, 2022, Phys. Rev. Res. **4**, L032036.

Stahl, C., N. Dasari, J. Li, A. Picano, P. Werner, and M. Eckstein, 2022, Phys. Rev. B **105**, 115146.

Stefanucci, G., and R. Van Leeuwen, 2013, *Nonequilibrium Many-Body Theory of Quantum Systems: A Modern Introduction* (Cambridge University Press, Cambridge, England).

Stojchevska, L., I. Vaskivskyi, T. Mertelj, P. Kusar, D. Svetin, A. Brazovskii, and D. Mihailovic, 2014, Science **344**, 177.

Stoliar, P., L. Cario, E. Janod, B. Corraze, C. Guillot-Deudon, S. Salmon-Bourmand, V. Guiot, J. Tranchant, and M. Rozenberg, 2013, Adv. Mater. **25**, 3222.

Stoudenmire, E., and S. R. White, 2012, Annu. Rev. Condens. Matter Phys. **3**, 111.

Strack, R., and D. Vollhardt, 1992, Phys. Rev. B **46**, 13852.

Strand, H. U. R., D. Golež, M. Eckstein, and P. Werner, 2017, Phys. Rev. B **96**, 165104.

Strohmaier, N., D. Greif, R. Jördens, L. Tarruell, H. Moritz, T. Esslinger, R. Sensarma, D. Pekker, E. Altman, and E. Demler, 2010, Phys. Rev. Lett. **104**, 080401.

Subedi, A., 2021, C. R. Phys. **22**, 161.

Subedi, A., A. Cavalleri, and A. Georges, 2014, Phys. Rev. B **89**, 220301.

Sugimoto, K., and S. Ejima, 2023, arXiv:2305.09909.

Sun, H., B. Yang, H.-Y. Wang, Z.-Y. Zhou, G.-X. Su, H.-N. Dai, Z.-S. Yuan, and J.-W. Pan, 2021, Nat. Phys. **17**, 990.

Sun, P., and G. Kotliar, 2002, Phys. Rev. B **66**, 085120.

Sun, Z., and A. J. Millis, 2020, Phys. Rev. X **10**, 021028.

Sur, S., A. Udupa, and D. Sen, 2022, Phys. Rev. B **105**, 054423.

Suzuki, T., *et al.*, 2019, Commun. Phys. **2**, 115.

Taguchi, Y., T. Matsumoto, and Y. Tokura, 2000, Phys. Rev. B **62**, 7015.

Tai, W. T., and M. Claassen, 2023, arXiv:2303.01597.

Takahashi, A., H. Gomi, and M. Aihara, 2002, Phys. Rev. Lett. **89**, 206402.

Takahashi, A., S. Yoshikawa, and M. Aihara, 2002, Phys. Rev. B **65**, 085103.

Takahashi, M., T. Tohyama, and S. Maekawa, 2002, Phys. Rev. B **66**, 125102.

Takamura, N., T. Miyamoto, S. Liang, K. Asada, T. Terashige, Y. Takahashi, T. Hasegawa, and H. Okamoto, 2023, Phys. Rev. B **107**, 085147.

Takasan, K., M. Nakagawa, and N. Kawakami, 2019, arXiv:1908.06107.

Takasan, K., and M. Sato, 2019, Phys. Rev. B **100**, 060408.

Takasan, K., and M. Tezuka, 2021, arXiv:2111.03857.

Takayoshi, S., H. Aoki, and T. Oka, 2014, Phys. Rev. B **90**, 085150.

Takayoshi, S., Y. Murakami, and P. Werner, 2019, Phys. Rev. B **99**, 184303.

Takayoshi, S., M. Sato, and T. Oka, 2014, Phys. Rev. B **90**, 214413.

Tanaka, Y., and K. Yonemitsu, 2011, Phys. Rev. B **83**, 085113.

Tancogne-Dejean, N., M. J. T. Oliveira, and A. Rubio, 2017, Phys. Rev. B **96**, 245133.

Tancogne-Dejean, N., M. A. Sentef, and A. Rubio, 2018, Phys. Rev. Lett. **121**, 097402.

Tayagaki, T., and K. Tanaka, 2001, Phys. Rev. Lett. **86**, 2886.

Teitelbaum, S. W., B. K. Ofori-Okai, Y.-H. Cheng, J. Zhang, F. Jin, W. Wu, R. D. Averitt, and K. A. Nelson, 2019, Phys. Rev. Lett. **123**, 267201.

Terashige, T., T. Ono, T. Miyamoto, T. Morimoto, H. Yamakawa, N. Kida, T. Ito, T. Sasagawa, T. Tohyama, and H. Okamoto, 2019, Sci. Adv. **5**, eaav2187.

Thoenniss, J., A. Lerose, and D. A. Abanin, 2023, Phys. Rev. B **107**, 195101.

Thoenniss, J., M. Sonner, A. Lerose, and D. A. Abanin, 2023, Phys. Rev. B **107**, L201115.

Tindall, J. and B. Buča, J. R. Coulthard, and D. Jaksch, 2019, Phys. Rev. Lett. **123**, 030603.

Tindall, J., F. Schlawin, M. Buzzi, D. Nicoletti, J. R. Coulthard, H. Gao, A. Cavalleri, M. A. Sentef, and D. Jaksch, 2020, Phys. Rev. Lett. **125**, 137001.

Titvinidze, I., A. Dorda, W. von der Linden, and E. Arrigoni, 2015, Phys. Rev. B **92**, 245125.

Tohyama, T., 2006, J. Phys. Soc. Jpn. **75**, 034713.

Tohyama, T., 2013, Eur. Phys. J. Special Topics **222**, 1065.

Tokura, Y., and N. Nagaosa, 2000, Science **288**, 462.

Torre, E. G. D., and D. Dentelski, 2021, SciPost Phys. **11**, 040.

Trotzky, S., P. Cheinet, S. Fölling, M. Feld, U. Schnorrberger, A. M. Rey, A. Polkovnikov, E. A. Demler, M. D. Lukin, and I. Bloch, 2008, Science **319**, 295.

Trugman, S. A., 1988, Phys. Rev. B **37**, 1597.

Tsuji, N., P. Barmettler, H. Aoki, and P. Werner, 2014, Phys. Rev. B **90**, 075117.

Tsuji, N., M. Eckstein, and P. Werner, 2013, Phys. Rev. Lett. **110**, 136404.

Tsuji, N., T. Oka, and H. Aoki, 2008, Phys. Rev. B **78**, 235124.

Tsuji, N., T. Oka, P. Werner, and H. Aoki, 2011, Phys. Rev. Lett. **106**, 236401.

Uchida, K., G. Mattoni, S. Yonezawa, F. Nakamura, Y. Maeno, and K. Tanaka, 2022, Phys. Rev. Lett. **128**, 127401.

Uchida, S., T. Ido, H. Takagi, T. Arima, Y. Tokura, and S. Tajima, 1991, Phys. Rev. B **43**, 7942.

Udono, M., T. Kaneko, and K. Sugimoto, 2023, Phys. Rev. B **108**, L081304.

Udono, M., K. Sugimoto, T. Kaneko, and Y. Ohta, 2022, Phys. Rev. B **105**, L241108.

Ueda, R., K. Kuroki, and T. Kaneko, 2024, Phys. Rev. B **109**, 075122.

Valmispild, V., E. Gorelov, M. Eckstein, A. Lichtenstein, H. Aoki, M. Katsnelson, M. Ivanov, and O. Smirnova, 2023, arXiv:2208.04647.
Vampa, G., T. J. Hammond, N. Thiré, B. E. Schmidt, F. Légaré, C. R. McDonald, T. Brabec, D. D. Klug, and P. B. Corkum, 2015, Phys. Rev. Lett. **115**, 193603.
Vampa, G., C. R. McDonald, G. Orlando, P. B. Corkum, and T. Brabec, 2015, Phys. Rev. B **91**, 064302.
Vampa, G., C. R. McDonald, G. Orlando, D. D. Klug, P. B. Corkum, and T. Brabec, 2014, Phys. Rev. Lett. **113**, 073901.
Vaskivskyi, I., I. A. Mihailovic, S. Brazovskii, J. Gospodaric, T. Mertelj, D. Svetin, P. Sutar, and D. Mihailovic, 2016, Nat. Commun. **7**, 11442.
Vedeneev, S. I., D. K. Maude, and J. M. Byrne, 2008, Phys. Rev. B **78**, 052509.
Verdozzi, C., 2008, Phys. Rev. Lett. **101**, 166401.
Verma, A., *et al.*, 2023, arXiv:2304.02149.
Vidal, G., 2004, Phys. Rev. Lett. **93**, 040502.
Vidal, G., 2007, Phys. Rev. Lett. **98**, 070201.
Vidas, L., *et al.*, 2020, Phys. Rev. X **10**, 031047.
Vidmar, L., J. Bonča, T. Tohyama, and S. Maekawa, 2011, Phys. Rev. Lett. **107**, 246404.
Viebahn, K., J. Minguzzi, K. Sandholzer, A.-S. Walter, M. Sajnani, F. Görg, and T. Esslinger, 2021, Phys. Rev. X **11**, 011057.
Vilk, Y., and A.-M. Tremblay, 1997, J. Phys. I (France) **7**, 1309.
Vitalone, R. A., *et al.*, 2022, Nano Lett. **22**, 5689.
Vogelgesang, S., G. Storeck, J. G. Horstmann, T. Diekmann, M. Sivis, S. Schramm, K. Rossnagel, S. Schäfer, and C. Ropers, 2018, Nat. Phys. **14**, 184.
Wais, M., M. Eckstein, R. Fischer, P. Werner, M. Battiato, and K. Held, 2018, Phys. Rev. B **98**, 134312.
Wall, S., L. Foglia, D. Wegkamp, K. Appavoo, J. Nag, R. F. Haglund, J. Stähler, and M. Wolf, 2013, Phys. Rev. B **87**, 115126.
Wall, S., D. Prabhakaran, A. T. Boothroyd, and A. Cavalleri, 2009, Phys. Rev. Lett. **103**, 097402.
Wall, S., *et al.*, 2018, Science **362**6414, 572.
Wang, X., *et al.*, 2022, Faraday Discuss. **237**, 300.
Wang, Y., C.-C. Chen, B. Moritz, and T. P. Devereaux, 2018, Phys. Rev. Lett. **120**, 246402.
Wang, Y., Y. Chen, T. P. Devereaux, B. Moritz, and M. Mitrano, 2021, Commun. Phys. **4**, 212.
Wang, Y., Y. Chen, C. Jia, B. Moritz, and T. P. Devereaux, 2020, Phys. Rev. B **101**, 165126.
Wang, Y. H., H. Steinberg, P. Jarillo-Herrero, and N. Gedik, 2013, Science **342**6157, 453.
Wegkamp, D., *et al.*, 2014, Phys. Rev. Lett. **113**, 216401.
Weidinger, S. A., and M. Knap, 2017, Sci. Rep. **7**, 45382.
Weissman, M. B., 1993, Rev. Mod. Phys. **65**, 829.
Werner, D., J. Lotze, and E. Arrigoni, 2023, Phys. Rev. B **107**, 075119.
Werner, J. H., S. Kolodinski, and H. J. Queisser, 1994, Phys. Rev. Lett. **72**, 3851.
Werner, P., and M. Casula, 2016, J. Phys. Condens. Matter **28**, 383001.
Werner, P., and M. Eckstein, 2013, Phys. Rev. B **88**, 165108.
Werner, P., and M. Eckstein, 2015, Europhys. Lett. **109**, 37002.
Werner, P., and M. Eckstein, 2016, Struct. Dyn. **3**, 023603.
Werner, P., M. Eckstein, M. Müller, and G. Refael, 2019, Nat. Commun. **10**, 5556.
Werner, P., D. Golez, and M. Eckstein, 2022, Phys. Rev. B **106**, 165106.
Werner, P., E. Gull, M. Troyer, and A. J. Millis, 2008, Phys. Rev. Lett. **101**, 166405.
Werner, P., K. Held, and M. Eckstein, 2014, Phys. Rev. B **90**, 235102.
Werner, P., S. Johnston, and M. Eckstein, 2021, Europhys. Lett. **133**, 57005.
Werner, P., J. Li, D. Golež, and M. Eckstein, 2019, Phys. Rev. B **100**, 155130.
Werner, P., and A. J. Millis, 2007a, Phys. Rev. B **75**, 085108.
Werner, P., and A. J. Millis, 2007b, Phys. Rev. Lett. **99**, 126405.
Werner, P., and Y. Murakami, 2020, Phys. Rev. B **102**, 241103.
Werner, P., and Y. Murakami, 2021, Phys. Rev. B **104**, L201101.
Werner, P., T. Oka, M. Eckstein, and A. J. Millis, 2010, Phys. Rev. B **81**, 035108.
Werner, P., T. Oka, and A. J. Millis, 2009, Phys. Rev. B **79**, 035320.
Werner, P., H. U. R. Strand, S. Hoshino, and M. Eckstein, 2017, Phys. Rev. B **95**, 195405.
Werner, P., H. U. R. Strand, S. Hoshino, Y. Murakami, and M. Eckstein, 2018, Phys. Rev. B **97**, 165119.
Werner, P., N. Tsuji, and M. Eckstein, 2012, Phys. Rev. B **86**, 205101.
White, S. R., 1992, Phys. Rev. Lett. **69**, 2863.
White, S. R., and A. E. Feiguin, 2004, Phys. Rev. Lett. **93**, 076401.
Wolf, F. A., I. P. McCulloch, and U. Schollwöck, 2014, Phys. Rev. B **90**, 235131.
Woynarovich, F., 1982, J. Phys. C **15**, 97.
Yada, H., T. Miyamoto, and H. Okamoto, 2013, Appl. Phys. Lett. **102**, 091104.
Yamakawa, H., *et al.*, 2017, Nat. Mater. **16**, 1100.
Yamakawa, H., *et al.*, 2021, Nat. Commun. **12**, 953.
Yamakawa, T., T. Miyamoto, D. Sakai, and H. Okamoto, 2023, New J. Phys. **25**, 093044.
Yang, C. N., 1989, Phys. Rev. Lett. **63**, 2144.
Yonemitsu, K., 2022, J. Phys. Soc. Jpn. **91**, 104702.
Yonemitsu, K., and N. Maeshima, 2009, Phys. Rev. B **79**, 125118.
Yonemitsu, K., and N. Miyashita, 2003, Phys. Rev. B **68**, 075113.
Yonemitsu, K., S. Miyashita, and N. Maeshima, 2011, J. Phys. Soc. Jpn. **80**, 084710.
Yonemitsu, K., and K. Nasu, 2008, Phys. Rep. **465**, 1.
Yoshikawa, N., H. Suganuma, H. Matsuoka, Y. Tanaka, P. Hemme, M. Cazayous, Y. Gallais, M. Nakano, Y. Iwasa, and R. Shimano, 2021, Nat. Phys. **17**, 909.
Yuzbashyan, E. A., and M. Dzero, 2006, Phys. Rev. Lett. **96**, 230404.
Zaanen, J., G. A. Sawatzky, and J. W. Allen, 1985, Phys. Rev. Lett. **55**, 418.
Zadik, R. H., *et al.*, 2015, Sci. Adv. **1**, e1500059.
Zawadzki, K., and A. E. Feiguin, 2019, Phys. Rev. B **100**, 195124.
Zener, C., 1934, Proc. R. Soc. A **145**, 523.
Zener, C., 1951, Phys. Rev. **82**, 403.
Zhang, F. C., and T. M. Rice, 1988, Phys. Rev. B **37**, 3759.
Zhang, J., X. Tan, M. Liu, S. W. Teitelbaum, K. W. Post, F. Jin, K. A. Nelson, D. N. Basov, W. Wu, and R. D. Averitt, 2016, Nat. Mater. **15**, 956.
Zhu, W., B. Fauseweh, A. Chacon, and J.-X. Zhu, 2021, Phys. Rev. B **103**, 224305.
Zong, A., *et al.*, 2019a, Phys. Rev. Lett. **123**, 097601.
Zong, A., *et al.*, 2019b, Nat. Phys. **15**, 27.
Zong, A., *et al.*, 2021, Phys. Rev. Lett. **127**, 227401.